Aerosol-Jet Printed Nanocomposites for Flexible and Stretchable Thermoelectric Generators

Canlin Ou

King's College

University of Cambridge

Supervisor: Dr Sohini Kar-Narayan

This thesis is submitted for the degree of

Doctor of Philosophy

October 2019

Declaration

This thesis is submitted for the degree of Doctor of Philosophy at the University of Cambridge. This thesis is the result of my own work and includes nothing which is the outcome of work done in collaboration except as declared in the Preface and specified in the text. It is not substantially the same as any that I have submitted, or, is being concurrently submitted for a degree or diploma or other qualification at the University of Cambridge or any other University or similar institution, except as declared in the Preface and specified in the text. I further state that no substantial part of my thesis has already been submitted, or, is being concurrently submitted for any such degree, diploma or other qualification at the University of Cambridge or any other University or similar institution except as declared in the Preface and specified in the text. It does not exceed the word limit of 60,000 words including abstract, tables, footnotes and appendices, but excluding table of contents, photographs, diagrams, figure captions, list of figures/diagrams, list of abbreviations/acronyms, bibliography and acknowledgements.

Canlin Ou

October 2019

Cambridge, United Kingdom

Abstract

Aerosol-Jet Printed Nanocomposites for Flexible and Stretchable Thermoelectric Generators

Canlin Ou

Converting waste heat from the environment into usable electricity, via thermoelectric generators (TEGs) based on thermoelectric (TE) materials, is predicted to be one of the most promising renewable energy solutions of the future. TE materials produce a current when subjected to a temperature gradient as a result of the Seebeck effect, and are characterised by a TE figure of merit, $ZT = S^2\sigma T/\kappa$, where S is the Seebeck coefficient, σ is the electrical conductivity, T is the operating temperature, and κ is the thermal conductivity. TEGs can be used as an energy source for 'small-power' applications, such as wireless sensors and wearable devices. Nonetheless, traditional inorganic TE materials pose significant challenges owing to their high cost, toxicity, scarcity, and brittleness, particularly when it comes to applications requiring flexibility and/or stretchability. On the other hand, organic TE polymers are less expensive, environmentally friendly, and flexible. However, they typically suffer from poor TE performance due to their comparatively low S and σ. This thesis therefore seeks to explore solutions for high-performance and mechanically conformable TEGs based on organic-inorganic TE nanocomposites, adopting a material engineering approach to enhancing TE properties while ensuring the flexibility and/or stretchability of TEGs.

In this work, a flexible and robust TEG based on a novel hybrid nanocomposite structure for harvesting energy from low-grade waste heat, has been successfully fabricated via a customised and scalable aerosol-jet printing (AJP) technique. Firstly, Bi_2Te_3 nanoparticles and Sb_2Te_3 nanoflakes were fabricated using a solvothermal synthesis approach, and their resulting morphological and microstructural properties were studied. They were then incorporated into a conducting polymer matrix poly(3,4-ethylenedioxythiophene) polystyrene sulfonate (PEDOT:PSS) via the AJP method, resulting in well-dispersed TE nanocomposites on flexible polyimide substrates. These TE nanocomposites comprised Bi_2Te_3/Sb_2Te_3 nano-inclusions with higher S and σ embedded within a polymeric PEDOT:PSS matrix having lower κ. The compositions were dynamically tuned and controlled by the in-house developed *in situ* mixing

method to optimise the resulting power factor (PF = $S^2\sigma$). The AJP technique used in this work allows functional materials to be printed from inks with a wide range of viscosities and constituent particle sizes and shapes. The morphological and TE properties of AJ-printed nanocomposite structures were then evaluated as a function of the composition so that optimum ink formulation and printing conditions could be found to maximise the final TE performance. Importantly, these TE nanocomposites were found to be particularly stable and robust upon repeated flexing. They can be directly integrated into high-performance TEGs with minimal post-possessing treatment, making them particularly suitable for flexible TE applications.

Subsequently, multiwall carbon nanotubes (MWCNTs) were introduced to enhance σ of AJ-printed nanocomposites, thereby achieving even higher PF values. A novel *in situ* mixing method was capable of simultaneously incorporating high-S Sb_2Te_3 nanoflakes and high-σ MWCNTs that could provide good inter-particle connectivity, to significantly enhance the TE performance of PEDOT:PSS. Rigorous flexing and fatigue tests also confirmed the excellent mechanical robustness and stability of these AJ-printed MWCNTs-based TE nanocomposites. The added MWCNTs have led to not only higher σ, but they also have improved the mechanical flexibility and fatigue robustness of the resulting nanocomposites.

Since the *ZT* and PF of TE materials often have a strong dependence on temperature, a single TE material spanning a given temperature range is unlikely to have an optimal *ZT* or PF across the entire range, leading to the inefficient TEG performance. The temperature-dependent TE properties of AJ-printed TE nanocomposites were therefore studied as a function of the loading fraction, with a view to enhancing the overall TE performance of a TEG by varying its composition accordingly across a given temperature range. For the first time, compositionally graded thermoelectric composites (CG-TECs) have been developed and shown to improve TE performance over TEGs having a single composition across the same temperature range. The composition of the TE nanocomposite was systematically tuned along the length of the TEG in order to optimise the PF along the temperature gradient between which it operates.

Lastly, the AJP technique was used to fabricate free-standing and stretchable TE structures, by printing serpentine patterns of the TE ink onto a sacrificial substrate that was subsequently removed. The TE performance and stretchability under different imposed mechanical conditions were evaluated, including testing for the reliability of prolonged stretching cycles. The CG-TEC concept was also incorporated into the stretchable structure to achieve further improvement of TE performance.

Acknowledgements

This work was supervised by Dr Sohini Kar-Narayan in the Department of Materials Science and Metallurgy, the University of Cambridge.

First and foremost, I am indebted to Dr Sohini Kar-Narayan for the provision of experimental facilities necessary to conduct my research, and her patient guidance and encouragement all the time. Many thanks to her excellent supervision and extremely thorough proof-reading on my thesis. I am also very grateful for the financial support from the European Research Council through an ERC Starting Grant (Grant no. ERC-2014-STG-639526, NANOGEN) as well as from an EPSRC grant (Centre for Advanced Materials for Integrated Energy Systems (CAMIES), EP/P007767/1), in which I benefitted in the form of facilities and consumables.

Sincere thanks are also owed to Dr Qingshen Jing, Dr Abhijeet Sangle, and Dr Anuja Datta for their demonstration, fruitful discussions, extensive academic supports, and personal encouragements on my sample preparation, characterisation, data analysis, and thesis writing.

I sincerely thank Dr Michael Smith, Dr Sanjiv Sambandan, Dr Vijay Narayan, Dr Pedro Sanchez Jimenez, Zipeng Liu, Tommaso Busolo, Dr Yeonsik Choi, Yi Zhu, Dr Chess Boughey, Nordin Catic, Dr Anke Husmann, Dr Yonatan Calahorra, and Bhaskaran Nair for their valuable discussions and instruments training. I thank all research staffs and students in Device Materials group for providing me helps and friendly research atmosphere. I would also like to thank Lu Zhang, Thomas Chalklen, and Alex Zanre for their enthusiasm and patience when supervising their research projects.

I gratefully thank China Scholarship Council and Cambridge Commonwealth, European and International Trust for offering me the fully-funded studentship.

Last but not least, I would like to thank my friends and my beloved family, especially Jingsi Liang and Canjiang Ou, for their unwavering love, encouragement, and financial support all the time during my whole PhD study.

Contents

Publications and Presentations xiii

List of Figures xv

List of Tables xxi

List of Abbreviations xxiii

List of Symbols xxv

Chapter 1 Introduction **1**

1.1 Challenges and Objectives 1

1.2 Thesis Outline 5

Chapter 2 Background and Theory **7**

2.1 Energy Harvesting Technologies 8

2.2 Thermoelectric Energy Harvesting 10

2.3 Fundamentals of Thermoelectrics 14

2.3.1 Thermoelectric Effect 14

2.3.2 Thermoelectric Properties 15

2.3.3 Thermoelectric Performance 17

2.4 Thermoelectric Materials 18

2.4.1 Inorganic Thermoelectric Materials 18

2.4.2 Organic Thermoelectric Materials 20

2.4.3 Carbon-based Thermoelectric Materials 23

2.4.4 Hybrid Thermoelectric Nanocomposites 25

2.5 Thermoelectric Generators 27

2.6 Microscale Additive Manufacturing Routes 30

2.6.1 Printing Techniques 31

2.6.2 Other Deposition Techniques 37

2.6.3 Design of Flexible Thermoelectric Generators 37
2.7 Functionally Graded Thermoelectric Materials 41
2.7.1 Functionally Graded Material Concept 41
2.7.2 Segmented Structures 42
2.7.3 Continuous Structures 45
2.8 Stretchable Thermoelectric Generators 47
2.8.1 Material Modification Approaches 47
2.8.2 Device Structure Modification Approaches 49
Chapter 3 Materials and Methods 53
3.1 Nanomaterial Fabrication 54
3.1.1 Top-down Fabrication Approach 54
3.1.2 Bottom-up Fabrication Approach 55
3.2 Structural Characterisation 57
3.2.1 Scanning Electron Microscopy (SEM) 57
3.2.2 X-ray Diffraction (XRD) 58
3.2.3 Transmission Electron Microscopy (TEM) 58
3.3 Aerosol-Jet Printing 59
3.3.1 Printing Process 59
3.3.2 Printing Control 67
3.3.3 Pattern Printing 68
3.4 Ink Preparation 69
3.4.1 Ultrasonic Atomiser 70
3.4.2 Pneumatic Atomiser 70
3.4.3 Printing Conditions 71
3.5 Post-processing Treatments 73
3.5.1 Thermal Annealing 73
3.5.2 Surface Treatment 73
3.6 Measurement of Dimensions 74
3.7 Thermoelectric Measurements 74
3.7.1 Meandering Structure 77

3.7.2 Strip Structure 82
3.7.3 Serpentine Structure 84
3.8 Mechanical Tests 87
3.8.1 Flexibility Test 87
3.8.2 Fatigue Test 88
3.8.3 Stretchability Test 89
3.9 Finite Element Analysis 90
3.9.1 COMSOL Simulation 90
3.9.2 ABAQUS Simulation 91
3.10 Thermoelectric Generator Fabrication 92
3.10.1 Flexible Thermoelectric Coasters 92
3.10.2 Compositionally Graded Thermoelectric Generators 94
3.10.3 Free-standing Stretchable Thermoelectric Generators 95
3.10.4 Substrate-based Stretchable Thermoelectric Generators 100
3.10.5 Stretchable Compositionally Graded Thermoelectric Generators 102
Chapter 4 Bi_2Te_3/Sb_2Te_3-based Thermoelectric Nanocomposites 103
4.1 Nanomaterial Characterisation 104
4.1.1 Hand-ground Bi_2Te_3 and Sb_2Te_3 Particles 104
4.1.2 Ball-milled Bi_2Te_3 and Sb_2Te_3 Particles 106
4.1.3 Solvothermal-synthesised Bi_2Te_3 and Sb_2Te_3 Particles 107
4.2 Inorganic Film Printing 111
4.3 Organic Film Printing 113
4.4 Conventional Composite Printing 115
4.5 Novel Composite Printing 120
4.5.1 In situ Mixing Method 120
4.5.2 Transporting Process Modification 123
4.5.3 Comparison of Printed Layers 125
4.5.4 Morphology Characterisation of Printed Nanocomposites 126
4.5.5 Thermoelectric Measurements of Printed Nanocomposites 129
4.5.6 Simulation of Printed Nanocomposites 132

4.6 Flexibility Tests 133
4.7 Flexible Thermoelectric Coasters 134
4.8 Summary 137
Chapter 5 Multiwall Carbon Nanotube-based Thermoelectric Nanocomposites 139
5.1 Printing of Carbon Nanotube-based Nanocomposites 140
5.2 Influence of Surfactant Addition on Printed Nanocomposites 141
5.3 Surface Treatment of Printed Nanocomposites 142
5.4 Morphology Characterisation of Printed Nanocomposites 144
5.5 Thermoelectric Measurements of Printed Nanocomposites 147
5.6 Flexibility and Fatigue Tests 150
5.7 Summary 153
Chapter 6 Compositionally Graded Thermoelectric Composites 155
6.1 Temperature-dependent Power Factor of Printed Nanocomposites 156
6.1.1 Pristine PEDOT:PSS Film 1577
6.1.2 Bi_2Te_3-PEDOT:PSS Thermoelectric Nanocomposites 158
6.1.3 MWCNTs-PEDOT:PSS Thermoelectric Nanocomposites 160
6.1.4 Sb_2Te_3-PEDOT:PSS Thermoelectric Nanocomposites 160
6.2 Compositionally Graded Thermoelectric Composites 163
6.2.1 Design of Compositionally Graded Thermoelectric Composites 163
6.2.2 Thermal Conductivity Calculation and Prediction of Nanocomposites 165
6.2.3 Simulation of Compositionally Graded Thermoelectric Composites 168
6.2.4 Fabrication of Compositionally Graded Thermoelectric Composites 172
6.2.5 Interfaces of Compositionally Graded Thermoelectric Composites 175
6.3 Compositionally Graded Thermoelectric Generators 177
6.3.1 Performance of Compositionally Graded Thermoelectric Generators 177
6.3.2 Prototype of Compositionally Graded Thermoelectric Generator 181
6.4 Summary 183
Chapter 7 Stretchable Thermoelectric Generators 185
7.1 Morphology Characterisation of Stretchable Structures 186

7.1.1 In-plane Structure 186
7.1.2 Out-of-plane Structure 188
7.1.3 Multilayered Structure 189
7.2 Simulation of Stretchable Structures 191
7.2.1 In-plane Structure 191
7.2.2 Out-of-plane Structure 193
7.3 Stretchability Tests 195
7.3.1 In-plane Structure 196
7.3.2 Out-of-plane Structure 199
7.4 Fatigue Tests 202
7.5 Multilayered Stretchable Thermoelectric Generators 207
7.6 Prototype of Stretchable Thermoelectric Generator 210
7.7 Stretchable Compositionally Graded Thermoelectric Generator 213
7.8 Substrate-based Stretchable Thermoelectric Generators 217
7.9 Summary 221
Chapter 8 Conclusions and Future Work 223
8.1 Conclusions 223
8.2 Future Work 227
8.2.1 Materials Selection 227
8.2.2 Characterisation and Measurement Techniques 229
8.2.3 Device Fabrication 230
Appendix 231
Reference List 251

Publications and Presentations

Publications

1) **C. Ou**, L. Zhang, Q. Jing, V. Narayan, S. Kar-Narayan, "Compositionally Graded Organic-inorganic Nanocomposites for Enhanced Thermoelectric Performance". *Adv. Electron. Mater.*, 2019, 6 (1), 1900720.

2) **C. Ou**, Q. Jing, T. Busolo, S. Kar-Narayan, Invited Book Chapter in "Advances in Nanostructured Materials and Nanopatterning Technologies for Healthcare, Environment and Energy Applications". Editor: Dario Pisignano. *Elsevier*, 2019, 381-437.

3) **C. Ou**, A. L. Sangle, T. Chalklen, Q. Jing, V. Narayan, S. Kar-Narayan, "Enhanced Thermoelectric Properties of Flexible Aerosol-Jet Printed Carbon Nanotube-Based Nanocomposites". *APL Materials*, 2018, 6 (9), 096101.

4) **C. Ou**, A. L. Sangle, A. Datta, Q. Jing, T. Busolo, T. Chalklen, V. Narayan, S. Kar-Narayan, "Fully Printed Organic-Inorganic Nanocomposites for Flexible Thermoelectric Applications". *ACS Applied Materials & Interfaces*, 2018, 10 (23), 19580–19587.

5) Q. Jing, Y.S. Choi, M. Smith, **C. Ou**, T. Busolo, S. Kar-Narayan, "Freestanding Functional Structures by Aerosol-Jet Printing for Stretchable Electronics and Sensing Applications". *Advanced Materials Technologies*, 2019, 4, 1900048

6) Q Jing, Y.S. Choi, M Smith, Catic N., **C. Ou**, S. Kar-Narayan, "Aerosol-Jet Printed Fine-Featured Triboelectric Sensors for Motion Sensing". *Advanced Materials Technologies*, 2018, 4, 1800328

7) Y. Calahorra, **C. Ou**, C. Boughey, S. Kar-Narayan, "Piezoelectric Semiconducting Nanowires". Invited book chapter in "Nanowires for Energy Applications". Editors: Sudha Mokkapati & Chennupati Jagadish. *Elsevier*, 2018, 98, 445-478.

8) A. Datta, Y. Choi, E. Chalmers, **C. Ou**, S. Kar-Narayan, "Piezoelectric Nylon-11 Nanowire

Arrays Grown by Template Wetting for Vibrational Energy Harvesting Applications". *Advanced Functional Materials*, 2017, 27 (2), 1604262.

9) A. Datta, P. Sanchez-Jimenez, Y. Calahorra, **C. Ou**, S. Sahonta1, M. Fornari, S. Kar-Narayan, "Lead-free Polycrystalline Ferroelectric Nanowires with Enhanced Curie Temperature". *Advanced Functional Materials*, 2017, 27 (29), 1701169.

10) R. A. Whiter, Y. Calahorra, **C. Ou**, S. Kar-Narayan, "Observation of Confinement-Induced Self-Poling Effects in Ferroelectric Polymer Nanowires Grown by Template Wetting". *Macromolecular Materials and Engineering*, 2016, 301 (9), 1016-1025.

11) **C. Ou**, Q. Jing, S. Kar-Narayan, "Free-standing Stretchable Thermoelectric Generator for Thermal Energy Harvesting Applications". *In preparation*.

12) **C. Ou**, S. Sambandan, S. Kar-Narayan, "Extracting Thermal Conductivity and Seebeck Coefficient in Printed Thermoelectrics from the Transmission Line Model". *In preparation*.

Patents

1) S. Kar-Narayan, **C. Ou**, "Thermoelectric Materials, Devices and Methods of Production Thereof". 2019, United Kingdom (GB) Patent Application No: 1905395.8,2019 (Filed)

Presentations

1) **Oral**, "Aerosol-Jet Printed Flexible Thermoelectric Nanocomposites for Thermal Energy Harvesting", *2019 International Conference on Thermoelectrics,* Gyeongju, Korea.

2) **Oral**, "Flexible Printed Thermoelectric Nanocomposites and Nanogenerators Based on Hybrid Materials", *2018 CAM-IES Meeting*, Cambridge, UK.

3) **Poster**, "Flexible Printed Thermoelectric Nanocomposites and Nanogenerators Based on Hybrid Materials", *2018 Interfaces in Energy Materials Conference*, Cambridge, UK.

4) **Oral,** "Turning up the Heat on Energy Harvesting --- Flexible Printed Thermoelectric Nanogenerators", *2017 MRS Fall Meeting & Exhibit*, Boston, USA.

List of Figures

Figure 2.1 Schematic showing some potential applications of TEGs 13

Figure 2.2 Schematic showing the operating principles of basic TE devices 15

Figure 2.3. The trade-off between S, σ, and κ with increasing free carrier concentration 17

Figure 2.4 Comparison of ZT values of various inorganic TE materials 20

Figure 2.5 Schematic of a basic TEG and a commercial TEG module. 29

Figure 2.6 Schematic of different additive manufacturing techniques 35

Figure 2.7 Different types of currently developed flexible TEG designs 39

Figure 2.8 Schematic showing three different types of FGM structures 41

Figure 2.9 Comparison of temperature-dependent ZT values for various TE materials 44

Figure 2.10 Schematic showing current fabrication processes for stretchable TEGs 52

Figure 3.1 Overview of fabrication processes for AJ-printed TE nanocomposites 53

Figure 3.2 Schematic showing the growth process of Bi_2Te_3 and Sb_2Te_3 56

Figure 3.3 Annotated photograph of the Optomec AJP 200 system 60

Figure 3.4 Schematic of atomisation processes by different atomisers 61

Figure 3.5 Annotated photograph depicting the fine-feature deposition print head 64

Figure 3.6 Annotated photograph displaying the motion system 65

Figure 3.7 Flow chart demonstrating some basic steps to design pattern printing 67

Figure 3.8 Various design patterns AJ-printed on a silicon substrate 68

Figure 3.9 Schematic representation of the TE measurement setup 76

Figure 3.10 Schematic of the AutoCAD-designed meandering structure 77

Figure 3.11 Schematic depicting the AJP process and AJ-printed samples 79

Figure 3.12 Enlarged view of AJ-printed TE patterns 81

Figure 3.13 Schematic of the AutoCAD-designed strip-shaped structure 82
Figure 3.14 Schematic of the temperature-dependent TE measurement setup. 83
Figure 3.15 Schematic of serpentine structures for stretchable TEGs 84
Figure 3.16 Schematic illustration of the TE performance measurement setup 86
Figure 3.17 Photographic images of AJ-printed TE nanocomposites being flexed 87
Figure 3.18 Flexing test on AJ-printed TE nanocomposites under hand-bending. 88
Figure 3.19 Stretchability test on AJ-printed free-standing stretchable structures 89
Figure 3.20 Photographic images of 5-layer AJ-printed TE nanocomposites 93
Figure 3.21 Photographic image of a setup for measuring voltage and power outputs 94
Figure 3.22 Fabrication processes of the free-standing stretchable TE structure 95
Figure 3.23 Photographic images of AJ-printed PI and PEDOT:PSS films 97
Figure 3.24 Schematic of AutoCAD-designed patterns depicting design structures 99
Figure 3.25 Photographic images of the AJ-printed single-layer stretchable structure 99
Figure 3.26 Schematic of AutoCAD-designed serpentine structure and strip structure. 100
Figure 3.27 Designed pattern and photographic image of the stretchable CG-TEG 102
Figure 4.1 SEM images of hand-ground Bi_2Te_3 and Sb_2Te_3 particles 105
Figure 4.2 SEM images of ball-milled Bi_2Te_3 and Sb_2Te_3 particles 107
Figure 4.3 SEM images of solvothermal-synthesised Bi_2Te_3 and Sb_2Te_3 particles 108
Figure 4.4 XRD results of solvothermal-synthesised Bi_2Te_3 and Sb_2Te_3 particles 110
Figure 4.5 SEM images of AJ-printed Sb_2Te_3 nanoflakes on the silicon and PI substrates .. 112
Figure 4.6 SEM images of 10-layer AJ-printed Bi_2Te_3 and Sb_2Te_3 particles 112
Figure 4.7 Optical microscope image and SEM micrograph of PEDOT:PSS film 114
Figure 4.8 Thermoelectric measurements on AJ-printed PEDOT:PSS films 114
Figure 4.9 Morphology comparison 1-layer, 5-layer and 10-layer printed nanocomposites. 116
Figure 4.10 Profilometer thickness measurements of different printed layers 117
Figure 4.11 Thermoelectric measurements on S, σ, and PF of different printed layers. 117
Figure 4.12 Morphology and microstructure of 10-layer AJ-printed nanocomposites 118

Figure 4.13 Width and thickness measurements of 10-layer AJ-printed nanocomposites 118
Figure 4.14 Thermoelectric measurements AJ-printed nanocomposites 119
Figure 4.15 Schematic illustration of the AJP setup and the printing process. 122
Figure 4.16 SEM images presenting the overspray phenomena 123
Figure 4.17 Schematic illustrations of the tube used for transporting aerosol droplets..... 124
Figure 4.18 Comparison of overspray and fine feature of printed nanocomposites 124
Figure 4.19 Morphology comparison of printed nanocomposites loaded with Sb_2Te_3 125
Figure 4.20 Profilometer thickness measurement of printed nanocomposites. 126
Figure 4.21 Thermoelectric measurements of nanocomposites loaded with Sb_2Te_3. 126
Figure 4.22 Schematic of a novel *in situ* mixing method for the nanocomposite printing.... 127
Figure 4.23 Morphology and microstructure comparisons of printed nanocomposites 128
Figure 4.24 Morphology and microstructure comparisons of printed nanocomposites 128
Figure 4.25 Width and thickness measurements of printed nanocomposites 129
Figure 4.26 Thermoelectric measurements of printed nanocomposites 131
Figure 4.27 Temperature profile of AJ-printed TE nanocomposites..... 132
Figure 4.28 Flexing test on AJ-printed nanomposites with different loading ratios..... 134
Figure 4.29 Photographic images of AJ-printed TEG prototype in parallel or series mode.. 136
Figure 5.1 Schematic showing the fabrication of MWCNTs-PEDOT:PSS nanocomposite.. 142
Figure 5.2 Thermoelectric measurements of MWCNTs-PEDOT:PSS nanocomposites. 143
Figure 5.3 SEM image of representative MWCNTs-PEDOT:PSS nanocomposite lines 145
Figure 5.4 SEM images of AJ-printed with 100 wt.% MWCNTs and Sb_2Te_3-MWCNTs..... 146
Figure 5.5 EDX mapping of MWCNTs-PEDOT:PSS nanocomposites 146
Figure 5.6 Thermoelectric measurements of MWCNTs-PEDOT:PSS nanocomposites 149
Figure 5.7 Flexing test on AJ-printed nanocomposites with MWCNTs and Sb_2Te_3 151
Figure 5.8 SEM images of AJ-printed nanocomposite before and after fatigue test 152
Figure 6.1 Temperature-dependent PF measurements of AJ-printed nanocomposites..... 157
Figure 6.2 Temperature-dependent PF measurements of AJ-printed PEDOT:PSS films..... 158

Figure 6.3 Temperature-dependent PF measurements of Bi_2Te_3-based nanocomposites 159
Figure 6.4 Temperature-dependent PF measurement of MWCNTs-based nanocomposites . 161
Figure 6.5 Temperature-dependent PF measurements of Sb_2Te_3-based nanocomposites..... 162
Figure 6.6 Temperature-dependent measurements of Bi_2Te_3-PEDOT:PSS nanocomposite.. 164
Figure 6.7 Temperature-dependent measurements of Sb_2Te_3-PEDOT:PSS nanocomposite. 164
Figure 6.8 Temperature-dependent measurements of MWCNTs-based nanocomposites 165
Figure 6.9 Calculation and prediction of the effective thermal conductivity 167
Figure 6.10 Temperature distribution profiles of the 'good design' and 'bad design' 170
Figure 6.11 Temperature distribution profiles of the 'good design' and 'bad design' 171
Figure 6.12 COMSOL simulation of the temperature distribution profile of CG-TEC 173
Figure 6.13 COMSOL simulation of the temperature distribution profile of CG-TEC 174
Figure 6.14 Photographic image of CG-TEC of Bi_2Te_3-PEDOT:PSS nanocomposite 176
Figure 6.15 Photographic and thermal images of CG-TEG under a constant applied ΔT..... 177
Figure 6.16 Voltage and power outputs against various external load resistance 179
Figure 6.17 Comparison of voltage and power outputs of different TEGs..... 180
Figure 6.18 Voltage and power output measurements of different CG-TEGs. 180
Figure 6.19 Voltage and power output measurements of different CG-TEGs 181
Figure 6.20 Photographic image of the AJ-printed CG-TEG on a flexible PI sheet 182
Figure 6.21 Photographic image of the coiled CG-TEG prototype 182
Figure 7.1 Top-down SEM image of the serpentine TE structure with in-plane design..... 186
Figure 7.2 Cross-sectional SEM images of the free-standing TE structure. 187
Figure 7.3 Profilometer thickness measurements of the PI supporting layer 187
Figure 7.4 Top-down SEM image of the AJ-printed stretchable TE structure..... 188
Figure 7.5 Profilometer thickness measurements of the PI supporting layer 189
Figure 7.6 Top-down SEM image of the 3-layer AJ-printed stretchable TE structure 190
Figure 7.7 Top-down SEM image of the 3-layer AJ-printed stretchable TE structure 190
Figure 7.8 Profilometer thickness measurements of AJ-printed stretchable TE structure..... 191

Figure 7.9 ABAQUS simulation on strain distribution of PI supporting structure.....192
Figure 7.10 ABAQUS simulation on strain distribution of PEDOT:PSS-PI composite 193
Figure 7.11 ABAQUS simulation on strain distribution of PEDOT:PSS-Ag-PI composite. 194
Figure 7.12 Resistance measurement of the free-standing stretchable TE structure 195
Figure 7.13 Voltage and power output measurements on printed stretchable TE structures. 197
Figure 7.14 Photographic and thermal images of printed stretchable TE structures 198
Figure 7.15 Voltage and power output measurements on printed stretchable TE structures .200
Figure 7.16 Photographic and thermal images of printed stretchable TE structures 201
Figure 7.17 Fatigue test on the stretchable TE structure with in-plane design. 203
Figure 7.18 Fatigue test on the stretchable TE structure with out-of-plane design 204
Figure 7.19 Photographic images of stretchable TE structures 205
Figure 7.20 SEM image of the stretchable TE structure with in-plane design 206
Figure 7.21 SEM image of the stretchable TE structure with out-of-plane design 206
Figure 7.22 Voltage and power output measurements on printed stretchable TE structures .208
Figure 7.23 Photographic and thermal images of 3-layer printed stretchable TE structures .209
Figure 7.24 Top-down and side-view images of the stretchable TEG with 5 TE legs.....212
Figure 7.25 Top-down and side-view images of the stretchable TEG with 10 TE legs.....212
Figure 7.26 Top-down SEM image of the stretchable CG-TEG with in-plane design. 214
Figure 7.27 Thermal images of the stretchable CG-TEG and the single-phase TEG. 214
Figure 7.28 Voltage and power output measurements on printed stretchable CG-TEG.....215
Figure 7.29 Photographic and thermal images of printed stretchable CG-TEG. 216
Figure 7.30 Photographic images of PDMS or PU substrate-based stretchable TEGs.....218
Figure 7.31 Photographic images of single-layer and 3-layer stretchable TE structures 219
Figure 7.32 Photographic and thermal images of 3-layer stretchable TE structures 220
Figure A.1 Schematic drawing of the distributed resistor-capacitor transmission line 234
Figure A.2 AutoCAD-design patterns and photographs of Ag thermometers 238
Figure A.3 Plotting of input temperature, output temperature, and voltage output. 239

Figure A.4 SEM images, EDX analysis, and EDX mapping of SnSe nanosheets.....242
Figure A.5 XRD results and TEM analysis of SnSe nanosheets 243
Figure A.6 DSC analysis of Bi_2Te_3 and Sb_2Te_3 powder 244
Figure A.7 Schematic drawing of the test bench for out-of-plane TE measurement.....245
Figure A.8 Schematic illustrations of sample preparation and measurement.....246
Figure A.9 SEM images of AJ-printed PEDOT:PSS-based nanocomposites. 247
Figure A.10 SEM images of AJ-printed PVDF-based nanocomposites 247
Figure A.11 Profilometer thickness measurements of PVDF-based nanocomposites.....248
Figure A.12 Photographic images of different AJ-printed PEDOT:PSS films 248
Figure A.13 Photographic image of the PDMS substrate-based stretchable TEG 249

List of Tables

Table 2-1 Comparison of current renewable energy harvesting technologies 12

Table 2-2 Comparison of existing organic TE polymers reported in the literature 24

Table 2-3 Comparison of traditional bulk TEGs with printed flexible TEGs. 30

Table 2-4 Comparison of some major additive manufacturing techniques 36

Table 2-5 Comparison of printed TE composites with different designs 40

Table 2-6 Comparison of different functionally graded thermoelectric materials 46

Table 2-7 Comparison of current stretchable thermoelectric materials and generators 51

Table 3-1 Comparison of the ultrasonic atomiser and pneumatic atomiser 62

Table 3-2 Comparison of different printing parameters used in the UA and PA 64

Table 3-3 Comparison of different applicable substrates for the AJP process. 66

Table 3-4 Some optimum printing conditions for different bespoke inks used in this work ... 72

Table 3-5 Summary of different material properties adopted in the ABAQUS simulation 91

Table 3-6 Comparison of different sacrificial substrate materials 97

Table 4-1 Comparison of TE properties of different EG-treated PEDOT:PSS films 114

Table 4-2 Investigation on the miscibility of various solvents and particles 115

Table 4-3 Optimum printing conditions for different Bi_2Te_3/Sb_2Te_3-based samples 122

Table 4-4 Measurements of open-circuit voltage and short-circuit current 136

Table 5-1 Optimum printing conditions for different MWCNTs-based samples 140

Table 6-1 Summary of material properties of different TE materials 167

Table A-1 Comparison of the oxidation and melting temperature of different materials 244

Table A-2 Comparison of voltage and power outputs as a function of TE leg dimension 248

List of Abbreviations

0D	Zero-Dimensional
1D	One-Dimensional
2D	Two-Dimensional
3D	Three-Dimensional
Ag	Silver
AJ	Aerosol-jet
AJP	Aerosol-jet Printing
Bi_2Te_3	Bismuth Telluride
CG-TECs	Compositionally Graded Thermoelectric Composites
CG-TEGs	Compositionally Graded Thermoelectric Generators
CG-TEMs	Compositionally Graded Thermoelectric Materials
CNTs	Carbon Nanotubes
Cu	Copper
DC	Direct Current
DI	De-ionised
DMSO	Dimethyl Sulfoxide
DMF	N,N-dimethylformamide
EDX	Energy Dispersive X-ray
EG	Ethylene Glycol
FEA	Finite Element Analysis
FR	Focus Ratio
FGMs	Functionally Graded Materials
HRTEM	High-Resolution Transmission Electron Microscopy
MWCNTs	Multiwall Carbon Nanotubes
NMP	N-Methyl-2-pyrrolidone
N_2	Nitrogen
PA	Pneumatic Atomiser

PDMS	Poly(dimethylsiloxane)
PVDF	Polyvinylidene Fluoride
PU	Polyurethane
PI	Polyimide
PVA	Polyvinyl Alcohol
PEDOT:PSS	Poly(3,4-ethylenedioxythiophene) Polystyrene Sulfonate
QF	Quality Factor
SEM	Scanning Electron Microscopy
Sb_2Te_3	Antimony Telluride
SnSe	Tin Selenide
TE	Thermoelectric
TEGs	Thermoelectric Generators
TEM	Transmission Electron Microscopy
UA	Ultrasonic Atomiser
XRD	X-Ray Diffraction

List of Symbols

A, a	Cross-section area [m^2]
c	Thermal capacitance [J/K]
d	Thermal diffusivity [m^2/s]
d_{out}	Outer width [m]
d_{in}	Inner width [m]
D_p	Average crystallite size [nm]
E	Electric field [V/m]
I_{sc}	Short-circuit current [A]
J	Current density [A/m^2]
L, x	Length [m]
κ	Thermal conductivity [W/(m.K)]
κ_l	Lattice conductivity [W/(m·K)]
κ_e	Electron conductivity [W/(m·K)]
K	Thermal conductivity of the medium [W/(m·K)]
K^*	Thermal conductivity of the spherical particulate [W/(m·K)]
K_{eff}	Effective thermal conductivity of nanocomposite [W/(m·K)]
n	Number of TE legs
PF	Power factor [$\mu W/(m.K^2)$]
P_{max}	Maximum power or power density output [W]
Q_{atm}	Atomiser gas flow rate [cm^3/min]
Q_{sh}	Sheath gas flow rate [cm^3/min]
Q_{exh}	Exhaust gas flow rate [cm^3/min]
r	Thermal resistance [K/W]
R	Electrical resistance [Ω]
R_L	External load resistance [Ω]
R_S	Internal sample resistance [Ω]
R_{sh}	Sheet resistance [Ω/sq]

s	Specific heat capacity [J/(kg·K)]
S	Seebeck coefficient [V/K]
t	Thickness [m]
T_c	Cold side temperature [K]
T_h	Hot side temperature [K]
T_x	Intersection temperature [K]
V_{oc}	Open-circuit voltage [V]
W	Thermal power [W]
wt.%	Weight Percentage [%]
ZT	Figure of merit
ΔT	Temperature difference between the hot and cold sides [K]
ΔV	Voltage difference between the hot and cold sides [V]
ΔQ	Atomiser–exhaust delta value [cm^3/min]
α	Thermopower [V/K]
β	Line broadening at half the maximum intensity
ρ	Mass density [kg/m^3]
σ	Electrical conductivity [S/m]
φ	Volume fraction [%]
χ	Energy conversion efficiency [%]
θ	Bragg angle [^{o}]
λ	X-ray wavelength [Å]
ε	Tensile strain [%]

Chapter 1

Introduction

1.1 Challenges and Objectives

Thermoelectric (TE) power generation is one of the most promising renewable energy harvesting technologies of the future, as this can potentially be environmentally friendly, long-lasting, and maintenance-free.[1] Thermoelectric generators (TEGs) could potentially address the massive energy demands of future self-powered electronic devices, in particular in remote, dangerous, and/or inaccessible locations. Consequently, there has been tremendous interest in developing low-cost, flexible, and efficient TEGs for thermal energy harvesting applications. However, one of the most pressing issues that researchers in this field are facing is the development of new classes of high-performance TE materials. Although the Seebeck effect, by which a material produces a voltage when subjected to a temperature gradient, was discovered in 1821, its potential for the power generation was recognised only in the mid-twentieth century. The difficulty of processing inorganic TE materials, low energy conversion efficiency, and high cost per Watt have largely limited their scope to niche applications, such as spacecraft and military applications.[1,2] Since the 1990s, research in thermoelectrics has thrived through the discovery of new and efficient inorganic TE material compositions, and also through the boost in TE performance achieved by the nanostructuring of materials.[1,3–7]

Nevertheless, TE power generation has still been a relatively under-utilised energy harvesting technique due to the lack of suitable TE materials with high performance and energy conversion efficiency, as well as the difficulty in processing existing inorganic TE materials into easily adaptable electronic devices, particularly in light of scarcity, high cost, and

toxicity.[8–10] Furthermore, their typically rigid and brittle nature significantly constrains their applicability in flexible and/or wearable devices.[9,11,12] The complexity of raw material fabrication and large-scale device production also poses major technological hurdles to the advancement of TE technologies for 'small-power' applications, such as wireless sensors and portable devices. More recently, solution-processable organic TE polymers have been proposed as substitutes, which have attracted great attention as low-cost and flexible, or even stretchable TE devices.[13–15] Although their TE performance still lags considerably behind their inorganic counterparts, and their applications are mostly constrained to a lower temperature range (at and close to room temperature), they are low-cost, light-weight, non-toxic, abundant, and solution-processable with low thermal conductivity, which is beneficial to achieve good TE performance.[10,16,17] Importantly, they are particularly well suited for the large-area deposition or printing that are critical for high-volume manufacturing of printed electronics.[18–21] Thus, the material selection is of vital importance, as the selected TE material not only determines the TE performance of the resulting TEGs, but it also places limits on parameters such as operating temperature ranges and imposed mechanical conditions. However, suitable TE materials that are performance-efficient and cost-effective are rare, and there exist associated difficulties with processing current TE materials into easily adaptable, conformable, and flexible TEGs.[1,3,5,8,9,22–25] In this context, nano-engineering tools can be employed to overcome some of the difficulties associated with single-phase TE materials by creating an organic-inorganic nanocomposite structure.[4,26,27] This has been intensively investigated as an effective approach to enhancing the TE performance of organic TE polymers, where high-performance inorganic TE nano-inclusions are embedded within the organic TE polymeric matrix to tune the final TE properties of nanocomposite structures. In addition, the ability to print them on flexible substrates is a particularly attractive feature, since the mechanical flexibility and stretchability are also crucial factors to be considered.[25] For some applications, like wearable electronics, stretchability is highly required. Nonetheless, the improvement of TE performance has been unsatisfactory owing to the poor distribution and dispersion of the inserted nano-fillers within the polymeric matrix. Uncontrollable interfaces and other defects are often introduced, which could result in poor electrical connections between particles and could give rise to other interface-related issues.[25] Thus, the main aims and objectives of this thesis are to achieve fully-printed well-dispersed TE nanocomposite structures with enhanced TE properties, and to obtain highly flexible and potentially stretchable TEGs.

In this work, *p*-type conducting polymer poly(3,4-ethylenedioxythiophene) polystyrene sulfonate (PEDOT:PSS) has been selected as the polymeric matrix, as it can be readily processed with high electrical conductivity.[28] Tellurides of bismuth and antimony (Bi_2Te_3/Sb_2Te_3) have been chosen as inorganic nano-inclusions by virtue of their excellent TE properties at or near room temperature.[1,3,5] Cost-effective, time-efficient, and solution-based material synthesis approaches have also been developed to yield high-quality inorganic TE nanomaterials in gram quantities. Subsequently, in order to obtain high-performance PEDOT:PSS-based nanocomposites, Bi_2Te_3/Sb_2Te_3 nanomaterials have been added for the enhancement of Seebeck coefficient, and multiwall carbon nanotubes (MWCNTs) have been included for the improvement of electrical conductivity. Furthermore, particular emphasis has been placed on developing surfactant-free printable inks for the fabrication of well-dispersed nanocomposite structures by using a state-of-the-art aerosol-jet printing (AJP) technique. This innovative printing technique can accommodate two separate ink sources (i.e. one for the organic component and the other for the inorganic component) and *in situ* mix different ink materials to form nanocomposite structures with effective control of dispersion and distribution of the loaded nano-fillers within the organic polymer matrix. By this process, the composition of nanocomposites can be dynamically tuned to optimise their overall TE performance as well as to overcome the TE performance constraints of constituent materials. Furthermore, in order to ascertain the correlation between the composition of the nanocomposite system and its TE properties, various loading ratios between organic and inorganic components have been carefully examined. In addition, different post-processing surface treatment routines have been conducted to further enhance their TE properties, and the optimum film printing and post-processing treatment conditions have been determined accordingly.

As current approaches to large-scale production of thermoelectric generator (TEG) still remain challenging, especially for flexible and stretchable TEGs, organic-based TEGs are well-suited in this respect. They can be easily integrated into flexible and wearable platforms by a variety of additive manufacturing routes. Since these flexible or stretchable TEGs are mostly deployed around low-grade heat sources (<100 ^{o}C), the high-performance organic-inorganic TE nanocomposite structures developed here can be incorporated into microscale flexible and/or stretchable TEG devices, by using the high-resolution AJP technique. Additionally, proper TEG device design, including the TE leg geometry optimisation, contact resistance minimisation, and *p*-*n* junction formation, should be taken into

consideration to achieve higher power output and improved efficiency. Computational modelling tools have also been employed to predict and optimise the device performance

While the field continues to be driven by the discovery of new TE materials, composites, and devices, a key issue that hinders TE performance across the board is often overlooked, as explained as follows. Since the figure-of-merit (*ZT*) or power factor (PF) used to evaluate thermal energy conversion efficiency and performance of TE materials has a strong dependence on temperature, a single TE material (whether single-phase or composite structure) spanning a given temperature range is unlikely to have an optimal *ZT* or PF value across the entire temperature range. This leads to the inefficient TE performance of the TEG in practical use. They therefore need to be optimised so that they can be fully and efficiently utilised across the whole operating temperature range. Here, a novel compositionally graded thermoelectric composite design has been adopted to enhance the overall thermal-to-electrical energy conversion efficiency of the printed TEG, where the PF has been optimised to work effectively over the whole temperature range by spatially varying the composition of the nanocomposite structure. The loading fraction of inorganic nano-insertions within a conducting polymeric matrix can be appropriately tuned along the length of the TE leg to give rise to such compositionally graded TE structures.

Finally, the author aims to fabricate a stretchable TEG that is based on an innovative free-standing serpentine structure for integration into wearable devices or waste heat recovery from curved surfaces, such as hot water pipes, where weight, flexibility, conformability, and stretchability are general requirements for the structural design of such TEG. A multilayered stretchable structure has also been proposed to further improve the power output so that it can be incorporated into a broader range of low-power miniature devices as a power supply.

1.2 Thesis Outline

This thesis systematically investigates the feasibility of fabricating flexible and/or stretchable TEGs based on novel hybrid organic-inorganic TE nanocomposites for thermal energy harvesting applications. This includes nanomaterial fabrication and characterisation, TE nanocomposite and generator fabrication, as well as TE property measurement. High-performance TEGs based on compositionally graded thermoelectric composite structures have also been explored. Furthermore, stretchable TEGs have been developed using an innovative free-standing serpentine structure.

Chapter 2 provides a comprehensive literature review covering the relevant background of thermal energy harvesting, fundamentals of thermoelectrics, thermoelectric materials, as well as microscale additive manufacturing techniques. This is followed by the background of flexible hybrid organic-inorganic TE nanocomposites being briefly discussed. Some existing additive manufacturing techniques and the feasibility of integrating functional nanomaterials into flexible and/or stretchable TEGs are also compared. The concept of functionally graded thermoelectric materials and the current development in stretchable TEGs are reviewed, which are followed by the aims and objectives of this thesis.

In Chapter 3, details of all experimental procedures and methodology for the TE nanomaterial and nanocomposite fabrication, morphological and microstructural characterisation, as well as TE property measurement of aerosol-jet (AJ) printed TE nanocomposites and their resulting prototypes of flexible and/or stretchable TEGs are provided. Importantly, the aerosol-jet printing (AJP) process is discussed in detail, as it is central to this thesis. The compositionally graded thermoelectric composite structure is also presented for the proof-of-concept investigation. Specific theoretical modelling and simulations are conducted to aid in the explanation and discussion of results in the following Chapters 4 to 7.

Chapters 4 to 7 present the major results and discussions of this thesis. In Chapter 4, the resulting morphology and crystal structure of different TE nanomaterials fabricated by various approaches are investigated. The AJP process for the Bi_2Te_3/Sb_2Te_3-based nanocomposite fabrication is then comprehensively described. A novel in-house developed *in situ* mixing method allows for precise control of nanomaterial dispersion and composition within the polymeric matrix. In order to demonstrate the feasibility of AJ-printed TE nanocomposites, a detailed study evaluating their morphology and microstructure as well as the resulting TE

properties is conducted. Various weight ratios of TE nanomaterials, such as solvothermal-synthesised Bi_2Te_3 nanoparticles and Sb_2Te_3 nanoflakes, loaded within a poly(3,4-ethylenedioxythiophene) polystyrene sulfonate (PEDOT:PSS) matrix are examined. After optimising the processing conditions, the as-grown PEDOT:PSS-based TE nanocomposites are forward to yield significant improvement of TE power factor. Subsequently, they are successfully incorporated into high-performance TEGs with excellent mechanical flexibility and good fatigue performance for stable and robust thermal energy harvesting. Multiwall carbon nanotubes (MWCNTs) are introduced to further enhance the TE performance, and the resulting AJ-printed TE nanocomposites are systematically analysed in Chapter 5. The added MWCNTs lead to not just higher electrical conductivity but also improved mechanical flexibility and fatigue robustness. In Chapter 6, since the composition of TE nanocomposites can be tuned by varying the loading ratio of inorganic nano-inclusions, various loading ratios of Bi_2Te_3 nanoparticles, Sb_2Te_3 nanoflakes, and MWCNTs are incorporated, respectively, into the PEDOT:PSS polymeric matrix to ascertain how the loaded nano-inclusions contribute to the TE properties of their resulting nanocomposites as a function of temperature. Accordingly, compositionally graded thermoelectric composites (CG-TECs) are developed to probe into the feasibility of utilising the concept of compositional grading for the enhancement of overall TE performance over a wide operating temperature range. Lastly, the author combines a stretchable serpentine structure with a facile and scalable AJP method and film lift-off technique for the fabrication of stretchable and wearable TEGs in Chapter 7. Single-layer free-standing TE structures with different device designs are formed for the investigation of fabrication process and material characterisation. A multilayered stretchable structure is also tested as a stretchable TEG prototype for self-powered wearable applications. The TE performance and mechanical stretchability under different mechanical strains are evaluated in detail. Also, the CG-TEC design is incorporated with the stretchable design to achieve higher TE performance.

Last but not least, Chapter 8 summarises this thesis and outlines related on-going projects, as well as some potential future research directions.

Chapter 2

Background and Theory

The purpose of this chapter is to provide an overview of the background and theory in thermoelectric research. Some general theories of thermal energy harvesting and thermoelectricity are provided. The fundamentals of thermoelectrics are also introduced, including the comparison of thermoelectric properties of existing inorganic and organic thermoelectric materials, as well as their composite structures. Subsequently, thermoelectric generator applications of inorganic and organic thermoelectric materials are compared in detail. The operating principles of different microscale additive manufacturing routes that may be used towards realising thermoelectric generators are briefly summarised. Among them, the aerosol-jet printing technique is elaborated upon, as it is central to this thesis. The concept of functionally graded thermoelectric materials is then discussed, including how it can be utilised to improve the energy conversion efficiency of existing thermoelectric generators. Lastly, some recent researches on stretchable thermoelectric generators are reviewed with a focus on various device fabrication routes.

2.1 Energy Harvesting Technologies

Ever-increasing energy consumption and the resulting environmental problems have attracted global attention in renewable energy research. Harvesting waste energy from ambient sources in the environment has therefore attracted increasing interest. Waste energy sources existing in the environment, such as sunlight, heat, mechanical vibrations, or magnetic energy, can be converted by using photovoltaic, thermoelectric, piezoelectric, triboelectric, or electromagnetic materials and devices, respectively. These energy harvesting technologies could aid in achieving the dual aim of alleviating the global warming issue by diminishing the CO_2 emission level of fossil fuel-based systems and improving the energy efficiency.[11]

At the same time, there is a growing need for alternative energy solutions to 'small-power' applications which typically run on more traditional sources, like batteries. Advances in nanoscience and nanotechnology have revolutionised technologies related to sensors and portable electronic appliances, thus opening up a whole new dimension to modern-day life. Nowadays, devices, such as smartphones, music players, activity and fitness trackers, heart-rate monitors and smartwatches, have become an integral part of modern lifestyle, with miniaturisation in size of electronic components. At the same time, the explosive growth witnessed by the Internet of Things (IoT) applications, including the wearable industry, has brought about new challenges in providing self-powered solutions that can be easily integrated, and that are conformable, lightweight, and flexible. Regardless of how much improvement has been achieved in reducing the power requirement of these portable appliances, they still need electric power to keep them running. However, batteries, as traditional power sources, require frequent replacing or recharging, and do not scale down easily with size and weight. Although battery technology itself has taken great strides in terms of environment-friendly materials and portability, their energy density remains insufficient to power these electronic gadgets without making them ungainly and bulky.[29,30] Thus, a more promising and sustainable way to power these 'small-power' electronic devices is by using ambient energy harvesting technologies. This can greatly supplement and extend the battery life, and can also solve the battery

replacement problem in challenging environments, such as those that may be difficult and/or expensive to access (e.g. sensors in off-shore oil rigs), or those embedded within building walls. Reliability and maintenance issues, as well as the cost and logistics of batteries, can be possibly mitigated by utilising energy harvesters to create autonomous self-powered systems.[23,25,31,32] These wearable energy harvester devices could also be deployed as power sources for wireless sensors, soft robotics, wearable electronics, or IoT applications.[23,33] For wearable appliances, such as wellness monitoring, health-related information is continuously gathered and transmitted via body-worn wireless sensors, such as GPS sensors, heart rate monitors, body movement monitors, and so forth.[32,34] These embedded wireless sensors also need to be fabricated at a lower cost so as to be integrated with current disposable medical devices.[34] Another key requirement of such sensors and their power sources is flexibility and conformability, in order to seamlessly be fitted onto skin or clothing, while affording minimal inconvenience to the user. Such concepts could be incorporated into 'smart' textiles that can generate power from human body heat and/or movements to power sensors within clothing for wireless physiological monitoring. The same concept in flexibility can be extended to other sensor applications to increase the usability of these devices, e.g. for deployment on curved surfaces or for flexibility in form factor.

In this context, different energy harvesting technologies, as summarised in Table 2-1, have drawn enormous attention. Tapping into these alternative energy sources could potentially satisfy the high demand for remote sensing and monitoring systems in industrial processes, equipment and buildings, self-powered wireless electronics, as well as implantable and wearable devices, to name a few, which are currently powered by traditional batteries.[23,25,31] For large-scale applications, photovoltaic and electromagnetic technologies are commonly used to harvest energy and convert into electricity by virtue of their relatively high power output and high conversion efficiency. Nevertheless, they are difficult to be scaled down to the sub-millimetre scale. Other major constraints are the positioning and operation period owing to the requirement of a large working surface area, as well as the variation of light intensity in the case of photovoltaics. These make them incompatible with small, embedded, and/or indoor

devices. In this regard, harvesting energy from human body heat,[32,35–37] mechanical motion or vibrations,[23,38,39] or tribological interactions[40–42] has become one of the major research themes to reduce the battery dependence or requirement. With the help of these energy harvesting technologies, wireless sensor nodes for the operation of micro/nano-systems and IoT applications can be truly sustainable, maintenance-free, and self-powered.[40] More importantly, since these energy harvesters can be easily scaled down to the sub-millimetre scale, and can easily access ambient energy sources, in particular heat or vibrations, there are a large number of possible applications where the energy harvesting can provide a power source or battery life enhancement for sensors or low-power systems-on-chip (e.g. Bluetooth).[43] However, there exist some key barriers to market, such as the device durability and reliability, biocompatibility and comfortability, conformability and wearability, adequate power generation, as well as autonomous power management and energy storage systems.[32]

2.2 Thermoelectric Energy Harvesting

Harvesting thermal energy has drawn considerable interest, as there are abundant heat sources in the environment. Nonetheless, a major part of this is wasted as presented in Figure 2.1 (a), viz., heat dissipated from exhausts, radiators and boilers, from chemical reactions in various industrial processes, from the combustion of fossil fuels in automobiles, from computers or moving parts in machineries, or even from human body, to name a few.[8,44] According to a U.S. Department of Energy report, an estimated ~60% of the energy consumed in the United States is lost to the environment in the form of heat.[8] Almost one third is wasted as low-grade heat (<100 ^{o}C), which renders the reuse of this waste heat increasingly indispensable.[8,45–47] Also, it is reported that an average adult human body dissipates ~100 W of heat to the surroundings, with a body temperature maintained at ~37 °C.[9,48] Even a fraction of this lost heat could lead to substantial energy generation, especially for wearable devices operating at sub-microwatts of power. Thermoelectric generators (TEGs) based on thermoelectric (TE) materials are prime candidates for thermal energy harvesting due to their ability to directly convert ambient and ever-present waste heat into usable electrical energy by

utilising the Seebeck effect.[49] At the same time, TEGs can offer promising potential for cooling applications without using any refrigerant gas, but via the Peltier effect.[49]

TEGs can be scaled to a variety of sizes to suit different applications, e.g. wearable devices with an area of 1-10 cm^2 or industrial devices with an area of up to 100 cm^2.[50] The market for flexible TEGs is significantly driven by the rapidly growing market in wireless sensor networks, autonomous systems, IoT devices, and wearable devices, which is predicted to increase by more than ten times over the next decade.[32] The power density requirement of a single sensor node is 10 $\mu W/cm^2$, while the mesh networks of multiple sensors require 100 $\mu W/cm^2$.[50] Current-developed TEGs can potentially achieve a power level of sub-microwatts by harvesting body heat under a small temperature difference (ΔT) of ~2-10 ^oC between the ambient air.[9,48,50] As illustrated in Figure 2.1 (b), TEGs can therefore be potentially integrated as energy sources to 'trickle charge' low-power miniature sensors, by being implanted in clothing or worn as patches, which typically cover hotter regions of the body, such as wrists, arms, etc.[9,51] In this context, Chen and Wright have provided a great insight into endless possibilities offered by TEGs in powering wearable and implantable gadgets, bio-sensors, pacemakers, and other medical applications.[48] For TEGs that are to be 'worn', a key technological challenge is making them lightweight, flexible, and even stretchable for the ergonomic convenience. Due to existing parasitic resistances that could deteriorate the performance of TEGs, as shown in Figure 2.1 (c), TEGs are required to be conformally attached onto various locations of the body so as to form better thermal contact with the skin. Thus, they need to be highly flexible, or even stretchable to create a steady-state heat flux flowing through them. Otherwise, most heat would be wasted through the skin and heatsink, leading to only a minimal ΔT across the TEG.[9] A large thermal resistance of TEG is desired to keep a possibly large and constant ΔT across it to generate a continuous power output.[32] Meanwhile, these wearable TEGs should be able to mechanically endure a wide range of dynamic motions that are carried out by the human body, e.g. bending, folding, twisting, or stretching.[52]

Table 2-1 Comparison of current renewable energy harvesting technologies from different energy sources, e.g. solar, thermal, mechanical, and magnetic energy.[31,53–59]

Energy Type	Power Density (mW/cm^2)	Pros	Cons	Potential Application
Photovoltaic	0.001-100	• Continuous DC power output • High power output and high efficiency • Abundant ambient light sources • No moving parts required, no noise or emissions • Mature technology and easy to scale up • High durability and long lifetime	• Incompatible with embedded or indoor devices that have a low light intensity • Limited positioning and operation period • Incompatible with embedded /indoor devices • Difficult to scale down to micron-size • Require large surface working area	Power stations, remote sensing and monitoring, wireless electronics, wearable devices, and spacecraft
Thermoelectric	0.001-1	• Continuous DC power output • Abundant ambient heat sources • Easy to scale down to micron-size • No moving parts required, no noise or emissions • High durability and long lifetime	• Low power output and low efficiency • Require large temperature gradient • High material cost, complicated and costly fabrication processes	Remote sensing and monitoring, wireless electronics, and wearable devices
Piezoelectric	0.1-1	• Abundant ambient vibration sources • Easy to scale down to micron-size • Mature technology and diverse applications • Broad working frequency and power ranges	• Low and non-continuous AC power output • Most lead-based materials, expensive and complicated fabrication processes • Low durability and prone to fail during use	Remote sensing and monitoring, wireless electronics, and wearable devices
Triboelectric	0.1-10	• High AC power output and high efficiency • Multiple working modes and easy to scale up • Low material cost and lightweight • Diverse choices of materials and applications	• Non-continuous AC power output • Difficult to scale down to micron-size • Low durability and prone to fail during use • High matched impedance	Remote sensing and monitoring, wireless electronics, and wearable devices
Electromagnetic	10-100	• High AC power output and high efficiency • Mature technology and easy to scale up • High durability and long lifetime	• Limited positioning and operation period • Very difficult to scale down to micron-size • High material cost and heavyweight	Power stations, remote sensing and monitoring

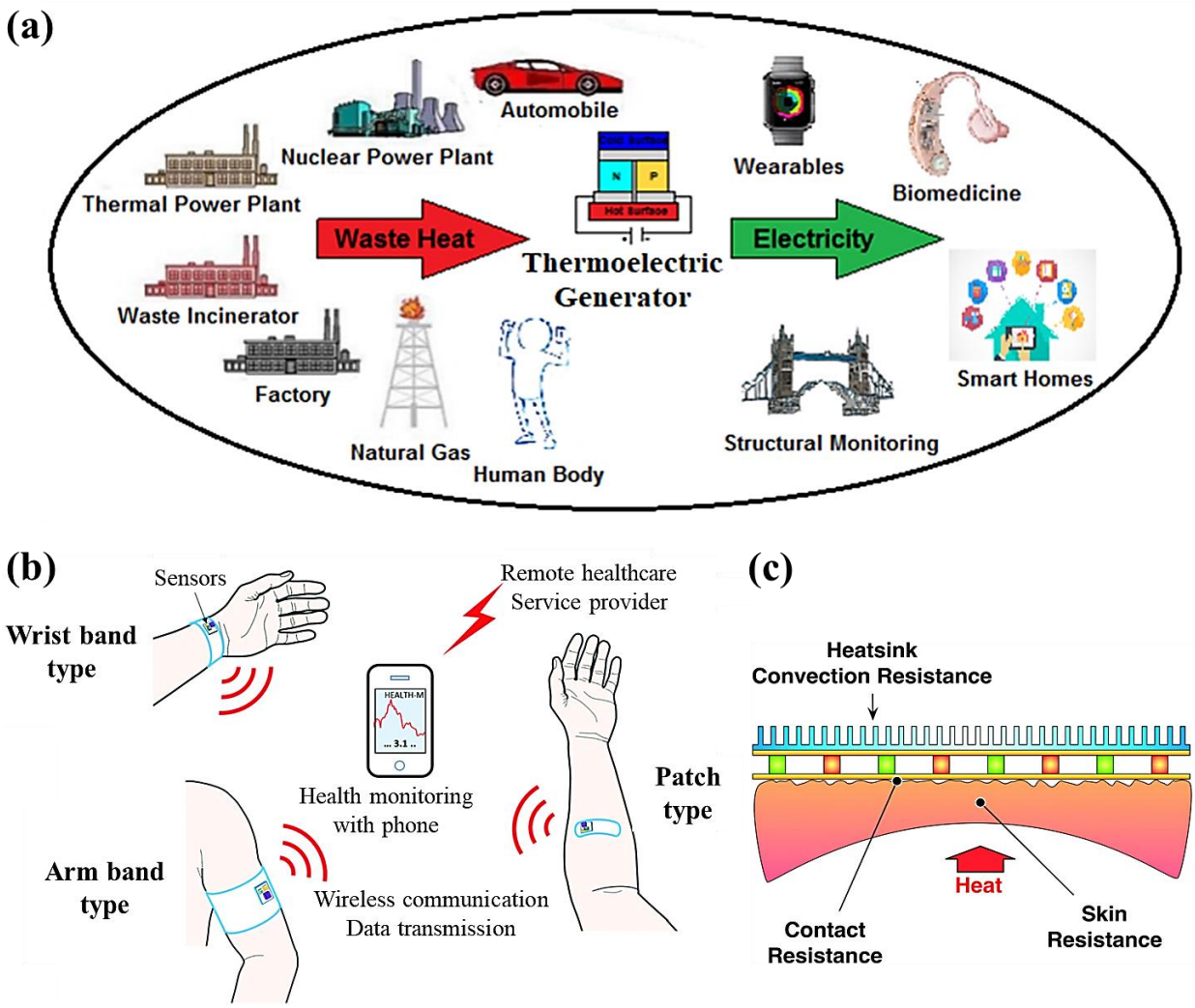

Figure 2.1 (a) Schematic showing potential applications of TEGs, ranging from industry to household applications. (b) Three types of wearable and wireless sensors that are powered by TEGs through human body heat. (c) Illustration of three types of parasitic resistances that can cause heat losses, thereby deteriorating the TE performance of TEGs. (Figure (b) reproduced with permission from [32]. Copyright 2015 Royal Society of Chemistry. Figure (c) reproduced with permission from [9]. Copyright 2016 RSC Publishing.)

2.3 Fundamentals of Thermoelectrics

2.3.1 Thermoelectric Effect

Thermoelectric effect, or thermoelectricity, is the result of the mutual interference of two irreversible processes occurring simultaneously in the system, i.e. heat transport and charge carrier transport.[60] They are usually described as below:[60]

(i) Seebeck effect is the generation of a charge gradient when a temperature gradient is applied. As the high-energy carriers diffuse away from the hot end and produce entropy by drifting to the cold end, an electric field is created across a material. This effect can be used for the power generation (Figure 2.2 (a)).

(ii) Peltier effect is the converse of the Seebeck effect, where a temperature gradient across a material (absorption or production of heat on either side) is created due to an applied voltage difference. This effect can be used for the active refrigeration (Figure 2.2 (b)).

(iii) Thomson effect is a thermal effect where heat (Q) is absorbed or produced when electrical current (I) flows through in the presence of temperature gradient. (Figure 2.2 (c))

In a TE material, there are free electrons or holes that can carry both charge and heat. If a TE material is *p*-type, the free charges are positive. These positive carriers (holes, h^+) will move from the heat source (hot surface) to the heat sink (cold surface), building up a positive potential on the cold side. If a TE material is *n*-type, the free charges are negative. These negative carriers (electrons, e^-) will accumulate on the cold side, generating a negative potential. As illustrated in Figure 2.2 (a), a potential difference is formed across the TE material between the hot and cold side in two different ways. In this regard, TEGs are solid-state devices that can directly convert thermal energy into electricity based on the Seebeck effect. The simplest TEG comprises 'legs' of alternating *p*-type and *n*-type TE materials that are connected electrically in series and thermally in parallel, as demonstrated in Figure 2.2 (a).[10]

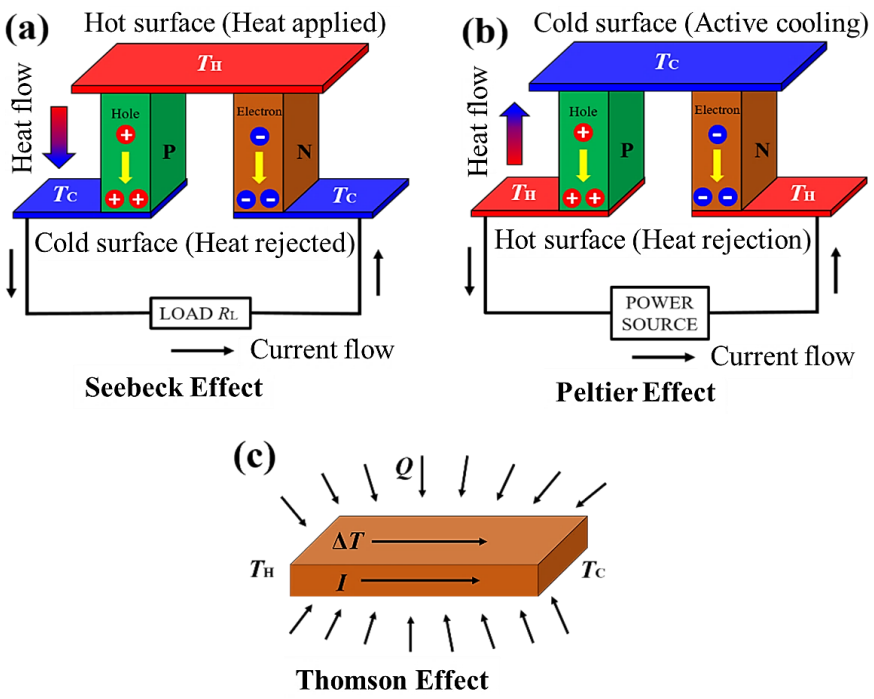

Figure 2.2 Schematic showing the operating principles of basic TE devices: (a) Seebeck effect for the power generation, (b) Peltier effect for the active refrigeration, and (c) Thomson effect.

2.3.2 Thermoelectric Properties

The TE performance of a material is governed by a combination of its intrinsic electrical and thermal properties: Seebeck coefficient, electrical conductivity, and thermal conductivity.

Seebeck coefficient (S), also known as 'thermopower' (α), as defined in Equation 2-1, is the ratio of the voltage, ΔV, generated as a result of a temperature difference, ΔT, across a TE material.[1,61] The ΔV can be a positive or negative value, depending on whether the mobile charges are holes (p-type) or electrons (n-type).[60]

Electrical conductivity (σ) is the conductance of a sample of a unit cross-section and unit length.[60] The resistance, R, can be calculated by Ohm's law, and the electrical conductivity can then be calculated by Equation 2-2. Commonly used techniques to measure σ are the four-probe method (e.g. Van-der Pauw measurement) or measurements made via the development of field-effect transistors using the organic polymer as the active layers. With the advent of organic electronics, the techniques and instruments used to measure σ in organic polymers are becoming significantly sophisticated.

Thermal conductivity (κ) is the rate of heat transfer through a unit area and thickness of a material induced by a unit temperature gradient in unit time.[61] The thermal conductivity can be measured by using a direct method as shown in Equation 2-3, or an indirect method as given in Equation 2-4.[62,63] There are two major measurement methods developed in the literature, which will be elaborated in Appendix A.1. (1) Steady-state method, which is based on forcing a constant heat flow through a material and measuring the steady-state temperature difference between two points separated a distance. (2) Transient method, which uses a time-varying current to heat the coil for extracting κ. The 3-ω method is a popular transient method. A periodic heat source is employed to generate a sinusoidal-varied heat wave traveling through two points separated a distance. The amplitude decay and phase shift of the heat wave are measured for the calculation of κ.[1] For a material, there are two mechanisms for the heat transport: (1) through the vibration of crystal lattices or individual atoms as the heat carrier (phonon) transport where phonons move from the high to low-temperature side across a material, and (2) through the charge carrier (electron) transport.[62] Therefore, the total thermal conductivity is comprised of two parts (see Equation 2-5 and Figure 2.3), where κ_l is independent from S and σ, and can be tuned without significantly affecting S and σ.[2,19,62]

$$S = -\frac{\Delta V}{\Delta T} \tag{2-1}$$

$$\sigma = \frac{L}{RA} \tag{2-2}$$

$$\kappa = \frac{W\,L}{A\,\Delta T} \tag{2-3}$$

$$\kappa = \rho\, d\, s \tag{2-4}$$

$$\kappa = \kappa_l + \kappa_e \tag{2-5}$$

where S is the Seebeck coefficient [V/K]; ΔV and ΔT are the voltage difference generated and the temperature gradient applied across a material, respectively; σ is the electrical conductivity [S/m]; L is the length between two ends [m]; R is the resistance [Ω]; A is the cross-section area [m^2]; κ is the total thermal conductivity [W/(m·K)]; W is the thermal power [W]; ρ is the mass density [kg/m^3]; d is the thermal diffusivity [m^2/s]; s is the specific heat capacity [J/(kg·K)]; κ_l is the lattice contribution; and κ_e is the electronic contribution.[2,61–64]

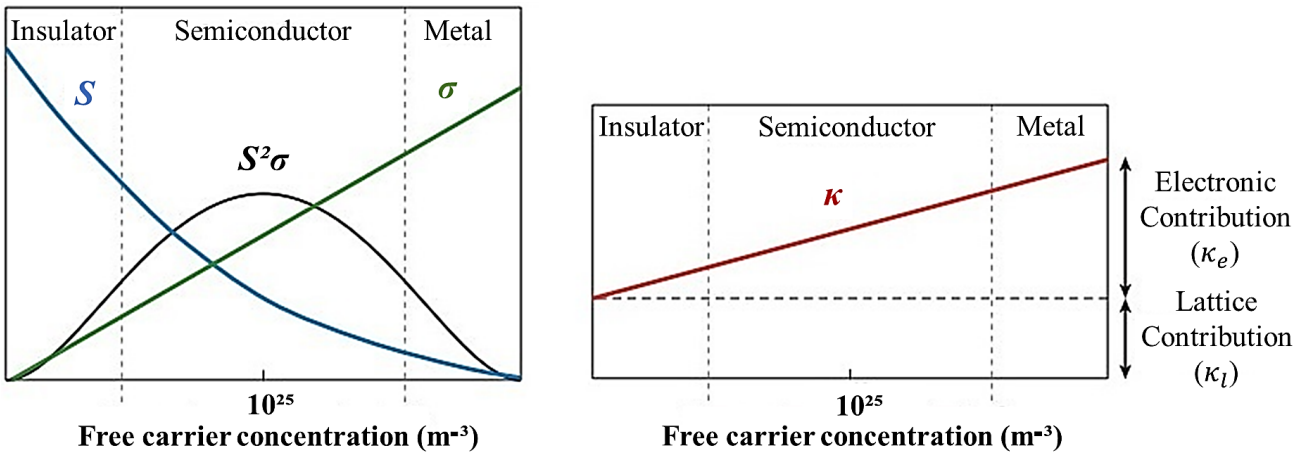

Figure 2.3. The trade-off between *S*, σ, and κ with increasing free carrier concentration, from the insulator to semiconductor and metal. (Figure reproduced with permission from [2]. Copyright 2011 Annual Reviews.)

2.3.3 Thermoelectric Performance

To evaluate the potential TE performance i.e. the conversion efficiency of a TE material in converting thermal to electrical energy (or vice versa) at a given operating temperature, the dimensionless figure of merit (*ZT*) and power factor (PF) are usually used as major criteria, as defined in Equations 2-6 and 2-7, respectively.[10,62,65] The *ZT* value of a good TE material therefore needs to be maximised by appropriately tuning *S*, σ, and κ, thereby achieving a high *S* to ensure a high voltage output at a given ΔT, a high σ to minimise the Joule heating, and a low κ to prevent the thermal shorting.[66] However, as illustrated in above Figure 2.3, increasing σ generally leads to a decrease of *S* and an increase of κ. Therefore, it is necessary to overcome the trade-off between these variables and to predict the optimised balance for the maximum overall material efficiency.[49,62] In the absence of thermal conductivity data, PF is often used as an alternative way to evaluate TE materials. TE materials with higher PF values can convert more heat into electricity. Increasing the PF value has been recognised as a key strategy in optimising the *ZT* value, particularly in the case of organic TE materials whose κ values are intrinsically low.[65] The maximum device efficiency (η_{max}) of a TEG is determined by both *ZT* and the temperature gradient, as expressed in Equation 2-8.[1]

$$ZT = \frac{S^2\sigma}{\kappa}T \tag{2-6}$$

$$\mathrm{PF} = S^2\sigma \tag{2-7}$$

$$\eta_{\max} = \frac{T_\mathrm{h} - T_\mathrm{c}}{T_\mathrm{h}} \frac{\sqrt{1 + ZT_\mathrm{m}} - 1}{\sqrt{1 + ZT_\mathrm{m}} + T_\mathrm{c}/T_\mathrm{h}} \tag{2-8}$$

where ZT is the figure of merit; PF is the power factor [$\mu W/(m \cdot K^2)$]; S is the Seebeck coefficient [V/K]; σ is the electrical conductivity [S/m]; κ is the thermal conductivity [W/(m·K)]; T is the temperature [K]; $\eta_{\max}$ is the maximum device efficiency; ZT_m is the average ZT; T_h and T_c are the temperature values of the hot and cold surface, respectively.

2.4 Thermoelectric Materials

2.4.1 Inorganic Thermoelectric Materials

As of now, most well-established inorganic TE materials are typically metallic alloys, semiconductors, or heavily doped metal oxides.[6,67–69] As can be seen from Figure 2.4, bulk layered structured chalcogenides, e.g. bismuth telluride (Bi_2Te_3), antimony telluride (Sb_2Te_3), and their doped alloys, are well-known as the best TE materials near room temperature with peak ZT values of more than 1.4, making them well-suited for most near-room-temperature TE applications, such as refrigeration and waste heat recovery up to 200 °C.[6,44] They can be either *n*-type or *p*-type depending on the doping conditions,[70] and they share similar crystal structure with 'Sb' atoms occupying 'Bi' lattice sites.[71] By controlling the Bi/Te or Sb/Te ratio, their compositions can be controlled stoichiometrically.[71] Their TE properties can also be tuned by the doping process, which can affect the concentration and mobility of charge carriers.[61] It has been proved by both theoretical and experimental results that nanotechnology and quantum theory can be effective approaches to achieving greater ZT optimisation in nanostructured chalcogenides. For instance, their S can be improved via the band convergence through doping, strain, temperature, and forming solid solutions to increase the number of valley degeneracies, or via the quantum confinement effect through decreasing

the dimensionality of the material to nanometer length scales.[4,11,19,24,71,72] The energy-band structure of the material can also be engineered by doping semiconductors with resonant impurities to enhance the interaction between wavefunctions of impurities and free electrons, thereby leading to higher PF values on the whole.[1,31,73] Their κ values can be reduced by nanostructuring, hierarchical architecturing, or matrix with nano-precipitates.[31] Nanostructuring is capable of effectively tuning the contribution of thermal carriers (phonons) and charge carriers (electrons) within the system, by splitting the interdependence of the electrical and thermal transport (σ and κ).[3,4,19,74–76] Since the electronic contribution to κ in the inorganic semiconductors is substantially less than the phonon contribution (see Figure 2.3), the total κ is mostly dependent on the phonon scattering.[1] By introducing defects, phonons can get scattered within the lattice structure, which can largely decrease κ_l without affecting κ_e.[1] The phonon transport can also be scattered across the interfaces, where the multilayered structure can have a range of phonon scattering events.[1,77] Moreover, nanostructuring can provide greater surface area and more interfaces that can further lower κ, while not compromising S and σ by selectively scattering phonons and electrons to efficiently reduce κ_l,[1,49,71,78] as well as increasing the density of states near the Fermi level.[4,66,72,77] The quantum confinement effect in quantum dots,[79] in quantum wells,[7], and in superlattices within nanocomposites[80,81] can also selectively block the phonon transport to significantly reduce κ without affecting the electron transport or σ.[60,82,83]

Apart from the traditional inorganic TE materials presented in Figure 2.4, recently developed tin selenide (SnSe) single crystals exhibited a very high ZT ~2.6 at 923 K.[84] SnSe is chemically and structurally akin to PbTe, but lighter.[73] SnSe has an unusual layered structure that derives from a three-dimensional distortion of the NaCl structure.[84] Owing to the lack of rare-earth or toxic component elements, SnSe has a promising prospect for practical use, and can be possessed with good reproducibility.[84,85] Other layered structured inorganic TE materials, such as TaS_2, MoS_2, and TiS_2, are also being researched for the development of higher TE performance.[83]

In addition, oxides are another category of inorganic TE materials, such as *p*-type Na_xCoO_2 and *n*-type doped $SrTiO_3$ or $CaMnO_3$ perovskites, doped ZnO, or doped In_2O_3 bixbyite.[86] Not only do these oxides possess excellent chemical stability in air and even at elevated temperature, they also constitute cheap, abundant and harmless elements, which make them appealing for a variety of applications. However, their *ZT* values remain limited to 0.4-0.6 at higher temperatures.[86] Other inorganic TE material systems, e.g. half-Heusler MgAgSb alloys, skutterudites, and clathrates, have been developed with ultra-low thermal conductivity by introducing mixed-lattice atoms and/or complex intermetallic phases to increase the disorder in the lattice of bulk materials, thereby enhancing their final TE properties.[87]

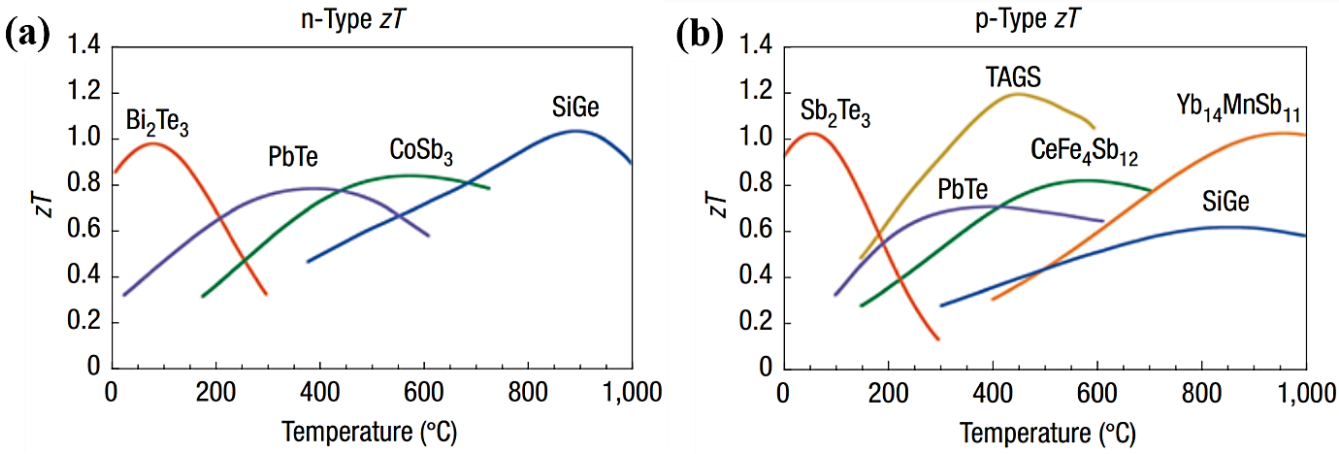

Figure 2.4 Comparison of *ZT* values of various current-developed or being-developed (a) *n*-type and (b) *p*-type inorganic TE materials as a function of the operating temperature, where most of them are metallic alloys with different dopants. (Figures reproduced with permission from [6]. Copyright 2008 Springer Nature.)

2.4.2 Organic Thermoelectric Materials

Organic TE materials, such as conjugated polymers, coordination polymers, and fullerene-based polymers, have been researched in great detail over the years. Despite lower *ZT* values of existing organic TE materials, their inherent advantages, e.g. light-weight, non-toxicity, low-cost, biocompatible nature, earth-abundant elements, solution processability, excellent mechanical flexibility and even stretchability, as well as chemically tunability with inherently low κ [(typically < 1 W/(m·K)], are beneficial for various technological and

ecological applications.[10,16,26,49,75,83,88–91] Also, there have been great advances in polymer processing techniques, which make large-scale production of printed organic-based electronics feasible and inexpensive by using low-temperature and scalable solution-based fabrication approaches as well as large-area printing techniques.[8,10,26,75,88,89] Nevertheless, the development of organic TE polymers is still in the initial stage. Compared to their inorganic counterparts, organic TE polymers possess comparatively lower PF and *ZT* values, which are far below the required level for practical applications. They are also constrained to deployment in lower-temperature applications because of the nature of polymers.[10,26,49,75,89–91] Table 2-2 summaries and compares some current-reported organic TE polymers in the literature. It can be seen that most organic TE polymers are conjugated polymers with extended π-conjugation along the molecular backbone. They are conductive due to the charge delocalisation across the polymer backbone, and their σ can be improved from a semiconducting state to a metallic state by doping.[92,93] Since as-synthesised organic TE polymers are comparatively insulating owing to their relatively wide bandgaps, doping is often required to enhance their σ. However, their *S* could be deteriorated with increasing amount of doping agents, because the increased concentration of charge carrier forces the Fermi energy level to the conduction band, which substantially diminishes the energy required to transport charge carriers. Appropriate doping level is therefore needed to synergetically improve both σ and *S*, thereby optimising their final PF.[77] On top of that, since their TE properties depend on their chemical structures and microstructures, doping and de-doping, surface treatment, as well as morphological control of the crystallinity and alignment of polymer chains are effective approaches to the partial decoupling of *S*, σ, and κ in order to maximise the overall *ZT* value.[10,83,94]

Among the most recently reported TE polymers, *p*-type poly(3,4-ethylene dioxythiophene) polystyrene sulfonate (PEDOT:PSS) has been shown to possess one of the highest TE performance capabilities, with a record-high *ZT* value of 0.42 at room temperature, as reported by Kim et al.[93] However, this has not been successfully replicated by other groups yet. PEDOT:PSS is one of the most well-researched and commercially used conducting polymers

by virtue of its low cost, ease of large-volume and/or large-area printed organic electronic manufacturing, and excellent environmental stability.[25,49,95,96] In comparison, several other conjugated polymers still remain at the laboratory research stage, and are limited to the small-scale use owing to their high cost and low yield in material production.[95] PEDOT:PSS is a polymer mixture of two ionomers: poly(3,4-ethylenedioxythiophene) (PEDOT) and polystyrene sulfonate (PSS). PEDOT is a conjugated polymer and carries positive charges, where the thiophene group is neither soluble nor fusible, rendering the hydrophobicity and poor solvent solubility of PEDOT.[97] In order to obtain a stable PEDOT suspension within de-ionised (DI) water or other solvents that can be solution-possessed for the thin/thick film deposition, some small hydrophilic moleculars carrying negative charges, such as polystyrene sulfonate (PSS) or tosylate (Tos), are usually doped as external ions to compensate the positive charges on PEDOT to form a macromolecular salt.[97] The excess hydrophilic PSS moleculars also form a shell-like structure surrounding the hydrophobic PEDOT clusters to prevent PEDOT from polymerising over time.[93,95] However, due to the insulating nature of PPS deteriorating σ of PEDOT, a de-doping process is desired on the deposited and cured PEDOT:PSS film to remove some of the insulating PSS molecules from the conducting PEDOT chains. As a result, better electrical contacts and enhanced transport of charge carrier are formed between neighbouring PEDOT chains by a hopping mechanism.[97,98] Various surface treatments or chemical treatments have been intensively reported in the literature to de-dope the insulating PSS molecules from the PEDOT:PSS.[89,93,99,100]

Apart from conjugated polymers, coordination polymers and fullerene-based polymers can be doped to exhibit *n*-type behaviour. Coordination polymers are comprised of metal cations and organic ligands with coordination bonds. Among current-developed *n*-type TE polymers, poly(nickel-ethylene tetrathiolate) (poly(Ni-ett)) presented the highest ZT value of 0.32 at a temperature of 400 K.[101] Nonetheless, it has fairly low dispersibility and is quite difficult to be processed in solution form, which severely restricts its applications. Up till now, most TE polymers and their corresponding TE composites are *p*-type. This mainly stems from problems of poor stability in air as well as low TE performance of *n*-type TE polymers. This has

significantly hindered the development of wearable TEGs.[83] Therefore, further efforts are urgently needed to develop high-performance and stable *n*-type TE polymers so that high-efficient TEGs with *n*-*p* junctions can be achieved.[102]

2.4.3 Carbon-based Thermoelectric Materials

Low-dimensional carbon-based materials, such as one-dimensional (1D) carbon nanotubes (CNTs) and two-dimensional (2D) graphene platelets, have been successfully introduced as effective additives to dramatically increase σ of formed polymer-based composites without decreasing their S.[88,103–105] For example, CNTs could be incorporated with TE polymers, e.g. P3HT [106] or PEDOT:PSS [88,107,108], to enhance their final σ. The record-high PF value was achieved by Cho et al., where the PANI/graphene-PEDOT:PSS/PANI/CNTs-PEDOT:PSS nanocomposite exhibited a PF value of 2710 μW/(m·K^2), with S ~120 μV/K and σ ~1900 S/cm.[46] In the composite system, CNTs provided a network for conducting charges while the polymer matrix thermally disconnected contacts between junctions.[16,109] It has shown that varying the loading ratio of CNTs within the PEDOT:PSS/CNTs composite has a significant influence on the improvement of S and σ, compared to the single-phase PEDOT:PSS films and CNTs bundles.[110] Additionally, the formation of numerous tube–tube connections and CNTs/polymer interfaces could scatter phonons and result in lower κ, and thus higher ZT value.[88,109] CNTs are intrinsically ambipolar that can be doped to *n*- or *p*-type without affecting their σ. They can also have higher charge carrier mobilities in networks, but reduced κ. CNTs are likely to exhibit *p*-type conduction due to the oxygen doping when exposed to air.[111] CNTs also possess superior mechanical and chemical robustness, leading to those formed composites being flexible and stretchable with superior tensile strength.[110] However, directly printing these materials can be very tricky because of the challenges involved in the ink preparation, such as functionalising the dispersed particles or nanotubes to form a stable suspension, achieving uniform particle size distribution, and tuning their viscosity for smooth printing by using the desired printing technique.[8,32,112]

Table 2-2 Comparison of existing organic thermoelectric polymers reported in the literature.

Type	Material	Structure	***S*** **(μV/K)**	***σ*** **(S/cm)**	***κ*** **[W/(m·K)]**	**PF [μW/(m·K²)]**	**Ref.**
***p*-type**	PEDOT:PSS	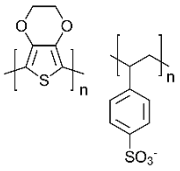	70	980	0.23	469	[93]
	PBTTT	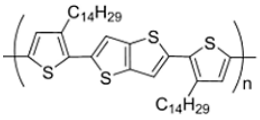	9.4	220000	–	1944	[113]
	PANI	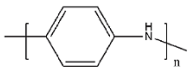	220	20	–	11	[114]
	P3HT	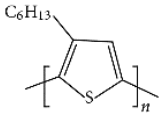	60	22	–	8	[115]
	PPy	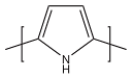	10.5	340	–	2	[116]
***n*-type**	PPV	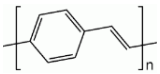	-349	47	0.25	78	[117]
	PDI	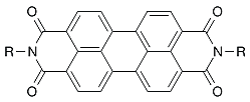	-167	0.5	–	1.4	[118]
	P(NDIOD-T2)	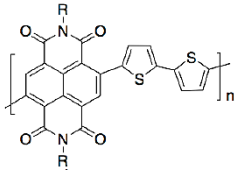	-850	0.008	–	0.6	[119]
	PA	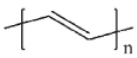	-43.5	5	–	1	[120]
	C_{60}	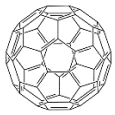	-175	4	–	12	[121]
	K_xC_{70}	–	-22.5	550	–	28	[122]
	Poly(Ni-ett)	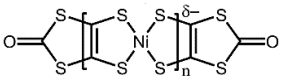	-130	270	0.50	453	[101]

Note: PEDOT:PSS = poly(3,4-ethylene dioxythiophene) polystyrene sulfonate, PBTTT = poly(2,5-bis(3-alkylthiophen-2-yl)thieno[3,2-b]thiophene), PANI = polyaniline, P3HT = poly(3-hexylthiophene), PPy = polypyrrole, PPV = poly(*p*-phenylene vinylene), PDI = perylene diimide, P(NDIOD-T2) = poly{N,N′-bis(2-octyl-dodecyl)-1,4,5,8-napthalene dicarboximide-2,6-diyl]-alt- 5,5′-(2,2′-bithiophene)}, PA = polyacetylene, Poly(Ni-ett) = poly(nickel-ethylene tetrathiolate).

2.4.4 Hybrid Thermoelectric Nanocomposites

In principle, an ideal TE material should be a thermal insulator and electrical conductor, i.e. 'phonon-glass electron-crystal' which has shorter phonon mean free paths for reduced κ and longer electron mean free paths for increased σ.[49] In this respect, a hybrid organic-inorganic composite structure might overcome some of the difficulties associated with single-component counterparts, and the ability to print them on flexible substrates is a particularly attractive feature.[4,25–27] The inorganic-organic composite system can be simply prepared by solution blending of polymers and inorganic materials, where the polymeric matrices can be insulating or conducting while the loaded additives can be a variety of inorganic nano-fillers, such as metallic alloys,[19,123–125] noble metals,[74] metal oxides,[126] or carbon nanostructures.[88,103–106] The TE performance of the composite is dependent on the properties of constituents and interfaces between them. If both components are active TE materials, being either all *p*-type or *n*-type, they could work synergistically to enhance the overall *ZT*.[92] However, if they are of opposing carrier types, the carrier behaviour of the blended composite could exhibit either *p*-type or *n*-type, depending on the loading ratio of constituents.[19,92] In this regard, an *n*-type composite can be produced by blending cost-effective insulating polymers with *n*-type TE materials. However, the problem is that they are prone to having fairly low σ and PF, owing to the intrinsic insulating matrix.[74,127] Hence, it is viable to achieve much greater improvement in the *ZT* value by employing conducting polymers as matrices with various nanostructured inclusions and concentrations.[16] Although conducting polymers still have relatively lower *S* and σ compared with their inorganic counterparts, the overall *ZT* of the composite can be modified by varying the loading ratio between organic and inorganic parts to overcome the constraints of single-component materials.[1,5,19,92] More importantly, in combination with the intrinsically low-κ polymeric matrix, the introduced phonon-boundary scattering and the large thermal boundary resistance at the interfaces can synergistically hinder the thermal transport, thereby further lowering κ of the composite.[3,4,19,49,74,75] The embedded nanoparticles can also create more interfaces and grain boundaries within the nanocomposite structure, which can

effectively improve the selective phonon scattering and the energy filtering effect at the interfaces.[31,83,123] Therefore, κ could be remarkably reduced without adversely affecting S and σ, thus leading to greater ZT values as a whole than that can be achieved in the bulk.[19]

It is found that the highest PF is not generated by either the highest S or highest σ, but by the moderately high σ of 1000-2000 S/cm and high S of 100-200 μV/K with a carrier concentration of ~10^{25} m^{-3} (see Figure 2.3).[49,71] The Fermi levels of inorganic nanostructures and organic polymers should be matched to lower the energy barrier for charge carriers travelling between different phases.[19,92] Thus, by the hybridisation of higher-PF inorganic TE materials, such as Bi_2Te_3 and Sb_2Te_3, with conducting polymers, such as PEDOT:PSS, P3HT, and PANI, the overall ZT value of the fabricated composite could be greatly enhanced.[19,25,123–125,128] However, introducing inorganic particles could also deteriorate the overall σ. This could stem from the poor connectivity between the inserted inorganic particles and the polymer matrix, which is a problem that needs to be addressed in order to achieve improved TE performance.[19,25,123–125,128–130] Therefore, the properties of TE composites can be further improved by optimising the material selection, composite formation, and device fabrication.[1,92] Apart from the improvement of TE performance, organic polymers can also serve as a protective matrix for the embedded inorganic particles.[19] Since polymers have greater mechanical flexibility, lighter weight, and excellent solution processing feasibility, organic-based TE composites can address some issues that their inorganic counterparts have,[10] and they can be integrated with high-volume manufacturing of printed organic electronics.[25] Both experimental and theoretical results have proved that nanocomposite structuring method can be an effective approach to splitting the interdependence of electrical and thermal transport, thereby tuning the contribution of charge carriers (electrons) and thermal carriers (phonons) in the system.[3,4,11,19,24,72,74–76]

2.5 Thermoelectric Generators

A thermoelectric generator (TEG) is a solid-state device. As illustrated in Figure 2.5 (a), a basic TEG is comprised of two TE legs, one *p*-type and one *n*-type, which are electrically connected in series and thermally connected in parallel. Typically, a TEG module is constructed of many pairs of alternating *p*–*n* TE legs placed in parallel to each other and sandwiched between two ceramic plates to maximise the final power output (see Figure 2.5 (b)).[131] The substrates employed here are required to be efficiently thermally conducting but electrically insulating, while metal interconnects should have low contact resistance. In the presence of a temperature gradient, the maximum power output can be optimised by impedance matching with an external load resistance.[131] From the literature, it is found that most current thermoelectrics research has focused on the material discovery and the development of enhancing the thermal-to-electrical energy conversion efficiency, i.e. PF and *ZT*. However, there are few efforts on the device physics level, from the contact-making to the assembly of the TEG module.[1] At present, traditional bulk TEGs are not yet mass-produced at low material and manufacturing cost. This mainly stems from the scarcity and high cost ('Te' rare-earth element), environmental hazard and toxicity ('Pb' element), intrinsic brittleness, and poor processability of currently utilised inorganic TE materials,[10] as well as the technical limitations of current joining and assembling technologies.[49] Existing manufacturing techniques consist of highly sophisticated processes, from the powder formulation, consolidation and metallisation, pellet machining, to the final module assembly, which are labour intensive, unscalable, and unsustainable with excessively large material wastage.[132] These bulky TEGs are also prone to delamination when bent during use, which has considerably reduced their usable strain levels. As a result, their applications in modern power generator devices are constrained, especially for integration into flexible and wearable devices.[11,12] Moreover, existing joining and assembling technologies largely constrain the device size to ~25 cm^2, resulting in only niche applications.[49] For the future of this technology, it is paramount to develop higher-performance and lower-cost TEGs, which can be

manufactured at a large scale and be incorporated into a variety of geometry designs. Their TE materials could be synthesised by scalable and inexpensive wet-chemical methods into various nanostructured dimensions, allowing for microscale additive manufacturing techniques and offering the scope for miniaturisation of flexible TE devices for small-scale energy harvesting technologies.[8,24,133,134]

TEGs can be easily scaled down to micron-size with minimal maintenance and no moving parts.[11] There thus has been tremendous interest in the development of high-performance, flexible, conformable, and even stretchable TEGs to enhance the capability and lifetime of self-powered electronic devices, as well as to power wireless sensors, wearable technology gadgets, and extreme weather clothing from human body heat.[9,11,12,37,92] As discussed in Table 2-3, printed flexible TEGs can address most issues that their bulky counterparts normally have. The challenge, involving the fabrication and assembly of several individual TE legs into one whole module with reduced material wastage as well as less solder material usage, can be ideally overcome by adopting additive manufacture routes.[1] The flexibility and stretchability of TEGs can be remarkably improved by applying some innovative geometrical architectures. For instance, Figure 2.5 (c) presents one of the most intensively used planar designs in the literature, where a polyimide (PI) substrate that is flexible and thermally stable at elevated temperature with a high thermal resistance is utilised. Since it is comparatively difficult to obtain a thicker film (>100 μm) by most printing techniques, the inherent in-plane structure can be converted to an out-of-plane structure with multiple TEGs stacking up together so as to extract more electric power for practical use, where the heat flow direction is parallel to the plane of printed TE materials and substrates (see Figure 2.5 (c)).[134] These polymer-based flexible TEGs can be achieved by solution-based processing approaches in combination with printing or painting techniques, which are low-cost, scalable, and continuous production processes with minimal material wastage and human interaction.[10,50,94,131] Although these polymer-based TEGs would be limited to a low-temperature operation environment due to the thermal stability of organic TE materials, concerning wearable applications, this is not a major issue.[92,135] Meanwhile, a higher PF or *ZT* value is not the only thing that should be aimed

for, but a lower κ value is also required to maintain a constant ΔT across the TEG so as to generate a continuous electrical output during use. Also, using expensive inorganic TE materials to harvest thermal energy is fairly impractical. Hence, all these factors have drawn significant interest in developing high-efficiency, scalable, inexpensive, flexible, and even stretchable polymer-based TEGs.

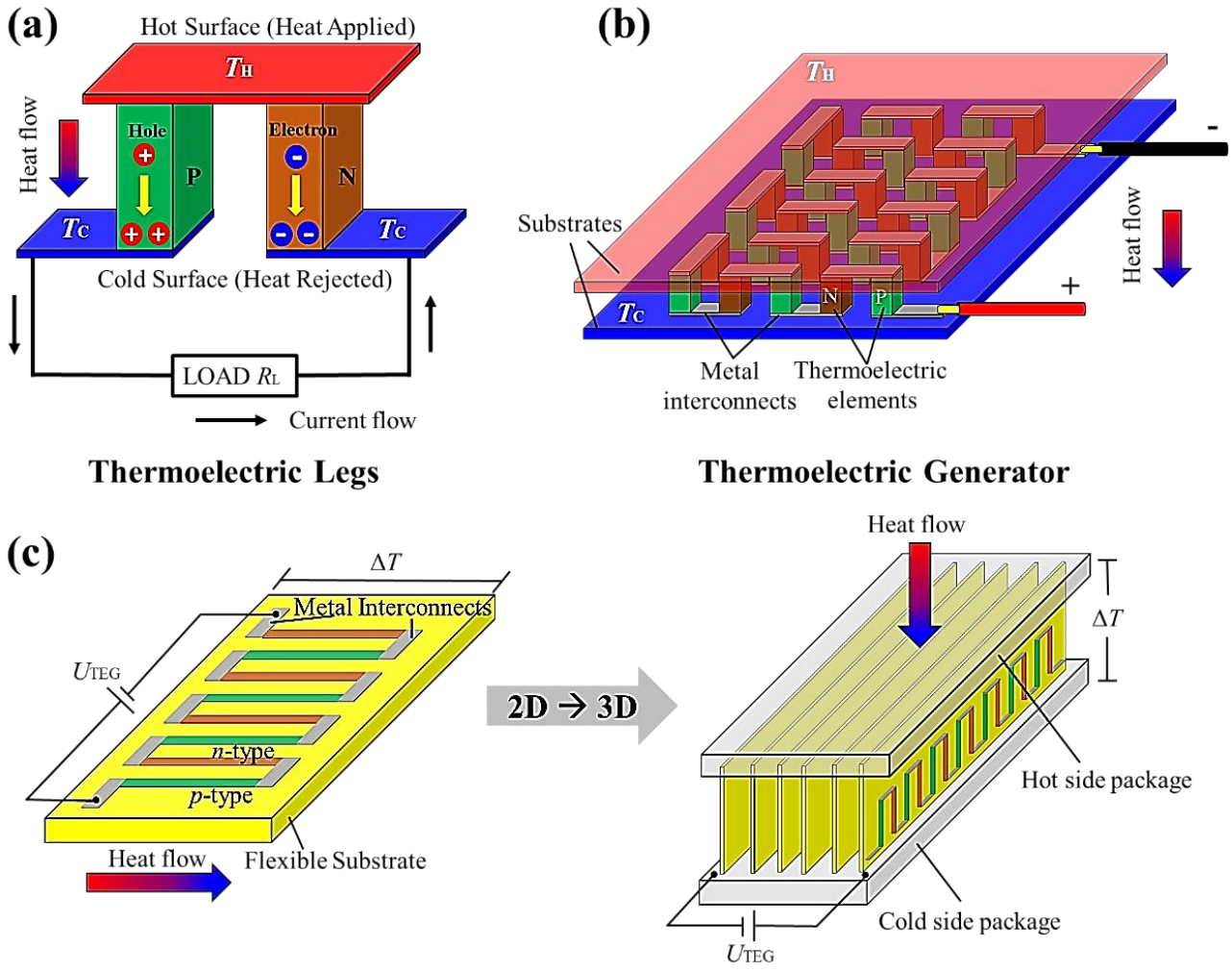

Figure 2.5 Schematic diagrams of (a) a basic TEG with two TE legs and (b) a TEG module connected with a series of TE legs. (c) Design diagram of a novel structure for flexible TEG applications.

Table 2-3 Comparison of traditional bulk TEGs with printed flexible TEGs.[50,95]

Traditional Bulk TEGs	**Printed Flexible TEGs**
Rigid and brittle	Flexible and bendable
Small size only < 40 cm^2	Customised sizes and shapes
Thick (~5 mm) and fixed module design	Thin (~200 μm) and flexible module design
Complicated manufacture processes	Easily scalable to a large area
Materials wasting and costly to manufacture	Material saving and low cost to manufacture
Harmful material exposure and maybe toxic	Safe and non-toxic materials used
Higher efficiency and power output	Lower efficiency and power output
Higher-grade temperature applications, e.g. industrial or automobile energy recovery	Lower-grade temperature applications, e.g. wireless electronics and wearable devices

2.6 Microscale Additive Manufacturing Routes

Microscale additive manufacturing routes, in particular printing techniques, are intensively used for nanomaterial deposition with specific design patterns. Not only can they fully utilise materials with minimal wastage, but they also provide high-precision and large-area material deposition on a variety of substrates, with the help of digital design software.[136] These processing routes can therefore be exploited to translate functional nanomaterials, typically in the form of nanoparticulate inks, into working energy harvesters or sensors with greater conformability, flexibility, and efficiency in energy harvesting or sensing for 'small-power' applications. Here, the author discusses several representative printing techniques that are widely used in the TE material deposition, which are drop-on-demand, maskless, easy in their operation, cost-effective and scalable, and thus ideally suited for this purpose. Their pros and cons are subsequently discussed in Table 2-4. In addition, these printing techniques can themselves be part of the material optimisation process, leading to better TE properties. Thin or thick film-based TEGs can be cheaply and quickly printed in the form of fully organic, fully inorganic, or even hybrid composite structures. Some printed organic-inorganic TE composites have been shown to improve the overall *ZT* or PF, as summarised in Table 2-5.

2.6.1 Printing Techniques

(i) Ink-jet Printing

Ink-jet printing possesses many strengths over other sophisticated deposition methods due to its scalability, simplicity, and cost-effectiveness. As demonstrated in Figure 2.6 (a), there are two modes of ink-jet printing: continuous and drop-on-demand. In continuous mode, inks supplied from a cartridge are charged by an electrode, and subsequently deflected by an electrostatic field when flowing through the nozzle to be jetted onto the substrate. In the drop-on-demand mode, the pressure is applied to the reservoir, through vaporisation or vibration methods, to propel the ink through an orifice of the nozzle. The formed fine droplets are then ejected onto the substrate. A computer numerical control system is used to precisely control the material deposition path for obtaining desired patterns. By tuning the printing speed and applied propelling force, the printed film thickness can be well controlled.[137] Ink-jet printing has a high degree of design freedom to easily modify the pattern design and direct-write features down to 4 μm.[137] Nonetheless, it may take very long processing time for the large feature printing. The required ink viscosity is as low as 10-40 cP with Newtonian behaviour,[138] and only fairly fine particles are viable to be printed owing to the size limitation of the nozzle orifice.[137] These ink requirements place restrictions on the compatibility in certain cases. In this regard, organic-based or chalcogenide-based inorganic inks with similar rheological properties can be applicable in the ink-jet printing.[94] This has been demonstrated in a number of studies that different inks comprising fully organic polymer-based,[126] fully inorganic chalcogenide-based,[139–141] fully graphene-based,[142] or their hybrid composites,[126,127] have been successfully printed into either thin or thick films by the ink-jet printing technique.

(ii) Screen Printing

Screen printing is the most popular technology in the field of functional printing. For example, it has been proved to be the most efficient and successful way to print large-size TEGs by virtue of the scalability, simplicity, and versatility of its printing process.[143] During

printing, a ‘paste’ is pushed down by the force from a rubber squeegee through a porous screen mask with fine mesh openings, as illustrated in Figure 2.6 (b). Then, it is transferred and coated onto the substrate with pre-designed emulsion patterns. The screen is generally positioned ~1 mm away from the substrate with the paste placing on top of the screen. A stencil is placed underneath the screen for patterning, and different stencils are created for different designed patterns.[143] Once the squeegee finishes passing over the screen, the screen will subsequently return to its original shape.[137] The printing resolution can be down to 20-50 μm with a printed film thickness of 10-30 μm, depending on the mesh size and the emulsion thickness of the screen.[137] Inks or pastes with a high viscosity range of 10000-20000 cP as well as with non-Newtonian and viscoelastic behaviour are ideal for the screen printing.[137] Also, binders and surfactants are often employed for the ink formulation to achieve a lower surface tension so that the deposited films can have strong adhesion to the substrate. Ideally, the added binder and surfactants should be burned out, as they could have a detrimental effect on the performance of printed films.[143] Various particle sizes, ranging from sub-microns to hundreds of microns, can be easily printed via different deployed mesh geometries. If a thicker film is desired, multiple prints can easily build up the film thickness into a 3D structure. A good alignment accuracy of the stencil is required to maintain the printed feature size. As demonstrated by Søndergaard et al., screen printing can be combined with the roll-to-roll processing for fast, low-cost, and large-area mass production of PEDOT:PSS polymer films.[20] It is reported that both fully organic [144] and inorganic [145–154] inks can be successfully printed, and chalcogenide-based composites are also achievable with enhanced TE properties via the screen printing technique.[35,128] However, there exist some weaknesses that largely constrain their applicability, such as low printing resolution and large material waste. Moreover, due to the possibility of delaminating and pulling of the previous prints when printing several overlapped layers, the snap-off distance, squeegee speed, and squeegee pressure must be optimised.[143] A careful post-process clean-up on the screen is also required to avoid the mesh clog and film contamination for the next use.

(iii) Dispenser Printing

Dispenser printing can directly create the desired design feature in the form of a 2D film or 3D bulk structure, where the inks with a viscosity ranging from 100-10000 cP and with non-Newtonian and viscoelastic behaviour are suitable for use here.[155] As presented in Figure 2.6 (c), the ink is ejected through the nozzle via a computer-controlled pneumatic system, and subsequently deposited onto the substrate with confined features. The printing pattern is pre-defined by computer-aided design software.[94] For practical applications, the aspect ratio of height to width is crucial for the TE leg. Achieving a film thickness up to several hundreds of microns is viable through some solution-based printing techniques, like screen printing, but higher than that, only the dispenser printing can achieve desired high-aspect-ratio arrays via its scalable multilayer printing process.[156] 3D structured TE legs are also feasible through the successive ink deposition by the dispenser printing presented by Cao et al., provided that the elasticity of the inks is high enough to maintain their structural integrity.[155] However, since the printing time of these 3D structures would be prolonged compared to their planar counterparts, it is currently limited only to the inorganic-based ink.[155] High performance dispenser-printed planar TEGs have also been achieved in combination with different chalcogenide-based composite structures on flexible substrates.[18,156,157]

(iv) Aerosol-Jet Printing

As summarised in Table 2-4, although aerosol-jet printing (AJP) is a relatively recent-developed printing technique compared to other printing toolboxes, it possesses more versatile features, in particular with regards to the ink compatibility and the printing resolution. The concept of the AJP technique is transferring functional inks directly on a substrate under the effect of confined airflow (see Figure 2.6 (d)).[138] The AJP technique is a promising direct-write deposition technique for developing next-generation flexible or even stretchable microscale electronic devices, since it enables large-area deposition of fine-scale features from a multitude of functional inks on various planar or non-planar substrates.[138,158] It has been widely applied in different research areas, ranging from bioelectronics,[138] sensors,[159]

flexible transistors and circuits,[160,161] batteries,[162] microfluidic devices,[163] to piezoelectric,[164] triboelectric,[165] and thermoelectric,[25,96,166] for energy harvesting and storage applications. Since the AJP technique offers several distinct advantages, it can potentially solve some critical problems of existing printing techniques as discussed below.

(1) It can be installed with either a wide-area nozzle setting for high-volume prototyping production, or a fine-feature nozzle setting for high-resolution printing line production.[136] A very high-resolution layer-by-layer deposition can be obtained with a working area up to 200 mm × 200 mm. The achievable fine-feature sizes are of the line width as small as ~10 μm, and the thickness down to ~100 nm. On the other hand, the maximum feature size can be ~3 mm or even greater if using a wide nozzle print head setting.[136]

(2) Micropatterning, masking, or sophisticated lithography processes are not needed, leading to the possibility of more efficient material usage as well as a high degree of design freedom.[138] This high-resolution controlled deposition process with minimal loss of material is also advantageous, when dealing with small quantities of expensive materials. On top of that, it is beneficial to the new ink material development, as it requires a fairly small amount of ink (~1 mL).[138]

(3) As the AJP process is non-contact and conformal, functional inks can be directly transferred on various planar or non-planar substrates (either rigid or flexible) under the effect of confined airflow, with a high printing speed of up to 100 mm/s.[136,138] It also allows patterning over existing structures or printing high-resolution functional components directly on 2D or 3D surfaces, e.g. complex-geometry antennas and interconnects within printed circuit board applications.[136] This can promote a host of research and development applications, ranging from embedded flexible electronics to advanced biomedical devices. [136,167]

(4) It supports two different atomisers that can accommodate functional inks over a wide range of viscosities, covering nanomaterial-based or biomaterial-based solution to polymer-based solvents, such as conductive metals, semiconductors, dielectrics, adhesives, and

polymers.[138] The acceptable particle sizes and shapes can be much larger and less uniform than other printing techniques, such as the ink-jet printing which requires very fine feature sizes. A recent work implemented by Saeidi-Javash et al. demonstrated that the AJP technique could be used to print fully inorganic TE films onto a flexible substrate by using solution-processed $Bi_2Te_{2.7}Se_{0.3}$ nanoplates as the ink.[166]

(5) The dual ink sources and atomisers enable *in situ* mixing two different inks to form a composite structure, where the composition can be controlled by dynamically tuning the ink flow during the printing process.[25,96,159] For instance, Jing et al. employed the AJP technique to blend silver nanoparticles with polyimide to form conducting composite structures, which could be used as stretchable conducting wires or strain sensors.[159]

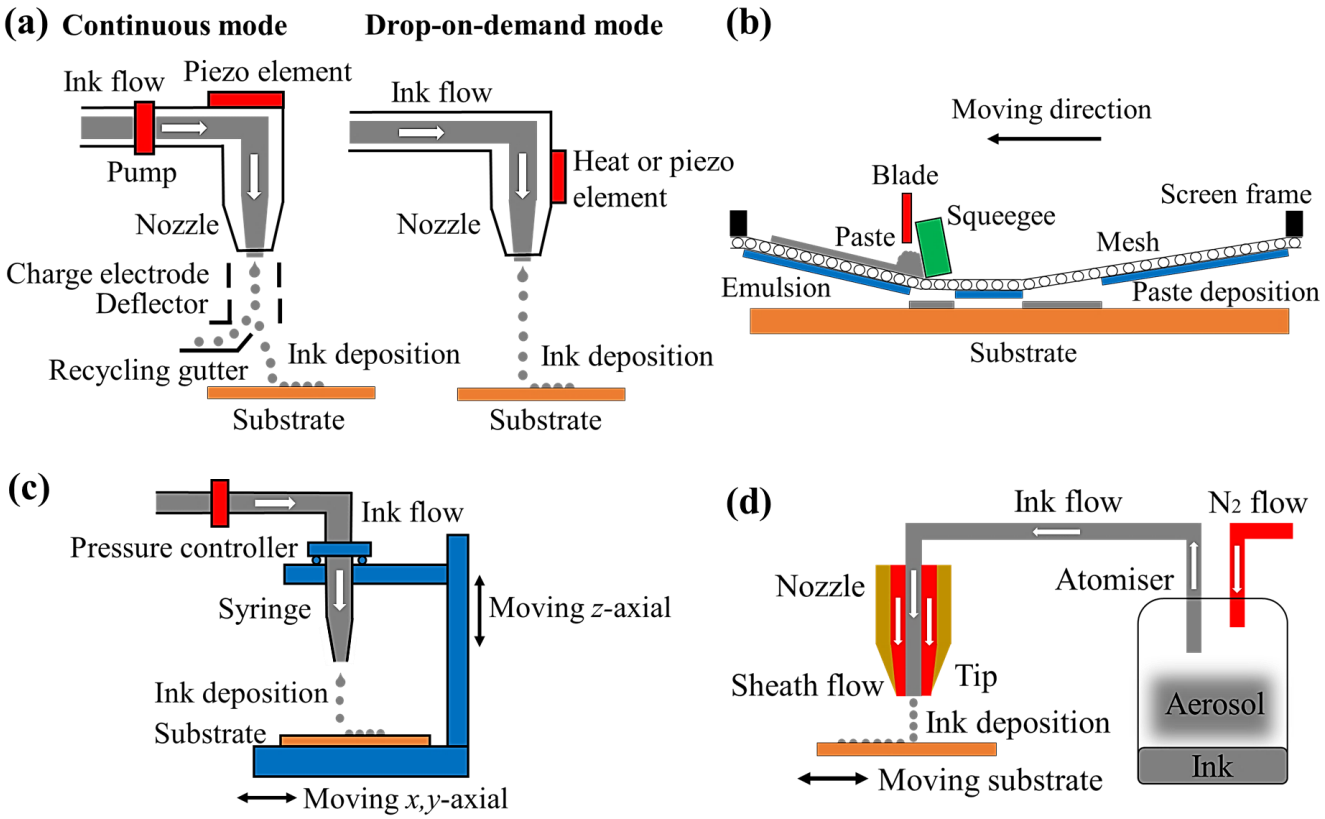

Figure 2.6 Schematic diagrams of different microscale additive manufacturing techniques: (a) ink-jet printing with continuous mode or drop-on-demand mode, (b) screen printing, (c) dispenser printing, and (d) aerosol-jet printing.

Table 2-4 Comparison of some major printing techniques with other deposition techniques reported in the literature.[136–138,143,155]

Technique	Advantage	Disadvantage
Aerosol-Jet Printing	• Minimal material waste and fast printing speed • Non-contact printing and no micropatterning needed • Wide ink viscosity range 1-1000 cP[138] • Printable on planar or non-planar substrates • Very high line resolution down to 10 μm[138]	• Require multiple printing for thick and large-area films • Slightly complicated to implement (too many adjustable parameters) • Ease of clogging printer head with prolonged printing time • Less control of spreading issue with prolonged printing time • Large splatters form and affect feature resolutions with prolonged printing time
Ink-jet Printing	• Minimal material waste and fast printing speed • Non-contact printing and no micropatterning needed • Very high line resolution down to 4 μm[137] • Good control of spreading issue	• Require very small ink viscosities 10-40 cP[138] • Only printable on planar substrates • Require multiple printing for thick and large-area films • Ease of clogging printer head with time
Screen Printing	• Low material waste and fast printing speed • Suitable for thick and large-area films • High line resolution down to 20-50 μm[137]	• Micropatterning needed with minimal design flexibility • Require very large ink viscosities 10000-20000 cP[137] • Only printable on planar substrates and need careful post-process clean-up
Dispenser Printing	• Minimal material waste and no micropatterning needed • Non-contact printing on planar or non-planar substrates • Wide ink viscosity range 100-10000 cP[155] • Suitable for thick 3D structure printing	• Low line resolution and slow printing speed • Less suitable for large-area films • Slightly complicated to implement • Ease of clogging printer head with time
Spray Printing	• Printable on planar or non-planar substrates • Suitable for thick and large-area films • Wide ink viscosity range and fast printing speed	• Large material waste • Micropatterning needed with minimal design flexibility • Low line resolution and need careful post-process clean-up
Drop Casting	• Low material waste and wide ink viscosity range • Printable on planar or non-planar substrates • Cheap, fast, and easy to implement	• Micropatterning needed with minimal design flexibility • Low line resolution and non-uniform in thickness

2.6.2 Other Deposition Techniques

Other deposition techniques, such as doctor blading,[168] drop casting,[169] spin coating,[93], spray printing,[129] painting,[170] electrochemical deposition,[24] and sputtering,[171] are also intensively used in depositing and shaping thin and/or thick films onto flexible substrates. In particular for drop casting and spin coating, almost any imaginable combinations of inks and substrates are feasible, with fewer restrictions in terms of ink viscosity and rheological behaviour. These deposition approaches might be fast and cheap to fabricate larger-size films. However, they have less control of the feature resolution and uniformness. Micropatterning or masking is required to form specific film patterns, thereby resulting in lower design flexibility as well as considerably massive material waste.

2.6.3 Design of Flexible Thermoelectric Generators

In the literature, there are two different device designs for flexible TEGs. One design is a lateral layout that is printed in just one plane (2-D structure) with the in-plane thermal gradient parallel to the substrate (see Figures 2.7 (a) - (d)). This in-plane design is likely to have a smaller film thickness. Higher internal resistance is also seen in this design, which results in comparatively lower voltage and power outputs.[172] The other design is a vertical layout that is built up with a certain height in a 3D structure with the out-of-plane thermal gradient perpendicular to the substrate (see Figures 2.7 (e) and (f)). However, this out-of-plane design is prone to quick temperature equilibrium across the TEG due to the relatively shorter length of individual TE leg, and the resulting ΔT across the TEG is also low.[172] Meanwhile, since alternating *n*- and *p*-type TE legs are not easily obtained from the same printing method owing to the difficulty of possessing *n*-type organic TE materials, conductive metal interconnects, such as silver, are often employed to replace *n*-type legs for the final device fabrication. Since most TE materials, including organic TE polymers, require high-temperature sintering for the alloy formation or thermal treatment after the film deposition, the PI substrate is preferred by virtue of its good mechanical flexibility and excellent thermal stability (up to 450 ^{o}C), with inherently high thermal resistance.

For different printing methods, the required ink compositions and viscosities differ significantly to each other. In this context, printing inorganic TE materials can be very tricky because of the challenges involved in the ink preparation, such as functionalising the dispersed particles to form a stable suspension, achieving uniform size distribution of these particles, and tuning their viscosity for the smooth printing by using the desired printing technique. Printable inks or pastes with appropriate rheological behaviour should be optimised in advance, because the ink/paste formulation and the resulting printed film morphology are crucial for achieving higher TE properties, and thus higher power output.[8,32,112] Ideally, a good printing should result in continuous electrical contact and good thermal contact with uniform surfaces. Nonetheless, some printing pitfalls, e.g. poor wetting, overspray, edge thickening (i.e. coffee ring effect), or cracks, could be introduced in printed TE materials or electrodes during the printing process, drying and baking/curing processes, or flexing of substrates. These defects could result in electrical shorting or higher leg resistance, both of which could reduce the device power output. These printing issues could be solved by the modification of ink formulation, printing process control, or substrate surface energy engineering. Thus, a proper adoption of printing materials and methods according to the specific ink used is of vital importance for mass production with low cost and high process simplicity.

Table 2-5 summarises some currently developed *p*-type and *n*-type TE composites which are fabricated by a variety of printing techniques as well as with different device designs. Different types of organic and inorganic TE materials have been mixed into inks or pastes (chalcogenide-based, carbon-based, and other hybrids) to ascertain their printability as well as final TE properties. It is found that most high-performance TE composites are *p*-type, while *n*-type composites are rarely reported. This mostly stems from the lack of *n*-type organic TE polymers used as matrices, as previously discussed in Section 2.4.

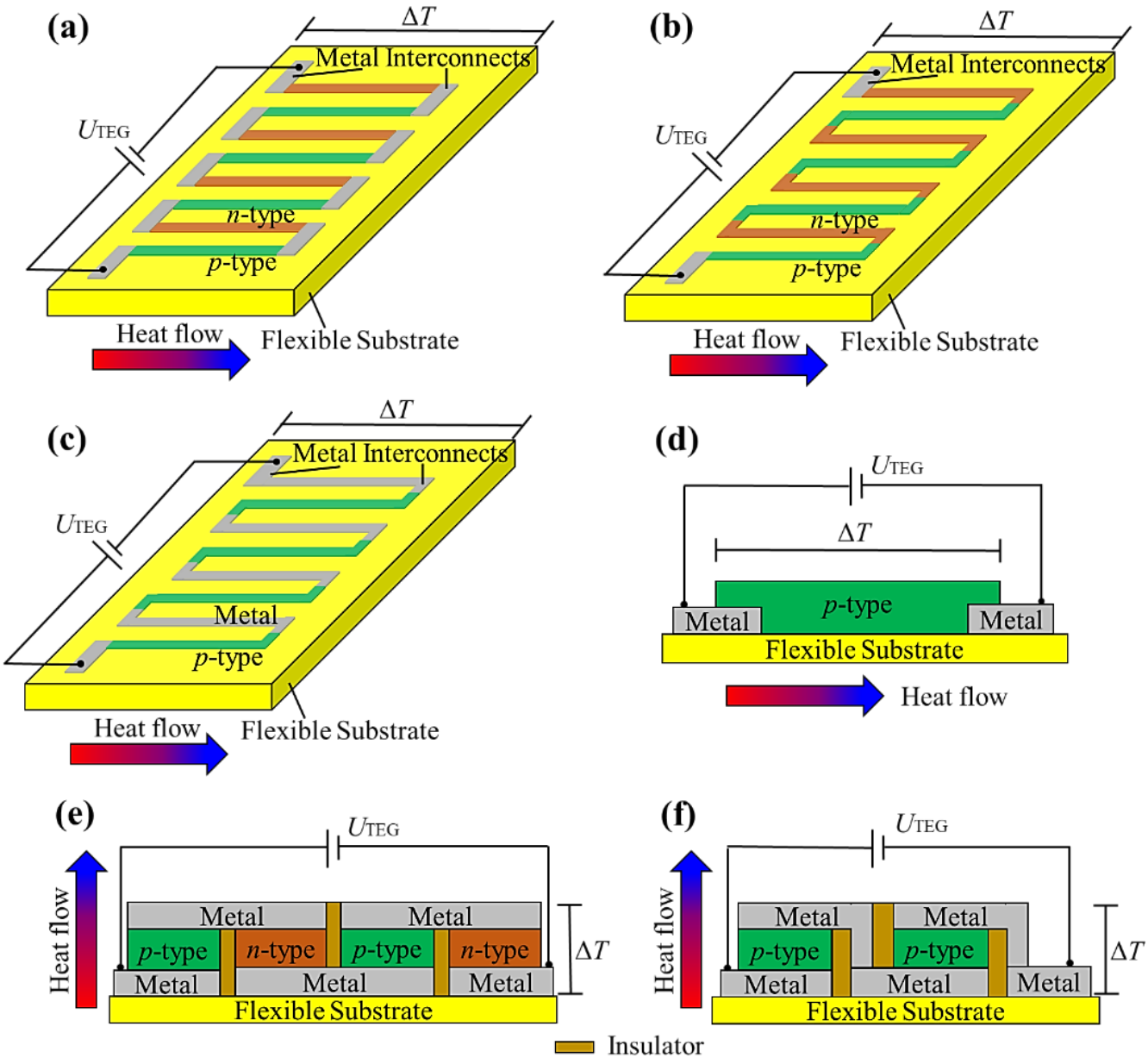

Figure 2.7 Schematic diagrams showing some major types of currently developed flexible TEG designs, where (a), (b), (c), and (d) are with a lateral layout working with the in-plane thermal gradient (parallel to the substrate), while (e) and (f) are with a vertical layout working with the out-of-plane thermal gradient (perpendicular to the substrate).

Table 2-5 Comparison of printed thermoelectric composites with different design structures.

Method	Material	S (μV/K)	σ (S/cm)	κ W/(m·K)	PF μW/(m·K²)	ZT	Design	Ref.
Aerosol-Jet Printing	Sb_2Te_3/PEDOT	33.8	247.3	–	28.3	–	d	[25]
	Sb_2Te_3/CNTs/PEDOT	29	496	–	41	–	d	[96]
Ink-Jet Printing	V_2O_5/PEDOT	-350	0.16	0.68	2	0.001	a	[126]
	Poly[Cu_x(Cu-ett)] /PVDF	41.0	5.1	–	0.9	–	a	[127]
	Poly[K_x(Ni-ett)] /PVDF	-44.9	2.1	–	0.4	–	a	[127]
Screen Printing	Sb_2Te_3/epoxy	98	1500	1.48	1441	0.29	e	[35]
	Bi_2Te_3/epoxy	-145	650	1.25	1367	0.33	e	[35]
	Sb_2Te_3/PEDOT	92.6	341	0.44	292.4	0.20	a	[128]
	Bi_2Te_3/PEDOT	-137.8	73	0.25	138.6	0.16	a	[128]
Dispenser Printing	Sb_2Te_3/epoxy	160	63	0.24	160	0.19	a	[157]
	Bi_2Te_3/epoxy	-157	61	0.24	150	0.18	a	[157]
	Bi_2Te_3/Se/epoxy	-170	96	0.38	277	0.31	c	[156]
	Te/PEDOT	115	215	0.22	284	0.39	c	[18]
Spray Printing	Te/Bi_2Te_3/PEDOT	93.6	69.9	–	60.1	–	c	[129]
	Te/CNTs/PEDOT	118	139	–	206	–	c	[173]
	CNTs/P3HT	97	345	–	325	–	c	[174]
Drop Casting	*p*-Bi_2Te_3/PEDOT	150	60	–	130	–	d	[19]
	n-Bi_2Te_3/PEDOT	-120	55	–	80	–	d	[19]
	SnSe/PEDOT	110	320	0.36	400	0.32	d	[123]
	Te/PEDOT	163	19.3	0.23	70.9	0.10	d	[175]
	CNTs/PEDOT	34	1350	–	160	–	d	[88]
	Graphene/PEDOT	14.6	71.7	–	1.5	–	d	[103]
	Bi_2Te_3/PANI	110	62.5	–	51	–	d	[124]
	Bi_2S_3/PANI	-42.8	0.4	–	0.07	–	d	[130]
	Te/PANI	102	100	0.21	105	0.156	c	[176]
	CNTs/PANI	61	610	–	220	–	d	[104]
	Graphene/PANI	26	814	–	55	–	d	[105]
	Bi_2Te_3/P3HT	118	4.5	–	6.3	–	d	[125]
	CNTs/P3HT	29	1100	–	95	–	d	[106]

Note: The design type here corresponds with Figure 2.7. All these parameters are measured at the temperature of 300 K. PEDOT = PEDOT:PSS, PVDF = polyvinylidene fluoride.

2.7 Functionally Graded Thermoelectric Materials

2.7.1 Functionally Graded Material Concept

The functionally graded material (FGM) concept has been proposed to achieve favourable chemical, mechanical, magnetic, thermal, or electrical properties, by gradually tuning the chemical composition, microstructure, porosity/pore size of a material according to the spatial position along the material, as illustrated in Figure 2.8.[177] FGMs are inhomogeneous materials with gradually changing structures and continuous interfaces to replace sharp interfaces within traditional composites or layered structures, in which cracks and other forms of defects are likely to concentrate.[178] For the chemical composition-graded structure, the composite can be single-phased or multiple-phased materials, with a spatial gradation in the chemical composition, leading to a corresponding spatial variation in its properties. For the other two types, the variants are their microstructure grain size and porosity/pore size, respectively. FGM structure has been widely shown to achieve higher performance compared to that of monolithic structure in the literature.[179]

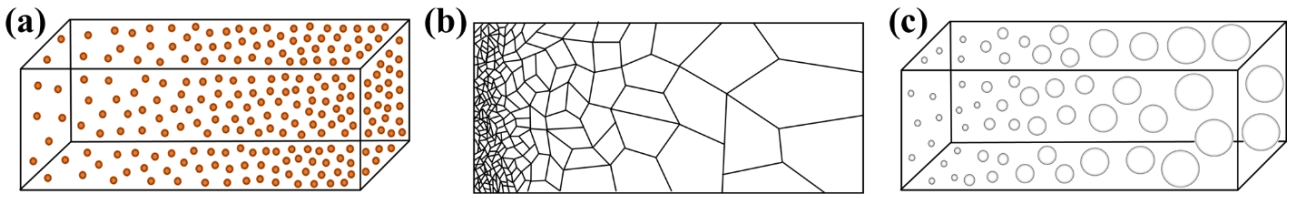

Figure 2.8 Schematic diagram showing three types of FGM structure reported in the literature: (a) chemical composition graded, (b) microstructure graded, and (c) porosity/pore size graded.

Concerning TE materials, numerous studies have been conducted on the enhancement of TE properties of single-phase TE materials, with relatively fewer studies on the development of hybrid composite structures, which have been shown to overcome some of the difficulties associated with single-phase materials.[12,15,25,26,96] Moreover, all TE materials suffer from a problem that their *ZT* or PF values often have a strong dependence on temperature. Although it is possible to provide alternative TE materials which overcome some known problems of traditional TE materials, there is still the issue that TE materials can only ever be efficient within a small temperature range because of the variation of *ZT* or PF with temperature, as shown in the temperature-dependent *ZT* values in Figures 2.4 and 2.9. This leads to a more serious and often overlooked issue, particularly when using a homogeneous single-phase TE material over a wide temperature range, without considering the position-dependent *ZT* or PF.

Consequently, this results in inefficient thermal-to-electrical energy conversion of current TEGs. This problem was, for the first time, considered in the work done by Ioffe et al.[180] The concept of functionally graded thermoelectric material (FG-TEMs) design was proposed with the use of existing inorganic TE materials, which could create more efficient TEGs with improved temperature bandwidth, energy conversion efficiency, and device lifetime, compared to that of their homogeneous counterparts.[28,179,181,182]

FG-TEMs can be designed as segmented structures (e.g. segmentation, cascading, or staging [28]) or continuous graded structure along the temperature gradient of a TE leg to effectively achieve maximum TE performance at each position.[28] However, most research has been focused on the theoretical simulation with conventional inorganic TE materials, and few experimental results that verify the FG-TEM concept. Four major types of current-researched FG-TEMs: (1) material species-graded, (2) composition-graded, (3) dopant concentration-graded, and (4) microstructure-graded. The device configuration is dependent on material selection, joining technology, device fabrication, and their practical applications,[179] which will be further discussed in the following sections.

The procedures to realise the FG-TEM concept are elaborated as follows: (1) deciding the working temperature range and temperature gradient for specific applications; (2) determining suitable segmented or continuous graded TE materials and joining technologies locally; (3) designing optimal TE leg dimensions, i.e. length and cross-sectional area of different segments; (4) assembling different segmented or continuous graded TE legs along the temperature and spatial gradient to maximise the power output; (5) modelling and measuring power output and energy conversion efficiency of the optimised TE legs, and thus TEGs.[178]

2.7.2 Segmented Structures

The segmented structure has been widely utilised to verify the FG-TEM concept by stacking together multiple dissimilar homogeneous materials with different TE properties to achieve a higher energy conversion efficiency over wider operating temperature ranges.[28] This design has been the most intensively used in the literature, as it can be easily fabricated with different TE materials having optimum *ZT* values at different operating temperature ranges. For instance, by combining the temperature-dependent *ZT* values with the spatially

varying temperature profile, as highlighted in the red line in Figure 2.9 (a), it allows the local selection of particular materials or compositions to optimise the performance and efficiency across the whole length of TEG.[28] A segmented FG-TEM can be physically joined with the required spatial arrangement, as schematically sketched in Figure 2.9 (a), which are composed of Bi_2Te_3 at the low-temperature range (<520 K), PbTe at the medium temperature range (520 K - 870 K), and SiGe at the high-temperature range (>870 K). A higher overall *ZT* value over the temperature range from 300 K up to 1300 K can be expected.[181] The augmented energy conversion efficiency is calculated to be 23.3%, which is twice of that for the single-phase material, e.g. SiGe.[179] However, this three-part segmented TEG has not been implemented yet due to electrical current matching issues.[28] One study reported how this configuration could be realised with a proper device design, but it has not been experimentally proved yet.[183] More research is hence needed to probe into the feasibility of segmented FG-TEMs, as summarised in Table 2-6, where material species-graded, composition-graded, dopant concentration-graded, and microstructure-graded structures can be applied to verify the usefulness of FG-TEM concept.

For the material species-segmented TEG with multiple joints between completely dissimilar materials, such as *p*-type Bi_2Te_3–Zn_4Sb_3–$CeFe_4Sb_{12}$ or *n*-type Bi_2Te_3–$CoSb_3$,[184] the diffusion/contamination phenomenon and degradation problems would arise inevitably because of the thermal fatigue, thermal shock, thermal expansion mismatch, and high-temperature corrosion at the interfaces.[28,179] These could have a detrimental effect on the device performance and lifetime owing to the device efficiency being lost at the interfaces and metal interconnects.[28,179] Therefore, it is paramount to select proper diffusion barrier, metallisation, and brazing materials in order to reduce the interface contact resistance while improving their mechanical stability.[179] The high flatness of the segment interface is also required to mitigate thermal degradation issues.[28] In comparison, composition-segmented TEG could avoid the problem of joining different material species. If a proper stepwise change of the composition, i.e. carrier concentration, is modified to fit with the temperature at each part along the ΔT, a twofold higher TE performance than that of its homogeneous counterparts could be expected.[179,182] Dopant concentration-graded[185] and microstructure-graded [186] structures are other alternatives for segmented TEG fabrication using similar TE materials. Nevertheless, they are less popular due to the difficulty of controlling dopant concentration or microstructure change with spatial precision. Therefore, they are not further discussed in this thesis.

One significant drawback of this segmented structure approach is the difficulty of connecting multiple dissimilar materials without the introduction of interconnects and interfaces that are prone to cracks or even delamination failure. This is mainly attributed to the thermo-mechanical stress accumulated at such interfaces in the presence of different thermal expansion coefficients during practical use. The introduction of such physical interfaces also reduces the overall electrical conductivity, which has a negative impact on TE performance. Additionally, elemental diffusion and contamination, especially at a higher temperature, could also significantly deteriorate the device performance and lifetime.[28,178,179,181,182,187]

With existing joining technologies and manufacturing processes, it is still quite challenging to assemble dissimilar TE segments without affecting their properties. As summarised in Table 2-6, the joints between dissimilar TE materials can be produced by pressureless sintering,[188,189] plasma activated sintering,[190] pulse discharge sintering,[191,192] hot pressing,[185,193,194] spark plasma sintering,[186] or other diffusion bonding techniques, according to the selected TE materials.

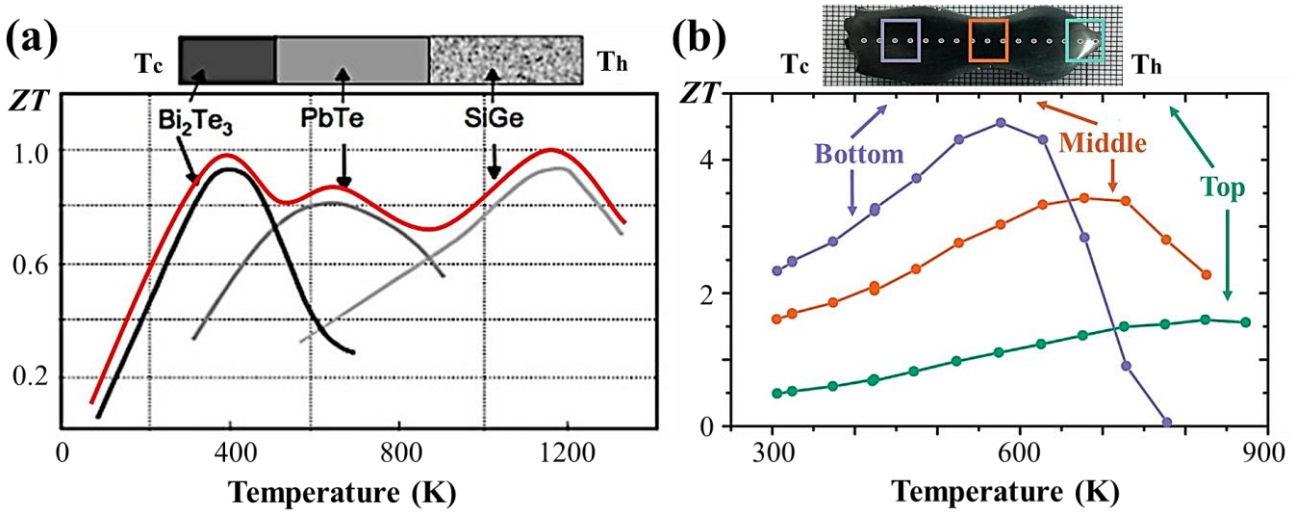

Figure 2.9 (a) Comparison of temperature-dependent *ZT* values for various TE materials, where the red line indicates the principle of performance optimisation in FG-TEMs by stacking them according to their spatially varying temperature profiles with maximum *ZT*. (b) Cross-sectional view of the Czochralski pulled composition-graded sample $Ge_{1-x}Si_x$ (x = 0 to 0.25), and experimentally measured *ZT* values at three positions along the sample. (Figure (a) reproduced with permission from [181]. Copyright 2003 Elsevier. Figure (b) reproduced with permission from [195]. Copyright 2014 American Chemical Society.)

2.7.3 Continuous Structures

On the other hand, continuous FG-TEMs can be made by progressively changing the composition, dopant concentration, or even microstructure along different regions of the TE material for performance enhancement, as discussed in Table 2-6. This continuous graded design can avoid interface problems, such as thermal misfit, chemical incompatibility, and diffusion/contamination issues. As presented in Figure 2.9 (b), composition-graded *p*-type $Ge_{1-x}Si_x$ sample was grown by the Czochralski pulling technique, where its compositions and Seebeck coefficient values were changed along the pulling direction of the sample, thereby increasing its *ZT* values over the whole temperature range.[195] Another example is where a progressive carrier concentration gradient was achieved in an *n*-type PbTe crystal by Czochralski crystal growth with varying dopant concentrations.[196,197] The peak *ZT* could be tuned by manipulating the amount of carrier concentration.[28]

Graded microstructure (i.e. grain size) in the material can also lead to a gradual change of TE properties along its spatial distribution. Also, microstructure-graded TEM has shown to greatly mitigate the thermo-mechanical stress cracking to extend the device lifetime owing to its large thermal conductivity differences. Because the coarse grains can spread heat more quickly under the transient heating, their thermal stability is largely enhanced.[28,198]

Although no additional interface is introduced between different regions in these continuous FG-TEMs, it has proven to be rather difficult to fully optimise the *ZT* values within specific temperature ranges studied. Meanwhile, it is challenging to control the diffusion of carriers through the TE material, in particular when used at elevated temperatures, which could substantially deteriorate the device performance and lifetime. Furthermore, the current research on continuous FG-TEMs is still at the proof-of-concept stage, and it is still doubtful whether they could be well controlled in the manufacturing process and utilised for practical TEG applications.

Table 2-6 Comparison of different types of functionally graded thermoelectric materials and generators developed in the literature.

Type	Material	Graded	Configuration	Joining technology	Temperature range	Ref.
***p*-type**	$PbTe$ / $(PbTe)_{0.8}$–$(SnTe)_{0.2}$ / $(PbTe)_{0.6}$–$(SnTe)_{0.4}$	Segmented	Material species	Pressureless sintering	25 – 467 ºC	[188]
	Bi_2Te_3 / $FeSi_2$	Segmented	Material species	Plasma activated sintering	30 – 600 ºC	[190]
	$AgSbTe_2$ / Sb_2Te_3 / $Bi_{0.4}Sb_{1.6}Te_3$	Segmented	Material species	Pulse discharge sintering	27 – 427 ºC	[191]
	$Pb_{0.9}Sn_{0.1}Te$ / $Pb_{0.75}Sn_{0.25}Te$ / $Pb_{0.5}Sn_{0.5}Te$	Segmented	Composition	Pressureless sintering	50 – 600 ºC	[189]
	$Bi_{0.52}Sb_{1.48}Te_3$ / $Bi_{0.5}Sb_{1.5}Te_3$	Segmented	Composition	Hot pressing	50 – 300 ºC	[193]
	$Ge_{1-x}Si_x$ (x = 0 to 0.25)	Continuous	Composition	Czochralski crystal growth	50 – 600 ºC	[195]
	$(PbTe)_{1-x}(SnTe)_x$ (x = 0.11 to 0.25)	Continuous	Composition	Bridgman crystal growth	25 – 350 ºC	[199]
***n*-type**	$Co_{0.92}Ni_{0.08}Sb_{2.96}Te_{0.04}$ / Bi_2Te_3	Segmented	Material species	Pulse discharge sintering	32 – 612 ºC	[192]
	$Bi_2Te_{2.7}Se_{0.3}$ / $Bi_2Te_{2.4}Se_{0.6}$ / $Bi_2Te_{1.5}Se_{1.5}$	Segmented	Composition	Hot pressing	50 – 300 ºC	[193]
	$PbTe$ / $Pb_{0.999}Ti_{0.001}Te$	Segmented	Composition	Hot pressing	50 – 500 ºC	[194]
	0.01% / 0.055% PbI_2 doped $(PbSn_{0.05}Te)_{0.92}(PbS)_{0.08}$	Segmented	Dopant concentration	Hot pressing	50 – 500 °C	[185]
	180 / 320 / 540 / 950 / 1400 nm grain size ZnO	Segmented	Microstructure	Spark plasma sintering	127 – 577 ºC	[186]
	0.01% to 0.1% PbI_2 doped PbTe	Continuous	Dopant concentration	Czochralski crystal growth	50 – 450 ºC	[196]
	0.1% to 4% In doped PbTe	Continuous	Dopant concentration	Czochralski crystal growth	50 – 600 ºC	[197]
	180 to 1200 nm grain size ZnO	Continuous	Microstructure	Spark plasma sintering	100 – 400 ºC	[198]

2.8 Stretchable Thermoelectric Generators

By incorporating a degree of stretchability, multi-functional electronics, like sensors and transistors, can be extended for various wearable and biomedical applications, where large mechanical deformation and stretching are experienced at asymmetric and non-planar surfaces, e.g. wrists and elbows of the human body.[200–202] This can also improve the reliability of some health-care parameter measurements via wearable and/or implantable sensing electronics, where it is a challenge for traditional rigid materials, such as silicon, owing to their intrinsic brittleness that largely constrains their ability to be bent or stretched during use.[203] Furthermore, in order to fit in future wearable electronic applications, innovative materials and device designs are required to make existing TE materials and TEGs stretchable so that they can be integrated into textile or fabrics for the low-grade waste heat harvesting from the human body, as well as for the battery-free operation of 'small-power' miniature devices.[49,50,74] The stretchability can also ensure TEGs conform to the human body (i.e. heat source) and form excellent thermal contact so as to create higher power outputs.[204]

Considerable research efforts have been devoted to the achievement of stretchability in various functional electronic devices over the last decade.[205,206] However, due to the constraint of current TE materials and device structures, the advancement of stretchable TEGs still remains at an early stage. As summarised in Table 2-7, there are two mainstream approaches to achieving stretchable systems by modifying existing rigid and non-stretchable inorganic and organic materials.[203,206–208] This will be elaborated in the following section.

2.8.1 Material Modification Approaches

In the literature, the most facile and scalable means to design conducting stretchable materials is through embedding a variety of conductive fillers (either inorganic or organic) within the stretchable matrix of elastomers or soft materials to form soft and rubbery composite structures towards stretchable electronics.[203] Stretchable elastomers, such as rubber, latex, polyurethane (PU), poly(dimetylsiloxane) (PDMS), poly(styrene-ethylene/butylene-styrene) (SEBS), to name a few, can be employed as a stretchable supporting substrate or a stretchable encapsulant matrix. Among them, PDMS is widely used by virtue of its advantages of being inexpensive and biocompatible with excellent deformability and stretchability. PDMS is also easy to bond with other material layers if a multilayered structure is desired. The bonding interaction, as well as the elastic modulus difference between filler materials and elastomeric

encapsulants or substrates are essential factors to be considered. Huge differences in elastic modulus between hosting elastomers and embedded filler materials could result in highly concentrated stresses at the interfaces, thereby causing failure during operation.[206] Highly conducting metal-based or carbon-based nanomaterials, such as Ag,[201] CNTs,[209] or their composites,[210] are the commonly used conductive filler materials for the fabrication of stretchable conductors, which can be deployed as electrodes and/or interconnects for wearable devices.[211] Organic conducting polymers are also promising candidates as conductive fillers by virtue of their acceptable electrical conductivity and mechanical ductility.[207] Among them, PEDOT:PSS is the most researched conducting polymer, which has been intensively utilised for stretchable conductor or TEG applications.

When it comes to the stretchable TEG fabrication, the material selection is restricted to a small category of conducting materials, as previously discussed in Section 2.4. Organic TE polymers, like conjugated polymers and coordination polymers, possess good thermoelectric and mechanical properties, they therefore have been used for the fabrication of stretchable TE composite. For example, *p*-type stretchable TE composites have been developed by solution blending of *p*-type PEDOT:PSS polymer with various elastomers, in particular with PU[212] and PDMS[211]. Also, as reported by Wan et al., *n*-type poly-nickel-ethenetetrathiolates [Na_x(Ni-ett)$_n$] polymer has been blended with PU to form a highly stretchable TE composite structure, which has demonstrated its potential as a self-powered wearable sensor.[213]

As summarised in Table 2-7, chemical modification on organic TE polymers is one of the most researched approaches apart from the elastomer blending method discussed above. Although PEDOT:PPS exhibits the highest electrical conductivity among existing conducting polymers, it possesses very limited toughness and tear resistance as well as low elasticity and fracture strain (<5%) owing to its rigid conjugated backbone. In this regard, chemical modification is required to achieve mechanical stretchability.[200,212] For instance, Wang et al. proposed that the stretchability of PEDOT:PSS could be remarkably improved while maintaining excellent electrical conductivity, by doping with an optimum concentration of ionic additives as stretchability and electrical conductivity enhancers, e.g. Zonyl or Triton plasticisers.[200] Moreover, stretchable TE composites can also be developed by embedding high-performance inorganic TE materials within stretchable elastomers via solution blending or dip-coating methods,[214] or by forming TE thin films and transferring/coating them onto stretchable elastomers via different deposition or printing methods.[52] However, there still

exist some issues with inorganic TE materials due to their poor dispersion within the insulating elastomeric matrix as well as the difficulty of forming electrical connections between the inserted TE materials.

2.8.2 Device Structure Modification Approaches

Engineered stretchable geometries, such as helical or wavy shapes, that resemble the structure of a spring, can be another approach to realising stretchable TE materials and generators. From an engineering perspective, there should be no constraint on the TE material selection by this device structure modification approach, as the stretchability is ensured by the benefit of the architectural design rather than the material itself. The applied TE materials can range from rigid inorganic TE materials, particularly semiconductors or metallic alloys with excellent TE performance, to organic TE polymers. Stretchable structures can be achieved by geometrically patterning them into in-plane or out-of-plane wavy lines or buckled films via a variety of microscale additive manufacturing technologies, as described by Dang et al. in their review.[203]

Considerable research efforts have been focused on stretchable electronic systems, which are comprised of islands of stiff electronic components being electrically connected by geometrically stretchable interconnects. They can be either fully encased within a stretchable elastomer substrate or free-standing without a supporting substrate. This stretchable architecture has been explored as the most effective strategy for the development of wearable electronics.[202,203,215] In this regard, stretchable TEGs can also be realised by making the interconnecting electrodes stretchable, such as introducing spiral-shaped[216] or origami-like[217] stretchable electrodes or using liquid alloys[218] to connect different rigid islands, while the main bulk of the TEG still remains rigid. The work of Rojas et al., as demonstrated in Figure 2.10 (a), is a good example of how the spiral-shaped stretchable TEGs can be developed to obtain an extra degree of freedom for the purpose of being a wearable power source.[216] Liquid alloys, like galinstan, were adopted as stretchable electrodes for the connection of individual inorganic TE legs, as described by Jeong et al. in Figure 2.10 (b).[218] Since liquid alloys do not require a special shape to be encased within a stretchable elastomer, they can be patterned easily via simple deposition processes. However, they are restricted to form short segments of wire, because the capillary force might induce fluid instabilities during stretching and deforming liquid metals.[219]

Another scheme to obtain stretchability is the deployment of extremely thin films of brittle inorganic TE materials that are coated or printed onto wavy or buckled stretchable substrates. As investigated by Kim et al., strain engineering is a simple and effective solution to produce geometrically stretchable TEGs.[220] The wrinkled or buckled substrate, as illustrated in Figure 2.10 (c), is formed by being pre-strained to a certain degree prior to the TE film deposition, in which the applied strain value indicates the stretchability limit of deposited TE films, after releasing the pre-strain from the substrate.[203,220] These deformations render rigid TE films to act like a rubber with significantly improved stretchability while not deteriorating their TE performance considerably.

For the achievement of greater stretchability, self-supported and free-standing stretchable structures have been intensively investigated to get rid of the constraint of the supporting substrate. As presented by Jing et al., free-standing conducting wires with multilayered serpentine structures were fabricated via a scalable aerosol-jet printing technique.[159] Their obtained composite structures, in which conductive silver nanoparticles were inserted within a polyimide supporting matrix, exhibited excellent mechanical stretchability and robustness even when being deformed at large strains.[159] A recent study conducted by Nan et al. also demonstrated the feasibility of developing silicon-based stretchable TEGs by transforming a 2D precursor system into an interconnected array of 3D helical coil architecture via a compressive buckling method, as illustrated in Figure 2.10 (d).[204] Nevertheless, their device size was limited and only available at the microscale owing to the substantial material cost as well as the sophisticated and time-consuming fabrication procedure of the photolithography process employed. In this regard, printing techniques are favoured for large-scale production of large-area electronic applications.[203] Another 3D helical stretchable TEG, as introduced by Xu et al., was produced via a facile coating method. Chalcogenide-based metallic alloys were coated on a stretchable PU substrate with a 3D helical shape to form a geometrically stretchable structure.[221]

Table 2-7 Comparison of stretchable TE materials and TEGs by adopting various material modification or device structure modification approaches reported in the literature.

Approach	Material	Processing treatment	Electrical characteristic	Stretchability test	Ref.
Material Modification	PEDOT:PSS	Ionic liquid doping	σ ~3000 S/cm	1000 cycling at ε ~1 ~12% loss in σ	[200]
	PEDOT:PSS	Zonyl/DMSO doping	σ ~393 S/cm S ~18.5 μV/K	300 cycling at ε ~0.5 ~50% loss in σ and S	[222]
	PEDOT:PSS	Hydrogel forming	σ ~40 S/cm	Max. loading at ε ~0.3 no change in σ	[223]
	PEDOT:PSS + PU	Elastomer blending	σ ~79 S/cm S ~16 μV/K	Max. loading at ε ~7 no change in σ and S	[212]
	PEDOT:PSS + PDMS	Elastomer blending	R_{sh} ~2 Ω/sq	5000 cycling at ε ~0.1 no change in σ	[211]
	Na_x(Ni-ett)$_n$ + PU	Elastomer blending	σ ~0.01 S/cm S ~ -40 μV/K	Max. loading at ε ~5 no change in σ and S	[213]
	Graphene + PDMS	Elastomer blending	ΔV ~0.48 mV at ΔT ~15 K	1000 cycling at ε ~1 no change in ΔV	[214]
	PEDOT:PSS + PEG/PEO/PVA	Soft material blending	σ ~172 S/cm	Max. loading at ε ~0.5 no change in σ	[224]
	n-WS_2 + *p*-$NbSe_2$ + PDMS	Contact printing	P_{max} ~38 nW at ΔT ~60 K	100 cycling at ε ~0.5 ~45% loss in P_{max}	[52]
Device Structure Modification	*n*-Si + *p*-Si + PI	Helical coil structure	ΔV ~51.3 mV at ΔT ~20 K	200 cycling at ε ~0.6 ~22% loss in σ	[204]
	n-Bi_2Se_3 + *p*-Bi_2Te_3 + PU	3D helical structure	ΔV ~10 mV at ΔT ~15 K	1000 cycling at ε ~0.6 no change in ΔV	[221]
	n-Bi_2Te_3 + *p*-Sb_2Te_3 + PI	Spiral structure	P_{max} ~35 nW at ΔT ~75K	500 cycling at ε ~0.3 ~50% loss in σ	[216]
	PEDOT:PSS + Ag + graphene + fabric	Knitted loop structure	ΔV ~1.1 mV at ΔT ~100 K	800 cycling at ε ~0.2 ~7% loss in ΔV	[225]
	WS_2 + CNTs + PDMS	Pre-strain wrinkled film	PF ~38 μW/(m·K^2)	10000 cycling at ε ~0.3 no change in σ and S	[220]
	p-$Bi_{0.3}Sb_{1.7}Te_3$ + *n*-Bi_2Te_3 + PI	Origami-Like folding	P_{max} ~40.7 μW at ΔT ~95 K	Max. loading at ε ~0.2 no change in P_{max}	[217]
	n-/*p*-doped Bi_2Te_3 + PDMS	Liquid alloy interconnects	P_{max} ~40.6 μW/cm^2 at ΔT ~20 K	1000 cycling at ε ~0.2 ~10% increase in σ	[218]

Note: DMSO = dimethyl sulfoxide, poly-nickel-ethenetetrathiolates = Na_x(Ni-ett)$_n$, PEG = poly(ethylene glycol), PEO = poly(ethylene oxide), PVA = poly(vinyl alcohol), PI = polyimide, ε = tensile strain, R_{sh} = sheet resistance, P_{max} = maximum power or power density output.

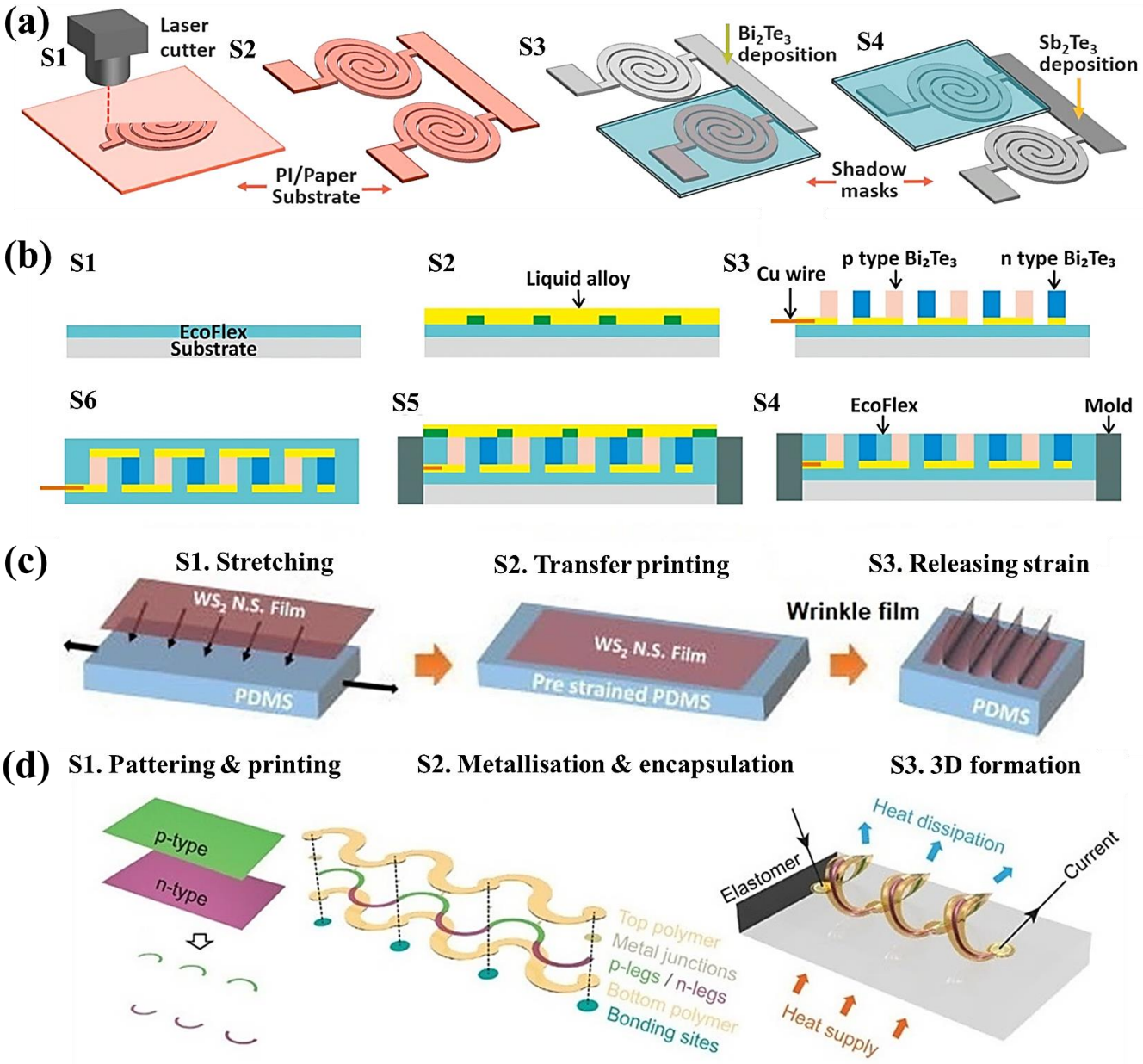

Figure 2.10 (a) Schematic illustrating the fabrication process of a spiral-shaped stretchable TEG via the laser cutting method. (b) Schematic showing the fabrication process of a stretchable TEG by using liquid alloys as stretchable electrodes. (c) Schematic of the formation of the wrinkled film by pre-straining the PDMS substrate, which was later released to achieve a stretchable TEG. (d) Schematic representing the fabrication and assembly processes of a 3D helical-coil stretchable TEG via the photolithography method. (Figure (a) reproduced with permission from [216]. Copyright 2016 Elsevier. Figure (b) reproduced with permission from [218]. Copyright 2017 American Chemical Society. Figure (c) reproduced with permission from [220]. Copyright 2019 AIP Publishing. Figure (d) reproduced with permission from [204]. (CC BY-NC))

Chapter 3

Materials and Methods

This chapter outlines the materials and methods used for the fabrication of TE nanomaterials and nanocomposites, as well as the characterisation and measurement protocols employed for the data acquisition. Experimental details of different fabrication approaches for Bi_2Te_3 and Sb_2Te_3 nanomaterials are described here to compare their material yield, quality, and scalability (Stage 1 in Figure 3.1). The aerosol-jet printing technique, morphological and structural characterisation methods, thermoelectric measurement and mechanical test setups, as well as modelling tools are elucidated in the rest of the chapter (Stages 2 and 3 in Figure 3.1). Finally, different design structures used for flexible and/or stretchable TEGs are fabricated for the investigation of their TE performance (Stage 4 in Figure 3.1).

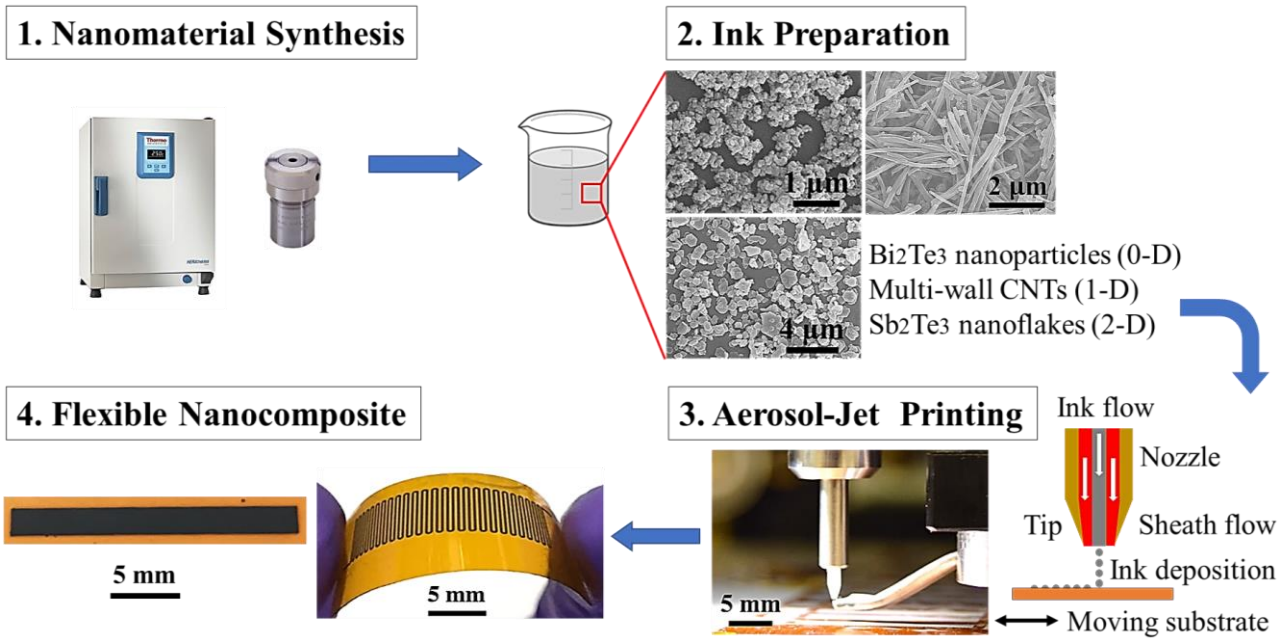

Figure 3.1 Overview of fabrication processes for aerosol-jet printed TE nanocomposites and TEGs in this thesis.(Figure reproduced from the author's work [25]. (CC-BY))

3.1 Nanomaterial Fabrication

For the inorganic TE material fabrication, two different approaches were attempted here. (1) Top-down approach: the crystals are derived from bulk materials by physical or chemical processing routes, e.g. hand grinding, ball milling, or exfoliation.[71] These approaches have some drawbacks, e.g. defects and imperfections, high processing cost, and difficulty in producing uniform structures, but they are scalable for mass production.[66] (2) Bottom-up approach: the compounds are formed through self-assembly from atoms or ions by chemical synthesis, including solvothermal, polyol, electrochemical, or sol-gel methods.[71] They allow better control of crystal sizes and compositions, and are reproducible and economical.[66]

3.1.1 Top-down Fabrication Approach

(i) Hand Grinding

Commercially available bismuth telluride (Bi_2Te_3, powder, ≥ 99.99%, Sigma-Aldrich) and antimony telluride (Sb_2Te_3, beads, ≥ 99.99%, Sigma-Aldrich) were purchased for the subsequent material fabrication. Agate mortar and pestle (Sigma-Aldrich) were used for crushing and grinding Bi_2Te_3 powders and Sb_2Te_3 beads manually for 30 minutes so that the ground powders were fine enough to be subsequently printed via the AJP method (Section 3.3). This is the quickest and most straightforward method to fabricate microscale or even nanoscale particles, but it is difficult to control the size and shape homogeneity of obtained particles.

(ii) Ball Milling

Ball milling is another way to prepare Bi_2Te_3 and Sb_2Te_3 nanoparticles with significantly reduced particle sizes. Nonetheless, it might reduce crystallinity and form clusters and agglomeration.[1] In this project, Bi_2Te_3 and Sb_2Te_3 powders, which were purchased from the same supplier as discussed above, were milled for 10-40 hours via a high-energy planetary ball mill (Fritsch Pulverisette 7) with the help of Dr Pedro Sanchez-Jimenez. Different types of mills, ball diameters, and additives were tried here. Because using smaller balls could effectively break large particles into smaller ones, and adding liquid media and surfactants (e.g. oleic acid) could prevent cold-welding and reduce agglomeration issues. It was found that the milling time of 20 hours and the grinding ball diameter of 10 mm (zirconium oxide) were the optimum milling conditions for fabricating nanoscale particles with good crystallinity. There might remain some residual organic compounds on the surface of powders that should be

completely burned out at temperatures of 500-600 ºC. But this high-temperature heat treatment could cause some powders to be oxidised or even decomposed. Therefore, the as-obtained powders were annealed at 200 ºC to partially decompose and remove some residual liquid media and surfactants.

3.1.2 Bottom-up Fabrication Approach

(i) Solvothermal Synthesis

As demonstrated by Datta et al., Bi_2Te_3 and Sb_2Te_3 nanomaterials could be synthesised by a facile, scalable, and surfactant-free solvothermal synthesis process.[72] It is a promising low-temperature synthesis approach that has been shown to achieve high-yield TE nanomaterials with good control of the composition, phase purity, shape, and size distribution.[66,72,226] In this project, Bi_2Te_3 nanoparticles were fabricated by an ethylene glycol-mediated solvothermal synthesis method, involving a redox reaction between the bismuth nitrate and sodium tellurite. Additionally, no templates were employed in this synthesis method to confine nanocrystals into different shapes.[72] 0.25 mmol (0.1213 g) of bismuth nitrate pentahydrate ($Bi(NO_3)_3 \cdot 5H_2O$, 98.0%, Sigma-Aldrich) was firstly dissolved in 1 mL of acetic acid (99.7%, Sigma-Aldrich). Subsequently, 9 mL of ethylene glycol (EG, 99.8%, Sigma-Aldrich) was added as a reaction medium that served as a reducing and capping agent to form a protective layer around the particle surfaces and inhibit the particle growth and agglomeration (see Figure 3.2).[72,226] After stirring for 10 minutes, 0.375 mmol (0.0831 g) of sodium tellurite (Na_2TeO_3, 99%, Sigma-Aldrich) was added as the 'Te' source, and stirred for 30 minutes for homogeneity. Finally, when all the added powders were completely dissolved, 5 mL of hydrazine hydrate ($N_2H_4.H_2O$, 50-60%, Sigma-Aldrich) was added as a reducing reagent to reduce the sodium tellurite and also to prevent the surface oxidation of synthesised nanocrystals.[72] It should be noted that hydrazine is highly corrosive and toxic, and easily oxidised. Adequate safety precautions were taken during its handling, such as working in a fume hood and wearing personal protective equipment. The final mixed solution with a volume of 15 mL was sealed within a Teflon-lined stainless-steel chamber and then inserted into an autoclave (Kankun Instrument, 25 mL). The solvothermal reaction was performed at 175 ºC for 12 hours in a gravity convection oven (Thermo Scientific).

For the Sb_2Te_3 nanoflake synthesis, the same procedure was followed as above, but where the bismuth nitrate was replaced with an equal molar quantity of antimony acetate as a

precursor. 0.25 mmol (0.0747 g) of antimony acetate ($C_6H_9O_6Sb$, 99.99%, Sigma-Aldrich) was used as the 'Sb' source, and all reactions were carried out under the same conditions as in the case of Bi_2Te_3. In this respect, this synthesis process can be extended to other telluride or selenide alloy nanocrystals.[72] It should be noted that all chemical reagents used here were of analytical grade from Sigma-Aldrich and were used as received without further purification.

After synthesis, the obtained nanocrystals were subsequently rinsed using DI water and ethanol, and then collected by centrifugation (Sigma 1-14 microfuge). Between each washing, they were treated within an ultrasonic bath to clean as-received nanocrystals thoroughly, which should not affect the particle size and crystallinity of nanocrystals. By doing these steps, unreacted chemicals and solvents that remained on the surface were cleaned and removed.[72] Lastly, the nanocrystals were dried in a vacuum desiccator overnight, which provided a non-oxidising atmosphere to prevent the oxidation of metallic alloys.[72] It was found that each batch of solvothermal synthesis could yield ~0.3 g of powder with a uniform particle size distribution. Mass production of these nanomaterials is paramount for large-scale fabrication of TE devices. Importantly, the above-discussed solvothermal synthesis method is not limited to these telluride-based materials, it can also be employed for other layered-structure materials, such as tin selenide (SnSe) nanosheets with good crystalline quality (see Appendix A.2).

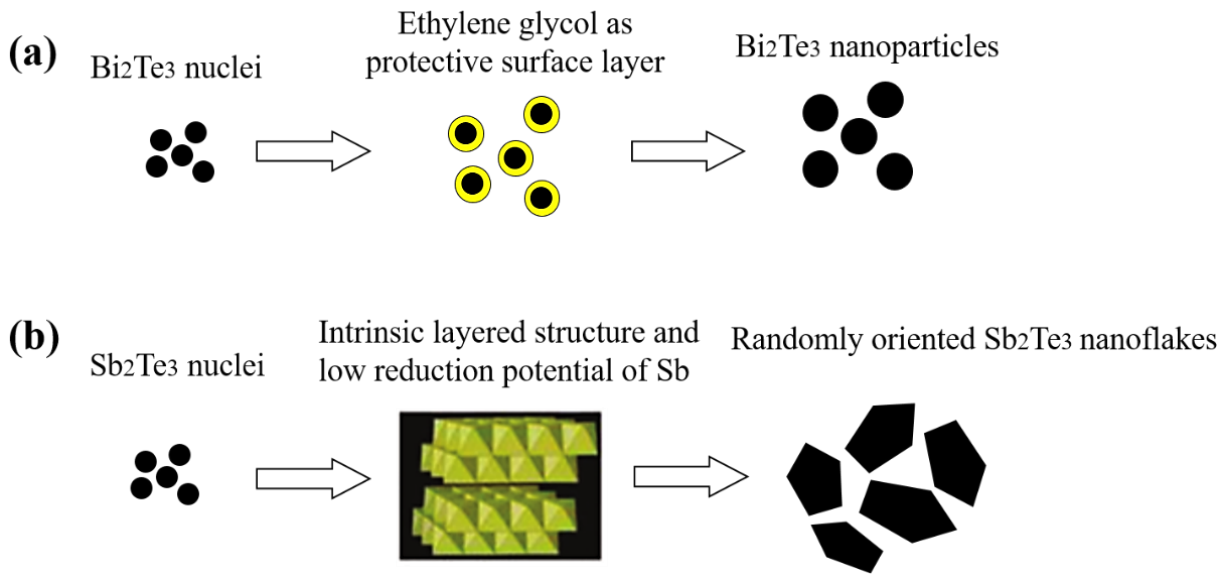

Figure 3.2 Schematic illustrating the growth processes of (a) Bi_2Te_3 and (b) Sb_2Te_3 with different nanostructured morphologies. (Figures reproduced with permission from [72]. Copyright 2010 American Chemical Society.)

(ii) Polyol Synthesis

As reported by Datta et al., Bi_2Te_3 and Sb_2Te_3 nanocrystals could also be obtained by a low-temperature polyol synthesis process.[226] 1 mmol (0.4851 g) of $Bi(NO_3)_3.5H_2O$ or 1 mmol (0.2989) of $C_6H_9O_6Sb$, and 1.5 mmol (0.3324 g) of Na_2TeO_3 were added as the 'Bi' or 'Sb' and 'Te' precursors, respectively. 2 g of polyvinylpyrrolidone (PVP, Sigma-Aldrich) was employed as a complexing agent and capping agent to control the crystal growth so as to obtain pure phase, good crystalline quality, and narrow size distribution.[226] 50 mL of ethylene glycol was served as the reaction medium and reducing agent. 2.5 g of sodium borohydride ($NaBH_4$, 99%, Sigma-Aldrich) dissolved in 5 mL DI water was also added as a reducing agent. Lastly, acetone and ethanol were used to dissolve and clean the unreacted PVP and EG, and the rinsed nanocrystals were subsequently collected by centrifuging. However, this polyol process was found to be a less effective method compared to the above solvothermal synthesis method. Since this process was simply conducted within a beaker heating on a hot plate, the open-air environment made the as-synthesised nanocrystals to be easily oxidised during the reaction, leading to fairly low crystalline quality and poor TE properties. Thus, this synthesis method was not further discussed in this thesis.

3.2 Structural Characterisation

This section provides a brief explanation of the structural characterisation tools used throughout this work: including scanning electron microscopy (SEM), energy dispersive X-ray spectroscopy (EDX), X-ray diffraction (XRD), and transmission electron microscopy (TEM). Specific instrument details are also given here.

3.2.1 Scanning Electron Microscopy (SEM)

In order to visualize the surface morphology and microstructure of fabricated TE nanomaterials, and to measure the dimensions of the resulting AJ-printed TE nanocomposites, the obtained nanomaterials and nanocomposites were coated with platinum (Pt) or palladium (Pd) by sputter-coating at the deposition current of 40 mA for 40 seconds (K575 Sputter Coater, EMITECH) to form an electrically conducting thin film so as to prevent the charge accumulation and to minimise the charging effect during SEM imaging. These samples were mounted on the SEM stub by the adhesive carbon conducting tape. Field-emission Scanning Electron Microscope (SEM, FEI Nova NanoSEM 450), operating at an accelerating voltage of

10 kV and equipped with an Energy Dispersive X-ray Spectroscopy (EDX, Bruker XFlash 6100), was used to perform imaging on nanomaterial and nanocomposite samples in order to investigate their dimensional, morphological, and compositional properties. The EDX analysis was also conducted on both fabricated TE nanomaterials and AJ-printed nanocomposites to ascertain their stoichiometry and homogeneity of chemical composition, at an accelerating voltage of 15 kV and spot size of 4. A table-top scanning electron microscope (Hitachi TM3000) was also employed for the quick morphological characterisation of AJ-printed films.

3.2.2 X-ray Diffraction (XRD)

The crystallinity, crystallite size, orientation, and phase purity of fabricated TE nanomaterials were investigated by using X-ray diffraction (XRD). The powder samples were attached flat onto a zero-diffraction silicon sample holder, and then the XRD analysis was performed on a powder X-ray diffractometer (Bruker D8 ADVANCE) equipped with Lynx Eye position-sensitive detector (Cu-Kα radiation, λ = 1.5406 Å), diffraction angle (θ, 20° < 2θ < 80°), and a step size of 0.05° at the room temperature. The obtained intensity-2θ spectra were analysed with the aid of HighScore Plus software (Version 4.1) for phase indexing. The average crystallite size was calculated by using Debye-Scherrer equation in Equation 3-1:[227]

$$D_p = \frac{0.94\lambda}{\beta \cos\theta} \tag{3-1}$$

where D_p is the average crystallite size of crystalline domains which may be smaller or equal to the grain size [nm]; β is the line broadening at half the maximum intensity (FWHM) that is calculated by non-linear fitting Gaussian Function, in radians; θ is the Bragg angle [°]; λ is the X-ray wavelength [Å].

3.2.3 Transmission Electron Microscopy (TEM)

The crystallinity of fabricated nanomaterials was confirmed by using the high-resolution transmission electron microscope (HRTEM, FEI Tecnai F20). The HRTEM samples were prepared by firstly dispersing the synthesised powders into ethanol by sonication treatment for 1 minute to obtain a uniform dispersion, and then drop-casting 2-5 drops of the suspension on the 300-mesh carbon-coated copper TEM grids. The TEM grids were air-dried under ambient conditions. The HRTEM images were obtained at an accelerating voltage of 200 kV.

3.3 Aerosol-Jet Printing

This section discusses the aerosol-jet printing (AJP) technique as a multilayered thin and thick film fabrication tool with submicron patterning capability. To modify the AJP for the nanocomposite printing, it is vital to thoroughly understand its operating mechanism. Thus, a broad framework for the AJP process is provided here, where detailed atomisation and aerodynamic focusing mechanisms, as well as the processing parameter control are described, with examples of process optimisation for some preliminary printing results. Details of the AJP technique for multilayered nanocomposites by the in-house developed *in situ* mixing method are given in Chapter 4. The author also shows that the AJP technique can serve to mitigate some of the critical issues that other contemporary printing techniques have, e.g. screen printing and ink-jet printing. The AJP technique can offer distinct advantages regarding the possibility of using inks with an extensive range of viscosities. The acceptable particle size for the printable ink here can also be much larger and less uniform.

3.3.1 Printing Process

A wide-area and fine-featured Optomec Aerosol-Jet Printing 200 system (AJP 200, Optomec Inc) installed in the author's lab allows for high-resolution rapid prototyping of multilayer electronic and structural patterns for circuits and devices on various substrates.[138] It involves creating an 'aerosol' of ink and using a carrier gas to propel this aerosol towards a substrate. As displayed in Figure 3.3, the AJP 200 system comes standard with the following major components: 1. Computer; 2. Control system; 3. Atomiser; 4. Deposition head; 5. Substrate and platen; 6. Motion system; and 7. Vision system. These components play different roles in the operating principle of the AJP process, as explained later in this section. As described by Secor et al.,[158] the AJP method is comprised of four main processes: (i) atomisation; (ii) transporting; (iii) focusing; and (iv) deposition. Among them, the atomisation and focusing processes are the essential processes, as they define the distinct features of the AJP compared to other printing techniques. More details will be discussed in the following section.

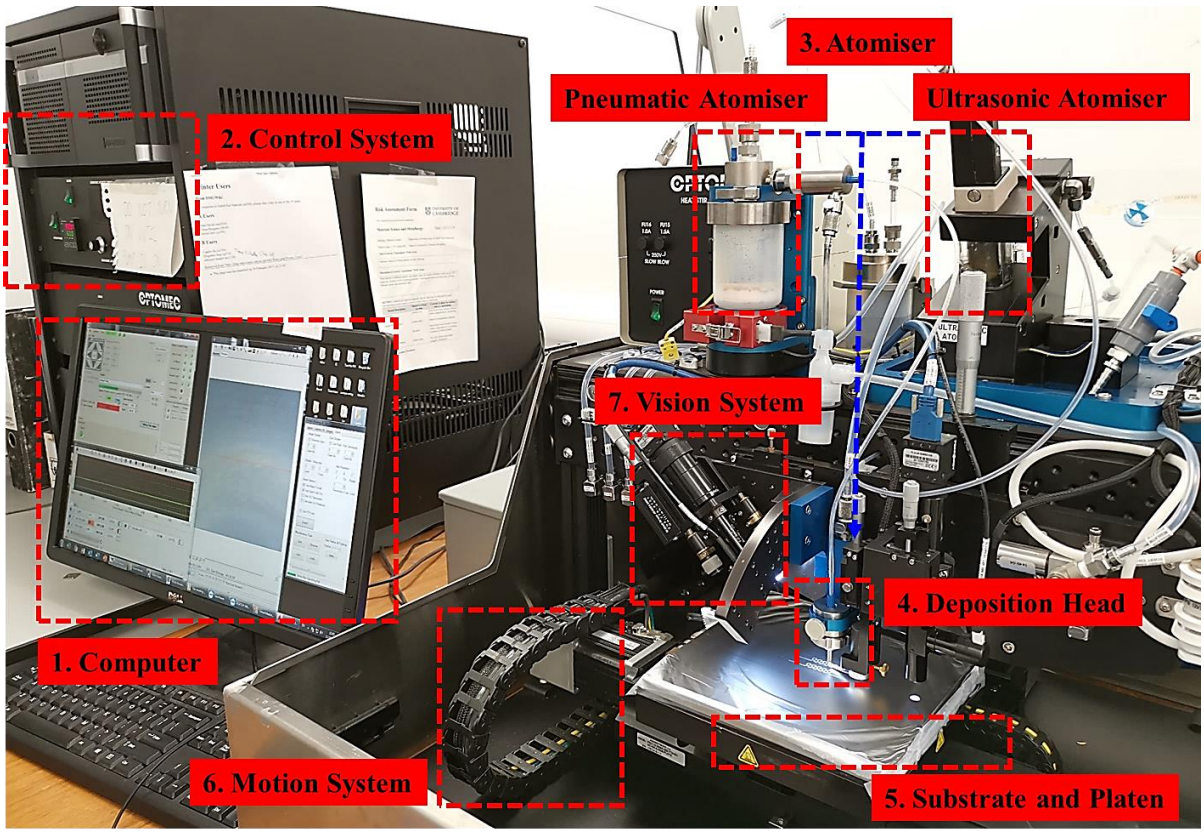

Figure 3.3 Annotated photograph showing the Optomec AJP 200 system configuration that consists of seven major components.

(i) Atomisation

For the atomisation process, the solution-based ink is atomised by creating a dense aerosol mist composed of highly loaded aerosol droplets with sizes typically ranging from 1 to 5 μm in diameter.[136,158] As illustrated in Figure 3.4, the AJP 200 system supports two different atomisation methods: ultrasonic atomiser (UA) and pneumatic atomiser (PA).

The UA atomises the liquid ink with the help of high-frequency ultrasonic waves generated by an ultrasonic transducer (see Figure 3.4 (a)).[138] Considering the maximum ultrasonication power in the system, the ideal viscosity and amount of ink are constrained at the range of 1-10 cP and 2 mL, respectively. However, in the case of the PA, its atomisation mechanism is quite different from the UA (see Figure 3.4 (b)). High-velocity nitrogen (N_2) gas is injected into the ink chamber through the upper hole to shear the ink into a fine mist. As the pressure in

the atomiser chamber builds up, a large number of ink droplets impacting the sidewall through a tiny hole and draining back to the liquid ink can be seen. As a result, highly dense and small-sized droplets remain suspended in the mist.[136] At the same time, stirring and/or heating is often applied to modify the ink viscosity and surface tension so as to achieve a better pneumatic atomisation.[136] Finally, the created mist flow is connected to a virtual impactor (see Figure 3.4 (c)) to condense the aerosol stream, where an exhaust pump is used to remove excess gas and solvent from the aerosol flow.[228]

Either the UA or PA can be chosen for the atomisation process, mostly depending on the properties of the used ink. Table 3-1 summarises some major differences between the UA and the PA. It can be seen that the UA works better with a smaller amount and lower viscosity ink, while the PA prefers large volume printing and has a larger ink viscosity capacity. Additionally, the PA is more versatile and compatible with a broader range of inks, especially with larger particle size, and is also more suitable for large-scale manufacturing.

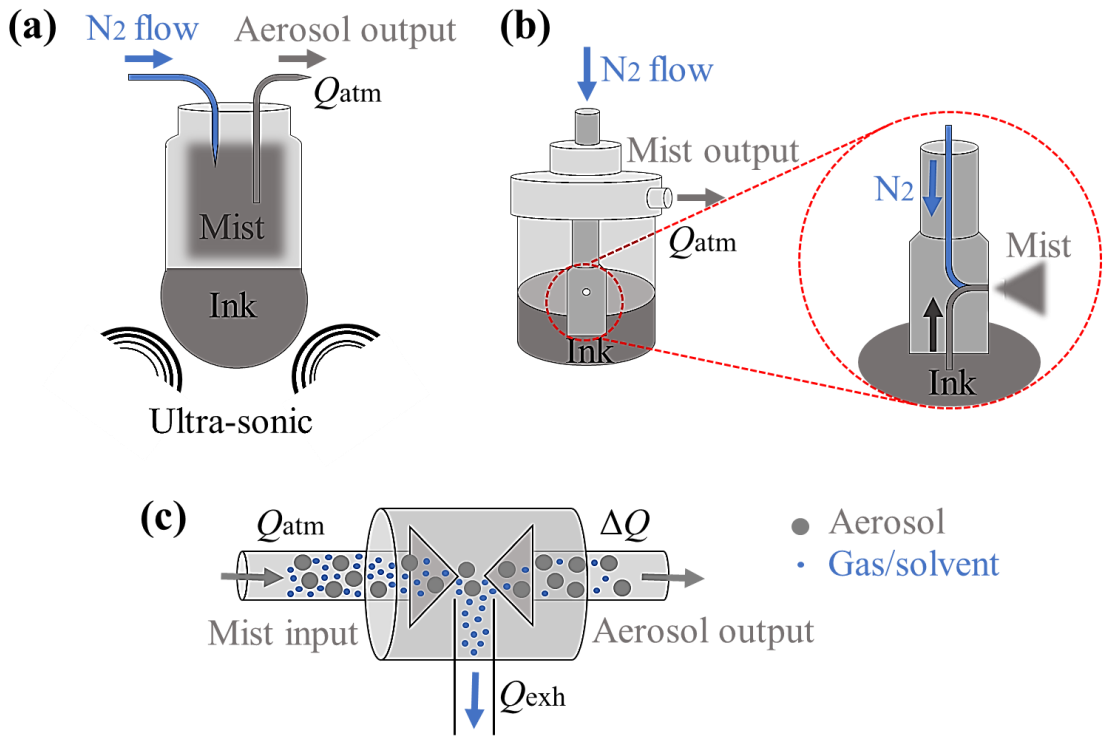

Figure 3.4 Schematic illustrating the atomisation process by (a) ultrasonic atomiser (UA) and (b) pneumatic atomiser (PA) in the AJP 200 system, where the enlarged inset illustrates the detailed atomisation mechanism of the PA. (c) A virtual impactor is connected to the PA.

Table 3-1 Comparison of the ultrasonic atomiser and the pneumatic atomiser.[136,138,229]

Atomiser	Ultrasonic atomiser (UA)	Pneumatic atomiser (PA)
Ink container	• Glass vial (fragile) • Small volume (~2 mL) of lower viscosity (1-10 cP) ink	• Teflon jar (robust) • Large volume (~20 mL) of higher viscosity (1-1000 cP) ink
Ink properties	• Used for liquid ink, nanoparticle suspensions, etc., with a smaller particle size up to 50 nm • Solvents with a higher vapour pressure	• Used for liquid inks, pastes, etc., with a larger particle size up to 500 nm • Solvents with lower to medium vapour pressure (i.e. higher boiling point)
Ink temperature	• Water bath to stabilise the ink • Temperature from 5 to 50 ºC	• Band heater and stirrer to stabilise the ink • Temperature from 25 to 60 ºC

(ii) Transporting

After the ink atomisation, the aerosol mist is entrained in a nitrogen carrier gas flow and then directly fed through a plastic tube towards the deposition print head. However, because of the large surface area of micron-sized droplets, there is a small number of aerosol droplet loss during the transport process, which can be ascribed to the rapid solvent evaporation or the impingement onto the tube wall.[158] It is worthwhile mentioning that some modifications on the aerosol transport process can be done to expand the application of this AJP technique, such as introducing a Y connector between the UA and the PA for *in situ* mixing of different aerosol droplets atomised from different ink sources or heating the plastic tube locally to modify the ink properties, just to name a few. These modifications will be further discussed in Chapter 4.

(iii) Focusing

Interchangeable fine or wide feature deposition print heads are included in the AJP 200 system, which allows printing features ranging from 10 μm to 1 mm in size.[136] The fine hollow nozzle tip diameter size ranges from 100 to 300 μm, while the wide nozzle tips are available in sizes from 0.5 to 2.0 mm.[136] In this work, a fine-feature deposition print head is

mainly used. Within the deposition print head illustrated in the enlarged view of Figure 3.5 (a), an innovative aerodynamic focusing technology is utilised here to realise the fine-feature printing. There are two nitrogen gases flowing co-axially through the nozzle and out of the tip,[138] where the atomiser gas flow (Q_{atm}) generated by the atomiser is cylindrically surrounded by a continuous annular sheath gas flow (Q_{sh}) that can focus and accelerate the aerosol stream. Then, the resulting high-velocity aerosol droplets are jetted towards the substrate.[136,138,230] This process is known as 'focusing'. By independently controlling the flow rate of Q_{atm} and Q_{sh}, the dynamics of the AJP process can be controlled with reasonable precision. The minimum printed feature that can be achieved in the AJP method is 10 μm on virtually any surface, planar or non-planar, while the single-pass layer thickness can be 100 nm to 2 μm.[136]

Since the atomisation and focusing conditions have a significant influence on the printed line profile and morphology, it is essential to find out the optimum printing conditions for various ink formulations. The relationship of different printing parameters and the resulting AJ-printed line dimensions and printing quality has been analysed in detail in a previously published work from the author's group.[138] Table 3-2 summaries and compares different printing parameters affecting the quality of the printed line. As derived by Binder et al., a simple analytical model is introduced to predict the printed line resolution, where the focus ratio (FR) is used to evaluate the aerosol droplet distribution exiting the capillary as well as the aspect ratio of the resulting printed line.[230] As defined in Table 3-2, the FR is the gas flow ratio between the sheath gas flow rate (Q_{sh}) and the atomised aerosol flow rate. Larger atomiser flow rate (Q_{atm}) in the UA or larger atomiser–exhaust delta (ΔQ) value in the PA can give a larger number of aerosol droplets loading and deposit, which leads to thicker and wider lines (i.e. lower FR). Higher sheath gas flow rate can produce narrower and higher-speed aerosol droplets impacting onto the substrate, which can result in more focused fine-feature lines (i.e. higher FR).[138,230,231] Moreover, as summarised in Table 3-2, different adjustable printing parameters, including nozzle tip size, tip height, printing speed, substrate temperature, ink temperature, and ink viscosity, can affect the final printed line width, thickness, morphology,

and uniformity. An 'overspray' phenomenon is often seen in the AJP process, The aerosol droplets deviate from the centre of gas flow when impinging onto the substrate, resulting in the increment of line width with ill-defined or 'fuzzy' edges.[138] The printed line quality can be evaluated via the quality factor (QF) defined in Equation 3-2 and Figure 3.5 (b):

$$\mathrm{QF} = \frac{d_{out} - d_{in}}{d_{in}} \tag{3-2}$$

where d_{out} is the outer width of the printed line [m], and d_{in} is the inner width [m].

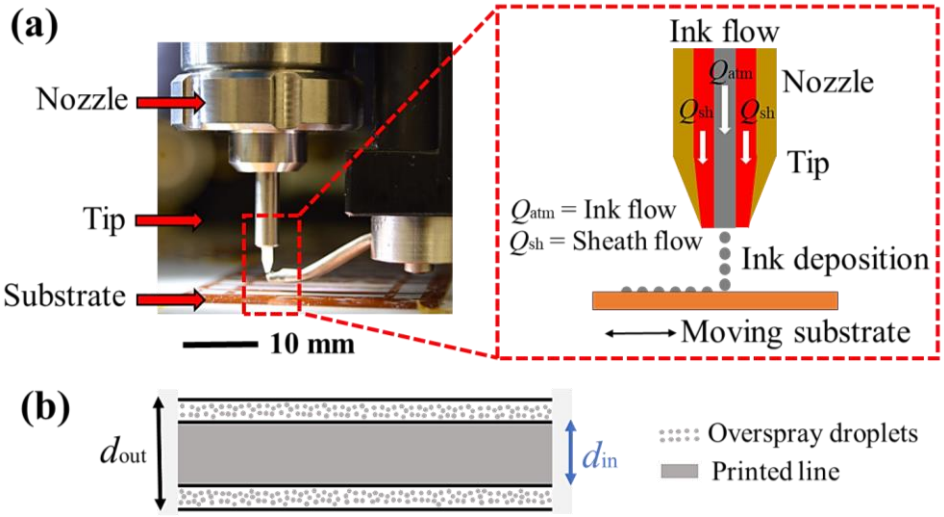

Figure 3.5 (a) Annotated photograph depicting the fine-feature deposition print head installed in the AJP 200 system. The enlarged diagram demonstrates the flow profile of aerosol and gas as well as the mechanism of focusing. (b) Illustration showing the quality factor of printed line.

Table 3-2 Comparison of different printing parameters in the UA and the PA.[136,138,230]

Atomiser	Ultrasonic atomiser (UA)	Pneumatic atomiser (PA)
Printing parameter	• Aerosol flow rate = atomiser flow rate • Focus ratio (FR) = $\frac{Q_{sh}}{Q_{atm}}$	• Aerosol flow rate = the difference of the atomiser flow rate and the exhaust flow rate, i.e. $\Delta Q = Q_{atm} - Q_{exh}$ • Focus ratio (FR) = $\frac{Q_{sh}}{\Delta Q}$
Adjustable parameter	• Sheath flow rate → focusing degree → inversely proportional to the line width • Atomiser flow rate → number of aerosol droplets → line width and thickness • Nozzle tip size, tip height, printing speed, substrate temperature, substrate surface feature, ink temperature, and viscosity → width, thickness, and morphology • Number of printed layers → directly proportional to the line width and thickness	

(iv) Deposition

Finally, aerosol droplets are deposited on a substrate, maintaining their velocity and focus ratio. As illustrated in Figure 3.6, a 200 mm x 200 mm platen installed with heating and vacuum system and controlled by a motion-control system is used here, where the substrate is mounted about 2 to 5 mm beneath the nozzle tip with the surface perpendicular to the jetted aerosol flow.[230] The motion system includes two motorised axes with the motion accuracy of ± 6 μm for each axis, and the printing speed can be up to 200 mm/s.[136] By moving the automated platen, a desired printing pattern is formed. A mechanical process shutter is used to interrupt the flow of the focused aerosol stream to pause or stop the deposition process. A vision system equipped with an optical digital camera and a high-resolution CCD camera is also employed for pattern alignment, online process monitoring during printing, and quick line morphology characterisation, which enables better control of the line width, density, continuity, and edge smoothness in order to ensure the functional integrity of printed structures.[136,138,167]

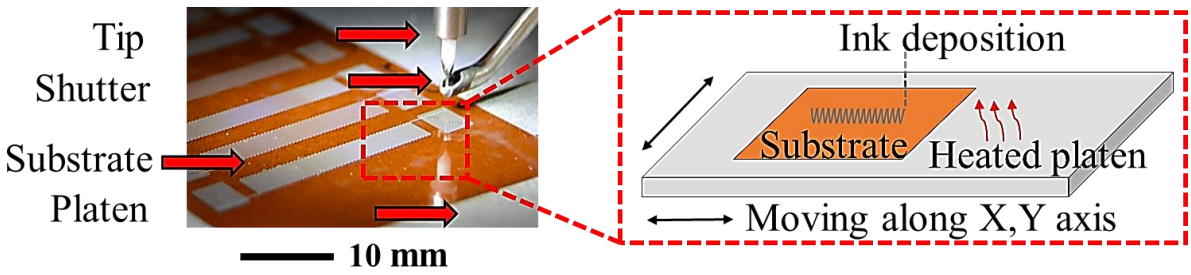

Figure 3.6 Annotated photograph displaying the motion system installed in the AJP 200 system. The enlarged inset illustrates the ink deposition process.

Importantly, since the platen can be heated up from 20 to 120 °C, the mounted substrate can be heated to a desired temperature.[136] The substrate temperature is crucial for creating fine-feature lines, as higher temperatures can reduce the coffee-ring effect (ring-like deposition pattern along the perimeter of droplet after it evaporates) and quickly cure the newly-deposited wet line to avoid the overspray issue. Besides, higher substrate temperature can increase the evaporation rate of solvent and reduce the time for the deposited droplets to spread out, thereby resulting in a narrower printed line.[138] However, the substrate temperature cannot be too high, because high temperature can cause solvent evaporating too quickly, which can result in

the poor printed line quality or the clogging of the nozzle tip.[138] Meanwhile, the wettability (i.e. contact angle) of atomised droplets can be modified by tuning the substrate surface energy via surface modifications, e.g. oxygen plasma treatment. As the substrate has a direct influence on the thermal efficiency of the TEG, substrates with minimum thickness and lowest κ are desired to help maintain the ΔT across the TEG. An ideal substrate should be electrically insulating to ensure no current passing through, and possess low κ to prevent thermal shorting.[92] Table 3-3 summarises different applicable substrates for printing, and their advantages and disadvantages are also compared. In this work, the polyimide sheet (PI, 75 μm thick, Goodfellow) was chosen, by virtue of its excellent flexibility and high-temperature stability. The PI substrate was washed in acetone and dried with nitrogen gas prior to printing. It is worth mentioning that no surface modification was undertaken on the PI substrate here.

Table 3-3 Comparison of different applicable substrates for the AJP process.

Type	Substrate	Advantage	Disadvantage
Flexible	Polyimide sheet	• Flexible and bendable • Thermally insulating • High working temp. (<400 °C)	• Expensive • Semi-transparent
	Acetate sheet	• Cheap and transparent • Flexible and bendable • Thermally insulating	• Low working temp. (<110 °C)
	Al/Al_2O_3 foil	• Cheap and flexible • Lightweight • High working temp. (<580 °C)	• Opaque • Easy to break • Thermally conducting
	Paper sheet	• Cheap and flexible • Thermally insulating	• Easy to break • Low working temp. (<200 °C)
Stretchable	Polydimethylsiloxane (PDMS)	• Cheap and transparent • Flexible and stretchable • Thermally insulating	• Low working temp. (<200 °C)
	Polyurethane (PU)	• Cheap and transparent • Flexible and stretchable • Thermally insulating	• Low working temp. (<200 °C)
Rigid	Silicon	• Good printing compatible • High working temp. (<1700 °C)	• Rigid and opaque • Expensive • Thermally conducting
	Glass	• Cheap and transparent • High working temp. (<550 °C)	• Rigid and opaque • Thermally conducting

3.3.2 Printing Control

The toolpath generation to material printing is realised with the aid of a knowledge engineered workstation application (KEWA™) that consists of three graphical user interfaces: motion control manager, printing process manager, and vision system manager.[136] The control system uses the geometric information contained in the AutoCAD software to automatically drive the AJP process as it builds up a component layer by layer.[136,138] The atomisation conditions, platen temperature, and printing speed can be adjusted via the KEWA^{TM} to tune the printing quality. The basic procedures of printing a desired pattern are described as follows and in Figure 3.7:[136,138]

1. The printing pattern (.dxf file) and toolpath (.prg file) are designed and generated by the AutoCAD software and the VMTools software, respectively.
2. Either the UA or the PA is chosen, depending on the ink viscosity. The ink is loaded for the atomisation.
3. Straight lines are printed for testing and production run, where the printed line quality is monitored and evaluated by the vision system in real-time.
4. The atomisation conditions, platen temperature, printing speed, and other adjustable parameters are varied via the KEWA^{TM} software to optimise the printing quality, according to the above-discussed Table 3-2.
5. After optimising the printing quality, the AutoCAD-designed toolpath is loaded for printing the desired pattern by applying optimum printing parameters from the previous step.
6. Lastly, monolayered or multilayered structures are printed for further characterisation.

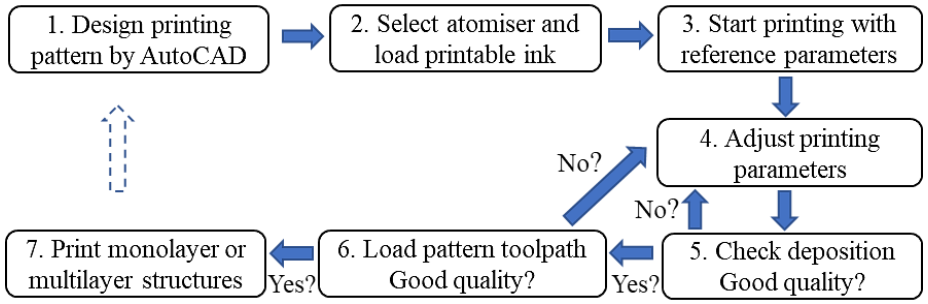

Figure 3.7 Flow chart demonstrating the basic steps to print design patterns by the AJP method.

3.3.3 Pattern Printing

The user-defined pattern can be designed and directly drawn by using the AutoCAD software, and be easily edited and modified as desired. The AutoCAD toolpath generation also provides large design flexibility, and is extremely useful for fabricating made-to-order devices that have unique features.[136] As displayed in Figure 3.8, a variety of design patterns, ranging from simple patterns, e.g. straight, square and curved lines, to highly sophisticated patterns, such as the Penrose pattern, can be printed by this state-of-the-art AJP technique. The minimum printable feature size that can be achieved here is ~10 μm. The printing resolution is an ink-dependent property, and this can be varied for different inks. Conductive Ag-nanoparticle-based ink is one of the most investigated commercial inks utilised in this AJP technique. [136,138] To further exploit the AJP technique, bespoke inks were prepared by using the in-house synthesised TE nanomaterials, which would be AJ-printed into TEG structures in the following chapters. The actual printed device structures were varied according to their specific applications, e.g. flexible TEGs, compositionally graded TEGs, or stretchable TEGs.

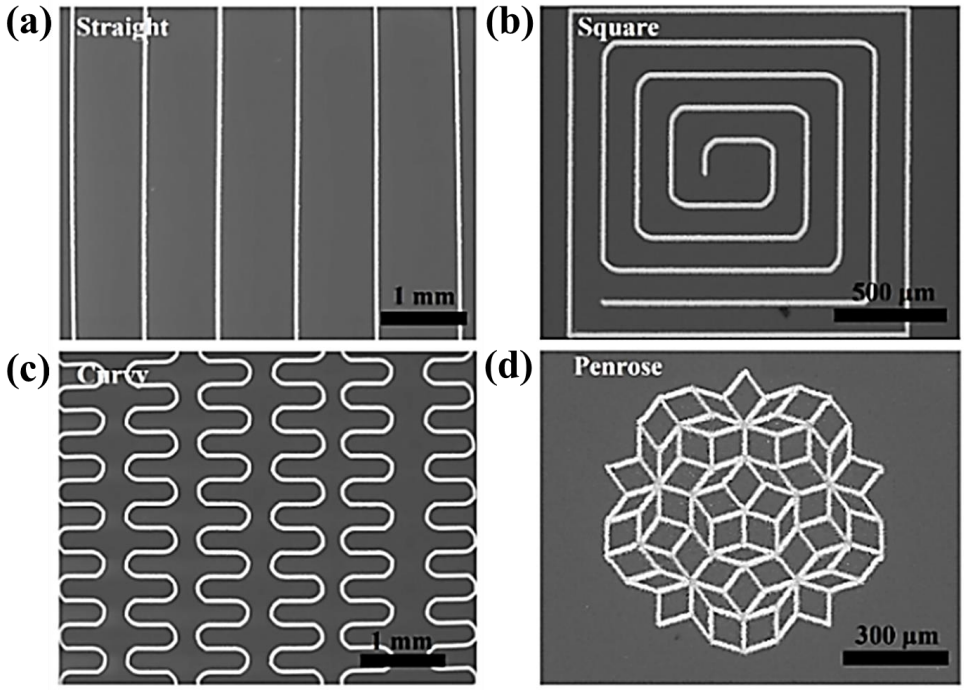

Figure 3.8 SEM images showing various design patterns, such as (a) straight, (b) square, (c) curvy, and (d) Penrose, which were printed on a silicon substrate by the AJP method. Ag ink was used here for demonstration.(Courtesy of Dr Michael Smith)

3.4 Ink Preparation

Successful atomisation mostly depends on the viscosity of the ink. This AJP 200 system has a wide viscosity capacity, ranging from 1 up to 1000 cP. A large variety of inks, pastes or other materials are compatible for the AJP process. The used inks here can be commercially available functional inks or in-house developed inks. The in-house developed ink may consist of a mixture of liquid chemical precursor, solid particles (e.g. metals, conductors, insulators, etc.), and solvents (e.g. water, polymer, organic solvent, etc.).[136] For the ink comprising nanoscale particles, the particle size should be smaller than the limit of atomised aerosol droplet size (i.e. 10 μm). Nanomaterials, such as nanoparticles or nanotubes with the size range of 10 nm to 10 μm, can be potentially printed by the AJP technique. Thus, a proper selection of the particle dimension and solvent is essential for ink preparation. Considerations for a 'good' ink are as follows: 1. low to moderate viscosity (highly viscosity inks are difficult to be atomised); 2. no shear-thickening behaviour (this prevents the atomisation process); 3. not too thin (overspray issue or coffee-ring effect); 4. not too low boiling point (solvent evaporates too quickly during the transporting process). The fluid dynamics, surface tension, wetting angle, solubility, and density of the as-obtained ink should also be considered for the subsequent printing quality optimisation. Since the atomisation and printing conditions have a great influence on the printed line profile and morphology, it is paramount to find out the optimum conditions for different ink formulations. More importantly, as reported in the literature, most fabrication methods for TE materials have a comparatively low yield. The material and manufacturing cost is also quite expensive. Hence, making full use of these TE materials, both inorganic powders and organic polymers, is of vital importance.

Since the ink can be aqueous or organic-based, different solvents were selected for the investigation of ink formulation in this work. The choice of atomiser for the ink atomisation depended on the ink viscosity. A total amount of 2 mL of as-prepared ink was placed into a glass vial designed for the UA, while 20 mL of ink was placed into a plastic jar designed for the PA. When not in use, the ink was stored in a fridge at 2-8 ^{o}C.

3.4.1 Ultrasonic Atomiser

(i) PEDOT:PSS Ink

Aqueous *p*-type conducting polymer poly(3,4-ethylenedioxythiophene) polystyrene sulfonate (PEDOT:PSS, 1 wt.%, Heraeus Clevious™ PH1000) used in this project was purchased from Ossila. Another PEDOT:PSS solution (1.3 wt.%, Sigma Aldrich) was also used in this work for comparison in Chapter 4. Additionally, 5 wt.% of ethylene glycol (EG, 99.8%, Sigma-Aldrich) or dimethyl sulfoxide (DMSO, 99.9%, Sigma-Aldrich) was added into the PEDOT:PPS ink to improve the TE properties of PEDOT:PSS.[93,95]

(ii) Ag Ink

A commercial silver-nanoparticle-based ink (Ag, Prelect TPS 50 G2, Clariant) was diluted by DI water at a volume ratio of 1:1 (ink: water) into a printable Ag ink. During printing, the Ag ink was maintained at a constant temperature (20 ^{o}C) by a water-bath cooling system.

3.4.2 Pneumatic Atomiser

(i) Bi_2Te_3/Sb_2Te_3 Ink

The Bi_2Te_3 and Sb_2Te_3 nanomaterials were fabricated by both top-down fabrication and bottom-up synthesis methods, as discussed in Section 3.1. These nanomaterials were then prepared into printable inks by dispersing them within DI water at different concentrations for the ease of mixing with other water-based inks to form nanocomposite structures, which will be discussed in detail in Chapter 4. It should be noted that no oxidation issue or colour change was seen from the surface of these nanomaterials, indicating their stability within DI water.

(ii) MWCNTs Ink

Multiwall carbon nanotubes (MWCNTs, >90% carbon basis, 5-9 μm in length, 110-170 nm in diameter) were purchased from Sigma Aldrich. Due to the agglomeration issue of these MWCNTs, different surfactants were added to facilitate the dispersion of MWCNTs within DI water, thereby achieving a printable ink. This will be further discussed in Chapter 5.

(iii) PVDF Ink

Since conducting polymers are comparatively expensive, cheaper insulating polymers were also used in this work for comparison. Polyvinylidene fluoride (PVDF) was prepared into a printable ink by dissolving 5 wt.% PVDF powder (M_w ~534000, Sigma-Aldrich) into N-methyl-2-pyrrolidone solvent (NMP, Sigma-Aldrich).

(iv) PI Ink

For the preparation of polyimide (PI) ink, poly(pyromellitic dianhydride-co-4,4'-oxydianiline) and amic acid solution (12.8 wt.% in 80% NMP/20% aromatic hydrocarbon, Sigma Aldrich) were mixed with N-Methyl-2-pyrrolidone (NMP, Sigma Aldrich) at a volume ratio of 1:1 and stirred overnight to fully blend all the precursors.

(v) PU Ink

5 wt.% of polyurethane (PU, beads, Elastollan Soft) was dissolved within N,N-dimethylformamide (DMF, Sigma Aldrich) solvent to obtain a printable PU solution.

3.4.3 Printing Conditions

The printing conditions of different inks were investigated and optimised by applying different combinations of gas-flow rates, where the sheath gas-flow rate (Q_{sh}) was varied from 50 to 250 cm³/min, and the aerosol flow rate Q_{atm} for the UA from 20 to 60 cm³/min while ΔQ for the PA from 10 to 200 cm³/min. Table 3-4 summarises some reference printing parameters concluded from several preliminary printing tests, which can give a rough idea of how to start selecting printing conditions when using different solvent-based inks. However, the actual printing conditions would typically be varied according to the functional inks used, e.g. concentration, miscibility, and formulation between the loaded particulates and solvent, as well as the actual working conditions of the printer. In addition, since the printing speed and the number of printed layers mutually decide the width and thickness of printed lines as well as the printing time needed, the trade-off between these parameters should also be considered and optimised during the printing process.

Table 3-4 Some optimum printing conditions for different bespoke inks used in this work.

Atomiser	Ink	Printing Condition	Line Quality
UA	PEDOT:PSS + Water	Q_{sh}: 150, Q_{atm}: 50 Process: 2 mm/s, Rapid: 40 mm/s Tip size: 300 µm Platen temperature: 80 °C	Thickness: ~3 µm Width: ~80 µm Printed 10 layers Cured at 130 °C for 2 hours
	Ag + Water	Q_{sh}: 90, Q_{atm}: 40 Process: 2 mm/s, Rapid: 40 mm/s Tip size: 150 µm Platen temperature: 80 °C	Thickness: ~2 µm Width: ~30 µm Printed 10 layers Cured at 200 °C for 2 hours
PA	Bi_2Te_3/Sb_2Te_3 nanomaterials + Water	Q_{sh}: 150, Q_{atm}: 600, Q_{exh}: 550 Process: 2 mm/s, Rapid: 40 mm/s Tip size: 300 µm Platen temperature: 80 °C	Thickness: ~5 µm Width: ~100 µm Printed 10 layers Cured at 130 °C for 2 hours
	MWCNTs + Water	Q_{sh}: 150, Q_{atm}: 600, Q_{exh}: 550 Process: 2 mm/s, Rapid: 40 mm/s Tip size: 300 µm Platen temperature: 80 °C	Thickness: ~3 µm Width: ~100 µm Printed 10 layers Cured at 130 °C for 2 hours
	PVDF + NMP	Q_{sh}: 100, Q_{atm}: 1000, Q_{exh}: 800 Process: 2 mm/s, Rapid: 40 mm/s Tip size: 300 µm Platen temperature: 80 °C	Thickness: ~5 µm Width: ~100 µm Printed 10 layers Cured at 100 °C for 12 hours
	PI + NMP	Q_{sh}: 100, Q_{atm}: 1200, Q_{exh}: 1000 Process: 2 mm/s, Rapid: 40 mm/s Tip size: 300 µm Platen temperature: 80 °C	Thickness: ~10 µm Width: ~100 µm Printed 10 layers Cured at 130 °C for 12 hours
	PU + DMF	Q_{sh}: 100, Q_{atm}: 1000, Q_{exh}: 800 Process: 2 mm/s, Rapid: 40 mm/s Tip size: 300 µm Platen temperature: 80 °C	Thickness: ~5 µm Width: ~100 µm Printed 10 layers Cured at 100 °C for 12 hours

Note: UA is the ultrasonic atomiser; PA is the pneumatic atomiser; PEDOT:PSS = poly(3,4-ethylenedioxythiophene)-poly(styrenesulfonate); PVDF = polyvinylidene fluoride; PI = polyimide; NMP = N-Methyl-2-pyrrolidone; PU = polyurethane; DMF = N,N-dimethylformamide; Q_{sh} = sheath gas flow rate, Q_{atm} = atomiser gas flow rate, and Q_{exh} = exhaust gas flow rate, with the flow unit of [cm^3/min] (i.e. standard cubic centimeter per minute); 'Process' describes the speed of the platen moving during deposition (shutter open); 'Rapid' describes the speed of the platen moving between depositions (shutter closed).[138] The tip height of 3 mm was used throughout the printing process.

3.5 Post-processing Treatments

3.5.1 Thermal Annealing

Thermal annealing process, or curing, was conducted immediately after the printing process via a pre-heated oven (HeraTherm - Thermo Scientific). The thermal behaviour and the stability to oxidation of fabricated TE particles were studied by differential scanning calorimetry (DSC), as discussed in Appendix A.3. The DSC analysis is necessary here, because it can determine the maximum temperature that the author can employ for the curing process, and it is also useful for the temperature-dependent measurements on S and σ that will be discussed in Chapter 6. Considering the oxidation and melting temperature of the utilised inorganic particles, as well as organic polymers that would be employed as polymeric matrices for the TE nanocomposite fabrication, the curing conditions were optimised here. Due to the low melting point of PEDOT:PSS (~145 ^{o}C) and PVDF (~177 ^{o}C), as well as the low oxidation temperature of Bi_2Te_3 and Sb_2Te_3 (~180 to ~250 ^{o}C), the AJ-printed samples were oven-cured at 130 °C for 2 hours to remove water and other undesirable organic solvents. The possibility of low-temperature curing was also explored.

3.5.2 Surface Treatment

The Seebeck coefficient and electrical conductivity of PEDOT:PSS-based nanocomposites could be dramatically improved by the surface treatment.[93] The PEDOT:PSS-based nanocomposites were dipped within a de-doping agent at a temperature of 80 ^{o}C for 2-hour submersion. Subsequently, the treated samples were rinsed thoroughly by dipping within DI water for several minutes to remove residual de-doping solvents and de-doped PSS molecules that remained on the surface, followed by gentle blow-drying with dry nitrogen gas.[93,232] In this work, different de-doping agents, namely, ethylene glycol (EG, 99.8%, Sigma Aldrich), dimethyl sulfoxide (DMSO, 99.9%, Sigma Aldrich), sulfuric acid (H_2SO_4, 20 vol.%, Sigma Aldrich), and glycerol (GYL, 99.5%, Sigma Aldrich), were first employed on the as-printed pristine PEDOT:PSS films to find out the best de-doping agent on the TE

performance enhancement. The selected de-doping agents would then be applied in the rest of AJ-printed PEDOT:PSS-based nanocomposite samples.

3.6 Measurement of Dimensions

Following the printing process, the length and width of AJ-printed structures were measured from top-down and cross-section SEM images by a table-top scanning electron microscope (Hitachi TM3000) or an optical microscope (Nikon OPTIPHOT), while the thickness and line profile were measured by a stylus profilometer (Veeco DEKTAK 6M). The length of serpentine structures printed in this work was estimated by their AutoCAD patterns.

In order to ensure good consistency and confirm the fabrication and measurement repeatability, two samples that were prepared in the same conditions were randomly chosen. For each sample, a minimum of three repeated measurements was carried out, with the average value being calculated to increase the accuracy. To calculate the cross-sectional area accurately, the AJ-printed film should be of uniform thickness and width. Following this, the electrical conductivity can be calculated by knowing the corresponding resistance value via the four-point probe resistance measurement, as discussed in the following Section 3.7. For the multilayer printed structure, it is difficult to distinguish the thickness of each layer of materials being printed, because each loop of printing may contain overlapped paths. As a result, single-layer films were AJ-printed separately to measure their thickness accurately.

3.7 Thermoelectric Measurements

This section gives a general description of how to measure the Seebeck coefficient and electrical conductivity of thin-film samples. Considering that different printed device structures were designed and developed for specific applications, the measurement set-up was modified accordingly, as described in the following sections. In this project, the thermal conductivity of these AJ-printed thin-film structures was not measured due to the lack of a proper measurement setup. Hence, in the absence of thermal conductivity data, the power factor (PF) provides an

alternative way to evaluate the potential TE performance of different samples. Some preliminary experiments on thermal conductivity measurements of AJ-printed thin-film structures were attempted with encouraging results, as discussed in Appendix A.1. However, further examination of the developed model is needed to verify its accuracy.

The Seebeck coefficient of a TE material can be estimated through the direct measurement of Seebeck voltage generation under different temperature gradients. Since it is fairly challenging to fabricate polymer-based materials into a dense block with thickness up to several hundreds of microns, their TE properties are often characterised in the form of thin-film structures.[89] Figure 3.9 depicts the general experimental setups for measuring Seebeck coefficient and electrical conductivity of a thin-film sample deposited on a substrate. For the in-plane heat flow direction illustrated in Figure 3.9 (a), the thin-film sample is clamped laterally, with the ΔT applied along the lateral direction of the thin-film sample and its edges contacting with thermometers and Seebeck voltage probes.[92] When one side of the sample is heated up and the other side is cooled down, the thermometers record the ΔT between both sides, and a voltmeter measures the voltage generated across the sample. It should be noted that the Seebeck voltage signal generated from the multimeter could be largely eliminated by stabilising the working temperature of the multimeter and setting it to a delta mode for more accurate Seebeck voltage measurement of the test sample. For the out-of-plane heat flow direction displayed in Figure 3.9 (b), the sample is mounted vertically with the ΔT created across the thickness of the film. However, due to the thickness constraint of the AJ-printed sample, the out-of-plane measurement setup discussed in Appendix A.4 is not applicable here.

The electrical conductivity can be determined by a four-point probe method using the same measurement setup discussed above. For an ideal four-point probe method, as illustrated in Figure 3.9 (c), there are four probes placed at equal intervals along the sample. An electrical current flow is passed through the outer electrodes, leading to a voltage drop across the inner probes that is measured by a voltmeter.[92] By adopting this method, the contact electrode resistance and the lead resistances can be eliminated, and the measured resistance is only

attributed to the sample under test, leading to more accurate results than those measured from the two-point probe method.[92] In this work, the resistance of the AJ-printed sample was measured in a four-probe two-terminal configuration, where the leads for applying a voltage and measuring a current are at the same positions (i.e. leads 1 and 2 at the same terminal, leads 3 and 4 at the same terminal). Electrical conductivity (σ) was then calculated from the equations, as presented in Figure 3.9 (c). Moreover, Hall-effect measurements were conducted to estimate the charge carrier density and confirm the charge carrier type of AJ-printed samples, which is discussed in Appendix A.5.

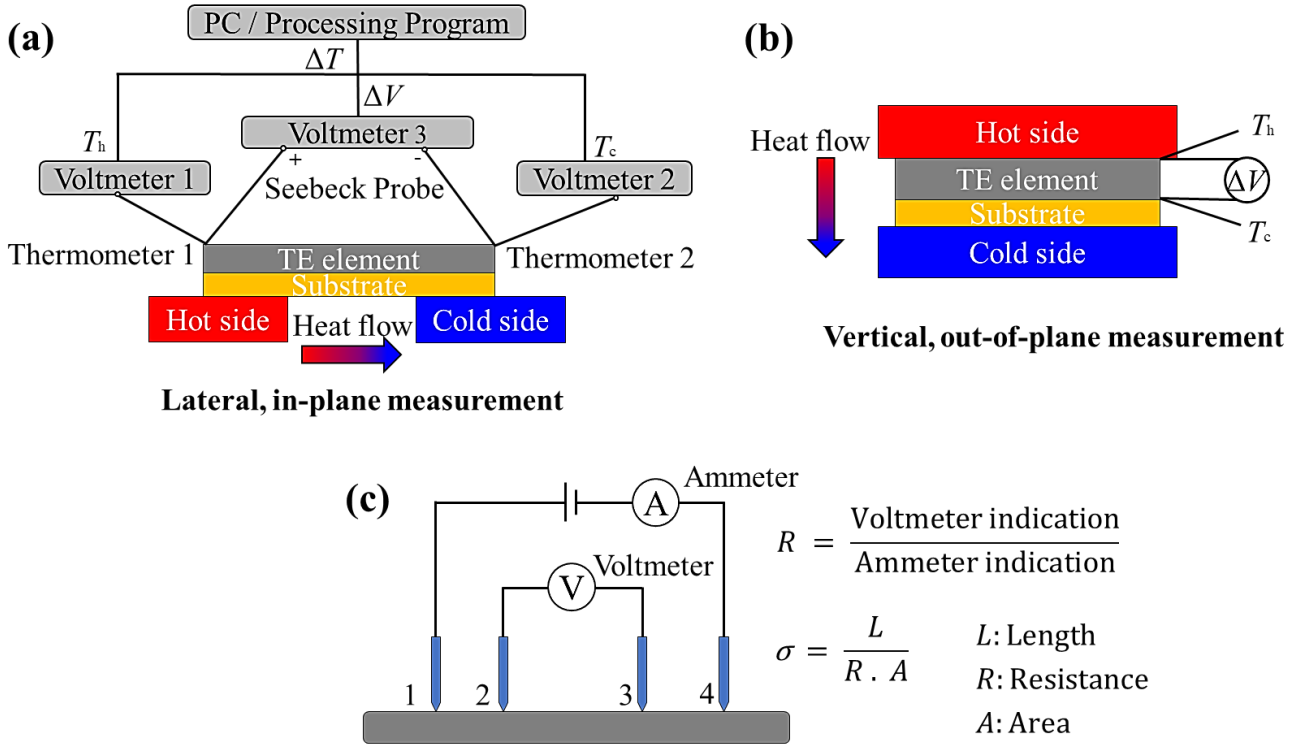

Figure 3.9 Schematic representation of setups for measuring (a) the in-plane (lateral) and (b) the out-of-plane (vertical) Seebeck coefficient and electrical conductivity of the thin-film structure, where (c) the four-point probe method is employed for the electrical conductivity measurement.

3.7.1 Meandering Structure

In this work, flexible PEDOT:PSS-based TE nanocomposites were fabricated in combination with bespoke TE inks and the AJP technique. For possible integration into wearable devices, a millimetre-scale meandering structure was designed here to achieve higher mechanical flexibility. Figure 3.10 presents the AutoCAD-designed pattern and experimentally AJ-printed TE nanocomposite on a flexible PI sheet. The printed lines were placed 0.4 mm apart, and the whole meandering structure was 20 mm in length and 5 mm in width.

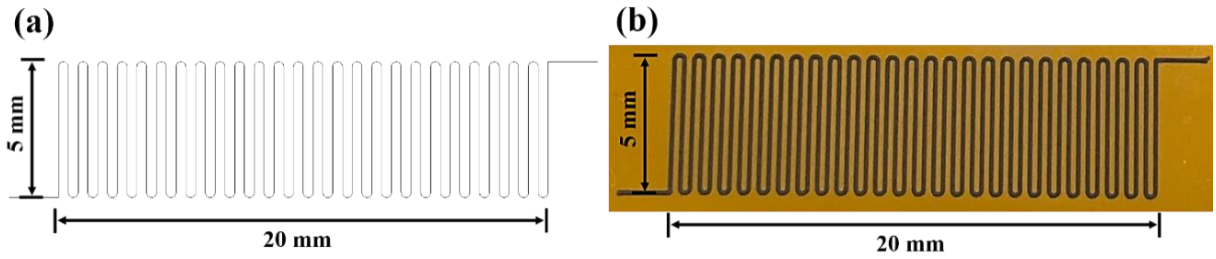

Figure 3.10 (a) Schematic of the AutoCAD-designed meandering structure. (b) Photograph of the experimentally AJ-printed 5-layer TE nanocomposite on a PI sheet by the AJP method.

Figure 3.11 schematically depicts the sample preparation process of AJ-printed nanocomposites for the TE property measurement. An enlarged schematic drawing in Figure 3.12 (a) presents the AJ-printed TE sample that was prepared for the subsequent TE measurement. Firstly, a 3-mm wide polyimide (i.e. PI or Kapton) tape was used to mask the middle portion of the printed pattern. It acted both as a mask when silver paint (RS Electrolube) was applied for making electrical contacts, and also as an encapsulant to protect AJ-printed patterns underneath from scratches and other physical damage during sample handling. Since the AJ-printed TE pattern was too small and too thin to be directly measured, silver paint was applied manually on both edges of the pattern as metallic pads so that a better electrical and thermal contact between the sample and inner Seebeck probes (copper wires, 0.2 mm in diameter) can be achieved, thereby reducing the measurement error on the Seebeck voltage as well as the sample resistance.[233] Although the additional Ag electrodes might slightly

change the effective length of the TE leg being tested, there should be no difference in the measured Seebeck coefficient or electrical conductivity values.[92] Subsequently, conducting copper wires were used as electric lead wires to make contacts with the sample in a four-probe two-terminal configuration, as illustrated in Figure 3.11 (e). The insulation was removed from both ends of the enamelled copper wires, and they were attached by silver paint. After silver paint was dried, the PI tape was used again to mask the silver-painted region, insulate the contacts, and protect the contacts from physical damage. Copper sticky tapes were then used to make good thermal contact on either side of the sample, as shown in Figure 3.11 (g). A thermal gradient could later be applied to the sample by attaching them to hot and cold ends with the aid of copper tapes. Eventually, PI tapes were again used on top of copper tapes for insulation (see Figure 3.11 (h)). A pair of commercially available platinum resistance temperature detectors (Pt-100 RTDs, Farnell) served as thermometers were taped down by PI tapes on the surface of the sample to detect the local real-time temperature on the hot and cold ends. A silicone thermal grease (Servisol heat sink compound, Farnell) was employed for the improved thermal contact.

A cross-sectional view of the sample (along a dotted line illustrated in Figure 3.11 (i)) showing the different layers of tapes and coatings is depicted schematically in Figure 3.11 (j). The PI tapes applied on top of copper tapes ensured that the temperature was measured symmetrically on either side of the copper tape (see Figure 3.11 (i)). On either side of the copper tape, there was a layer of PI tape. The lower PI tape was in direct contact with the sample, and the top PI tape was in direct contact with two Pt-100 RTDs, thus making a symmetric connection to allow precise temperature measurement. The heat loss was considered negligible here owing to the application of thermal grease.

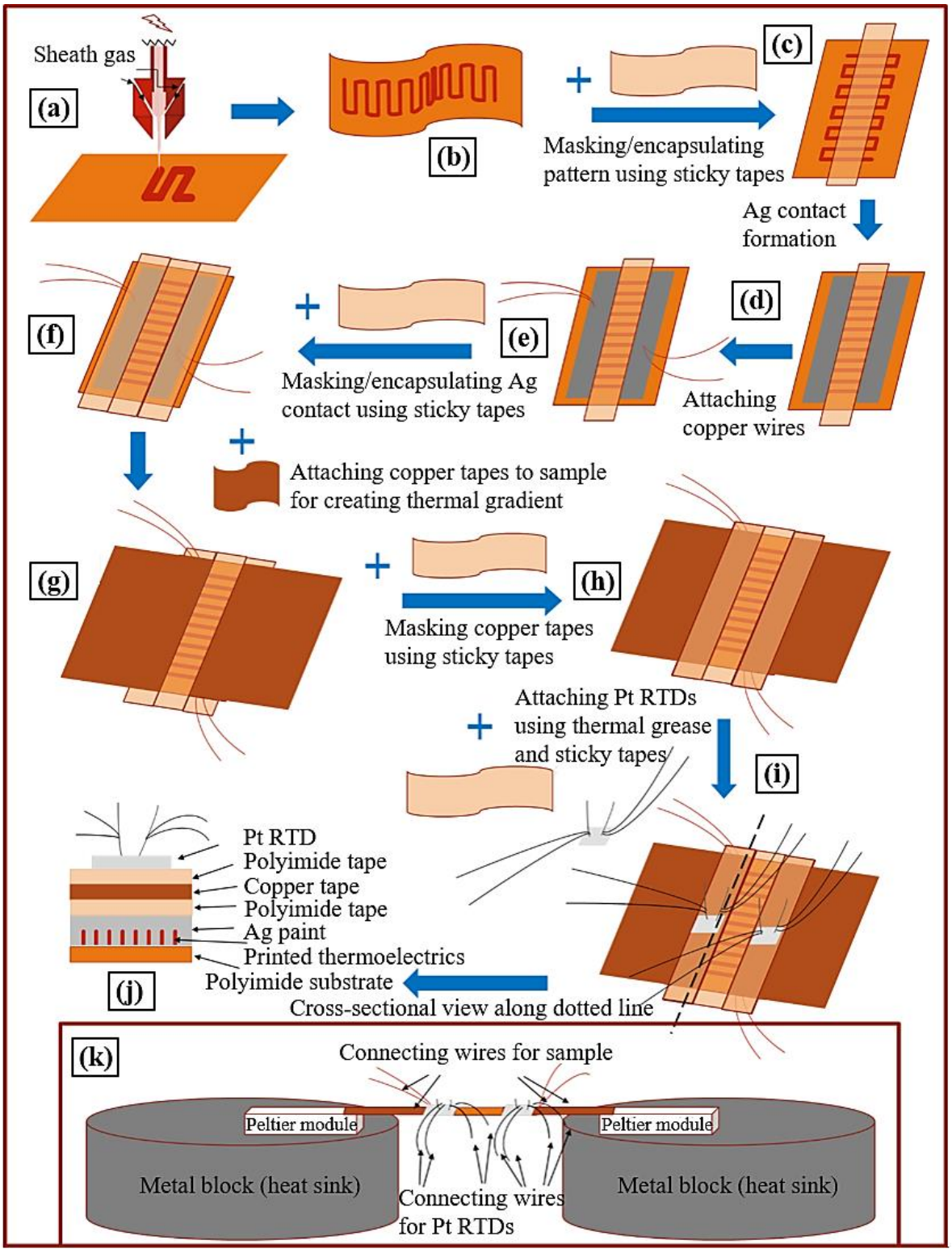

Figure 3.11 Schematic of (a) the AJP process, (b) the AJ-printed sample, (c) masking and encapsulating the pattern with PI tapes, (d) applying Ag paint to make electrical connections, (e) attaching copper wires in a four-probe two-terminal configuration, (f) encapsulating Ag contacts, (g) attaching copper tapes to create a temperature gradient, (h) masking copper tapes, and (i) attaching Pt RTDs. (j) Cross-sectional view showing the arrangement of different layers and/or coatings. (k) Schematic of the bespoke measurement setup.

A custom-built measurement setup was developed for the simultaneous measurement of the in-plane Seebeck coefficient and electrical conductivity of the AJ-printed sample by using a dynamic method. As shown in Figures 3.12 (b) and (c), a bespoke test bench was built by using two temperature-controlled Peltier modules (RS Components), one operating as a heat source while the other as a heat sink to create a small ΔT in between (-60 to +60 ^{o}C). Those two Peltier modules were connected in series, with opposite polarities, to a direct-current (DC) power source (Thurlby) so that when a DC voltage was applied, the top surface of one of the Peltier modules would get heated and that of the other would be cooled down relative to room temperature. The Peltier modules were glued, by using silver paint, onto two dense steel blocks that acted as heat sinks to keep the lower surface temperatures of the Peltier modules constant and close to the room temperature, thus maintaining a constant ΔT between the top surfaces of each Peltier module. By doing this, a higher ΔT could be reached. The ΔT could then be controlled by varying the applied DC voltage. Additionally, the whole test bench was placed in a nitrogen-filled chamber and tested at room temperature so that the ambient electrical and thermal noise could be minimised and the condensation of ambient water vapour on the cold surface of the Peltier module could be prevented during the measurement.[24] Finally, the sample was mounted in the middle by using copper tapes so that a stable ΔT could be created across the sample. At the same time, three separate Keithley digital multimeters were connected to continuously record the sample resistance, the Seebeck voltage generated across the sample, and the resistance of two Pt-100 RTDs. All the data were acquired simultaneously by the custom-made LabView data acquisition program. The custom-designed hardware and software data acquisition system was developed here for the semi-automatic data acquisition and analysis. As the resistance of the Pt-100 RTD was directly proportional to the temperature, the resistance data of both Pt-100 RTDs were recorded simultaneously by two Keithley 196 digital multimeters for the temperature measurement. A Keithley 2002 digital multimeter was used for the generated Seebeck voltage (ΔV) and sample resistance (R) measurement. These multimeters were all connected to the computer via GPIB interface, and the collected raw data was then processed via a LabVIEW program. By varying the temperature across the TE sample, the

temperature gradient (ΔT) was measured by the Pt-100 RTDs, while the voltage difference (ΔV) generated by the sample was measured by a voltmeter. The Seebeck coefficient (S) is defined by the equation $S = -\Delta V/\Delta T$, where the S value can be calculated by analysing the linear regression slope of the ΔV-ΔT curve. Here, the linear fitting for the ΔV-ΔT curve was computed and averaged to find the best possible fit with the aid of Origin software (Version 8.1) in Figure 3.12 (d). The electrical conductivity (σ) is expressed as $\sigma = L/(R.A)$, where L is the length between two ends of the sample, R is the resistance, and A is the cross-section area.

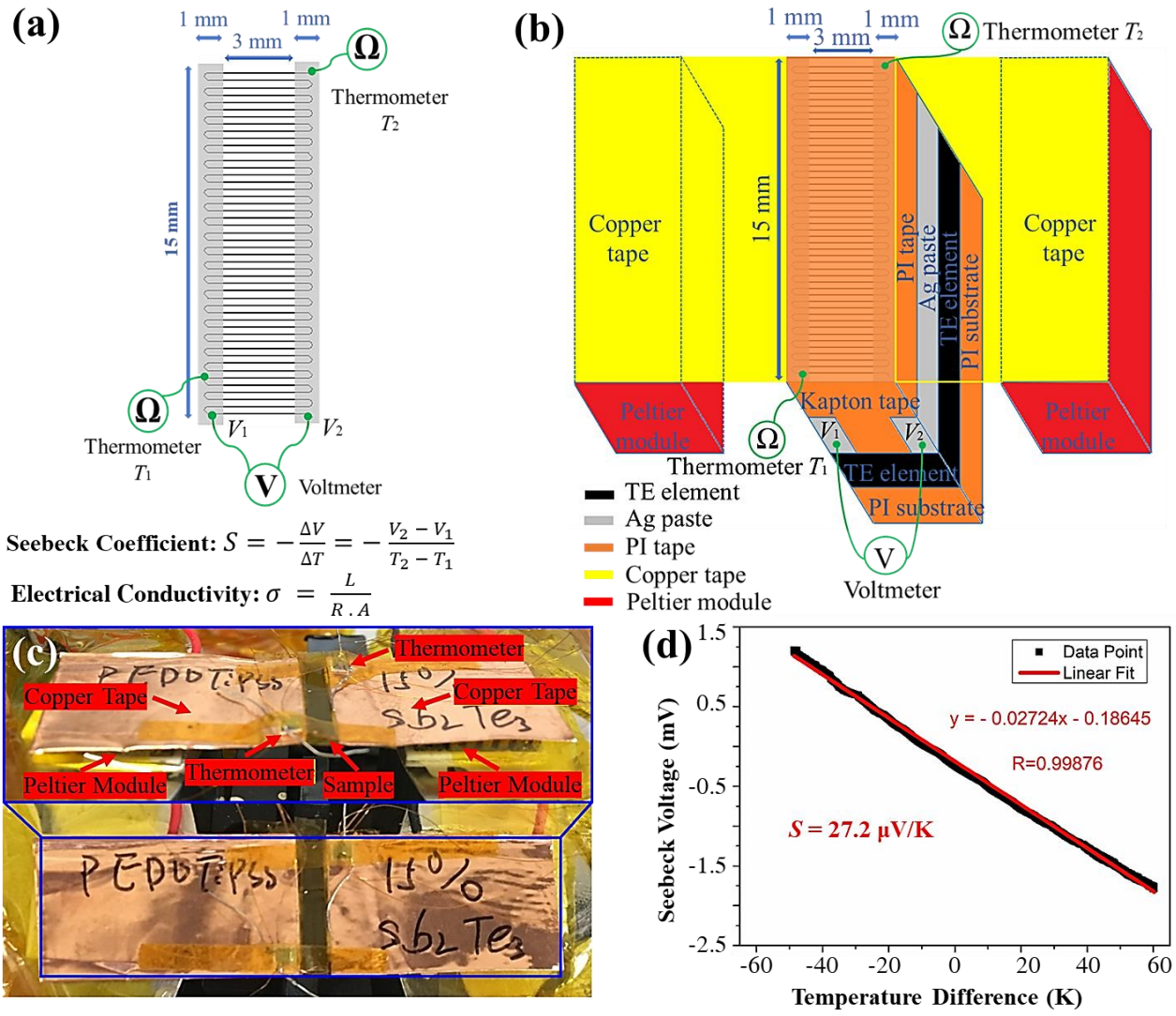

Figure 3.12 (a) Enlarged view of the AJ-printed TE pattern with a meandering structure, and (b) schematic drawing of the sample preparation for the in-plane Seebeck coefficient and electrical conductivity measurement. (c) Annotated photograph of the in-house designed measurement setup, where the enlarged image shows more details of the setup and the AJ-printed TE sample. (d) The linear fitting curve for the Seebeck coefficient calculation.

3.7.2 Strip Structure

For larger scale TE applications, such as hot water pipes, a strip-shaped pattern with dimensions of 20 mm in length and 2 mm in width was designed and fabricated by the AJP technique, as depicted in Figure 3.13. Since both S and σ are temperature-dependent TE properties, the PF is also temperature-dependent, i.e. PF (T). In order to obtain the highest power output and overall energy conversion efficiency of the TEG, appropriate material composition should be selected locally to achieve a desired PF response across the entire temperature range of the used TE material. To achieve this, different PEDOT:PSS-based TE nanocomposites loaded with different ratios of inorganic components (including Bi_2Te_3 nanoparticles, MWCNTs, and Sb_2Te_3 nanoflakes), were fabricated and measured to ascertain how these loaded nano-inclusions contribute to the final TE properties of the resulting nanocomposite structures as a function of the temperature.

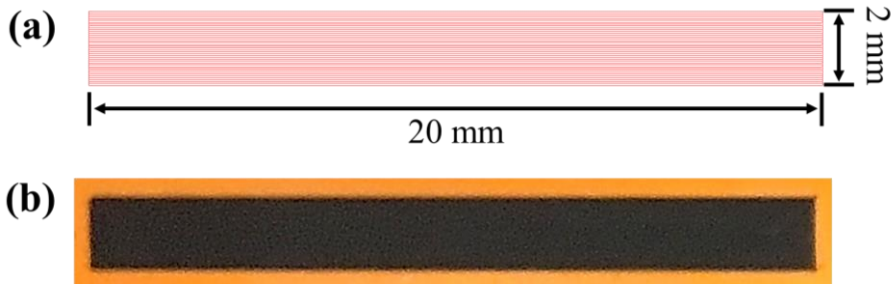

Figure 3.13 (a) Schematic of the AutoCAD-designed strip-shaped structure for temperature-dependent TE property measurements, and (b) photograph of the experimentally fabricated 5-layer TE nanocomposite on a PI sheet by the AJP method.

Similar to the TE measurement setup discussed in Figure 3.12, a modified setup for the temperature-dependent TE property measurement was built, as illustrated in Figure 3.14. The AJ-printed TE sample, as shown in Figure 3.13 (b), was fixed on top of two Peltier modules and laterally along the temperature gradient direction, with the edges thermally contacted with two Pt-100 RTDs for the real-time temperature recording as well as electrically connected with conducting copper wires for the Seebeck voltage and sample resistance measurement. Also, the entire test bench was situated in a sealed plastic box to ensure the minimisation of ambient

thermal noise as well as the prevention of heat dissipation, while the measurement was underway. Lastly, the same data acquisition system in combination with two Keithley 196 digital multimeters and a Keithley 2002 digital multimeter, as described in the above Section 3.7.1, was used to collect and analyse the semi-automated data for sample temperature, Seebeck voltage, and sample resistance measurements. The temperature of the sample was varied by the applied temperature of the hot plate and/or the water-cooling system underneath the measurement setup.

The S and σ values of different PEDOT:PSS-based nanocomposite samples were measured by using the same test setup and approach, as described in above Section 3.7.1, as a function of the sample temperature, ranging from 293K to 363K. The error bars were calculated from the measured values of two repeated measurements for the same material composition sample. In this work, the thermal conductivity was not measured due to the lack of a proper measurement setup in the author's lab for these thin-film structures. Hence, in the absence of thermal conductivity data, the power factor (PF) provides an alternative way to evaluate the potential energy-conversion performance of these AJ-printed structures.

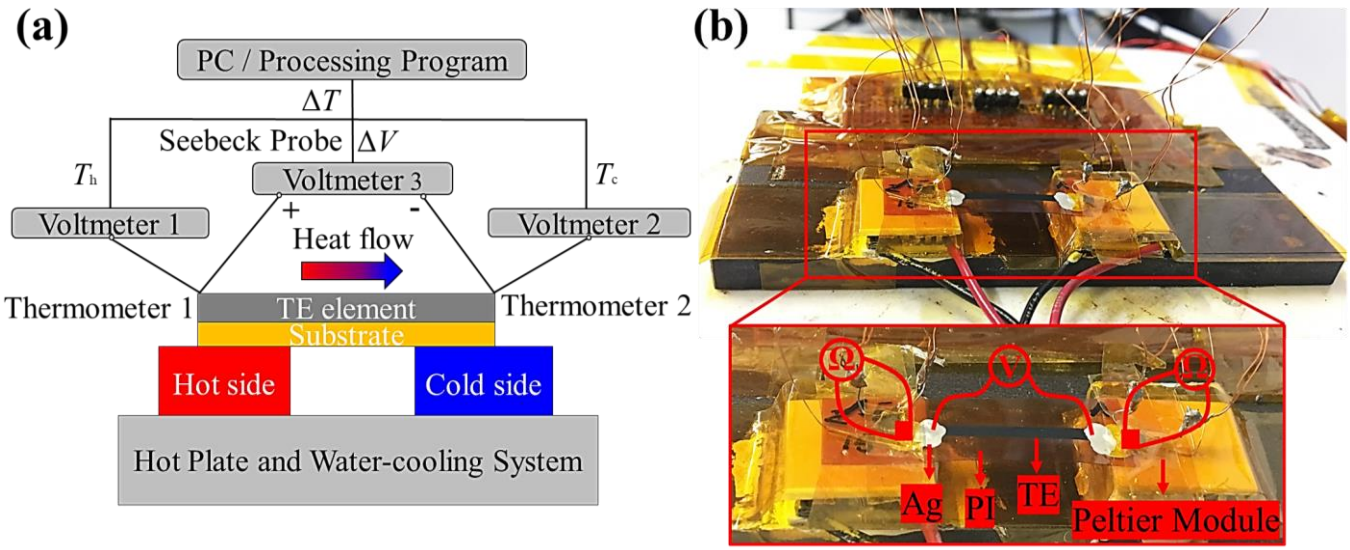

Figure 3.14 (a) Schematic drawing of the temperature-dependent Seebeck coefficient and electrical conductivity measurement technique. (b) Annotated photograph of the in-house designed measurement setup, where the enlarged image presents more details of the setup and the AJ-printed TE sample.

3.7.3 Serpentine Structure

In this study, serpentine geometry or winding shape was incorporated to achieve stretchability in the TEG. The intrinsic stretchable nature of the serpentine structure allows the TEG to conform to complex non-flat surfaces, thereby ensuring excellent thermal contact with the heat source. An out-of-plane design is also proposed as an architectural solution to overcoming the design challenge of the inefficient use of the in-plane temperature gradient, whereby the TE material can be aligned towards the out-of-plane heat flow direction. Two different serpentine patterns were hence designed, as illustrated in Figure 3.15, for harvesting thermal energy with different heat flow directions: (a) in-plane and (b) out-of-plane. For the AutoCAD design, each printing pattern consisted of multiple connected parallel winding-shaped lines with a small shift of around 20 μm in between each line, to build a wide enough yet structurally stretchable structure. The unit TE leg length of the in-plane structure was ~58 mm with a constant curvature, while the out-of-plane structure was ~7.6 mm, in which individual TE legs were alternately connected in series by Ag electrodes. The width of the structure could be controlled by the number of parallel lines designed in the pattern, while the thickness could be determined by the number of printed layers (i.e. multiple printing cycles piled on top of one another).[159]

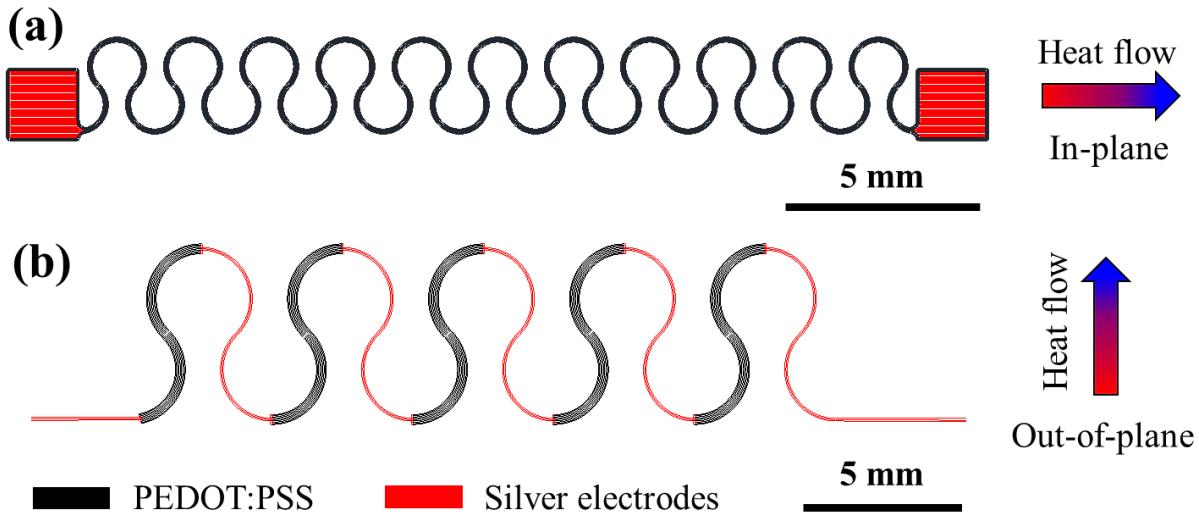

Figure 3.15 Schematic of AutoCAD-designed serpentine structures for stretchable TEG applications with (a) in-plane and (b) out-of-plane heat flow direction, respectively.

The TE performance of these stretchable TEGs under different imposed mechanical conditions was evaluated by the bespoke stretchability measurement setup, as illustrated in Figure 3.16. A linear motor (LinMot) was used here to control the mechanical deformation of the stretchable TE structure. It consists of two parts: the slider and the stator. With the aid of an internal position capture sensor and a microprocessor circuit, the real-time position can be measured and monitored when it is stopped or during motion. Also, it can provide either manual or programmed linear displacements at a minimum step distance down to 0.1 mm with precise control of both the travel speed and the acceleration.

Figure 3.16 (b) demonstrates the measurement setup for the in-plane structure. The in-plane stretchable TE structure was both electrically and physically connected via two copper sticky tapes at each end, which was mounted on top of two temperature-controlled Peltier modules attached to the linear motor and the fixed stage, respectively. The copper conducting tapes utilised here also served to make good thermal contact between the sample and the Peltier modules. Silver paint was then applied on both ends of the sample to form electrical contacts with external multimeters, as well as to make thermal contact with the Peltier modules. Finally, thin copper wires were used to form electrical contacts with the sample for the electrical characteristic measurement. A thermal gradient was created along the TE element through the copper tapes and the Peltier modules. Two Pt-100 RTDs were attached on top of the copper tapes to measure the applied temperature on the hot and cold ends. The Peltier modules were connected to two DC power sources, respectively, so that the top surfaces of both the Peltier modules could get either heated or cooled to create a steady in-plane ΔT across the TE structure. The data acquisition and analysis were performed using the same system detailed in Section 3.7.1, and the electrical characteristics were evaluated under different strain deformations.

For the out-of-plane measurement setup presented in Figure 3.16 (c), it was modified from the above in-plane measurement setup, where the stage for holding the sample was rotated. The out-of-plane stretchable TE structure was clamped by glueing it onto two conducting copper tapes with silver paint. A Peltier module was placed underneath so that all TE legs could be

thermally contacted in parallel with the heated surface of the Peltier module to form an out-of-plane heat flow. Subsequently, the real-time temperature values across the sample were monitored by thermal imaging using a compact thermal imaging camera (FLIR C3). The infrared thermal imaging camera has a temperature sensitivity of 0.1 °C and a thermal resolution of 4800 pixels. The thermal imaging camera was calibrated by a commercial Pt-100 thermometer before being used for the subsequent temperature measurement. However, the thermal imaging camera was not capable of continuous data acquisition, hence, the *S* value was not measured here. Instead, the voltage and power outputs generated from the TE structure under different applied temperature gradients as well as mechanical strains were measured for comparison. Lastly, the substrate-based stretchable TEGs encapsulated with the PU or PDMS elastomers were also characterised, as illustrated in Figure 3.16 (d).

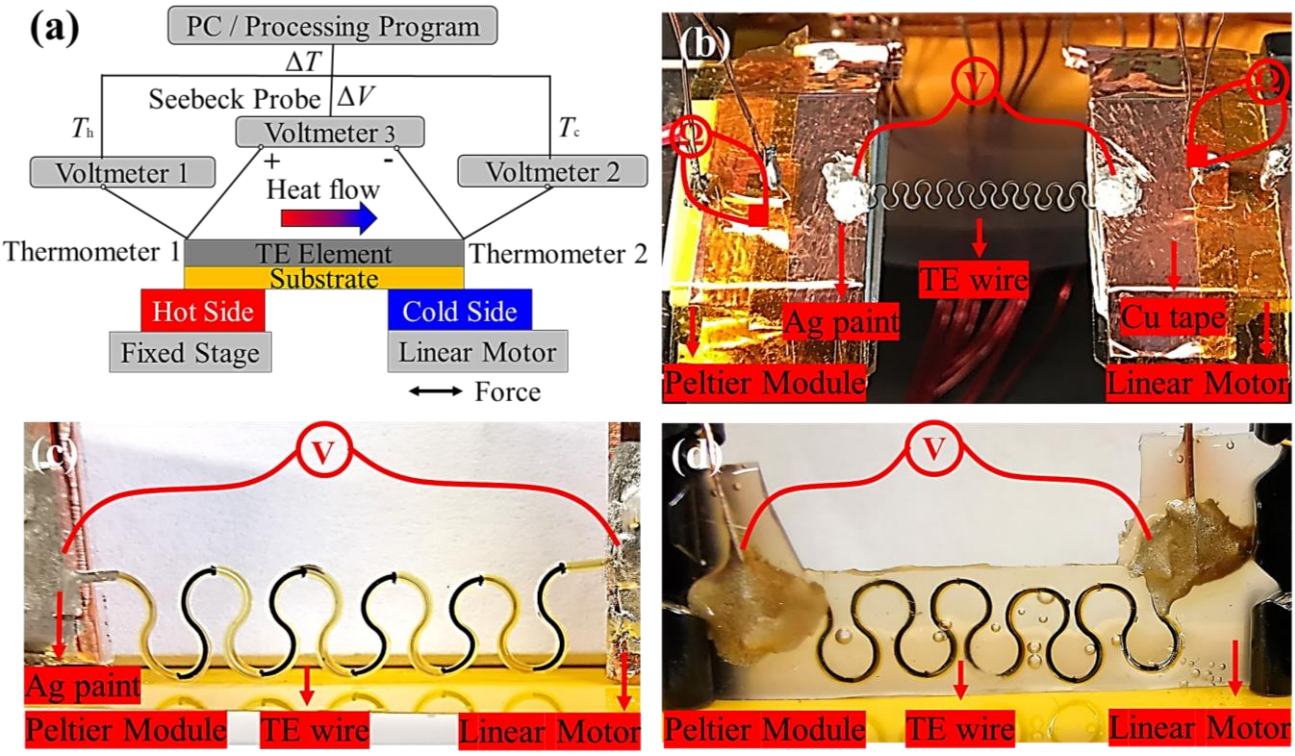

Figure 3.16 (a) Schematic illustration of the TE measurement technique for the in-plane stretchable structure. (b) Annotated photograph depicting more details of the in-house developed stretchability measurement setup for the in-plane structure. (c) Annotated photograph showing the stretchability measurement setup for the out-of-plane structure. (d) The stretchability measurement setup for the substrate-based stretchable TEG, which was encapsulated within PU or PDMS elastomers.

3.8 Mechanical Tests

Thus far, there has been a considerable number of reports on the enhancement of PF or *ZT* values in existing classes of thermoelectrics,[17,75,84,93,234] but the mechanical flexibility and robustness of these TE materials, when incorporated into practical applications, remain relatively under-reported in the literature. To address this issue, the author devised different rigorous mechanical tests, such as flexibility test, fatigue test, and stretchability test on different AJ-printed flexible and/or stretchable TE structures. Their mechanical stability and flexibility were further quantified under different bending radii, as well as their robustness and durability under prolonged flexing or stretching cycles, as described in the following sections.

3.8.1 Flexibility Test

A simple manual bending test on AJ-printed TE nanocomposites was implemented to assess their TE properties under various bending radii, as presented in Figures 3.17 (a) - (c). Further rigorous flexing tests were subsequently conducted on them to estimate their operation range. The samples were bent by being mounted on different surfaces having different curvatures, such as beaker, test tube, and pen, as shown in Figures 3.17 (d) - (g), and their room-temperature electrical resistance values were measured simultaneously.

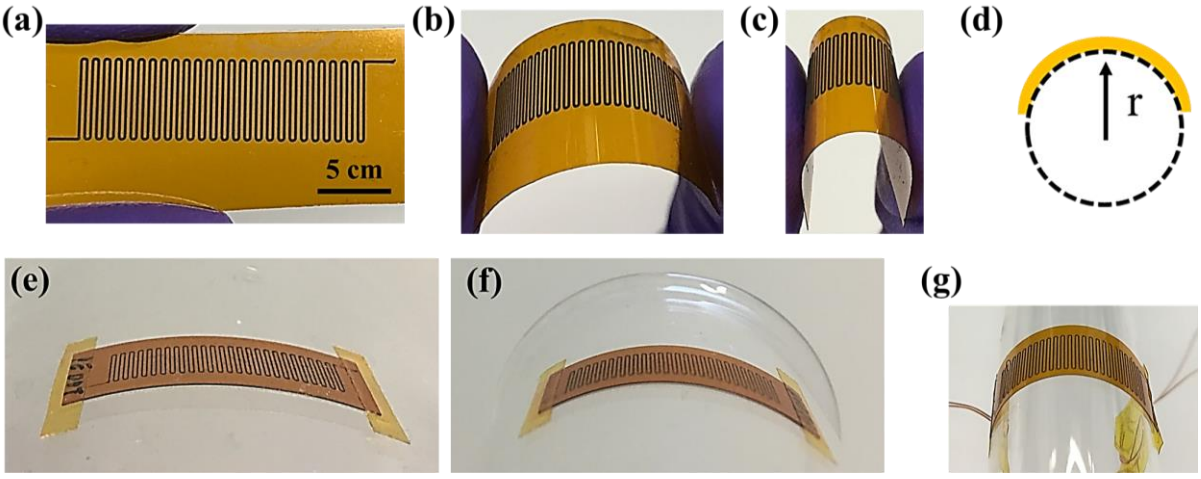

Figure 3.17 Photographic images of the AJ-printed TE nanocomposite being flexed and/or bent at different deformations: (a) unbent, (b) half bent, and (c) fully bent. (d) Schematic illustration of a rigorous way of flexing the sample, where the sample was subjected to a beaker or a test tube with different bending radii: (e) 35 mm, (f) 18 mm, and (g) 5.3 mm.

3.8.2 Fatigue Test

A manual bending test (see Figures 3.18 (a) - (c)) was initially conducted to estimate the mechanical flexibility and stability of AJ-printed nanocomposite structures. Subsequently, a more extensive, continuous, and long-cycle bending fatigue test was conducted by using a linear motor to fully understand the TE performance and fatigue limit of AJ-printed nanocomposites. The nanocomposite samples were subjected to up to 36,000 flexing cycles, i.e. 60 hours of continuous testing at a frequency of 0.15 Hz, as presented in Figures 3.18 (d) - (f). The used linear motor here could give better control of the compressive/tensile stresses and the number of flexing cycles. The electrical resistance change with time was measured during different mechanical tests. The fatigue test setup here is akin to the schematic in Figure 3.16 (a) with slight modifications on the sample mounting and the data acquisition program.

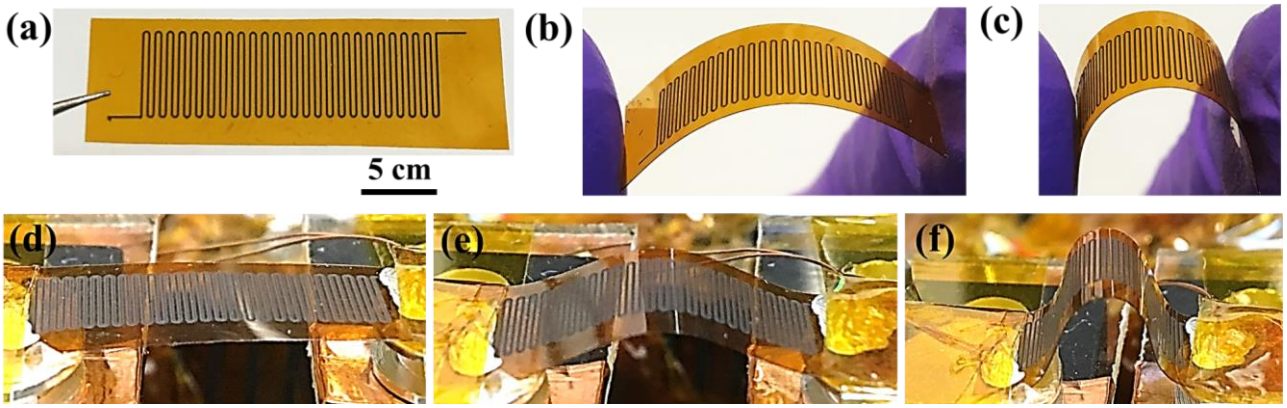

Figure 3.18 Flexing test on the AJ-printed TE nanocomposite under simple hand-bending at different degrees: (a) flat, (b) lower, and (c) higher degree. Fatigue test on the AJ-printed TE nanocomposite under the application of periodic compressive stress, where a linear motor is used to control the process. Different stages of the sample deformation are shown: (d) unbent, (e) half bent, and (f) fully bent.

3.8.3 Stretchability Test

The stretchability of the free-standing stretchable TE structure was assessed by measuring the resistance change as well as the voltage and power outputs in a four-probe two-terminal configuration, while uniaxially stretching the sample at different strain (%) by using a linear motor, as demonstrated in Section 3.7.3. As an example, the extensions of the stretchable TE structure at different strains produced by the linear motor are presented in Figure 3.19. Subsequently, a rigorous cyclic stretching test, i.e. fatigue test, was carried out on the stretchable TE structures to evaluate their mechanical robustness. The stretchable TE structures were periodically stretched till 50% of their original length along the uniaxial direction, and then released. They were subjected to up to 20,000 stretching cycles, i.e. 40 hours of continuous testing at a frequency of 0.15 Hz (i.e. at a rate of 9 cycles/min).

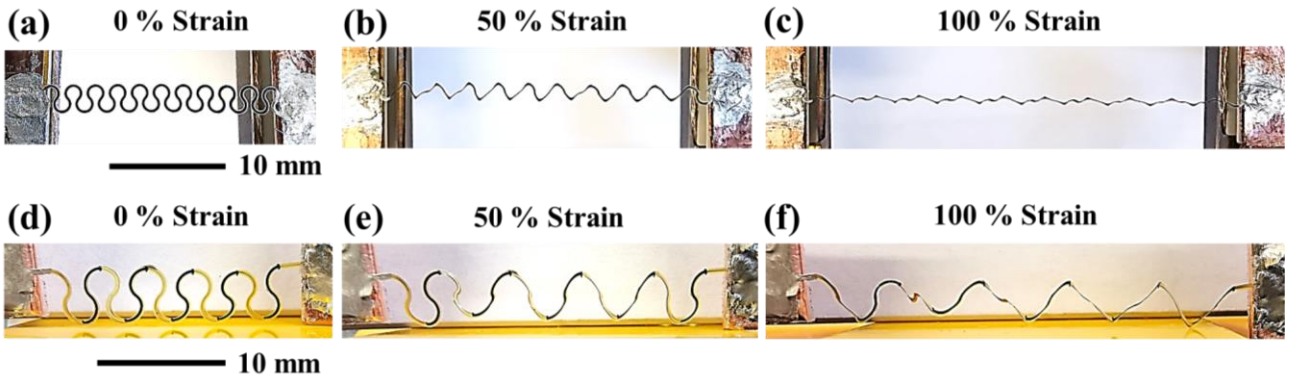

Figure 3.19 Stretchability test on AJ-printed free-standing stretchable TE structures with the in-plane structure under tensile stress at different strains: (a) 0%, (b) 50%, and (c) 100%; and with the out-of-plane structure at different strains: (d) 0%, (e) 50%, and (f) 100%.

3.9 Finite Element Analysis

Finite element analysis (FEA) is a useful means to rationalise and elucidate experimental data and phenomenon. In particular, it is an essential tool when developing new products or optimising design. Thus, COMSOL simulation and ABAQUS simulation have been conducted in this work, as discussed in greater detail in the following sections.

3.9.1 COMSOL Simulation

COMSOL simulation has been conducted by using a commercial software COMSOL Multiphysics (Version 5.2a) to simulate the TE performance and the temperature distribution profile of AJ-printed TE nanocomposite. To define the temperature variation throughout the AJ-printed TE nanocomposite, the *Heat Transfer in Solids* physics interface was used. The *Electric Currents* physics interface was also applied to calculate the electric field, current, and potential distribution. Finally, in order to couple the thermal and electrical behaviour of the model, the *Thermoelectric Effect* Multiphysics module was utilised for modelling the Seebeck voltage generation. The modelling geometry was built according to the experimental conditions (see Section 3.7). Some assumptions have been made here to simplify the simulation model: (1) the system is at the steady state; (2) the TE legs do not exchange radiation or reflections with themselves or with the heat source; (3) the material characteristics are independent to temperature and homogeneous in each position; (4) the temperature, heat flow, and electrical current flow are uniform across the cross-section of the TE leg; (5) the TE leg is discretised in the *z*-direction into a thin slice to calculate the thermal and electrical distribution; (6) there is no additional material at the interfaces.[179]

Moreover, the COMSOL simulation on the temperature distribution of different AJ-printed TE nanocomposites was performed for the device structure design of compositionally graded thermoelectric composites. The boundary position between different segments within a TE leg was determined. This will be further discussed in Chapter 6.

3.9.2 ABAQUS Simulation

To ascertain the root causes of the high stretchability and mechanical robustness exhibited in the stretchable serpentine structures, ABAQUS simulation has been performed to simulate and predict the mechanical deformation and local strain distribution within these serpentine structures, when being uniaxially stretched to 50% along the *x*-axis. In this model, one end of the stretchable TE structure was fixed in all directions, and the other end was moved along the in-plane direction to 50% extension of its original length. For the ease of ABAQUS simulation, only the middle part with 3 repeated serpentine units was selected here as a representative of the whole serpentine structure to investigate its strain distribution when being stretched. Two different serpentine structures, i.e. in-plane and out-of-plane, as discussed in Section 3.7.3, were compared here. The width and length values of different components were determined from the AutoCAD design patterns, while their thickness values were obtained from the experimental measurement results in Section 7.1. The refined meshes ensured the computational accuracy by using a commercial software ABAQUS (CAE 2016). The hexagonal mesh size was calculated to be 0.04 mm for the in-plane structure and 0.08 mm for the out-of-plane structure, respectively. The material properties utilised in the ABAQUS simulation are summarised in Table 3-5.

Table 3-5 Summary of different material properties adopted in the ABAQUS simulation.

Material	Density (x 10^{-9} ton/mm^3)	Young's modulus (x 10^3 MPa)	Poisson's ratio	Width (mm)	Thickness (mm)
PI, // [204]	1.42	2.5	0.27	0.11	0.03
PEDOT:PSS, // [235]	1.01	2	0.34	0.11	0.005
PI, ⊥ [204]	1.42	2.5	0.27	0.32	0.015
PEDOT:PSS, ⊥ [235]	1.01	2	0.34	0.17	0.004
Ag, ⊥ [204]	1.05	69	0.37	0.09	0.005

Note: // is the in-plane structure; ⊥ is the out-of-plane structure. The unit 'ton' represents tonne.

3.10 Thermoelectric Generator Fabrication

3.10.1 Flexible Thermoelectric Coasters

Conventional TEGs comprise several vertically aligned 3D bulk legs that are electrically connected in series by metallic contacts and thermally connected in parallel between two ceramic substrates, where the vertical heat flow is along the TE legs, as detailed in Section 2.5.[60] However, since most organic and/or solution-processed inorganic materials do not benefit from such geometrical configuration, in this work, a 2D device architecture with a lateral heat flow is purposed to exploit the possibility of printing flexible TEGs.[134]

Two different prototypes of flexible thermoelectric coasters, as illustrated in Figure 3.20, were fabricated by the AJP method, with inks comprising PEDOT:PSS polymer and Sb_2Te_3 particles. The advanced printing technique allowed the ease of fabricating lightweight and flexible TEGs and offered the possibility of large-scale production with little material wastage. To construct a working TEG module, individual TE legs should be electrically connected in series to add up their voltage outputs, and thermally connected in parallel to make full use of the ΔT across them. Ag-nanoparticle-based ink was AJ-printed here to form electrical interconnections, by virtue of its high electrical conductivity, low sintering temperature, as well as excellent physical and chemical stability over a broad operating temperature range.[1]

For the parallel-connected mode shown in Figures 3.20 (a) and (b), 340 *p*-type Sb_2Te_3-PEDOT:PSS nanocomposite arrays were AJ-printed on a 15cm x 15cm flexible PI sheet as TE legs, and two conducting Ag circular lines were AJ-printed on both ends of individual TE legs as electrical interconnects to electrically connect them in parallel. For the series-connected mode presented in Figures 3.20 (c) and (d), conducting Ag lines were AJ-printed as electrodes in between individual TE legs to join them electrically in series. It should be noted that these Ag electrodes were AJ-printed prior to the printing of TE nanocomposites, due to the higher curing temperature of Ag ink (cured at 200 °C). After curing the Ag electrodes, the TE legs were aligned and AJ-printed on top of then via the AJP technique.

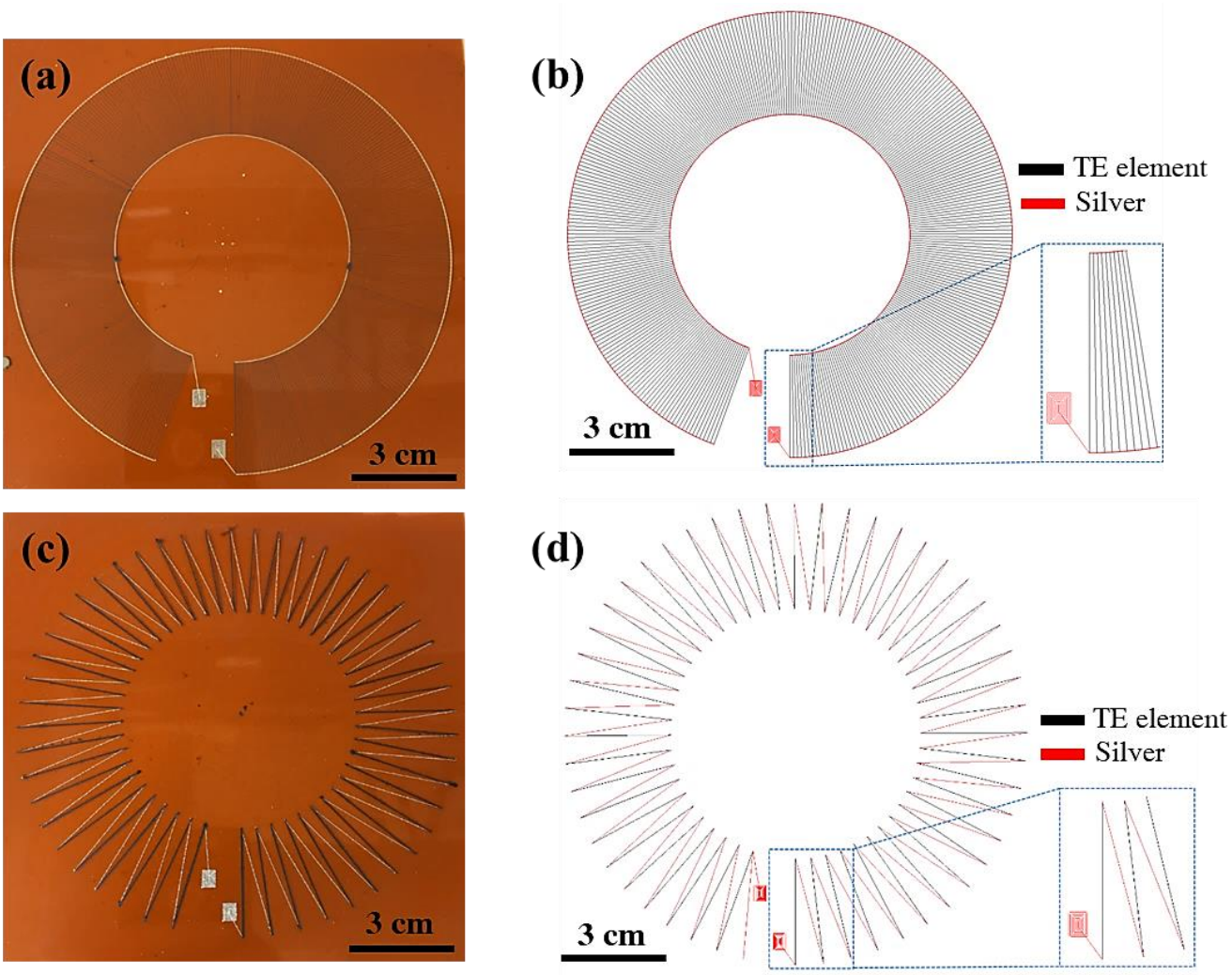

Figure 3.20 Photographic images of the 5-layer AJ-printed (a) parallel-connected and (c) series-connected TE nanocomposite arrays for the fabrication of flexible thermoelectric coasters. Schematic representation of AutoCAD-designed patterns for (b) parallel-connected mode and (d) series-connected mode, respectively.

3.10.2 Compositionally Graded Thermoelectric Generators

A home-built measurement setup, as illustrated in Figure 3.21, was designed for measuring the voltage generated by a TEG sample with a constant ΔT applied along the lateral direction. The compositionally graded thermoelectric generators (CG-TEGs) were designed, assembled, and tested by connecting them to a resistance decade box (TENMA), to determine their maximum power outputs via impedance matching across various external load resistors, under a constant applied ΔT ~70 K. These AJ-printed TEGs could be viewed as thermal batteries, where the electromotive force was the Seebeck voltage $\Delta V = -S\Delta T$. The external load resistance (R_L) was varied from 1 Ω to 1 MΩ, and the voltage outputs across them were measured via a Keithley 2002 digital multimeter. The power output was calculated by $P = (\Delta V)^2 / R_L$. The maximum power output (P_{max}) was achieved when the internal sample resistance (R_S) equalled the external load resistance, i.e. $R_S = R_L$. Thus, $P_{max} = n(\Delta V)^2/4R_S = nS^2(\Delta T)^2/4R_S$, where n is the number of TE legs connected in series, S is the Seebeck coefficient, and R_S is the resistance of the TEG. Since the power output per unit TEG is directly proportional to the square of ΔT, it is essential to ensure a constant ΔT applied in the tested samples. To achieve a consistent ΔT across the TE leg, two Pt-100 RTDs were attached on their edges so that the real-time temperature would be monitored and adjusted accordingly. Two Peltier modules were used to ensure a stable ΔT, where one was the heat source, while the other was the heat sink.

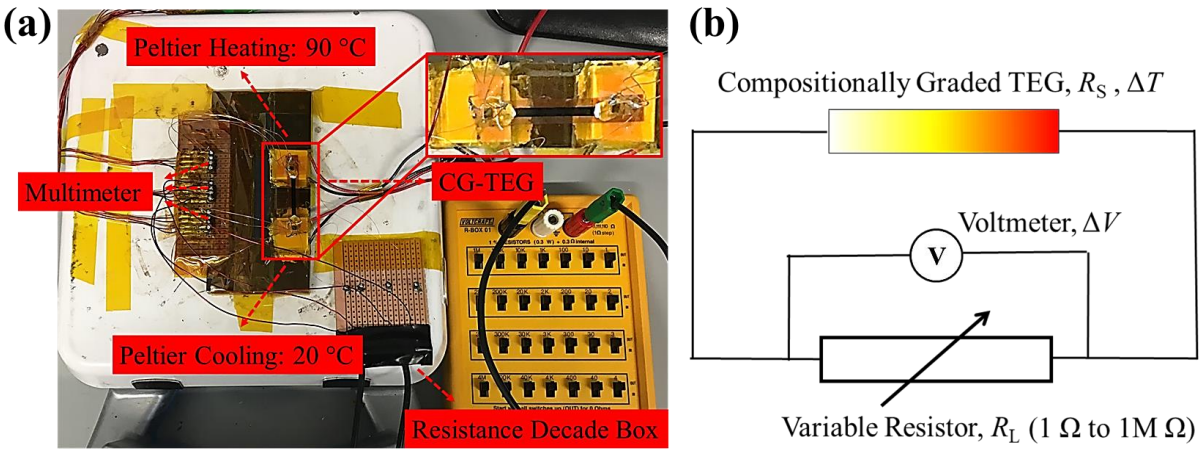

Figure 3.21 (a) Photographic image of a home-built setup for the measurement of voltage and power output as a function of external load resistance. (b) Schematic diagram of the operation circuit for the measurement of voltage and power output of CG-TEGs.

3.10.3 Free-standing Stretchable Thermoelectric Generators

The schematic in Figure 3.22 illustrates the fabrication processes of the free-standing stretchable TE structure by using the AJP technique. A pre-coated sacrificial layer was incorporated into the single-layer or multilayered TE structures, which could be fully removed after curing to produce a free-standing structure. It comprises four major steps: sacrificial layer preparation, film printing, film curing, and film lift-off. These individual steps will be elaborated in the following sections.

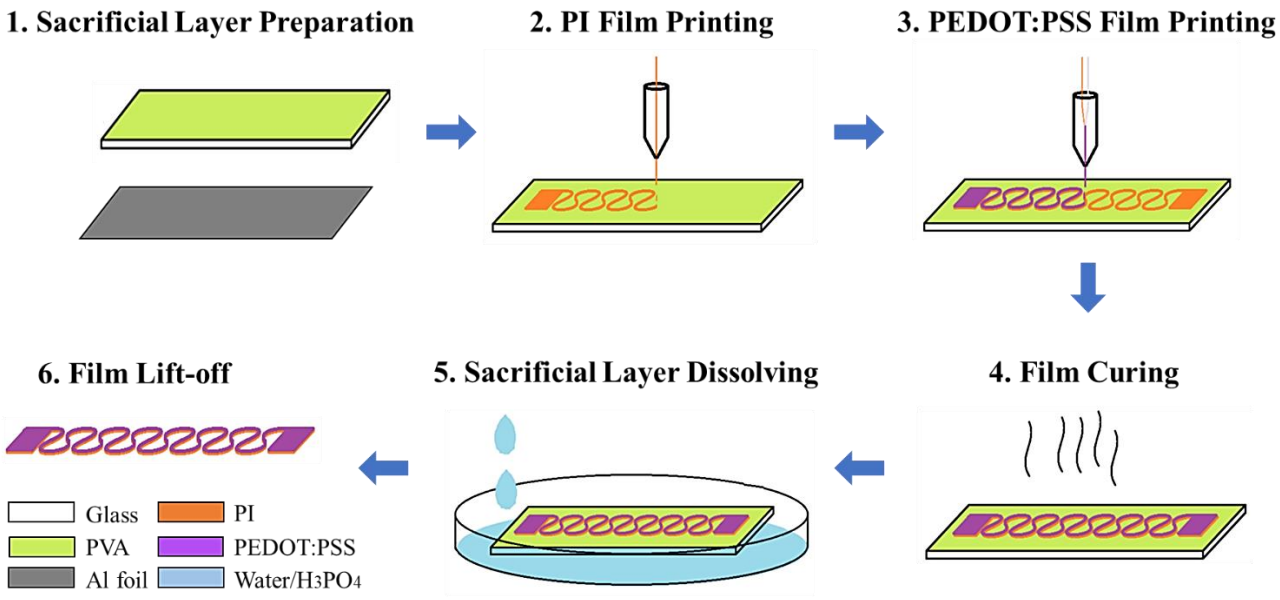

Figure 3.22 Schematic showing fabrication processes of the free-standing stretchable TE structure via the AJP method. (Figure reproduced from the author's work [159]. (CC BY 4.0))

(i) Sacrificial Layer Preparation and Film Lift-off

For the selection of sacrificial layer, two different types of sacrificial materials were investigated, as shown in Table 3-6 and Figures 3.23 (a) - (d): (1) polyvinyl alcohol (PVA) coated glass substrate; (2) aluminium (Al) foil substrate.

(1) PVA-coated glass substrate: 5 wt.% of polyvinyl alcohol powder (PVA, 87-90% hydrolysed, average molecular weight 30,000-70,000, Sigma-Aldrich) was dissolved within DI water. Then, PVA solution was spin-coated on an ethanol-cleaned glass substrate at a speed

of 500 rpm for 60 seconds by a spin-coater (Laurell). It was fully dried at 80 ºC for 1 hour to form a thin sacrificial layer (c.a. 400 nm in thickness), which served as a temporary substrate for hosting the AJ-printed pattern prior to the lift-off process, and to be subsequently dissolved at the later lift-off stage. It was found that the deposited PVA film could promote the wetting behaviour of PI and PEDOT:PSS inks, which largely improved their printing quality. For the film lift-off process, the as-printed sample was immersed in a petri-dish filled with DI water for 10 hours at room temperature to completely dissolve the PVA sacrificial layer between AJ-printed stretchable structures and the glass substrate. As illustrated in Figure 3.22, the stretchable structure was freed from the glass substrate.

(2) Al foil substrate: unlike the PVA-coated glass substrate, the PI and PEDOT:PSS inks could be directly AJ-printed on the Al foil substrate without introducing additional sacrificial layer, as the Al foil itself could be used as a sacrificial material. In this case, the same film printing and film curing processes were followed as above. However, for the film lift-off stage, the as-printed sample was immersed into phosphoric acid solution (H_3PO_4, 40 wt.% in H_2O, Sigma Aldrich) for 20 hours at room temperature to fully dissolve the Al foil. After that, the free-standing structure was released and then rinsed with DI water several times to remove the remaining H_3PO_4. It should be noted that the PEDOT:PSS is chemically resistant to both strong acid solutions and polar solvents, but the PI is not.[236,237] The higher the concentration of the acid, the faster the degradation process of the PI.[236] As a result, some strong acid solutions, such as hydrochloric acid (HCl) and sulfuric acid (H_2SO_4) cannot be used here. If the PEDOT:PSS-based nanocomposites as developed in Chapters 4 and 5 were used here, these strong acid solutions would dissolve the Bi_2Te_3 and Sb_2Te_3 metallic alloys.[238] An additional encapsulation layer might be required to protect them. In order to address these issues, diluted H_3PO_4 solution with the addition of imidazole was employed here to dissolve the Al foil while protecting other deposited materials from dissolving. The added imidazole could significantly improve the chemical oxidation stability of PI.[236] Additionally, H_3PO_4 solution could also largely enhance σ of the PEDOT:PSS by de-doping the PSS molecules, which is similar to the surface treatment via polar solvents, as discussed in Section 3.5.2.

After the lift-off stage, the obtained free-standing PEDOT:PSS structure was surface-treated for further improvement of its TE properties, as discussed in Section 3.5.2. As presented in Figures 3.23 (e) and (f), these free-standing and self-supported TE structures could be handled easily with tweezers or by hand, and also could be rolled into different curvatures or shapes. The out-of-plane serpentine structure as well as the multilayered structure were also fabricated following the same fabrication procedures, as discussed in the following sections.

Table 3-6 Comparison of different sacrificial substrate materials for the fabrication of free-standing TE structure in this work.

Substrate	Sacrificial material	Dissolving solvent	Surface treatment	Issue
PVA-coated glass	PVA	Water	EG	• Time-consuming and multiple-step PVA-coated glass preparation. • Some polar solvents, e.g. DMSO can partially dissolve the PI layer.[237]
Al foil	Al	Diluted H_3PO_4 + imidazole	H_3PO_4	• Some strong acids, e.g. HCl and H_2SO_4 can partially dissolve the PI layer.[236]

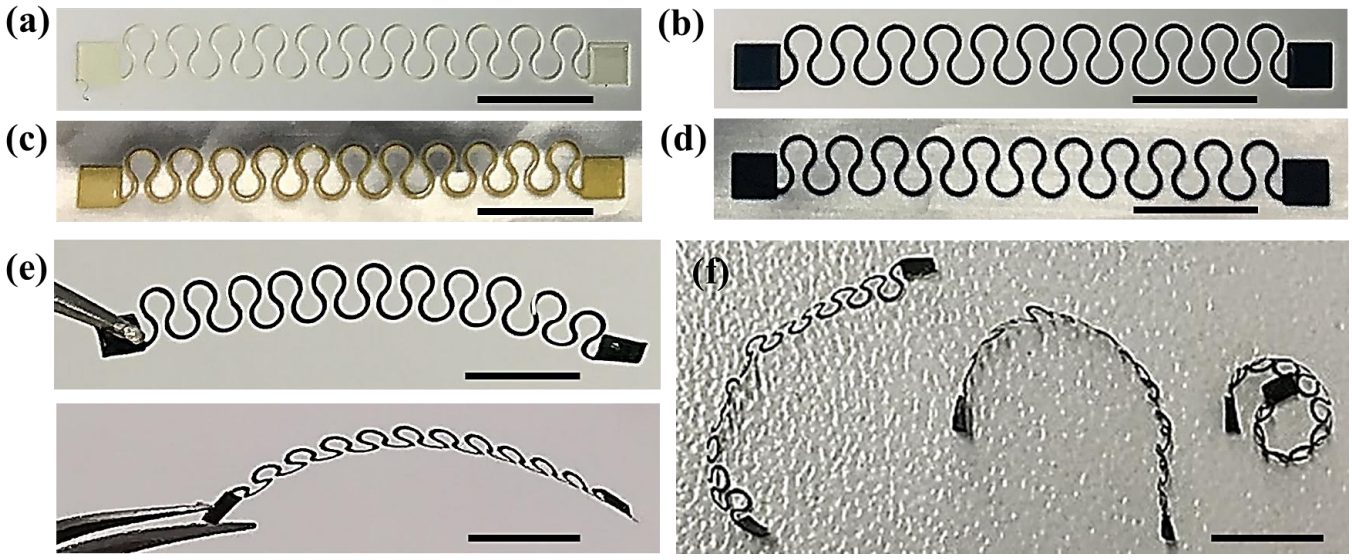

Figure 3.23 Photographic images of AJ-printed (a) PI and (b) PEDOT:PSS films on the PVA-coated glass substrate as well as AJ-printed (c) PI and (d) PEDOT:PSS films on the Al foil substrate, respectively. The obtained free-standing TE structure could be (e) handled easily with tweezers or (f) rolled into different curvatures and shapes. Scale bar: 5 mm.

(ii) Film Printing and Film Curing

At first, a PI film was AJ-printed on the as-prepared sacrificial layer (Al or PVA), patterned into the serpentine structure as a supporting layer for the subsequent active layer printing. Then, PEDOT:PSS films and Ag electrodes were AJ-printed on top of the deposited PI layer, following the same path but with a different number of printed layers. Since monolayers of PEDOT:PSS and Ag were quite rigid and fragile, they were prone to fracture when bent or stretched. However, by embedding them with the underlying PI supporting film, their overall mechanical stretchability and robustness could be substantially improved. For the enhancement of TE performance, the PEDOT:PSS film could be replaced by its nanocomposites, as developed in Chapters 4 and 5.

Lastly, the as-printed sample was oven-cured at 130 °C for 12 hours to solidify the deposited materials and burn away any remaining solvents. The curing temperature was set comparatively low here, because higher temperatures might degrade the PEDOT:PSS polymer, and importantly might carbonise the sacrificial PVA layer that could affect the subsequent lift-off process. For the Al-foil substrate, there was no limitation on the curing temperature. Consequently, this could broaden the selection of active materials to include inorganic TE materials. Monolayers of PI, PEDOT:PSS, and Ag were directly AJ-printed on the Al foil to obtain the dimensions of a single-printed layer via the method described in Section 3.6.

(iii) Multilayer Printing

With the aid of the versatile AJP technique, multiple TE layers can be easily achieved by the automatic deposition process, which can remarkably reduce the fabrication complexity and ensure high production quality.[159] Considering the fabrication time, only a 3-layer AJ-printed stretchable TE structure is demonstrated here. More layers can be easily stacked up by properly designing the printing pattern. In this work, a multilayered structure was formed to enhance the final power output of the stretchable TEG. The Ag ink was alternately AJ-printed as electrodes to electrically connect with individual AJ-printed PEDOT:PSS TE legs in series while thermally connecting them in parallel. The schematic representation of AutoCAD-

designed patterns in Figure 3.24 depicts the architecture of each layer, showing how each layer was AJ-printed and linked to add up the overall voltage and power outputs. Also, another PI film was AJ-printed on top to encapsulate the whole TE structure, which could be an effective approach to packaging these free-standing structures.[159] Figure 3.25 shows the photographic images of the single-layer structure and the 3-layer structure with out-of-plane design.

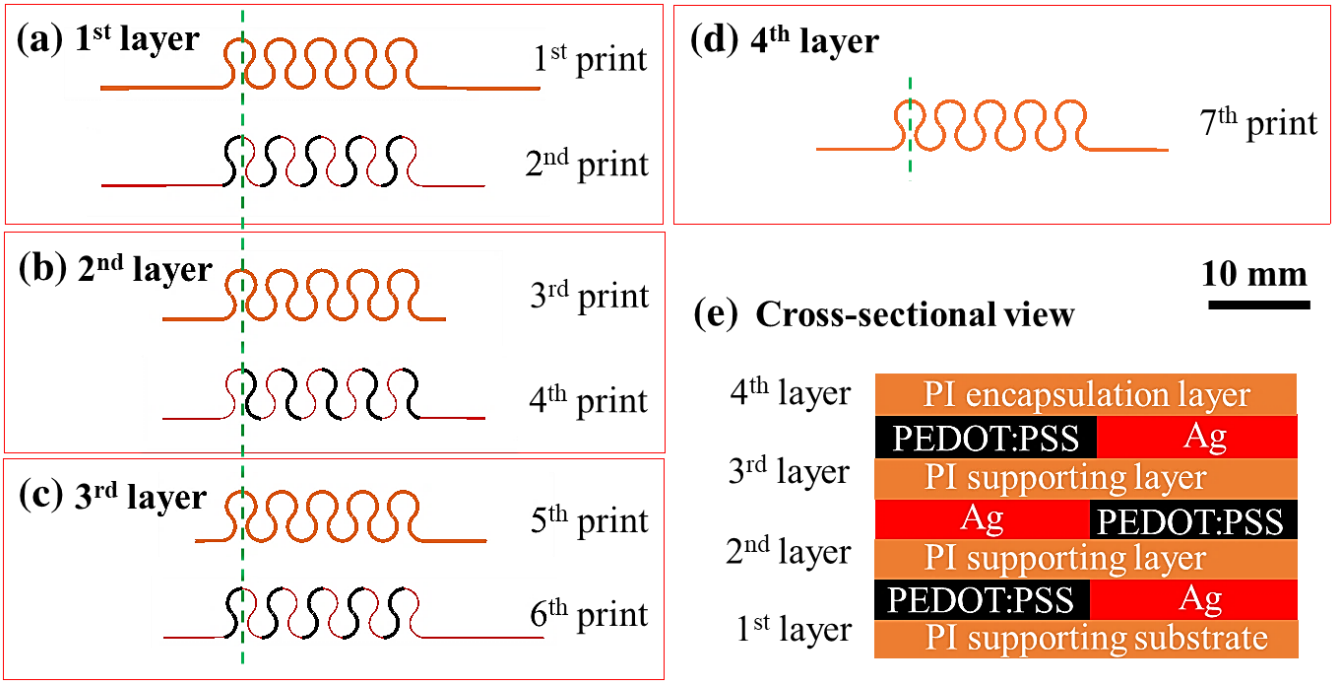

Figure 3.24 Schematic of AutoCAD-designed patterns depicting the design structures for the 3-layer stretchable structure with out-of-plane design. (a) is the first layer, (b) is the second layer, (c) is the third layer, and (d) is the final encapsulation layer. (e) The inset showing the cross-section of different stacked layers along the green dashed line.

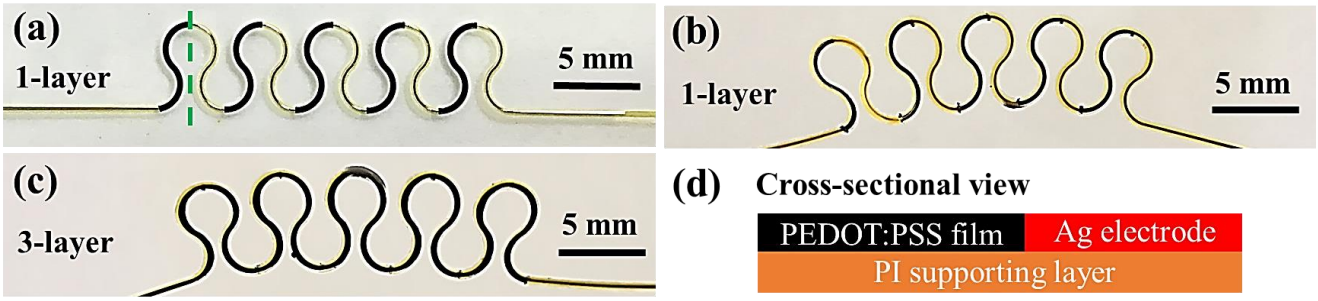

Figure 3.25 Photographic images of (a) the single-layer stretchable structure AJ-printed on the PVA-coated glass substrate, and (b) the free-standing TEG after being freed from the lift-off process, which could be handled easily with a tweezer. (c) The 3-layer stretchable structure was stacked into one whole free-standing TEG, with a protective PI layer encapsulated on top. (d) The inset showing the cross-section of different stacked layers along the green dashed line.

3.10.4 Substrate-based Stretchable Thermoelectric Generators

Since Young's moduli of soft elastomers, such as polydimethylsiloxane (PDMS) and polyurethane (PU) (E_{PDMS} ~1 MPa[203] and E_{PU} ~10 MPa[239]) are remarkably lower than that of PI, PEDOT:PSS, and Ag, as shown in Table 3-5, the PDMS or PU encapsulation can serve as a protective and supporting substrate to improve the mechanical robustness of AJ-printed TE materials, and also make the free-standing structures to be easier to handle.[159,204] Here, two different device structures were designed for the substrate-based stretchable TEG fabrication, as illustrated in Figure 3.26. PEDOT:PSS films formed TE legs, Ag electrodes provided electrical contacts, and PDMS or PU elastomers offered stretchable substrates. In order to achieve a higher power output, a number of TE legs were connected electrically in series and thermally in parallel with out-of-plane design. It was found that the serpentine structure could be stretched along all directions, i.e. horizontal, vertical, or diagonal directions. In comparison, a strip-shaped structure could only be stretched along the horizontal direction. Moreover, two different approaches to embedding PEDOT:PSS films and Ag electrodes within PDMS or PU elastomers were exploited as follows.

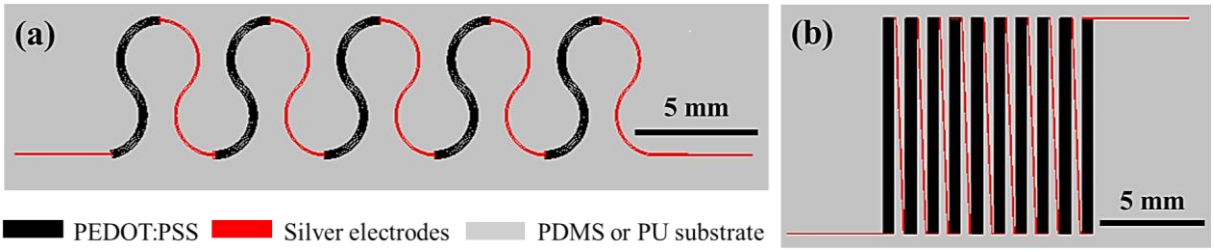

Figure 3.26 Schematic showing the AutoCAD-designed patterns of (a) serpentine structure and (b) strip structure for substrate-based stretchable TEGs with out-of-plane design.

(i) Printing on Elastomer Substrate

Firstly, PDMS solution was prepared by blending the pre-polymer (Sylgard 184 Silicone, Dow) with a curing agent using a weight ratio of 20:1, followed by stirring until a homogeneous mixture was achieved. The mixture was subsequently vacuum-treated for 10 minutes to reach a bubble-free state. PDMS solution was drop-cast on a glass substrate, which was then cured

at 80 ºC for 30 minutes for solidification. For PU solution, it was prepared by dissolving PU beads (Elastollan Soft) within N,N-dimethylformamide (DMF, Sigma Aldrich) solvent at 20 wt.%. Finally, PU solution was drop-cast on a glass substrate and cured at 80 ºC on a hot plate to remove DMF solvent as well as to solidify the PU polymer. Once DMF solvent was fully evaporated, a subsequent deposition was carried out. A total of five layers were drop-casted here to build up the thickness of the PU layer.

Following the design patterns in Figure 3.26, *p*-type PEDOT:PSS TE legs and Ag electrodes were directly AJ-printed onto stretchable PDMS or PU substrates. They were cured together at 130 ºC for 12 hours to obtain the electrical connection. Subsequently, a PDMS encapsulant was spin-coated on top of the previously printed layer through a PI-tape-based shadow mask. Due to the high viscosity of PDMS solution, PDMS could not be directly printed via the AJP method, and it could only be deposited via spin-coating or drop-casting method. For PU solution with much lower viscosity, a PU encapsulant could be AJ-printed with excellent control of the dimensions and positions of the printed film. Lastly, these encapsulated samples were cured at 80 ºC for 2 hours. After solidification, these PDMS-based or PU-based stretchable TEGs could be easily peeled off from the glass substrate manually. However, there existed some problems in these substrate-based stretchable TEGs, which will be discussed in more detail in Chapter 7.

(ii) Drop casting with Elastomer Encapsulant

Another approach to encapsulating AJ-printed PEDOT:PSS films and Ag electrodes is proposed here to overcome some of the issues that occurred in the above approach. At first, PDMS or PU solution was drop-cast onto a glass substrate to form a thin layer. Then, the free-standing stretchable TEG fabricated in Section 3.10.3 was placed on top of the pre-coated PDMS or PU films with the connection of external copper wires for the TE property measurement. After that, a subsequent PDMS or PU encapsulant was drop-cast on top to fully encapsulate the whole TEG. Once cured at 80 ºC on a hot plate, these encapsulated stretchable TEGs could be peeled off from the glass substrate and handled easily by hand or by tweezers.

3.10.5 Stretchable Compositionally Graded Thermoelectric Generators

In order to demonstrate the feasibility of incorporating the CG-TEC concept with the stretchable structure, a stretchable CG-TEG was designed and fabricated, as shown in Figure 3.27. The free-standing stretchable CG-TEG was comprised of 15 wt.% Bi_2Te_3-PEDOT:PSS nanocomposite (the left part) and PEDOT:PSS (the right part), according to the results discussed in Chapter 6.

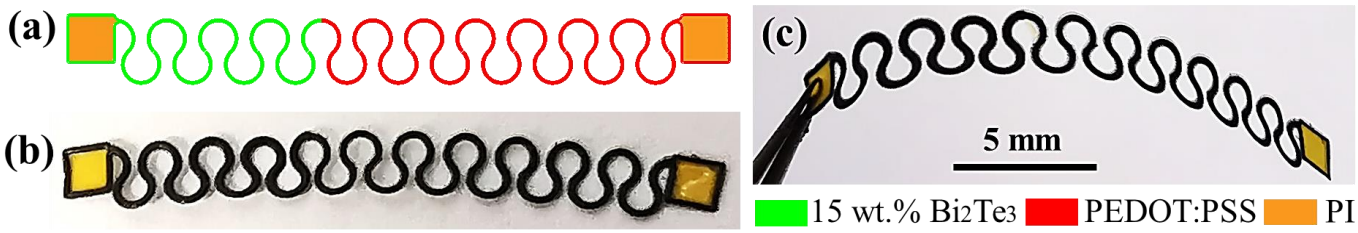

Figure 3.27 (a) Schematic representation of AutoCAD-designed pattern and (b) photographic image of the stretchable CG-TEG design structure, which was comprised of 15 wt.% Bi_2Te_3-PEDOT:PSS nanocomposite (the left part) and PEDOT:PSS (the right part). (c) The obtained free-standing stretchable CG-TEG could be handled easily with a tweezer.

Chapter 4

Bi_2Te_3/Sb_2Te_3-based Thermoelectric Nanocomposites

In this chapter, the author brings together all the work related to the fabricated Bi_2Te_3 and Sb_2Te_3 nanomaterials as well as the resulting TE nanocomposites and TEGs. Firstly, the morphology and crystallinity of Bi_2Te_3 and Sb_2Te_3 nanomaterials fabricated by various approaches have been characterised. Then, printable inorganic inks have been developed in combination with the PEDOT:PSS polymer for the fabrication of flexible TE nanocomposites. The AJP technique has been employed to print these bespoke inks, and the effect of nanoparticulate inclusions on the obtained TE properties has also been ascertained. In order to systematically study the mixed compositions, a novel *in situ* mixing method has been developed, which has shown to be an effective way of enhancing both S and σ, and hence the overall PF in formed nanocomposites. Their morphological, microstructural, thermoelectric and mechanical properties have been comprehensively studied as a function of the loading fraction of inorganic components to identify optimum compositions and printing conditions for the enhancement of PF. Finally, the feasibility of these AJ-printed nanocomposites for applications in flexible TEGs has been directly demonstrated through rigorous flexing testing. Some parts discussed here have been published in "Fully Printed Organic-Inorganic Nanocomposites for Flexible Thermoelectric Applications". *ACS Applied Materials & Interfaces*, 2018, 10 (23), 19580,[25] and they have been adapted from that text with granted

Copyright permission. It should be noted that the author performed all the experiment works and data analysis with the help of other co-authors of the paper.

4.1 Nanomaterial Characterisation

4.1.1 Hand-ground Bi_2Te_3 and Sb_2Te_3 Particles

The SEM micrographs in Figures 4.1 (a) and (b) show that Bi_2Te_3 and Sb_2Te_3 particles at the microscale or even nanoscale size could be simply and quickly fabricated by hand grinding commercially purchased powders. However, since this approach had less control of the grinding process, the obtained particles exhibited a very wide size distribution with an average particle size of ~644 (±623) nm and ~504 (±398) nm for Bi_2Te_3 and Sb_2Te_3, respectively. The EDX analysis was performed on these hand-ground powders to ascertain their compositions. According to their representative EDX spectrum presented in Figures 4.1 (c) and (d), the compositional analysis shows that the actual 'Bi' and 'Te' atomic concentration in Bi_2Te_3 were 53.05% (±0.6) and 46.95% (±0.6) (Bi : Te ≈ 3.39 : 3), respectively, while the actual 'Sb' and 'Te' atomic concentration in Sb_2Te_3 were 39.46% (±1.3) and 60.54% (±1.3) (Sb : Te ≈ 1.95 : 3), respectively. The hand-ground Bi_2Te_3 possessed much higher 'Bi' at.% than the stoichiometric amount. This might be ascribed to the contain of some impurities and/or secondary phases, such as Bi_2O_3 or Bi clusters detected by the XRD analysis, which also contributed to the *n*-type behaviour of Bi_2Te_3. On the other hand, the hand-ground Sb_2Te_3 was nearly stoichiometric with slightly less 'Te' at.% and without evident detectable impurities or secondary phases, thereby showing *p*-type behaviour. The XRD results in Figures 4.1 (e) and (f) also confirm that this hand-grinding process did not influence the crystal structure of Bi_2Te_3 and Sb_2Te_3, but only reduced their particle size in a mechanical way. The average crystallite sizes of Bi_2Te_3 and Sb_2Te_3 particles were calculated to be ~297 (±89) nm and ~249 (±76) nm, respectively, by Debye-Scherrer equation as expressed in Equation 3-1. It was found that their calculated crystallite sizes were much smaller than their particle sizes, which indicated the polycrystalline microstructure of these commercially procured powders.

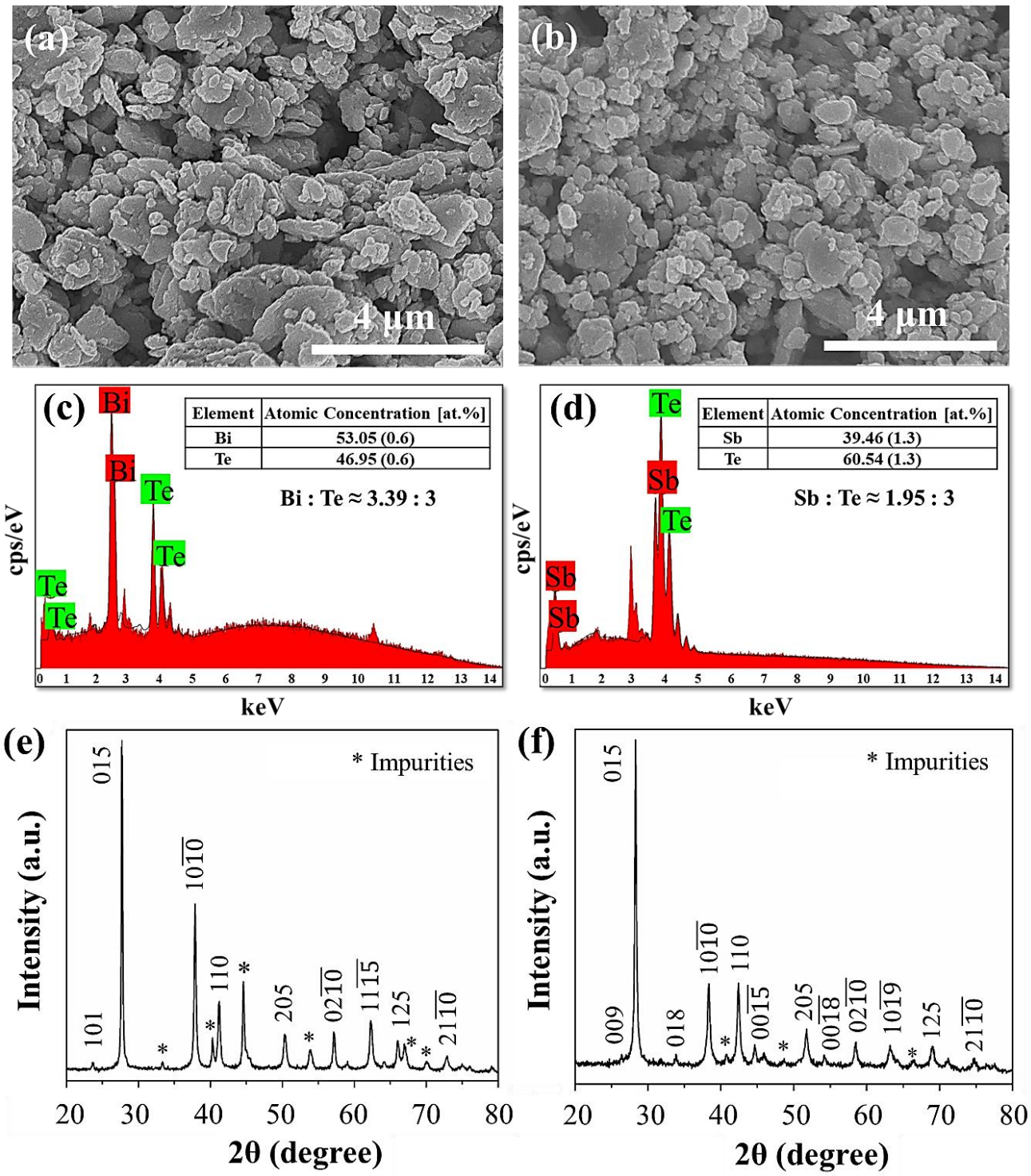

Figure 4.1 SEM images of hand-ground (a) Bi_2Te_3 and (b) Sb_2Te_3 particles, respectively. EDX analysis of hand-ground (c) Bi_2Te_3 and (d) Sb_2Te_3 particles, respectively. XRD analysis of hand-ground (e) Bi_2Te_3 and (f) Sb_2Te_3 particles, respectively.

4.1.2 Ball-milled Bi_2Te_3 and Sb_2Te_3 Particles

Figures 4.2 (a) and (b) present the SEM micrographs of Bi_2Te_3 and Sb_2Te_3 particles obtained from the ball milling process. It can be seen that these ball-milled particles were strongly aggregated with a wide size distribution. The average particle sizes of Bi_2Te_3 and Sb_2Te_3 were estimated to be ~409 (±298) nm and ~378 (±278) nm, respectively. This agglomeration phenomenon might be attributed to the fact that metallic alloys or intermetallics were highly prone to suffering from the cold-welding issue, whereby the resulting particles could be easily welded together into large clusters during the ball-milling process.[1] As shown in Figures 4.2 (c) and (d), the XRD results of these ball-milled powders reveal that there was minority impurity phase detected within these particles, which might be attributed to the contain of some impurities and/or secondary phases produced during the ball milling process, such as Bi_2O_3 or Bi clusters. This shows that the ball milling process did not affect their crystalline structures. The calculated crystallite sizes of these Bi_2Te_3 and Sb_2Te_3 particles were ~139 (±23) nm and ~164 (±27) nm, respectively. Their particle sizes were found to be much larger than their crystallite sizes, which might be ascribed to the agglomeration issue. Compared with their hand-ground counterparts, smaller crystallite sizes and particle sizes were obtained via this fabrication method. Another obvious advantage of this ball-milling approach is that a substantial amount of powders could be produced with less production time and human involvement (yielding 10 g of powder from each milling jar). This approach therefore is favoured for large-scale production of TEGs. However, the major drawback of this ball-milling method is that the agglomeration issue could largely limit these particles to be prepared into printable inks, where fine particle-size and well-dispersed are indispensable. Moreover, the high-temperature heat treatment conducted to remove residual solvents and surfactants could result in the oxidation and/or decomposition of Bi_2Te_3 and Sb_2Te_3 particles, thereby forming by-products e.g. oxides and significantly deteriorating their crystalline qualities and TE properties. As a result, the heat treatment was avoided here at the expense of some TE performance.

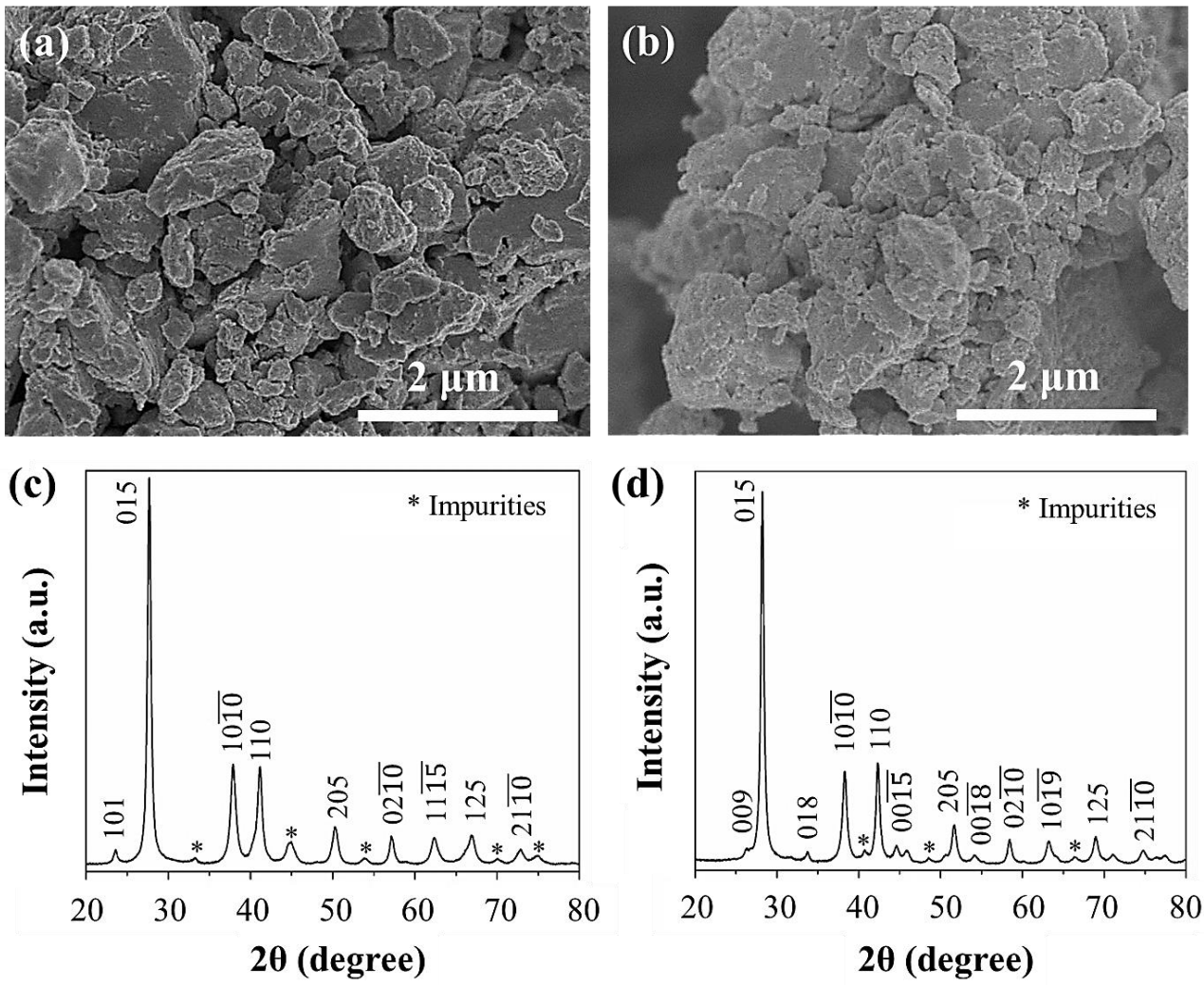

Figure 4.2 SEM images of ball-milled (a) Bi_2Te_3 and (b) Sb_2Te_3 particles, respectively. XRD analysis of ball-milled (c) Bi_2Te_3 and (d) Sb_2Te_3 particles, respectively.

4.1.3 Solvothermal-synthesised Bi_2Te_3 and Sb_2Te_3 Particles

The SEM images in Figures 4.3 (a) and (b) revealed that the as-synthesised Bi_2Te_3 with a spherical nanoparticle form exhibited an average particle size of ~129 nm and a size distribution of ± 49 nm, while Sb_2Te_3 nanocrystals were found to be randomly oriented in thin flake form with an average lateral diameter of ~534 nm and a size distribution of ± 281 nm. The flake-like structure was commonly observed in Sb_2Te_3 because of its inherent anisotropic and layered crystal structure.[72] As tabulated in Figures 4.3 (c) and (d), the EDX analysis reveals that the actual 'Bi' and 'Te' atomic concentration in Bi_2Te_3 were found to be 41.1% (±2.2) and 58.9% (±2.1) (Bi : Te ≈ 2.1 : 3), respectively, while the actual 'Sb' and 'Te'

atomic concentration in Sb_2Te_3 was found to be 39.6% (±1.9) and 60.4% (±2.9) (Sb : Te ≈ 1.9 : 3). By controlling the Bi/Te and Sb/Te ratio in the precursor solution, the synthesised composition could be adjusted. If Bi_2Te_3/Sb_2Te_3 were to be Bi-rich/Sb-rich or Te-deficient, the Bi/Sb would contribute to more hole carriers (h^+) and exhibit *p*-type behaviour, or vice versa.[72] The solvothermal-synthesised Bi_2Te_3 possessed slightly more 'Bi' at.% than the stoichiometric amount, leading to Bi-rich material that was hole carrier dominated, while the Sb_2Te_3 was nearly stoichiometric.

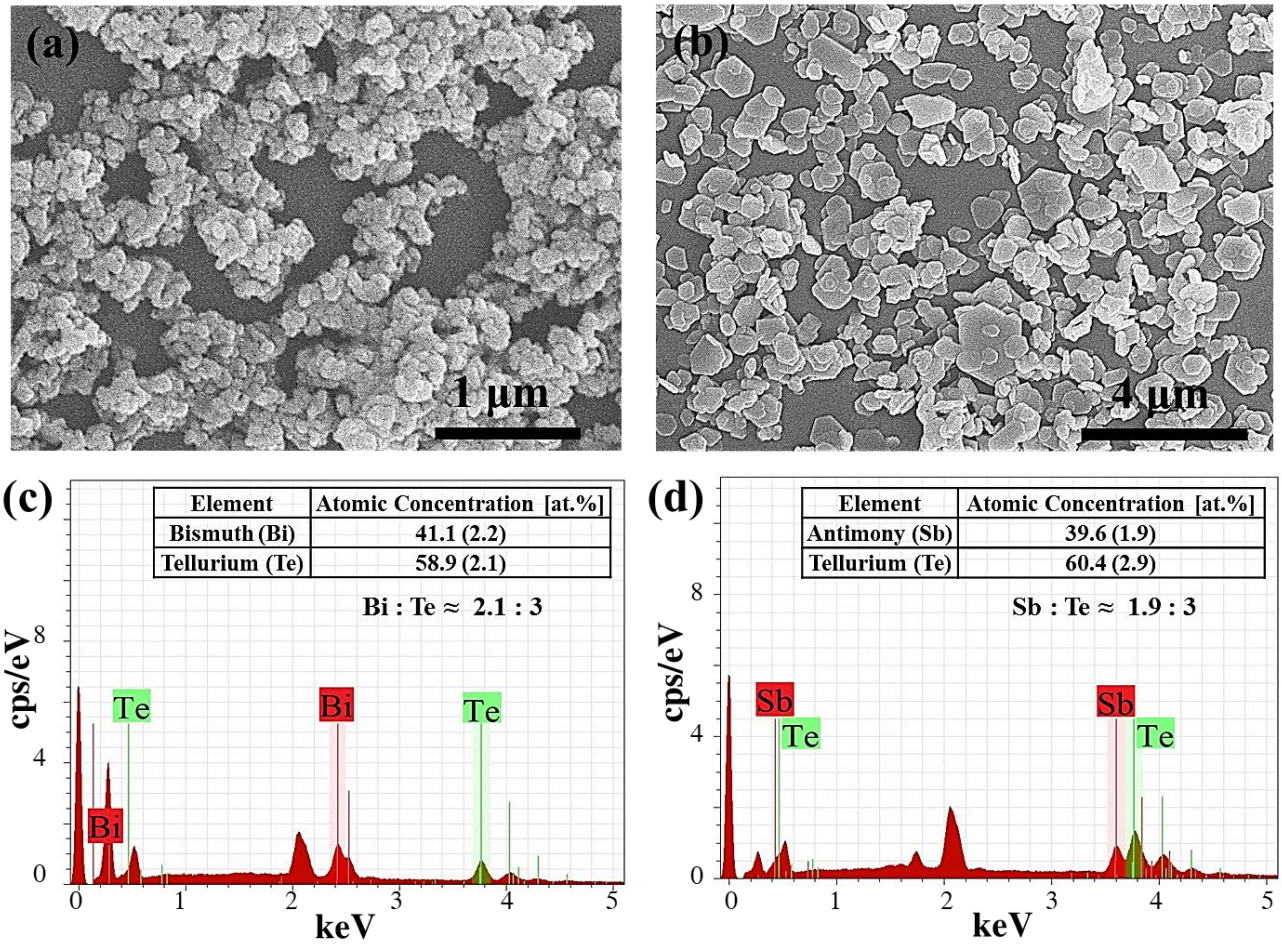

Figure 4.3 SEM images of solvothermal-synthesised (a) Bi_2Te_3 nanoparticles and (b) Sb_2Te_3 nanoflakes, respectively. EDX analysis of (c) Bi_2Te_3 nanoparticles and (d) Sb_2Te_3 nanoflakes, respectively. (Figures taken from the author's work [25]. (CC-BY))

XRD studies in Figures 4.4 (a) and (b) presented that the diffraction patterns obtained here were quite similar to that of the above-discussed hand-ground and ball-milled powders, where (015) was the sharpest and most intense diffraction plane for both Bi_2Te_3 and Sb_2Te_3 as expected. There was negligible detectable impurity peak within the resolution limits of the XRD, showing that good crystalline quality was obtained. The XRD spectra of Bi_2Te_3 and Sb_2Te_3 were both indexed with rhombohedral symmetry (space group *R-3m*), and indicated an average crystallite size of ~201 (±53) nm and ~479 (±59) nm, respectively, as calculated by Debye-Scherrer equation.[227] These calculated crystallite sizes were within reasonable agreement with the average particle sizes estimated from the SEM micrographs, which suggests that this solvothermal synthesis approach had much better control of the morphology with a fairly uniform size distribution. The crystal structure of the as-prepared Bi_2Te_3 and Sb_2Te_3 nanocrystals were investigated by the HRTEM, as shown in Figures 4.4 (c) - (f). Figure 4.4 (c) shows the polycrystalline nature of the Bi_2Te_3 nanoparticle, which was further revealed by the discontinuous lattice fringes oriented in the same direction in Figure 4.4 (e). The *d*-spacing of 0.33 nm was in good agreement with the (015) inter-planer spacing of the Bi_2Te_3 nanoparticle. The hexagonal-shaped Sb_2Te_3 nanoflake, as presented in Figure 4.4 (d), exhibited more continuous lattice fringes compared to that of the Bi_2Te_3 nanoparticle. The lattice fringe spacing of 0.32 nm was also in agreement with the (015) lattice plane in the hexagonal Sb_2Te_3 nanoflake (see Figure 4.4 (f)). Due to the limit of the used TEM equipment, the selected area electron diffraction (SAED) pattern was not shown here.

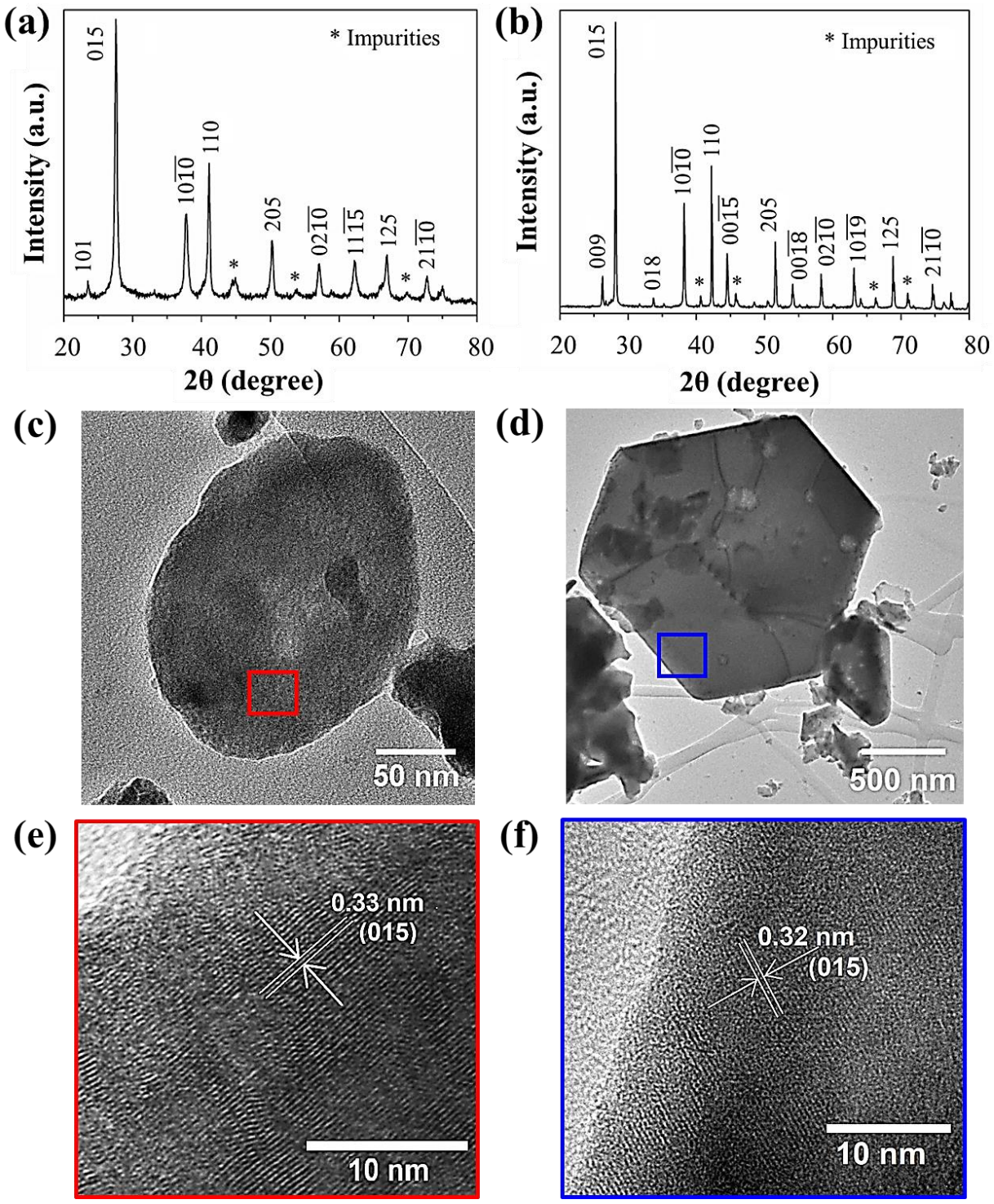

Figure 4.4 XRD results of solvothermal-synthesised (a) Bi_2Te_3 nanoparticles and (b) Sb_2Te_3 nanoflakes, respectively. TEM analysis of (c) Bi_2Te_3 nanoparticle and (d) Sb_2Te_3 nanoflake, where the enlarged HRTEM images reveal the lattice fringe patterns of (e) Bi_2Te_3 nanoparticle and (f) Sb_2Te_3 nanoflake. (Figures taken from the author's work [25]. (CC-BY))

4.2 Inorganic Film Printing

To start with, 20 wt.% of Bi_2Te_3 nanoparticles or Sb_2Te_3 nanoflakes was prepared into a printable ink by dispersing within DI water. For the preliminary printing test, Sb_2Te_3 nanoflakes were AJ-printed on a silicon substrate or a PI substrate via the pneumatic atomiser, as presented in Figure 4.5. Silicon substrate and PI substrate were selected here to compare the influence of different substrates on the printed line morphology. However, these AJ-printed lines were quite spread-out, and the deposited nanoflakes were likely to agglomerate on the edges, forming lots of isolated islands rather than a continuous dense film. This phenomenon might be attributed to the poor wetting behaviour on these substrates or the coffee-ring effect. In this regard, the printing conditions, such as the atomisation and focusing parameters, were modified to obtain the optimum printing quality. As a result, a significant improvement of the printed line quality was achieved in Figure 4.6. The Bi_2Te_3 nanoparticles and Sb_2Te_3 nanoflakes were successfully AJ-printed on a PI substrate with a line width of ~100 μm and ~80 μm, respectively, without requiring sophisticated surface treatments, e.g. oxygen plasma treatment. Although these AJ-printed inorganic films seemed to be quite dense and uniform, some noticeable pores could be seen, which might contain some cracks and/or voids that could lead to the high electrical resistance or even electrical insulating. These discontinuities within AJ-printed films might stem from the curing process that could induce thermal shocks and/or the flexing of the substrate that could cause mechanical strains in their internal microstructures.[71] In order to solve this issue, a polymeric matrix was introduced to host and connect these inorganic inclusions so as to form an electrically conducting network, which will be discussed in the following sections.

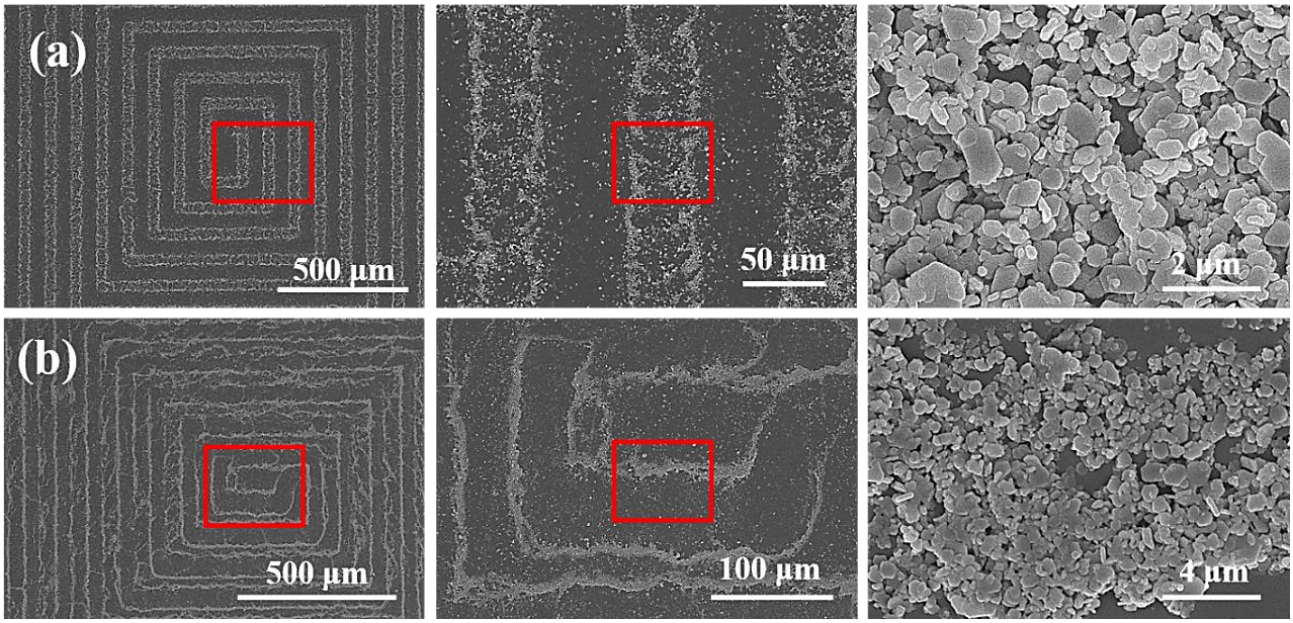

Figure 4.5 SEM images of AJ-printed Sb_2Te_3 nanoflakes on (a) a silicon substrate and (b) a PI substrate before optimising the printing conditions, where the enlarged SEM images show more morphological features.

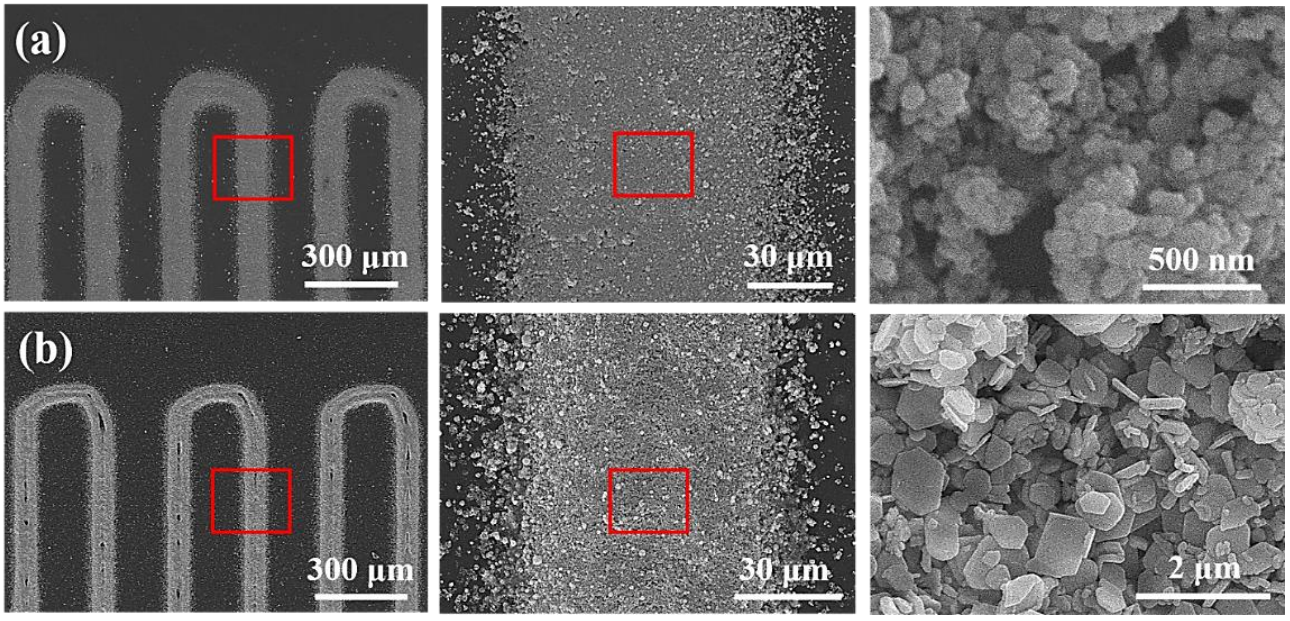

Figure 4.6 SEM images of the 10-layer AJ-printed (a) Bi_2Te_3 nanoparticles and (b) Sb_2Te_3 nanoflakes on a PI substrate after optimising the printing conditions, where the enlarged SEM images reveal more morphological features.

4.3 Organic Film Printing

Since the pristine PEDOT:PSS film exhibits fairly poor electrical conductivity ($\sigma < 1$ S/cm), surface treatment is indispensable to improve its σ.[240] Before moving to the nanocomposite printing, some preliminary experiments have been conducted to probe into the feasibility of enhancing the TE performance of PEDOT:PSS. As presented in Figure 4.7, a dense and uniform PEDOT:PSS film was successfully AJ-printed via the ultrasonic atomiser. Different numbers of printed layers (from 5 to 15 layers) were also prepared to investigate their influence on TE properties. Considering the printing process time, the maximum number of printed layers was limited to 15 in this work. The charge carrier density of the 5-layer printed pristine PEDOT:PSS film was estimated to be ~10^{26} m^{-3} from the Hall-effect measurement in Appendix A.5, which was slightly lower than the reported values in the literature.[93,99] Consequently, the AJ-printed PEDOT:PSS film was surface-treated with different solvents: sulfuric acid (H_2SO_4, 20 vol.%, Sigma Aldrich), ethylene glycol (EG, 99.8%, Sigma Aldrich), and dimethyl sulfoxide (DMSO, 99.9%, Sigma Aldrich). As plotted in Figure 4.8, both EG and DMSO surface treatments had a beneficial effect on the enhancement of TE performance, compared to that of the untreated and treated with H_2SO_4 samples. While the number of printed layers did not affect their TE performance much. Among them, the 5-layer printed EG-treated PEDOT:PSS film exhibited the best performance, with S ~14.8 μV/K, σ ~96.9 S/cm, and PF ~2.1 μW/(m.K^2). Furthermore, the TE properties of different PEDOT:PSS solvents obtained from various chemical suppliers were summarised in Table 4-1. It was found that the σ value of PEDOT:PSS solvent supplied from the Heraeus Clevios PH1000 considerably surpassed the one from the Sigma-Aldrich, which was more than 4 times higher, with S ~17.1 μV/K, σ ~444.2 S/cm, and PF ~12.9 μW/(m.K^2). In this regard, the adopted supplier of PEDOT:PSS solvent would be a major contribution to the final TE performance of nanocomposite structures discussed in the following section. Although the obtained PF value of the AJ-printed PEDOT:PSS film in this work was comparatively lower than some of the very best results reported by Kim et al.,[93] it still compared favourably with some reported values based on

PEDOT:PSS solvent from similar chemical suppliers.[25,99,241] It should be pointed out that the work of Kim et al.[93] has not been reproduced by any groups yet.

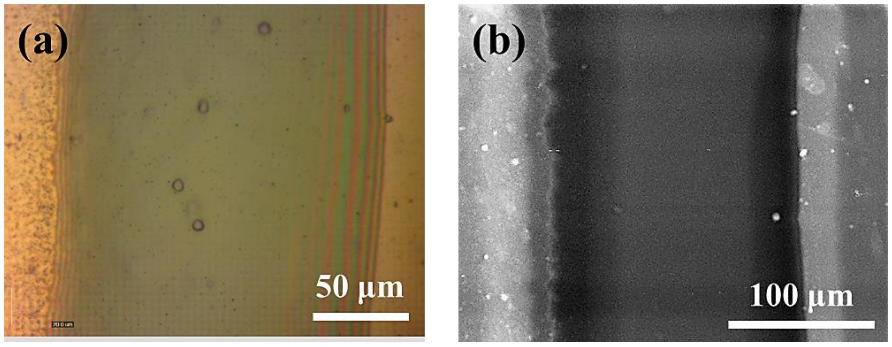

Figure 4.7 (a) Optical microscope image and (b) SEM micrograph showing the morphology of 5-layer printed pristine PEDOT:PSS film on a PI substrate.

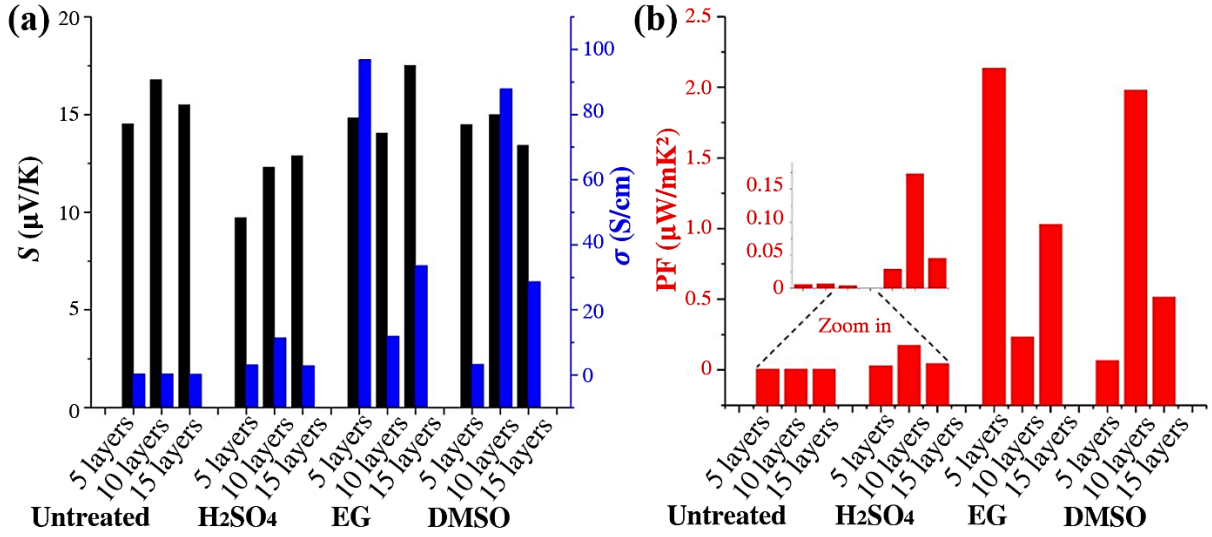

Figure 4.8 Thermoelectric measurements on (a) *S*, (b) σ and (c) PF of AJ-printed PEDOT:PSS films with different surface treatments and printed layers, where the PEDOT:PSS ink was provided from the Sigma Aldrich.

Table 4-1 Comparison of TE properties of different EG-treated PEDOT:PSS films obtained from various chemical suppliers.

Supplier	*S* (µV/K)	σ (S/cm)	PF (µW/(m.K^2))	Ref.
Starck PH1000	63 ± 2.7	890 ± 21	353	[93]
Clevios P	14.6 ± 0.3	211 ± 12	4.5	[99]
Clevios PH1000	22.6 ± 0.8	1222 ± 82	69.2	[99]
Sigma-Aldrich	14.8 ± 2.5	96.9 ± 5.3	2.1 ± 0.2	This work
Heraeus Clevios PH1000	17.1 ± 1.5	444.2 ± 34.8	12.9 ± 1.6	This work

4.4 Conventional Composite Printing

In order to obtain flexible high-performance TE nanocomposites, conducting polymer PEDOT:PSS or insulating polymer PVDF were employed in this work as the polymeric matrix with the incorporation of *p*-type TE nanostructured particles. At first, different blended solutions were prepared into printable inks, as summarised in Table 4-2. Different blended inks were magnetically stirred for 30 minutes, and then held still for 1 hour to investigate their miscibility. As can be seen from Table 4-2, the loaded particles were more likely to precipitate in the water-based solutions if not stirred. In this regard, a constant stirring is required to ensure a homogeneous suspension during the printing process. Various weight percentage (wt.%) of solvothermal-synthesised Bi_2Te_3 nanoparticles or Sb_2Te_3 nanoflakes (from 5 to 30 wt.% in nominal) were loaded into the PEDOT:PSS or PVDF solvents, respectively, to investigate the influence of the loaded inclusions on the morphological and TE properties of the resulting AJ-printed nanocomposites. It should be noted that the weight percentage (wt.%) discussed in this section represents the weight ratio of the loaded inorganic particles to the blended inks. Since both PEDOT:PSS and PVDF polymers are chemically inert over the potential temperature range used and they do not react with the loaded inorganic inclusions, they can therefore ideally serve as a protective matrix to prevent the embedded metallic alloys or semiconductors from oxidation.

Table 4-2 Investigation on the miscibility of various solvents and particles in blended inks.

Solvent and particle	Bi_2Te_3	Sb_2Te_3	MWCNTs
Water	↓	↓	↑
PVDF + NMP	–	–	↑
PEDOT:PSS + Water	↓	↓	↑

Note: ↓: sediment and leaving colourless solvent after 1 hour; ↑: floating and leaving colourless solvent after 1 hour; −: mixed and remaining coloured after 1 hour.

Initially, the ultrasonic atomiser was used for a small amount of blended inks (2 mL).

However, it failed to atomise these inks, as the viscosity of blended inks exceeded the maximum atomisation ability of the ultrasonic atomiser, as previously discussed in Section 3.4. Consequently, the pneumatic atomiser was employed with the ink amount of 20 mL, by which these blended inks could be atomised and printed after some optimisation in the printing conditions. Nevertheless, due to the insufficient amount of synthesised Bi_2Te_3 or Sb_2Te_3 nanomaterials, the high cost of PEDOT:PSS polymer, as well as the limited ink viscosity capacity of the atomiser, 30 wt.% was the maximum value that could be achieved here. If the loaded wt.% continued to increase, the mixed ink would become too viscous to be printed by the AJP method. As presented in Figures 4.9, 10 wt.% of Sb_2Te_3 nanoflakes were firstly AJ-printed with 1, 5, and 10 layers for comparison. Wider and thicker printed structures with denser packing of particles as well as fewer noticeable pores were obtained as the number of printed layers increased. The resulting thicknesses were estimated to c.a. 1-5 µm, as measured in Figure 4.10. As can be seen from Figure 4.11, both σ and PF increased with increasing number of printed layers, while the S slightly decreased. This might be due to the formation of denser nanocomposite structures as the number of printed layers increased. Considering the TE performance and the printing time, 10-layer printing was chosen for further investigation.

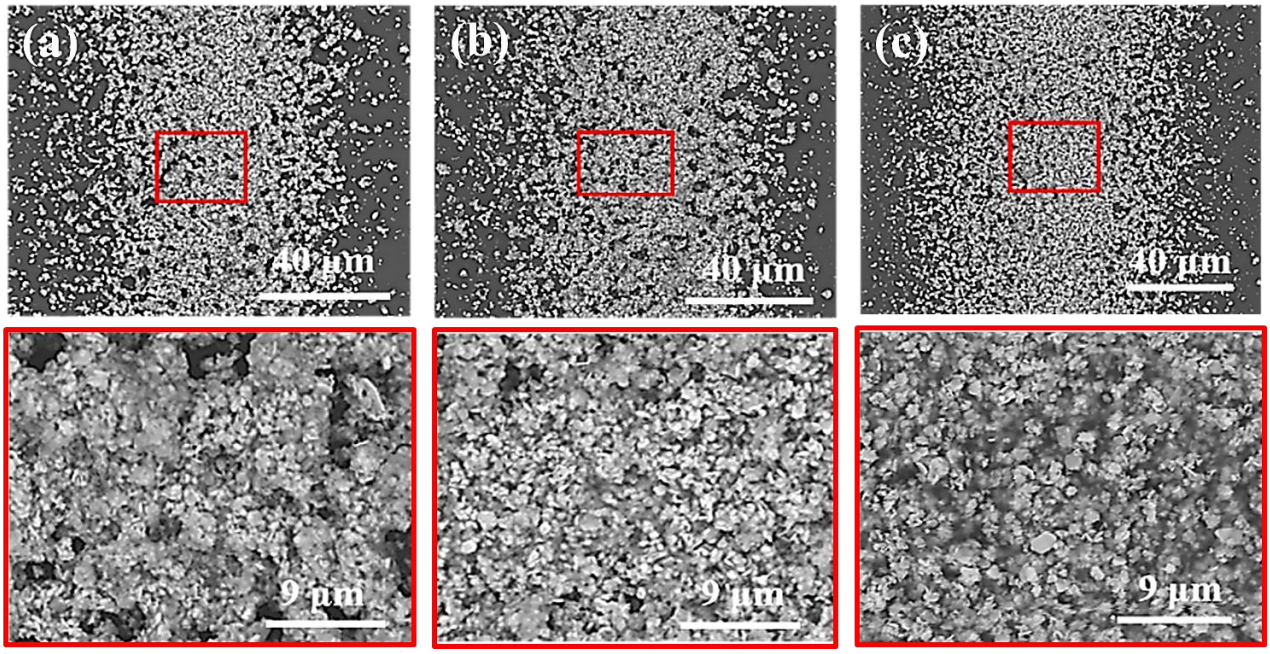

Figure 4.9 Morphology comparison of (a) 1-layer, (b) 5-layer, and (c) 10-layer printed PEDOT:PSS-based nanocomposites loaded with 10 wt.% (nominal) Sb_2Te_3 nanoflakes.

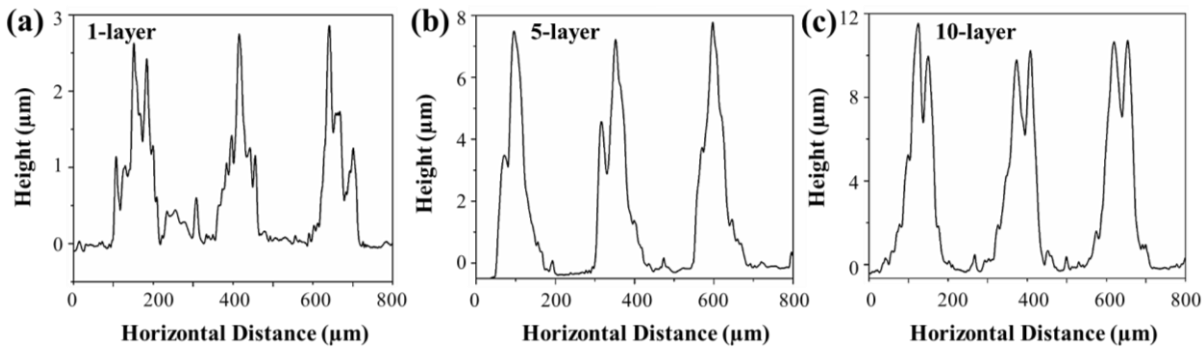

Figure 4.10 Profilometer thickness measurements of (a) 1-layer, (b) 5-layer, and (c) 10-layer printed PEDOT:PSS-based nanocomposites loaded with 10 wt.% (nominal) Sb_2Te_3 nanoflakes.

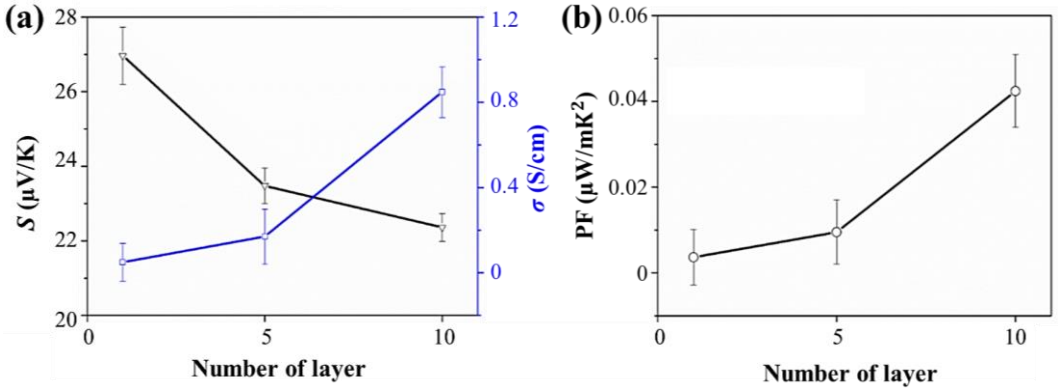

Figure 4.11 Thermoelectric measurements on (a) S, σ, and (b) PF of different printed layers of PEDOT:PSS-based nanocomposites loaded with 10 wt.% (nominal) Sb_2Te_3 nanoflakes.

As shown in the SEM micrographs in Figure 4.12, wider and thicker printed structures with denser packing of particles were seen with increasing loaded wt.% of Bi_2Te_3 or Sb_2Te_3, but there still existed some visible pores on the surface. Both of their width and thickness values peaked at 30 wt.%, as presented in Figure 4.13, indicating that more material was deposited. However, owing to the substantially low amount of PEDOT:PSS polymer within the blended ink, the matrix materials were mostly formed of Sb_2Te_3 nanoflakes instead, and there was only a small amount of PEDOT:PSS films coating on the surface of deposited particles after being cured. Due to the lack of forming a 3D conducting network and the remarkably high contact resistance introduced at the interfaces, substantially low σ and PF values were obtained in these nanocomposite structures, although their S values gradually increased with increasing loaded wt.% of Sb_2Te_3, as summarised in Figure 4.14. In this conventional printing method, since the inorganic and organic components were simply blended into an ink solution for the printing, it was difficult to confirm the actual loading wt.% of Sb_2Te_3 particles within the formed

nanocomposite structures. Therefore, the nominal loaded wt.% discussed here represented the nominal loaded wt.% of inorganic particles within the blended ink solution rather than within the formed nanocomposite structures. As a result, the actual loaded wt.% of inorganic particles within the nanocomposites should be much higher than those nominal values owing to the very small amount of PEDOT:PSS polymer added into the mixed ink.

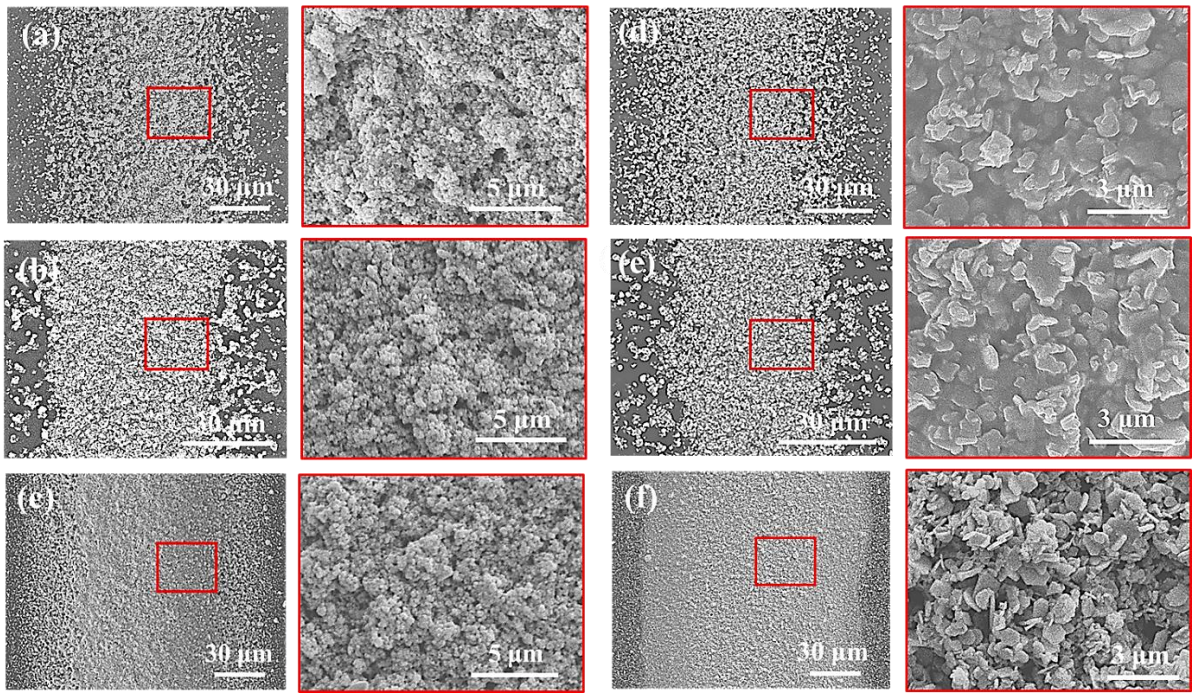

Figure 4.12 Morphology and microstructure comparisons of 10-layer printed PEDOT:PSS-based nanocomposites loaded with different nominal wt.% of Bi_2Te_3 nanoparticles from (a) 10 wt.%, (b) 20 wt.%, to (c) 30 wt.%, and with different nominal wt.% of Sb_2Te_3 nanoflakes from (d) 10 wt.%, (e) 20 wt.%, to (f) 30 wt.%, respectively.

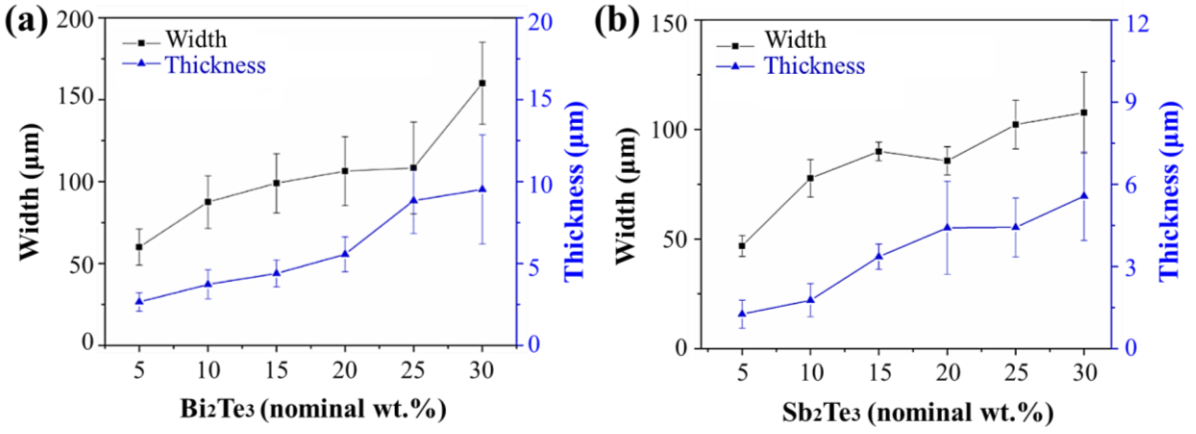

Figure 4.13 Width and thickness measurements of 10-layer printed PEDOT:PSS-based nanocomposites loaded with different nominal wt.% of (a) Bi_2Te_3 and (b) Sb_2Te_3, respectively.

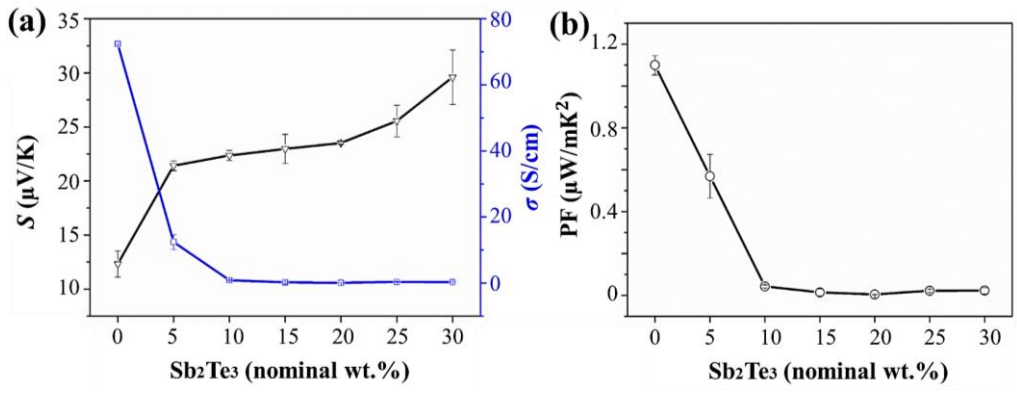

Figure 4.14 Thermoelectric measurements on (a) *S*, σ, and (b) PF of 10-layer printed PEDOT:PSS-based nanocomposites loaded with different nominal wt.% of Sb_2Te_3 nanoflakes.

Due to the time-consuming nature and the low yield of the solvothermal synthesis method, hand-ground or ball-milled Bi_2Te_3 and Sb_2Te_3 powders were also tried as substitutes for the investigation of producing flexible TEGs at a large scale, but at the expense of some TE performance. As shown in Appendix A.6, hand-ground submicron-size Sb_2Te_3 particles were employed for printing nanocomposite structures. Since the same printing conditions were applied, their printing quality was quite similar to that of solvothermal-synthesised counterparts. Nonetheless, some large chunks of particles were seen within these nanocomposites, which substantially deteriorated their TE performance. Moreover, since the commercially purchased Bi_2Te_3 particles used in this project were intrinsically *n*-type, they led to the cancellation of charge carriers with the *p*-type PEDOT:PSS polymer and resulted in a fairly low *S* value. Thus, they were not discussed in this project. Cheap but insulating polymer PVDF was also used here as the polymeric matrix for the comparison with PEDOT:PSS. As presented in Appendix A.7, different printed layers of PVDF-based nanocomposites loaded with 10 wt.% (nominal) Sb_2Te_3 nanoflakes were successfully printed on a flexible PI substrate by the AJP method. Similar to the PEDOT:PSS-based nanocomposites, thicker and denser packing of loaded particles were observed with few noticeable pores formed. Nevertheless, these PVDF-based nanocomposites were too insulating to measure their *S* and σ. 30 wt.% of Ag ink was added for the sake of converting these insulating PVDF-based nanocomposites into conductors through forming a 3D conducting network. However, they still retained highly insulating behaviour. No more Ag ink could be added further due to the considerably high cost of Ag ink.

4.5 Novel Composite Printing

4.5.1 In situ Mixing Method

As schematically depicted in Figure 4.15 (a), an innovative *in situ* mixing method for printing nanocomposite structures was developed by varying the ratio between the organic polymer ink and inorganic nanoparticulate ink in a controlled fashion during the mixing stage of the AJP process. Two different inks were simultaneously atomised via both the pneumatic atomiser (PA) and ultrasonic atomiser (UA) through the capillary action-assisted spraying and ultrasonic agitation, respectively. Generally, the UA is used in case of very low quantity of low viscous ink material, whereas the PA can be applied for a much broader range of ink viscosities. The PA can magnetically stir the ink mixture during the printing process, allowing better atomisation of the ink that has non-homogeneously suspended particles within the dispersion medium. Since two different ink materials are kept and atomised in two separate ink-containers and only the aerosols generated from the atomisation process are carried down through ink-carrying tubes, it is also feasible to use two different dispersion or solvent media (which might differ vastly in terms of properties, such as miscibility, boiling point, and chemical inertness) to form a stable dispersion for printing. More importantly, this separation of the inks at the source allows the inks to be kept at two different temperatures for the purposes of stability. The flow rate of inks from two separate atomisers can also be individually and independently controlled, allowing fine-tuning of the composition of materials being printed.

In this work, 2 mL of commercially purchased aqueous PEDOT:PSS (1 wt.%) was used with the addition of 5 wt.% EG via the UA. For the ink of the PA, the solvothermal-synthesised Bi_2Te_3 or Sb_2Te_3 nanocrystals were dispersed within DI water (20 mL) with the loading ratio of 1 wt.% and 10 wt.%, respectively, for nanocomposite printing later. They were stirred continuously throughout the printing to ensure the homogeneous suspension form. Subsequently, two different atomised aerosol droplets were *in situ* mixed within a commercially available Y-shaped junction or through a home-made T-shaped junction to form

the desired composition of the nanocomposite. This inset allowed the pre-mixing of aerosol droplets atomised from separate ink sources with an independently controllable feeding rate of each ink atomiser. During the printing process, different values of the atomisation flow rate were applied to obtain different loading ratios of Bi_2Te_3 or Sb_2Te_3 nanocrystals within the formed organic-inorganic nanocomposites (varying from 0 to 100 wt.%). It should be noted that the weight percentage (wt.%) discussed in this section represents the weight ratio of the loaded inorganic inclusions to the formed nanocomposites. Additionally, an overflow trap was installed with the ink-carrying tube to facilitate better mixing of different inks, as well as to capture the overflow of aerosol droplets with the prolonged printing process. The mixed aerosol droplets were further carried by the nitrogen gas to the deposition head, and then directly deposited on a flexible PI substrate that was kept at the temperature of 60 °C to avoid the overspray issue. There was no evidence of having any chemical reactions upon *in situ* mixing and/or printing on the polymeric substrate, according to the SEM images of AJ-printed nanocomposites. Finally, these AJ-printed samples were oven-cured at 130 °C for 2 hours and surface-treated with different solvents, as elaborated in Section 3.5. The mechanical flexibility and robustness of these AJ-printed nanocomposites were realised by using a novel meandering geometrical architecture, as shown in Figures 4.15 (b) and (c), while the PI substrate provided both flexibility and thermal stability at temperatures up to 400 °C. The optimum printing conditions for these Bi_2Te_3/Sb_2Te_3-based nanocomposites, e.g. ink formulation, atomisation conditions, substrate temperatures, curing conditions, to name a few, were summarised in Table 4-3. It should be noted that the optimum printing conditions discussed here mean the printing conditions that can produce the best printed line morphology and printing quality. Some preliminary printing tests have also been done to understand better how these parameters influence the printing process and the material deposition quality, as will be further discussed below.

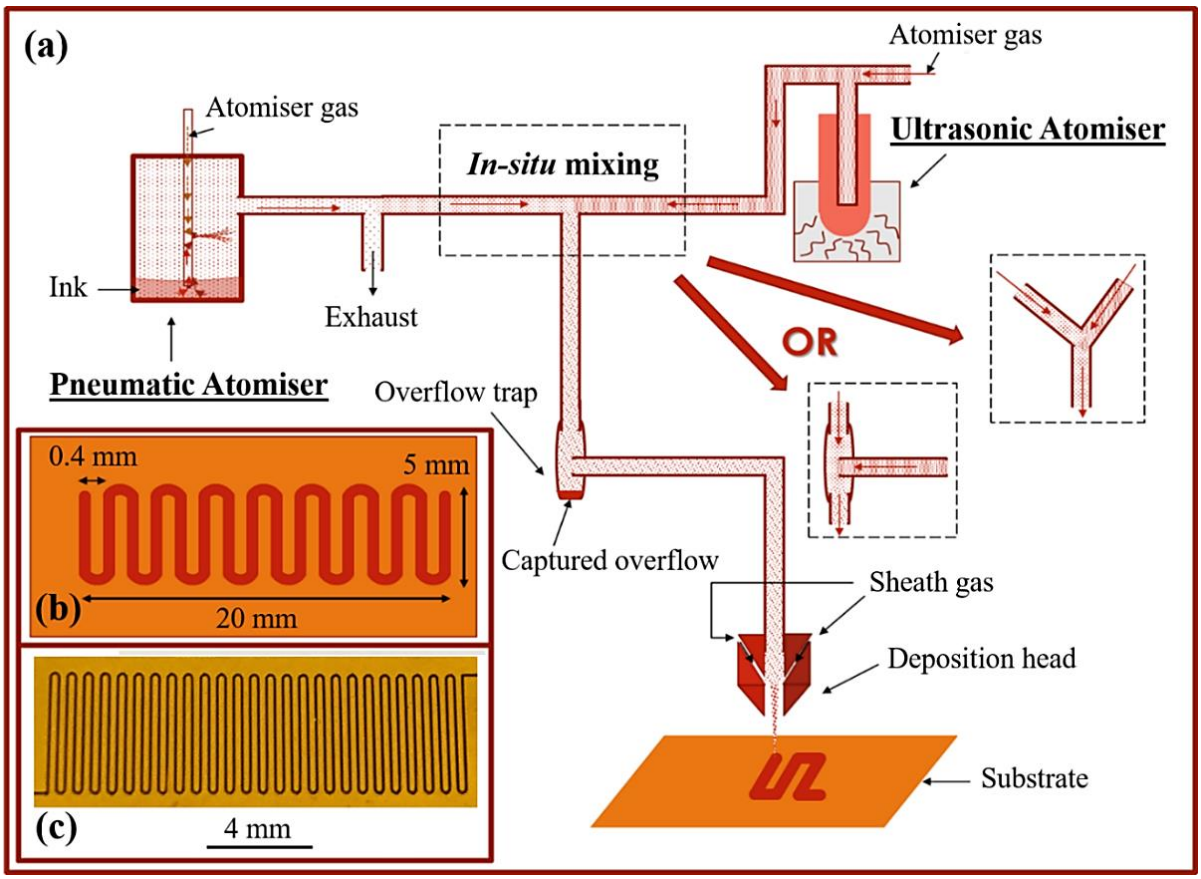

Figure 4.15 (a) Schematic illustration of the AJP setup and the printing process, where the *in situ* mixing method is also depicted. (b) Diagram of the printing pattern design. (c) A representative photograph of the AJ-printed TE nanocomposite on a flexible PI sheet.

Table 4-3 Optimum printing conditions for different Bi_2Te_3/Sb_2Te_3-based samples in this study.

Sample	Pneumatic Atomiser (PA)	Ultrasonic Atomiser (UA)
PEDOT:PSS	N/A	Ink: PEDOT:PSS Q_{sh}: 150, Q_{atm}: 50
PEDOT:PSS + Bi_2Te_3	Ink: Bi_2Te_3 Q_{sh}: 150, Q_{atm}: 550, Q_{exh}: 500-540	Ink: PEDOT:PSS Q_{sh}: 150, Q_{atm}: 50
PEDOT:PSS + Sb_2Te_3	Ink: Sb_2Te_3 Q_{sh}: 150, Q_{atm}: 550, Q_{exh}: 500-540	Ink: PEDOT:PSS Q_{sh}: 150, Q_{atm}: 50
Bi_2Te_3	Ink: Bi_2Te_3 Q_{sh}: 150, Q_{atm}: 550, Q_{exh}: 500-540	N/A
Sb_2Te_3	Ink: Sb_2Te_3 Q_{sh}: 150, Q_{atm}: 550, Q_{exh}: 500	N/A

Note: Q_{sh} = sheath gas flow rate, Q_{atm} = atomiser gas flow rate, and Q_{exh} = exhaust gas flow rate. All these parameters are with the flow unit of [cm^3/min].[138]

4.5.2 Transporting Process Modification

As mentioned above, since both inks used in this work were water-based, the atomised fine droplets were prone to converging within the mist tube and forming large droplets. As the printing process proceeded with time, some aerosol droplets impinged on the wall of the mist tube during the transporting process, thereby resulting in the increment of humidity within the plastic tube. The overspray phenomena occurred as presented in Figure 4.16, where the deposited aerosol droplets were deviated from the centre of gas flow, leading to the overspray of printed line with broad and ill-defined 'fuzzy' line edges.[138] The overspray phenomenon in the 1-layer printed nanocomposite was not very visible. However, when it came to multilayer printing, the overspray issue became more evident with increasing number of printed layers. This could be attributed to the fact that the newly printed layer was still quite wet when building up the subsequent layer on top, causing this non-uniform profile and overspray issue. Moreover, this issue was more prominent at the corners, as the printing speed was slightly slowed down, thereby depositing more ink material.

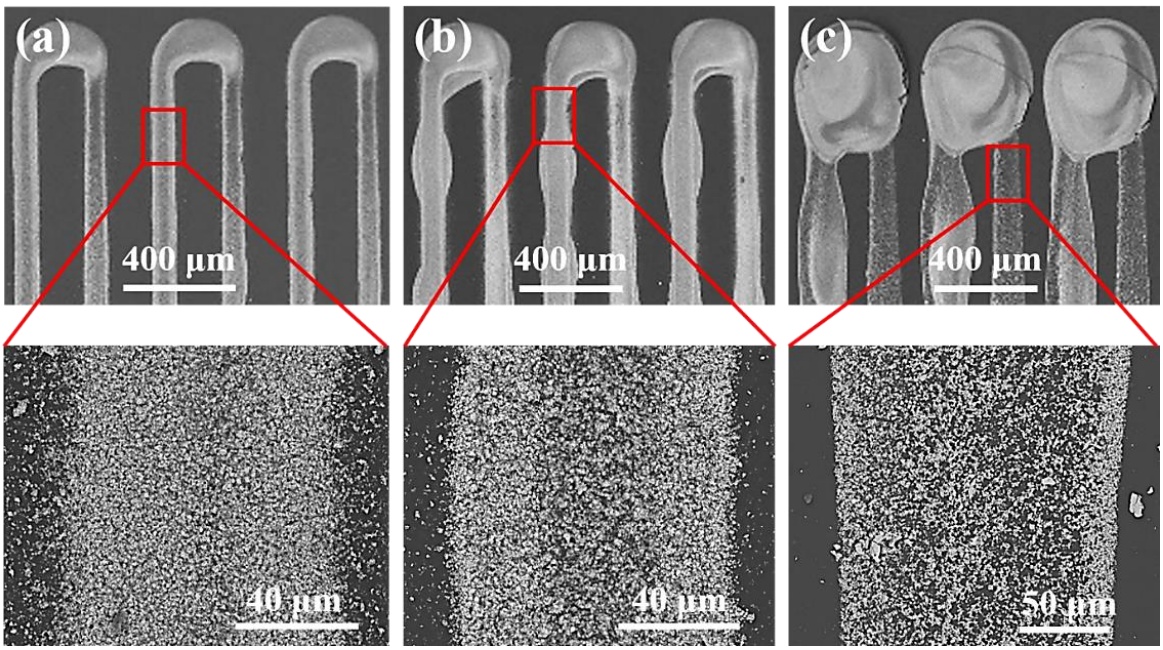

Figure 4.16 SEM images presenting the overspray phenomena occurred in (a) 1-layer, (b) 5-layer, and (c) 10-layer printed PEDOT:PSS-based nanocomposites loaded with 10 wt.% (nominal) Sb_2Te_3 nanoflakes.

In order to address this problem, a modification on the ink-carrying tube was done, as illustrated in Figure 4.17. The straight plastic tube was replaced by a custom-made overflow trap that was redesigned from a plastic pipette into a 'buffer container'. This modified overflow trap could capture and store the excess aerosol droplets to prevent them from merging into huge blobs of droplets that could otherwise flood the tip, clog the deposition head, or even ruin the as-printed patterns. It could also facilitate better control of the printing quality with prolonged printing process. Consequently, as shown in Figure 4.18, well-defined and uniform lines were achieved when being deposited into different printed layers. These optimised printing conditions were applied in the subsequent nanocomposite printing.

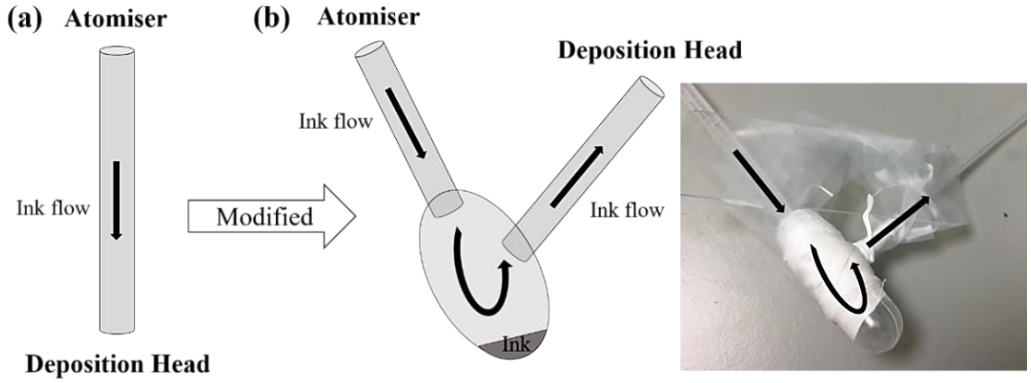

Figure 4.17 Schematic of the plastic tube used for transporting aerosol droplets from the atomiser to the deposition print head, (a) before and (b) after modifying the way of transporting aerosol droplets, with an installed overflow trap. The arrows indicate the direction of ink flow.

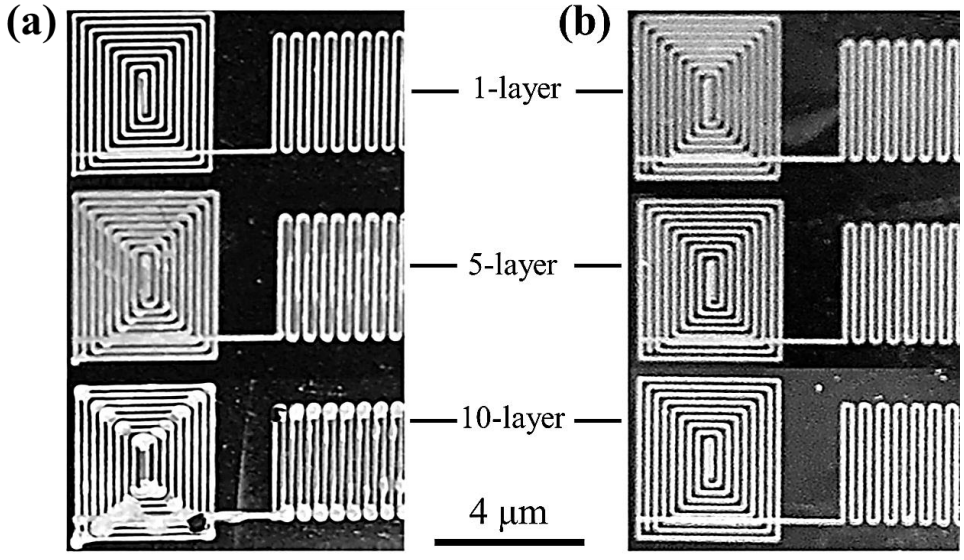

Figure 4.18 SEM images comparing (a) overspray and (b) fine feature of 1-layer, 5-layer, and 10-layer printed PEDOT:PSS-based nanocomposites loaded with 10 wt.% Sb_2Te_3 nanoflakes.

4.5.3 Comparison of Printed Layers

For the investigation of the printed line quality, 85 wt.% (nominal) Sb_2Te_3 nanoflakes were chosen here to be printed into 1, 5, and 10 layers for more detailed comparison. Similar to the previously discussed results in Section 4.4, denser and more uniform nanocomposite structures with fewer noticeable pores and/or cracks on the surface were obtained with increasing number of printed layers, leading to homogeneous printed structures of thicknesses ranging at c.a. 1-3 µm and widths ranging at c.a. 100-150 µm, as shown in Figures 4.19 and 4.20. The reproducibility of these AJ-printed nanocomposites was assessed on at least four different samples that were fabricated under the same printing conditions. As can be seen in Figure 4.21, their σ, S, and PF values increased with increasing number of printed layers, which might be attributed to the formation of denser nanocomposite structures. Considering the printing process time and the obtained TE properties, 5-layer printing was chosen as the optimum condition for the subsequent investigation of AJ-printed nanocomposites.

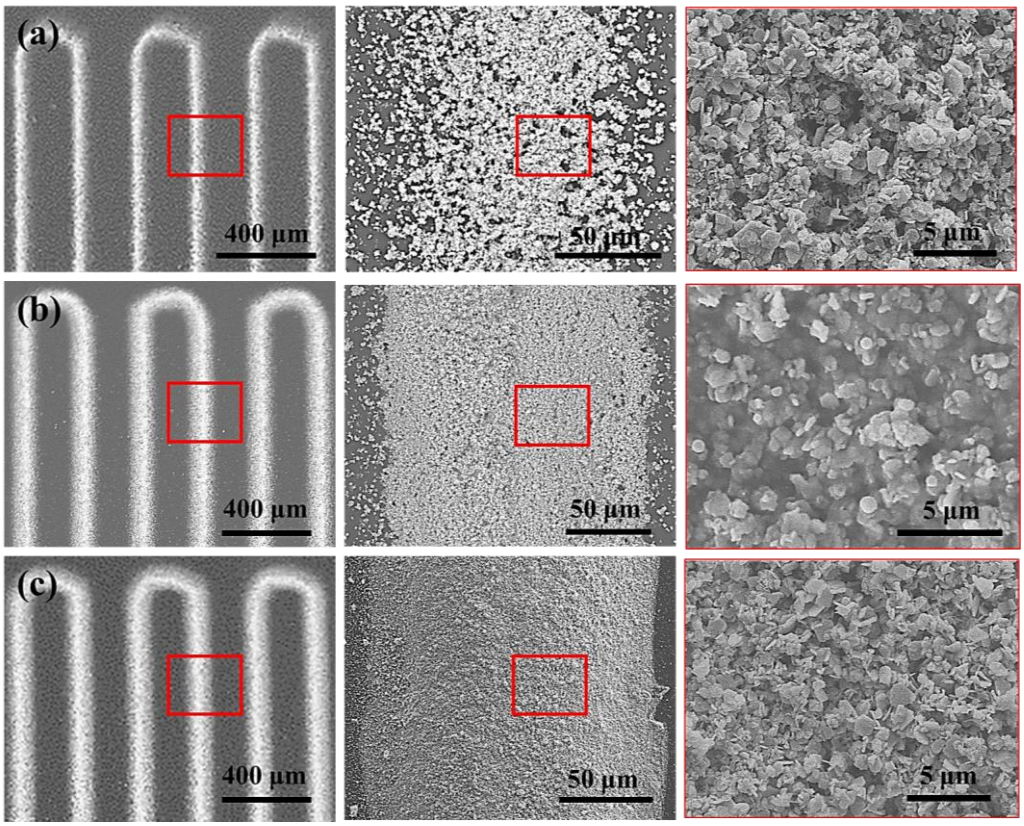

Figure 4.19 Morphology comparison of (a) 1-layer, (b) 5-layer, and (c) 10-layer printed PEDOT:PSS-based nanocomposites loaded with 85 wt.% (nominal) Sb_2Te_3 nanoflakes.

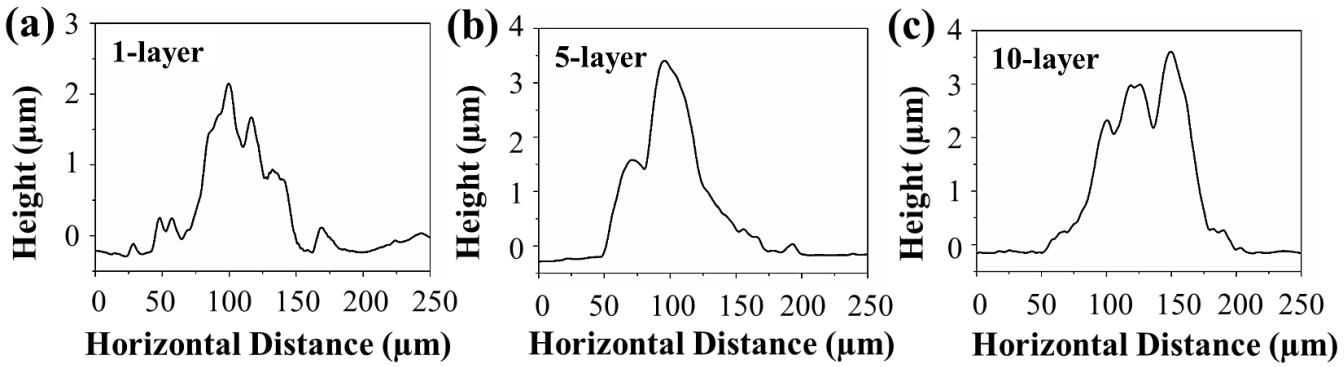

Figure 4.20 Profilometer thickness measurement of (a) 1-layer, (b) 5-layer, and (c) 10-layer printed PEDOT:PSS-based nanocomposites loaded with 85 wt.% (nominal) Sb_2Te_3 nanoflakes.

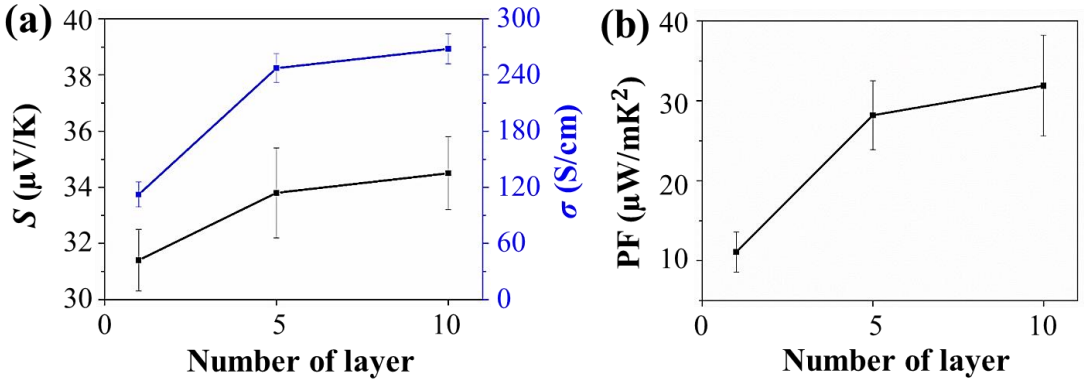

Figure 4.21 Thermoelectric measurements on (a) S, σ, and (b) PF of different layers printed PEDOT:PSS-based nanocomposites loaded with 85 wt.% (nominal) Sb_2Te_3 nanoflakes.

4.5.4 Morphology Characterisation of Printed Nanocomposites

With the aid of the novel *in situ* mixing method (see Figure 4.22 (a)), different loading ratios of solvothermal-synthesised Bi_2Te_3 nanoparticles or Sb_2Te_3 nanoflakes, ranging from 0 to 100 wt.% (nominal), were embedded within the PEDOT:PSS matrix, respectively, to ascertain the effect of these inorganic nano-fillers on the TE properties of AJ-printed PEDOT:PSS-based nanocomposites. The top surfaces of these AJ-printed nanocomposites, prior to the surface treatment, were studied by SEM. A distinct microstructural differentiation was seen in the images of nanocomposites compared to the pristine PEDOT:PSS film. The surface morphologies of two representative AJ-printed nanocomposite structures were displayed in Figures 4.22 (b) and (c), respectively, revealing uniformly distributed and

embedded Bi_2Te_3 or Sb_2Te_3 nanocrystals within the PEDOT:PSS polymer matrix. These nanocomposites displayed the close-packed microstructure and 3D conducting network with little clumping as well as improved mechanical strength, which were consistent across all different compositions studied (see Figures 4.23 and 4.24). A trend towards denser and more compact nanocomposite structure, as well as thicker and wider printed lines, was observed with increasing wt.% of the loaded nano-inclusions, as presented in Figure 4.25. Although some isolated nanocrystals were seen, especially in higher-wt.% nanocomposites, phase-segregated components were not found here, which proved the advantage of the *in situ* mixing method.

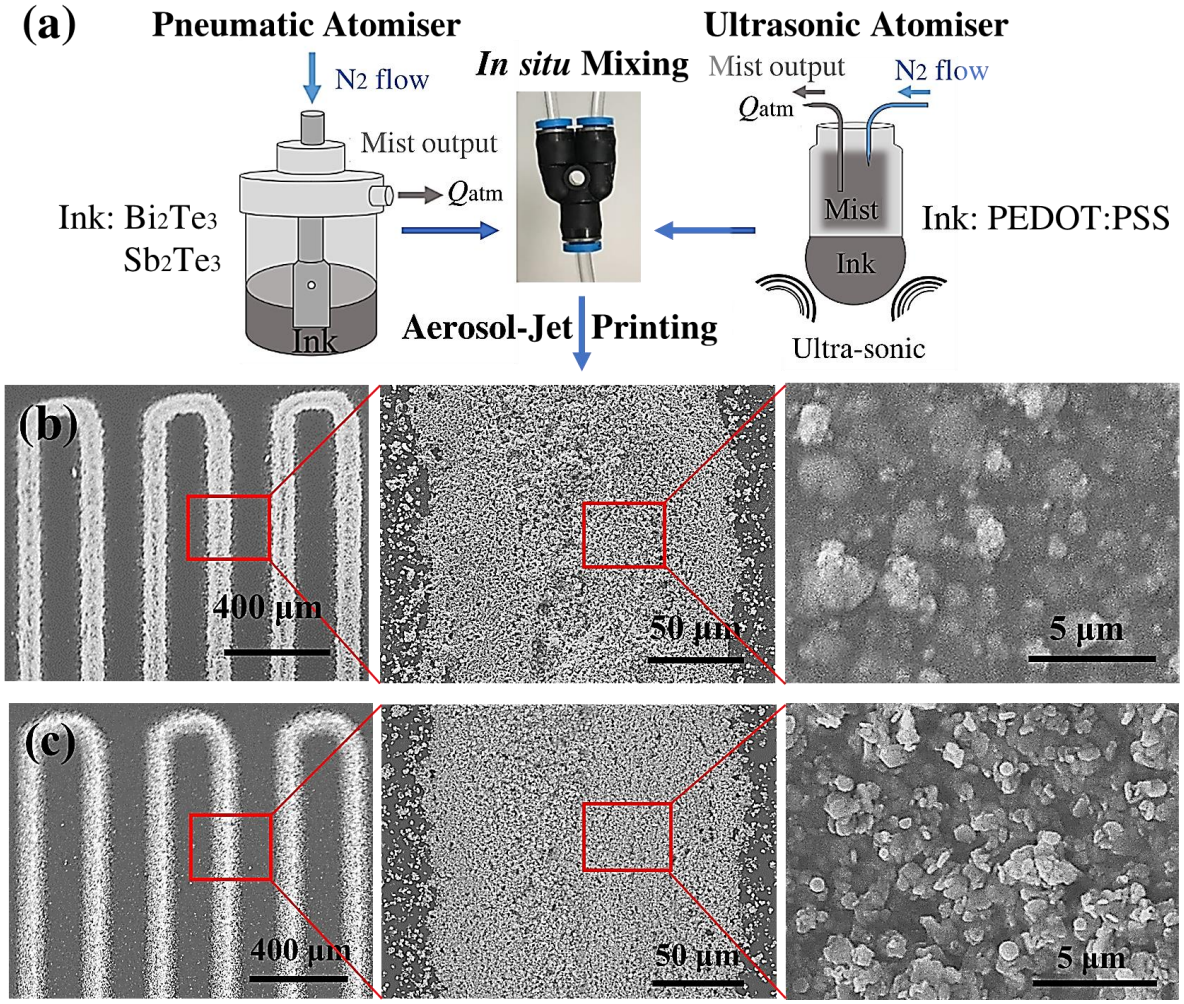

Figure 4.22 (a) Schematic of a novel *in situ* mixing method for the nanocomposite printing via the AJP method. SEM images of 5-layer printed PEDOT:PSS-based nanocomposites loaded with (b) 50 wt.% (nominal) Bi_2Te_3 nanoparticles and (c) 85 wt.% (nominal) Sb_2Te_3 nanoflakes, where the enlarged images show more details of their morphology and microstructure. (Figures taken from the author's work [25]. (CC-BY))

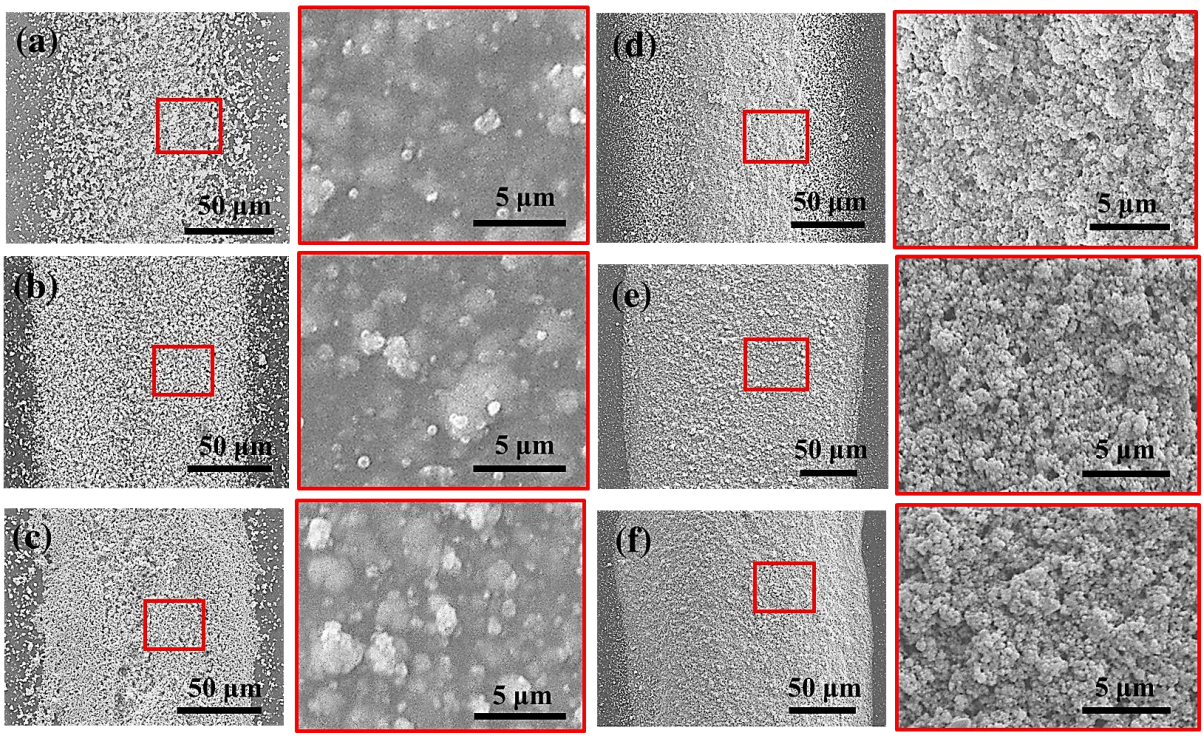

Figure 4.23 Morphology and microstructure comparisons of 5-layer AJ-printed PEDOT:PSS-based nanocomposites loaded with various nominal wt.% of Bi_2Te_3 nanoparticles from (a) 15 wt.%, (b) 35 wt.%, (c) 50 wt.%, (d) 65 wt.%, (e) 85 wt.%, to (f) 90 wt.%.

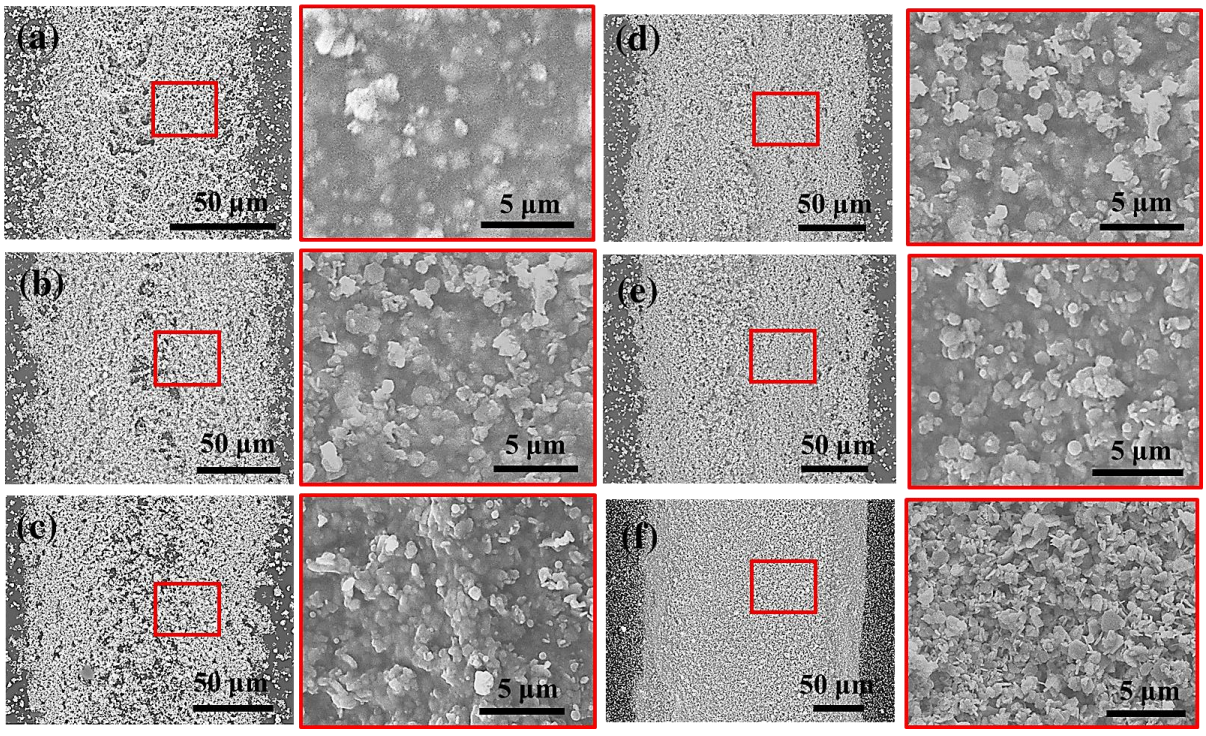

Figure 4.24 Morphology and microstructure comparisons of 5-layer AJ-printed PEDOT:PSS-based nanocomposites loaded with various nominal wt.% of Sb_2Te_3 nanoflakes from (a) 15 wt.%, (b) 35 wt.%, (c) 50 wt.%, (d) 65 wt.%, (e) 85 wt.%, to (f) 90 wt.%.

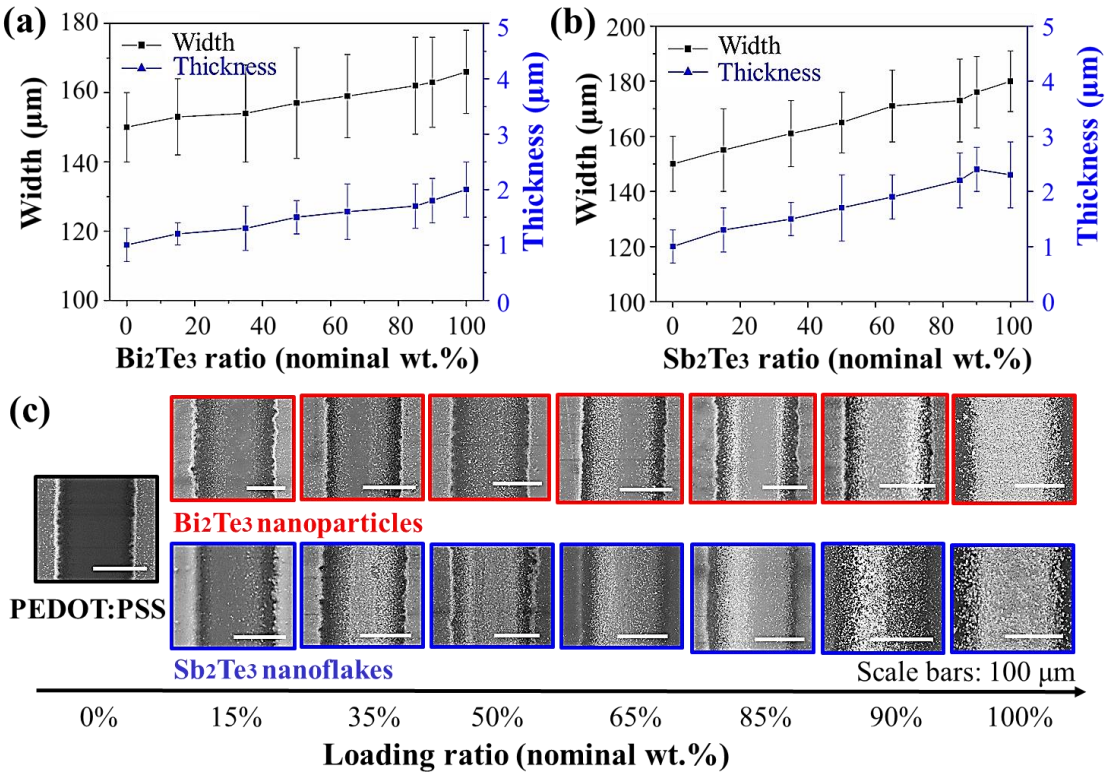

Figure 4.25 Width and thickness measurements of 5-layer printed PEDOT:PSS-based nanocomposites loaded with different wt.% of (a) Bi_2Te_3 nanoparticles and (b) Sb_2Te_3 nanoflakes, respectively. (c) Morphology comparison of 5-layer printed nanocomposites with different loading ratios of Bi_2Te_3 nanoparticles and Sb_2Te_3 nanoflakes, respectively.

4.5.5 Thermoelectric Measurements of Printed Nanocomposites

As investigated in Section 4.3, since the EG-treated PEDOT:PSS sample with 5-layer printing delivered the highest σ and PF values, EG solvent was chosen for all the subsequent surface treatments of AJ-printed nanocomposites. Figure 4.26 compares the TE properties of different AJ-printed PEDOT:PSS-based nanocomposites (both treated with EG and non-treated), which were measured by using the bespoke TE measurement setup described in Section 3.7.1. It can be seen that the EG surface treatment on all these PEDOT:PSS-based nanocomposites improved the σ value in particular, and was thus essential to enhance their overall TE properties. It was found that the S value increased with increasing loading ratio of Bi_2Te_3 or Sb_2Te_3, while the σ value slightly diminished on average, which might be attributed to the contact resistance at the interfaces between Bi_2Te_3 or Sb_2Te_3 nanocrystals and the PEDOT:PSS matrix. If both components are either *n*-type or *p*-type, they work synergistically

to enhance *S*. However, if both components present opposing carrier types, the final TE performance of the nanocomposite would depend on the relative ratio of the constituents.[19,92] In this case, the *S* values of both Bi_2Te_3-loaded nanocomposites and Sb_2Te_3-loaded nanocomposites largely increased with increasing loading ratio, and peaked at ~36.6 μV/K and ~33.8 μV/K, respectively, compared to that of the pristine PEDOT:PSS film with *S* of ~17.1 μV/K. The Hall-effect measurement also confirmed that both the solvothermal-synthesised Bi_2Te_3 nanoparticles and Sb_2Te_3 nanoflakes exhibited *p*-type charge carrier behaviour that matched well with the EDX results in Figure 4.3. From these measurements, the fact that the σ value of these nanocomposites slightly deteriorated with increasing loading wt.% while *S* was largely enhanced and retained at a comparatively high level, suggests that *S* and σ could be effectively decoupled to maximise the final PF. The actual variation of σ with composition is, in reality, more complex. A hypothesis was proposed here to explain the trend of σ. For the low loading wt.%, the introduction of organic-inorganic interfaces might lead to a decrease in σ. With increasing loading wt.%, the aggregation of inorganic nano-inclusions into a continuous 3D conducting network might facilitate the electron transport between embedded particles and the PEDOT:PSS matrix, thereby initially increasing σ slightly. However, continued aggregation might lead to the nanocomposite being inorganic-dominated, with a higher proportion of loaded particles not electrically connected by the PEDOT:PSS matrix. This thus might result in a drop in σ at the highest loading wt.% due to the large increment of inorganic-inorganic interface resistance. The trend of this variation was slightly different for Bi_2Te_3-based and Sb_2Te_3-based nanocomposites owing to the inherently different nanocrystal sizes and morphologies (nanoparticles vs. nanoflakes), which gave rise to different aggregation characteristics. The particles were prone to agglomeration, especially in the case of nanoparticles. In general, it was found that these AJ-printed nanocomposites were stable under ambient conditions over several weeks of testing. The best TE performance of these AJ-printed nanocomposites was achieved at 85 wt.% Sb_2Te_3, with *S* of ~33.8 μV/K, σ of ~247.3 S/cm, PF of ~28.3 μW/(m.K^2), and charge carrier density of ~10^{22} m^{-3}, which is comparable to what has been reported in the literature.[18,19,32,232,242] It should be noted that these results were obtained from a different

PEDOT:PSS starting material, which has been shown to have vastly superior σ compared to PEDOT:PSS from other vendors, as summarised in Table 4-1. The 100 wt.% samples referred to aqueous dispersions of Bi_2Te_3 or Sb_2Te_3 AJ-printed into dense films without the presence of the PEDOT:PSS matrix, as discussed in Section 4.2. The TE properties of these samples were found to be far inferior to the nanocomposite structures, which is attributed to the comparatively poor connectivity between nanocrystals in the absence of the PEDOT:PSS matrix. Their connectivity could have been improved by sintering at elevated temperatures, but this was avoided owing to the presence of the flexible plastic substrate.

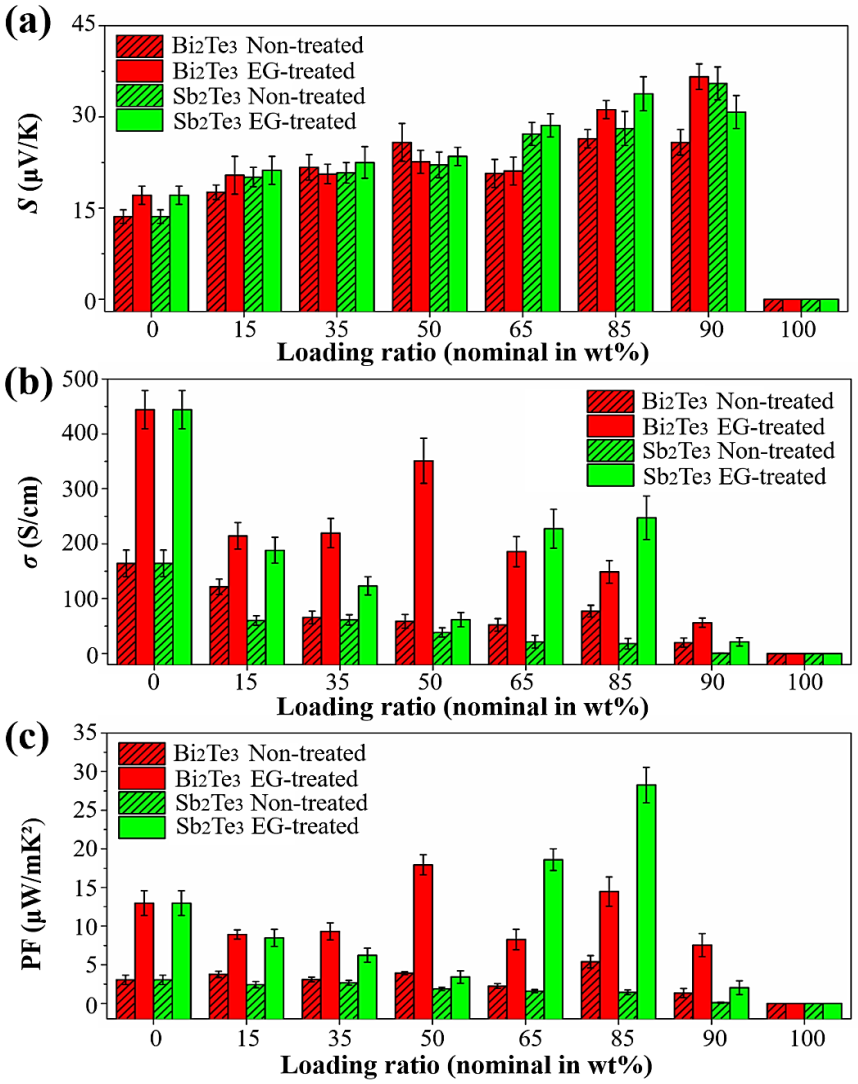

Figure 4.26 Thermoelectric measurements on (a) *S*, (b) σ, and (c) PF of non-treated and EG-treated 5-layer printed PEDOT:PSS-based nanocomposites loaded with different wt.% of Bi_2Te_3 nanoparticles and Sb_2Te_3 nanoflakes, respectively. Error bars indicate the standard deviation of the measured values of two separate nanocomposites with the same loading ratio.

4.5.6 Simulation of Printed Nanocomposites

Finite element analysis based on COMSOL Multiphysics simulation was performed to simulate the effect of an imposed ΔT across the AJ-printed TE nanocomposite, as shown in Figure 4.27. This simulation yielded a good match with the above TE measurement results. Figure 4.27 (a) illustrates that the temperatures at the top and the base of the model were set to 320 K and 260 K, respectively, to have a ΔT of 60 K. An open-circuit voltage output of ~2 mV was generated across the nanocomposite (see Figure 4.27 (b)). Furthermore, the simulation of temperature and electric potential distribution of the nanocomposite at the microscale has also been conducted in Figures 4.27 (c) and (d), with the matrix set to PEDOT:PSS polymer [κ ~0.3 W/(m.K)] and in-filled spheres set to Bi_2Te_3 nanoparticles [κ ~1.2 W/(m.K)]. The particle size of embedded nanoparticle was set to ~100 nm based on the SEM result in Figure 4.3. The contour plot demonstrates that the temperature distribution to an approximation is relatively unaffected by the inclusion of nanoparticles with higher κ over the large scale of interest.

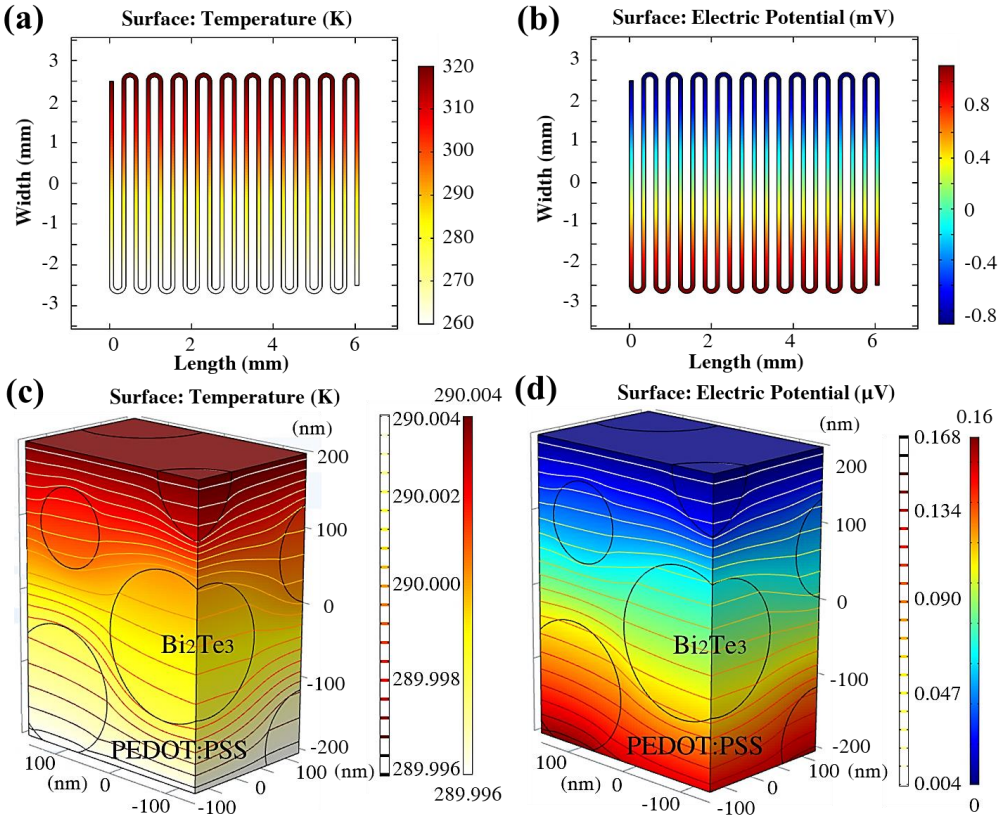

Figure 4.27 (a) Temperature profile and (b) the generated voltage of the 5-layer printed TE nanocomposite structure at the macroscale. (c) Temperature and (d) electrical potential distribution at the microscale, where the contour plot shows more details of their profiles.

4.6 Flexibility Tests

After a simple manual bending test, as previously discussed in Section 3.8.1, excellent conformability of the AJ-printed nanocomposite was observed. They retained their original shape and smooth surface without forming any visible cracks or deformations after several hand-bending cycles, and their electrical properties remained nearly the same throughout. The ratio of flat-to-flexed resistance was plotted as a function of the bending radius (mm), as shown in Figure 4.28 (a). The AJ-printed nanocomposites with relatively higher PF values were selectively compared here. The effect of flexing on *S* was also determined by measuring the *S* values of the sample before and after being flexed. Electrical resistance was selected here as the criterion to evaluate the film flexibility, as it was expectedly sensitive to any cracks or voids that might be introduced during the flexing test.[138] As the bending radius decreased, the electrical resistance of the nanocomposites slightly increased and then remained comparatively stable under very low bending radius, indicating their superior flexibility compared to their inorganic counterparts. However, for all the samples that were flex-tested, their electrical resistance values did not come back to the original values after being released, which might be ascribed to the formation of disconnects (possibly in the form of cracks) within the nanocomposite. The S/S_o ratio only decreased slightly even after being flexed to a very low bending radius (down to ~3.3 mm), which might be attributed to the formation of some micron-size cracks and/or voids within the nanocomposite structure. This result confirmed the excellent flexibility and mechanical strength of these AJ-printed nanocomposites. The overall PF of the best-performing nanocomposite structure was found to reduce by half, showing that the device was still useable as a TEG. These flexing results suggest that the novel nanocomposite structure design, comprising fine-grained nanocrystals within a ductile and flexible TE polymer that serves as a protective matrix, can offer greater mechanical support and protection while maintaining relatively good electrical conductivity between embedded TE nano-inclusions. These AJ-printed nanocomposites are therefore more flexible and robust than their bulk counterparts that are typically produced by directional solidification process.[3,5]

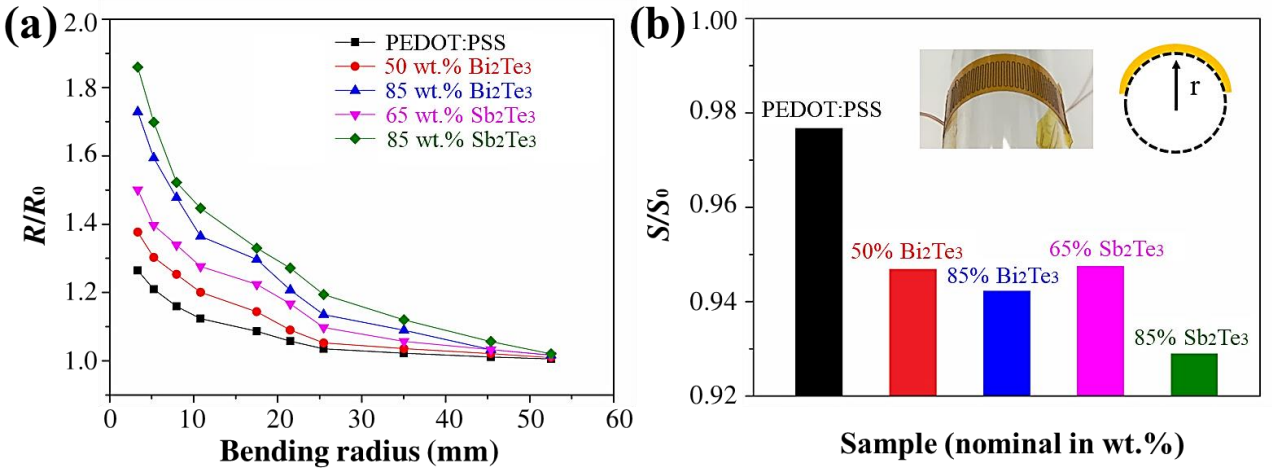

Figure 4.28 (a) Flexing test on AJ-printed PEDOT:PSS-based nanocomposites with different loading ratios of Bi_2Te_3 and Sb_2Te_3, where (a) the ratio of flat-to-flexed resistance was plotted as a function of the bending radius and (b) the ratio of flat-to-flexed Seebeck coefficient was charted as a function of the loading weight ratio. The inset demonstrates that the sample was subjected to a bending radius of 5.3 mm. (Figures taken from the author's work [25]. (CC-BY))

4.7 Flexible Thermoelectric Coasters

Notably, since the *in situ* mixing method required only fairly small amounts of both organic and inorganic constituent materials with little material wastage, these AJ-printed nanocomposites could be directly integrated into flexible TEG applications with minimal post-processing treatment. The author demonstrated this by designing a flexible AJ-printed TEG prototype in Section 3.10.1, which could be used as a flexible 'thermoelectric coaster' to convert the temperature gradient between a hot or cold source and the ambient environment into electricity. In order to demonstrate the practical TE performance of these AJ-printed TE nanocomposites, they were assembled in conjunction with an aluminium can (Coca-Cola) into a simple prototype flexible TEG, as presented in Figures 4.29 (a) and (b). To improve their overall power output, two identical AJ-printed TEGs were stacked up and electrically connected in series. A copper tape was employed as the thermally conducting medium between the hot or cold source (i.e. aluminium can) and TE legs. Subsequently, the aluminium can was filled with boiling hot water (~100 °C) to create a ΔT between the inner and outer of AJ-printed TE legs, where the ΔT was found to be ~20 °C with the aid of a compact thermal imaging

camera, as displayed in Figures 4.29 (c) and (d). It is worth mentioning that the hot water can be replaced by the cold ice water to create a temperature gradient. Also, opposite output signals were obtained when reversing the connection of the TEG to the applied ΔT direction, which confirmed that the measured output signals were generated from the thermoelectric effect. As summarised in Table 4-4, the parallel-mode TEG with 340 TE legs and a total internal sample resistance (R_S) of ~58 Ω generated an open-circuit voltage output (V_{oc}) of ~0.6 mV, a short-circuit current (I_{sc}) of ~7 μA, and a maximum power (P_{max}) of ~1.6 nW under a ΔT of ~20 °C. The series-mode TEG with 50 TE legs and R_S of ~2700 Ω produced V_{oc} of ~40 mV, I_{sc} of ~6 μA, and P_{max} of ~148.2 nW under a ΔT of ~20 °C. It was found that the series-connected mode presented much higher voltage and power output, while the parallel-connected mode gave a slightly higher current output. Importantly, these flexible AJ-printed TEGs could overcome some limitations that their rigid counterparts have, and the technical challenge of assembling many individual legs into one TEG module without using any solders could be ideally solved with the help of the versatile AJP technique. The TE performance of these AJ-printed TEGs can be further improved through stacking up several of them. Although these polymer-based TE devices can only be operated in a low-temperature environment due to the thermal stability nature of the polymer, with respect to wearable TEGs, the thermal stability is not a major issue to be considered. Furthermore, their TE performance can be further enhanced through employing other nanostructured TE materials with improved S and σ, through optimising the ink formulation and printing quality, as well as through conducting proper surface treatments on these PEDOT:PSS-based nanocomposites.

Since the dimensions of the TE leg play a significant role in the TE performance of the TEG, the voltage and power outputs as a function of the width and thickness of the TE leg are investigated in Appendix A.8. Different dimensions of AJ-printed PEDOT:PSS films were fabricated and measured to ascertain how the dimensions of the TE leg affect their voltage and power outputs. As summarised in Table A-2, the power output was directly proportional to the width and thickness, which means that the larger width and/or larger thickness of the TE leg was, the higher P_{max} could be generated from per TE leg. Since the same ΔT was applied along

the TE leg, the voltage output was nearly independent to the dimensions of the TE leg due to $\Delta V = - S \Delta T$, as expressed in Equation 2-1. As a result, the increased power output was mainly attributed to the drop of the sample resistance. According to this result, the power output of the above-discussed flexible printed TEGs can be further improved by optimising the dimensions of individual TE legs so as to achieve a lower device resistance, and thus generate a higher device power output. Therefore, the fill factor and printing process time should be considered for the geometry optimisation of each TE leg. The generated voltage can also be potentially boosted via a DC/DC voltage step-up converter to power some miniature sensors or wireless transmitters.[144]

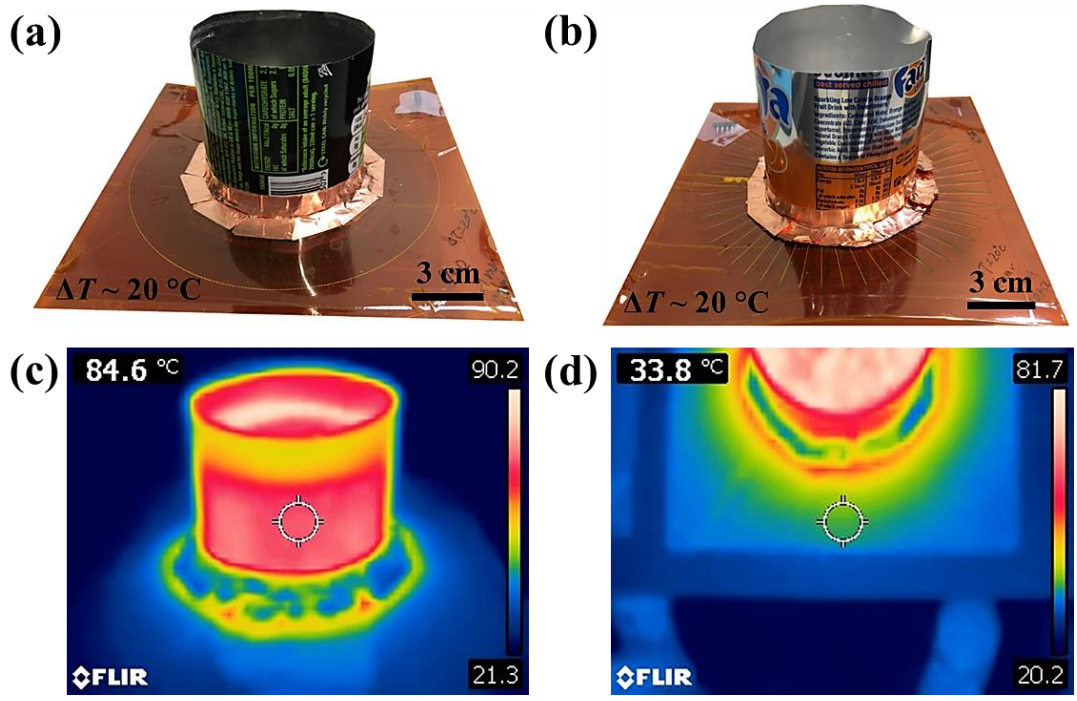

Figure 4.29 Photographic images of AJ-printed TEG prototype in (a) parallel or (b) series mode, respectively. (c) Side view and (b) top-down view of thermal images showing the temperature distribution of the TEG. The circle highlights the localised temperature reading.

Table 4-4 Measurements on the open-circuit voltage V_{oc}, short-circuit current I_{sc}, internal sample resistance R_S, and maximum power P_{max} of flexible AJ-printed TEGs operated in two different modes under a ΔT of ~20 °C.

Mode	TE leg number	V_{oc} (mV)	I_{sc} (μA)	R_S (Ω)	P_{max} (nW)
Parallel	340	0.6	7	58	1.6
Series	50	40	6	2700	148.2

4.8 Summary

To summarise, a versatile, cost-effective, and easily scalable AJP technique for depositing *p*-type PEDOT:PSS-based nanocomposites on flexible substrates has been successfully developed via the in-house high-yield and highly scalable solvothermal synthesis method for Bi_2Te_3 nanoparticles and Sb_2Te_3 nanoflakes. This low-temperature solution-based synthesis approach allowed good control of size and shape at the nanoscale, and thus enabled better control and enhancement of TE properties of the resulting PEDOT:PSS-based nanocomposite structures. Various weight percentages of solvothermal-synthesised nanostructured Bi_2Te_3 and Sb_2Te_3 particles with high S and high σ have been integrated with low-κ PEDOT:PSS conducting polymer, for printing TE nanocomposites on a cheap and flexible PI sheet via the AJP method. By properly tuning the flux ratio and flow speed by the *in situ* mixing method as well as by choosing the appropriate number of printed layers, the PEDOT:PSS-based nanocomposites could achieve excellent TE properties with reasonable mechanical flexibility and robustness. The *in situ* mixing method also opens up the possibility of using the same inks of individual constituent materials to print nanocomposite structures with various compositions. This is possible because the flow rate of inks from the two separate atomisers can be individually and independently controlled, allowing fine-tuning of the composite material being AJ-printed. Among them, the PEDOT:PSS-based nanocomposites loaded with 85 wt.% (nominal) Sb_2Te_3 nanoflakes have exhibited the best TE performance (S ~33.8 μV/K, σ ~247.3 S/cm, and PF ~28.3 μW/(m.K^2)) as well as excellent mechanical properties. The flexibility of these AJ-printed nanocomposite structures has been rigorously tested. They have shown fairly stable and robust TE performance upon repeated flexing. The demonstration of flexibility enables broader applications of these AJ-printed organic-inorganic nanocomposites.

Chapter 5

Multiwall Carbon Nanotube-based Thermoelectric Nanocomposites

This chapter discusses the results related to the flexible multiwall carbon nanotube-based TE nanocomposites fabricated by the aerosol-jet printing method. Here, commercially procured multiwall carbon nanotubes (MWCNTs) have been introduced, for the first time, into AJ-printed TE nanocomposites, by dispersing MWCNTs into DI water alongside the in-house solvothermal-synthesised Sb_2Te_3 nanoflakes. This was followed by the ink atomisation and *in situ* mixing with the PEDOT:PSS polymer into TE nanocomposites of different compositions, where the novel composite printing method developed in Chapter 4 was employed. Significant enhancement of TE properties as well as mechanical flexibility and robustness has been achieved here, even under prolonged flexing cycles and fatigue test for certain compositions. Accordingly, they could be directly incorporated into flexible or even wearable TEG applications with minimal post-processing treatment. Some parts discussed in this chapter have been published in "Enhanced Thermoelectric Properties of Flexible Aerosol-Jet Printed Carbon Nanotube-Based Nanocomposites". *APL Materials*, 2018, 6 (9), 096101,[96] and they have been adapted from that text with granted Copyright permission. It should be noted that the author performed all the experiment works and data analysis with the help of other co-authors of the paper.

5.1 Printing of Carbon Nanotube-based Nanocomposites

For the ink formulation, PEDOT:PSS and MWCNTs inks were loaded into ultrasonic atomiser and pneumatic atomiser, respectively. Solvothermal-synthesised Sb_2Te_3 nanoflakes were also added to the MWCNTs ink at the weight ratio of 1:1 (i.e. 50 wt.% Sb_2Te_3 and 50 wt.% MWCNTs for the loaded inorganic particles) to enhance the TE performance of AJ-printed nanocomposites. It is well-known that carbon nanotubes (CNTs) tend to aggregate in the form of bundles or ropes owing to their high Van der Waals attractions. Hence, surfactants are often employed to achieve the stability of CNTs suspension.[243–245] Here, 0.1 wt.% of sodium dodecyl sulphate (SDS, Sigma-Aldrich) and 0.5 wt.% of polyvinylpyrrolidone (PVP, average molecular weight 40,000, Sigma-Aldrich) were added into the MWCNTs ink, respectively, for the investigation of their influence on the formed nanocomposites. The resulting suspension was then magnetically stirred and ultrasonicated for 1 hour prior to the subsequent ink atomisation and nanocomposite printing processes. The printing conditions for different AJ-printed nanocomposite structures were adjusted so as to achieve the optimum printing quality, as summarised in Table 5-1. The meandering structure shown in Section 3.7.1 was used here as the TE device structure. These AJ-printed samples were cured at 130 °C for 2 hours.

Table 5-1 Optimum printing conditions for different MWCNTs-based samples in this study.

Sample	Pneumatic Atomiser (PA)	Ultrasonic Atomiser (UA)
PEDOT:PSS	N/A	Ink: PEDOT:PSS Q_{sh}: 150, Q_{atm}: 50
MWCNTs + PVP + SDS + PEDOT:PSS	Ink: MWCNTs Q_{sh}: 150, Q_{atm}: 550, Q_{exh}: 500-540	Ink: PEDOT:PSS Q_{sh}: 150, Q_{atm}: 50
MWCNTs + PVP + PEDOT:PSS	Ink: MWCNTs Q_{sh}: 150, Q_{atm}: 550, Q_{exh}: 500-540	Ink: PEDOT:PSS Q_{sh}: 150, Q_{atm}: 50
Sb_2Te_3 + MWCNTs + PVP + PEDOT:PSS	Ink: Sb_2Te_3 + MWCNTs Q_{sh}: 150, Q_{atm}: 550, Q_{exh}: 500-540	Ink: PEDOT:PSS Q_{sh}: 150, Q_{atm}: 50
Sb_2Te_3 + MWCNTs	Ink: Sb_2Te_3 + MWCNTs Q_{sh}: 150, Q_{atm}: 550, Q_{exh}: 500	N/A

Note: Q_{sh} = sheath gas flow rate, Q_{atm} = atomiser gas flow rate, and Q_{exh} = exhaust gas flow rate. All these parameters are with the flow unit of [cm^3/min].[138]

5.2 Influence of Surfactant Addition on Printed Nanocomposites

As reported in previous works from the literature, sodium dodecyl sulphate (SDS) and polyvinylpyrrolidone (PVP) have been mostly used as a surfactant and/or binder to disperse and stabilise CNT bundles homogenously within DI water, as well as to prevent them from agglomeration, which facilitates the formation of 3D connected networks with enhanced σ.[243–245] In this work, these two surfactants were tested for the printing of MWCNTs. However, it was found that adding SDS surfactant (0.1 wt.%) caused the generation of lots of bubbles within the pneumatic atomiser chamber during the atomisation process, which had a detrimental influence on the ink atomisation and the subsequent printing process.

Adding PVP surfactant, on the other hand, was found to have little effect on the atomisation and printing processes. Meanwhile, since the ink atomisation process itself entailed vigorous stirring and sonication, as discussed in Section 3.4, it helped to improve the homogeneous dispersion of MWCNTs significantly, without creating any bubbles during the whole AJP process. Therefore, only a fairly small amount of PVP surfactant (0.5 wt.%) was needed here. Figure 5.1 (a) illustrates the dispersion mechanism and the printing process of MWCNTs. The as-received MWCNTs bundles were suspended into the solution form with the aid of different added surfactants as well as the mechanical stirring and sonication treatments. These well-dispersed MWCNTs within the ink could significantly promote the subsequent printing process, thereby resulting in better printing quality. Figures 5.1 (b) - (g) reveal the morphology of different MWCNTs-based nanocomposites fabricated by the customised AJP technique. It can be seen that various loading wt.% of MWCNTs were homogeneously dispersed within the PEDOT:PSS matrix, without observing any agglomerations of MWCNTs. To the best knowledge of the author, no doping effect of the PVP surfactant on MWCNTs was found here.

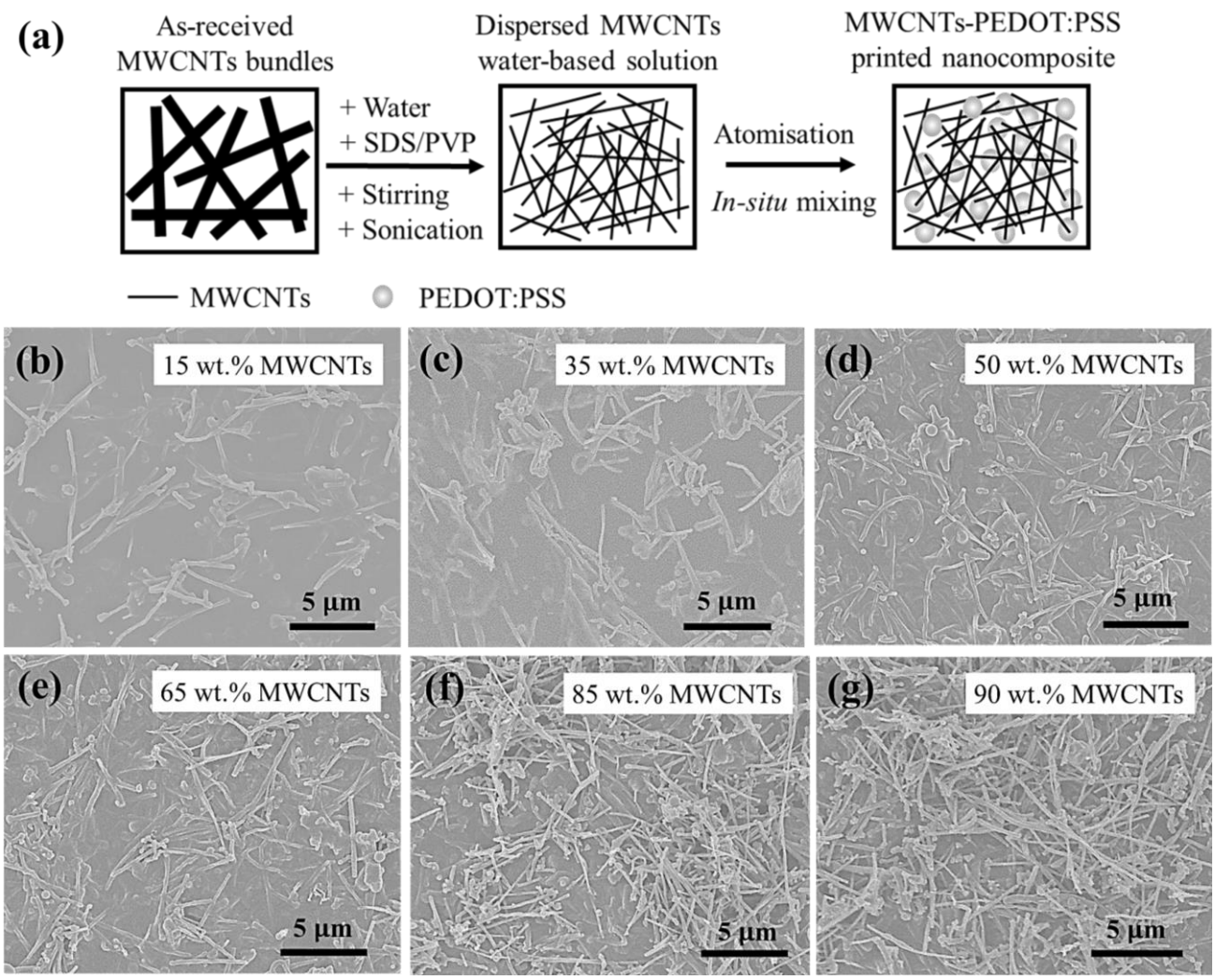

Figure 5.1 (a) Schematic describing the fabrication process of MWCNTs-PEDOT:PSS nanocomposites via the AJP technique. SEM images of AJ-printed MWCNTs-PEDOT:PSS nanocomposites with various loading ratios of MWCNTs, ranging from (b) 15 wt.%, (c) 35 wt.%, (d) 50 wt.%, up to (e) 65 wt.%, (f) 85 wt.%, up to (g) 90 wt.%.

5.3 Surface Treatment of Printed Nanocomposites

Several groups have attempted treating the deposited pristine PEDOT:PSS films by using different chemicals (e.g. polar solvents) to enhance their σ and S.[89,93,246–249] The commonly accepted mechanism explaining this chemical treatment is that the insulating PSS molecules are de-doped from the conducting PEDOT domains to obtain better electrical contacts between neighbouring PEDOT chains.[93] Importantly, CNTs can further improve σ of the PEDOT:PSS-based nanocomposites by forming continuous links between PEDOT

islands owing to their superior conductivity and by favourable π-π interactions.[88,107,108] In this context, MWCNTs were incorporated into AJ-printed MWCNTs-PEDOT:PSS nanocomposites with different loading fractions. Surface treatments with different polar solvents, including ethylene glycol (EG, 99.8%, Sigma-Aldrich),[89,93,246] dimethyl sulfoxide (DMSO, 99.9%, Sigma-Aldrich),[93,247] and glycerol (GYL, 5 vol.% aqueous solution, Sigma-Aldrich),[250] were subsequently conducted to ascertain their effect on these AJ-printed nanocomposites. The resulting TE properties were then compared in Figure 5.2. It can be seen that these surface treatments resulted in a significant improvement of σ, especially seen in the DMSO-treated samples which were found to show an increment in σ by a factor of 5 compared to the untreated samples. This therefore led to the highest PF obtained in the samples treated with DMSO. Meanwhile, it was found that the GYL-treatment caused the delamination of AJ-printed films off the substrate, and thus, this treatment was abandoned in the subsequent investigation.

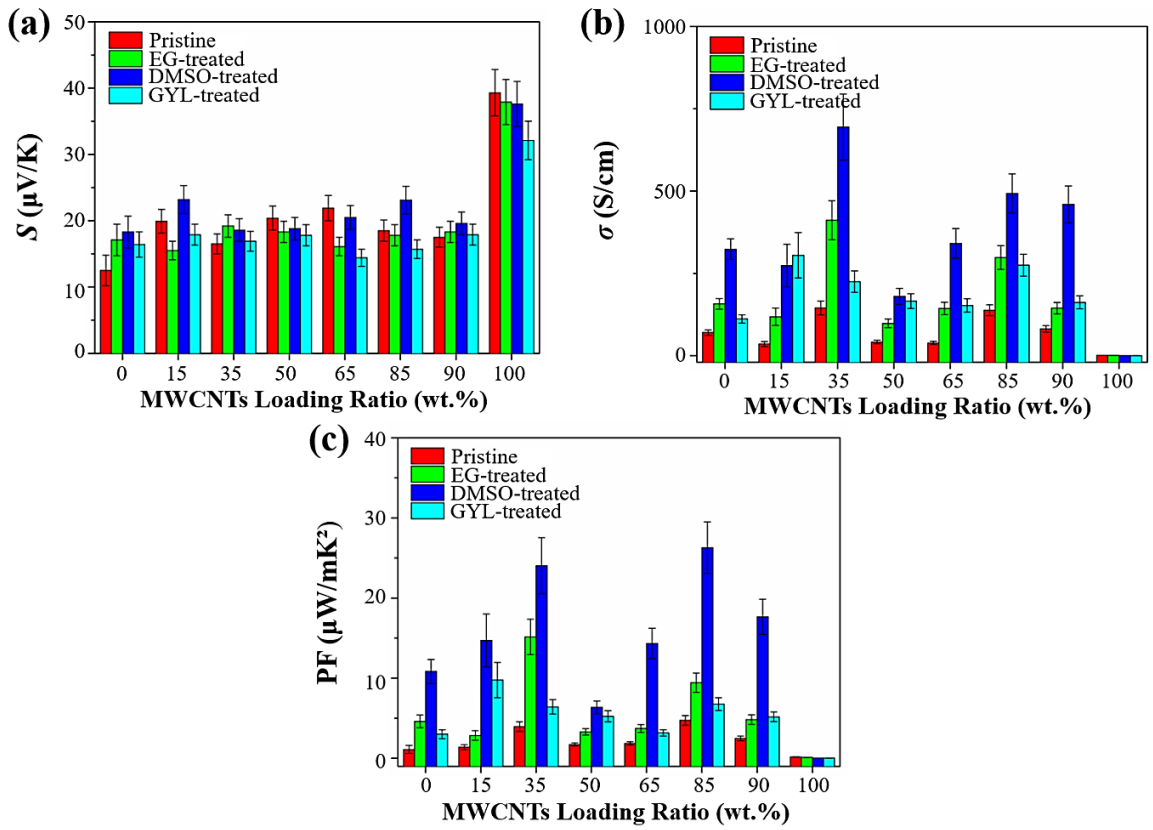

Figure 5.2 Thermoelectric measurements on (a) *S*, (b) σ and (c) PF of AJ-printed MWCNTs-PEDOT:PSS nanocomposites that were surface-treated with different polar solvents.

5.4 Morphology Characterisation of Printed Nanocomposites

Figure 5.3 (a) shows the SEM micrograph of typical MWCNTs-PEDOT:PSS nanocomposite lines fabricated by the AJP method, where the printing quality was found to be excellent with well-defined and smooth edges and surfaces, very minimal overspray, as well as an average line width of ~200 μm. A crack was formed by fracturing the AJ-printed nanocomposite to reveal more details of its morphology and microstructure, as shown in Figure 5.3 (b). Through the fracture surface, it can be seen that densely populated MWCNTs were embedded within the PEDOT:PSS matrix, which had been partially pulled out due to the cleaving process. From the high-resolution SEM images of the AJ-printed sample with 100 wt.% MWCNTs and 100 wt.% Sb_2Te_3-MWCNTs, respectively, in Figure 5.4, the diameter of these AJ-printed MWCNTs were found to be ~230 nm (± 65 nm) with a length of ~6.5 μm (± 2.3 μm). These results were in good agreement with supplier's specifications, and also confirmed that they remained intact even after the atomisation and printing processes owing to their excellent mechanical properties. Following this, Sb_2Te_3 nanoflakes were incorporated into the nanocomposites as well. Figures 5.3 (c) - (i) show the morphology of different AJ-printed Sb_2Te_3-MWCNTs-PEDOT:PSS nanocomposites loaded with various wt.% of Sb_2Te_3 nanoflakes and MWCNTs (in a 50:50 ratio), where a visibly larger amount of Sb_2Te_3 nanoflakes and MWCNTs were seen with increasing loading ratio, as expected. These nanoscale inclusions were uniformly distributed and embedded within the PEDOT:PSS matrix without forming any segregation of different phases, thus resulting in the uniform composition of AJ-printed nanocomposites. Analysis of the EDX mapping data on different PEDOT:PSS-based composites (see Figure 5.5) reveals the spatial distribution of Sb_2Te_3 and MWCNTs within the PEDOT:PSS matrix. The 'S' represents the distribution of sulphur elements from the PEDOT:PSS matrix, and the 'Sb' indicates the distribution of antimony elements from Sb_2Te_3 nanoflakes. This result further verified the uniformity as well as the homogeneous dispersion of Sb_2Te_3 and MWCNTs within the polymer matrix.

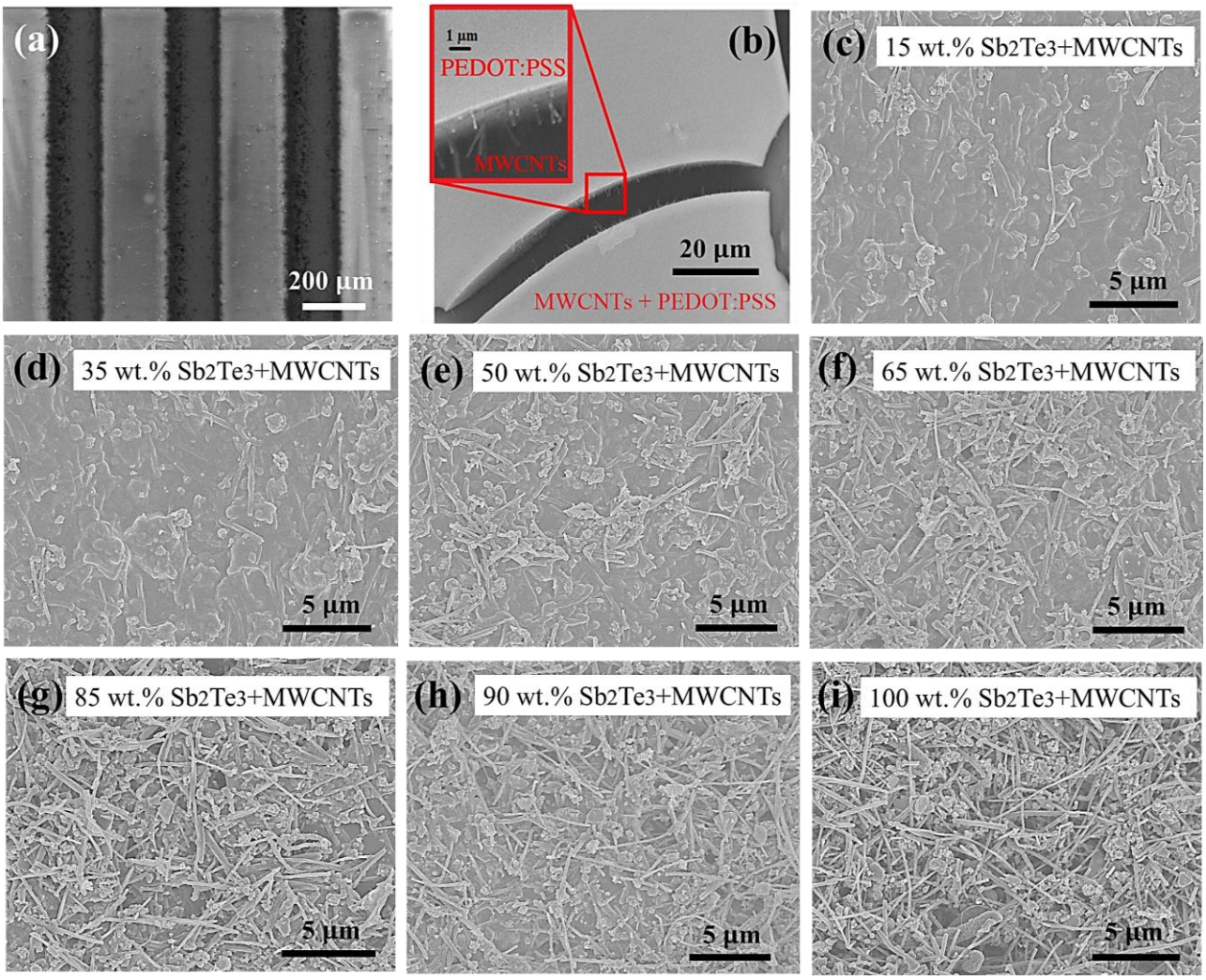

Figure 5.3 (a) SEM image of the representative MWCNTs-PEDOT:PSS nanocomposite lines fabricated by the AJP method. (b) A fracture surface revealing that the MWCNTs were embedded within the PEDOT:PSS matrix and partially pulled out after bending and fracturing the nanocomposite. High-resolution SEM images of AJ-printed nanocomposites with various loading ratios of Sb_2Te_3 and MWCNTs within the PEDOT:PSS matrix, ranging from (c) 15 wt.%, (d) 35 wt.%, (e) 50 wt.%, (f) 65 wt.%, (g) 85 wt.%, (h) 90 wt.%, and up to (i) 100 wt.%. (Figures taken from the author's work [96]. (CC BY 4.0))

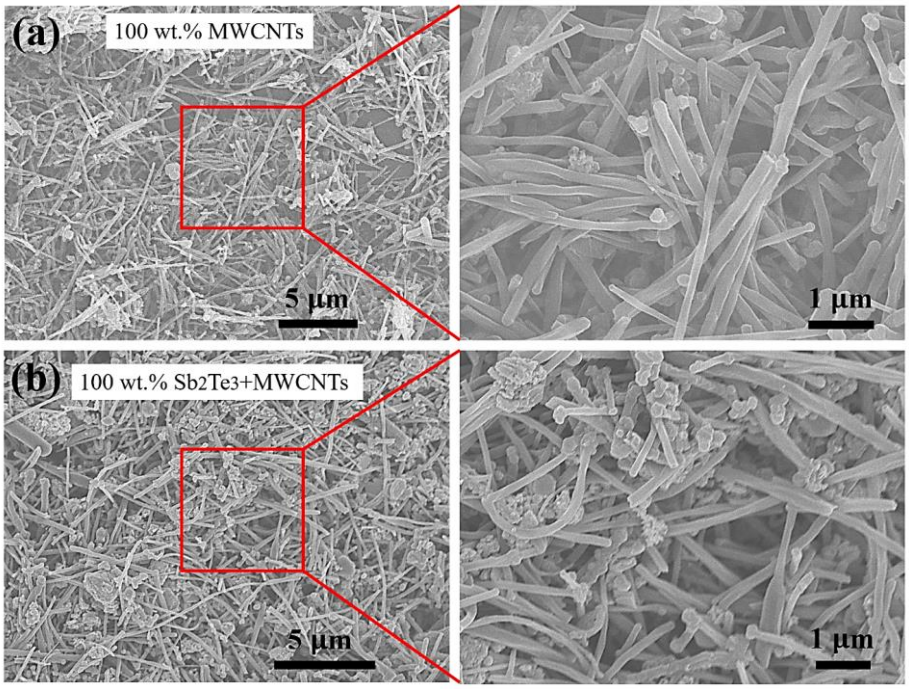

Figure 5.4 SEM images of AJ-printed samples with (a) 100 wt.% MWCNTs, and (b)100 wt.% Sb_2Te_3-MWCNTs, where enlarged images reveal more morphology and microstructure details.

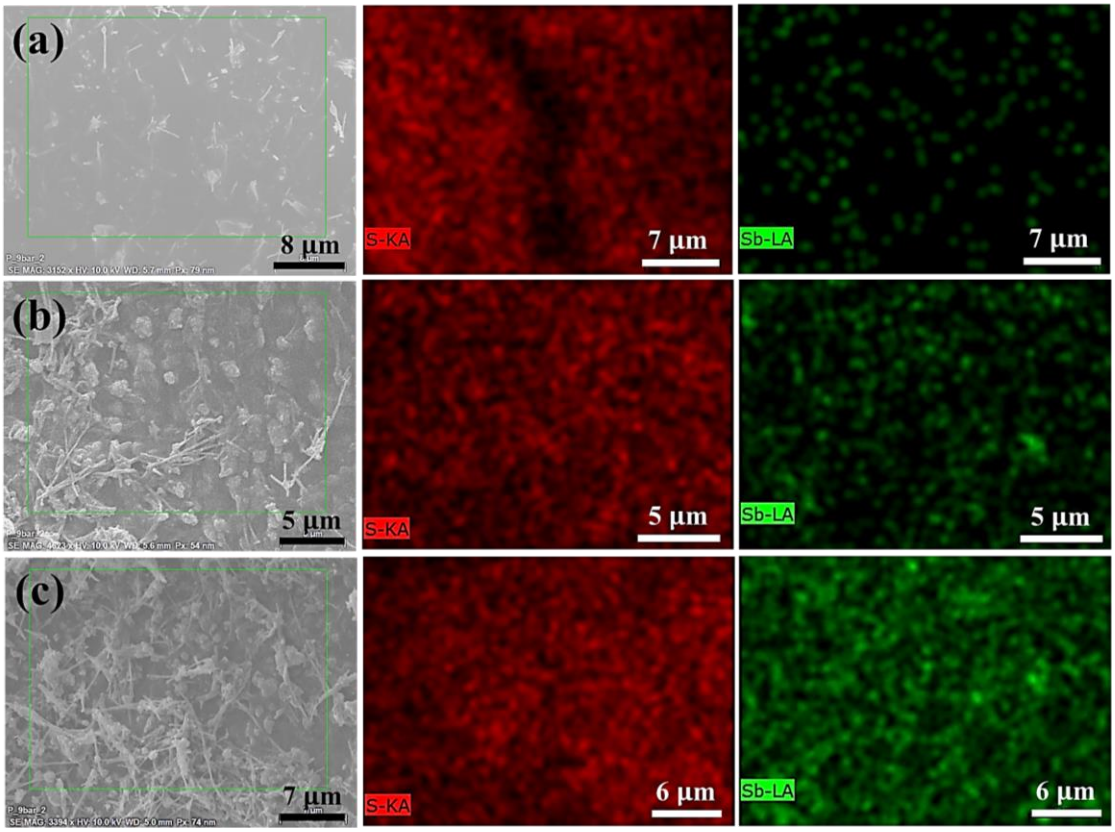

Figure 5.5 EDX mapping of 'S' and 'Sb' elements of AJ-printed PEDOT:PSS-based nanocomposites with different loading ratios of Sb_2Te_3 and MWCNTs: (a) 15 wt.%, (b) 50 wt.%, and (c) 85 wt.%.

5.5 Thermoelectric Measurements of Printed Nanocomposites

When considering the electrical conductivity of CNT-based composites, the introduction of surfactants is usually best avoided.[251] Figure 5.6 indicates that the removal of SDS surfactant could largely improve the final σ and PF values of these AJ-printed MWCNTs-PEDOT:PSS nanocomposites, because no bubbles were formed during the printing process, causing the deterioration of TE performance. Moreover, the pre-added EG or DMSO solvents within the PEDOT:PSS ink could serve as a surfactant to facilitate more homogeneous phase separation between the PEDOT:PSS matrix and the loaded inorganic nano-inclusions within the hybrid organic-inorganic nanocomposites, as demonstrated by Shin et al.[241] Therefore, to further confirm the influence of PVP surfactant on the TE properties, the AJ-printed pristine MWCNTs film (at 100 wt.%) was prepared and then heated up to 350 ^{o}C to burn away the remaining PVP surfactant. It was found that σ only increased marginally with little change in *S*. Since the amount of added PVP surfactant was very minimal, it had fairly little influence on the electrical network and the quality of contacts within the nanocomposite.

Meanwhile, Figure 5.6 shows these AJ-printed MWCNTs films exhibited very low σ (~1 S/cm) and consequently fairly poor PF [~0.1 μW/(m.K^2)], which might be attributed to the MWCNTs film featuring a very porous and poorly connected network as seen in Figure 5.4. Therefore, the PEDOT:PSS matrix was indispensable here, which could serve as the electrical contact medium between different inserted nano-fillers within the nanocomposite structure. Moreover, the addition of Sb_2Te_3 nanoflakes substantially enhanced *S*, albeit with a concomitant decrease in σ, specifically in the high loading ratio region, which resulted in their overall TE performance [*S* ~29 μV/K, σ ~496 S/cm, PF ~41 μW/(m.K^2)] slightly exceeding their non-Sb_2Te_3-added counterparts [*S* ~17 μV/K, σ ~1282 S/cm, PF ~37 μW/(m.K^2)].

Although the incorporation of Sb_2Te_3 nanoflakes and MWCNTs within the PEDOT:PSS matrix was seen to be quite dense in Figures 5.3 (c) - (i), there were still some poor electrical networks, which arose because of the introduction of comparatively lower-σ Sb_2Te_3 nanoflakes

creating larger interfacial resistance, where Sb_2Te_3 nanoflakes could hamper the electrical contact with neighbouring MWCNTs and PEDOT clusters. Nevertheless, these added Sb_2Te_3 nanoflakes could hinder the thermal transport and notably lower the overall thermal conductivity of AJ-printed nanocomposites via the introduction of the phonon-boundary scattering and the large thermal boundary resistance at the interfaces, as widely reported in the literature.[3,4,18,74,75] It would therefore be expected that the nanocomposite with both MWCNTs and Sb_2Te_3 nano-inclusions could have higher *ZT* values than that of composites containing only one of these components, particularly in instances where their respective PF values are comparable.

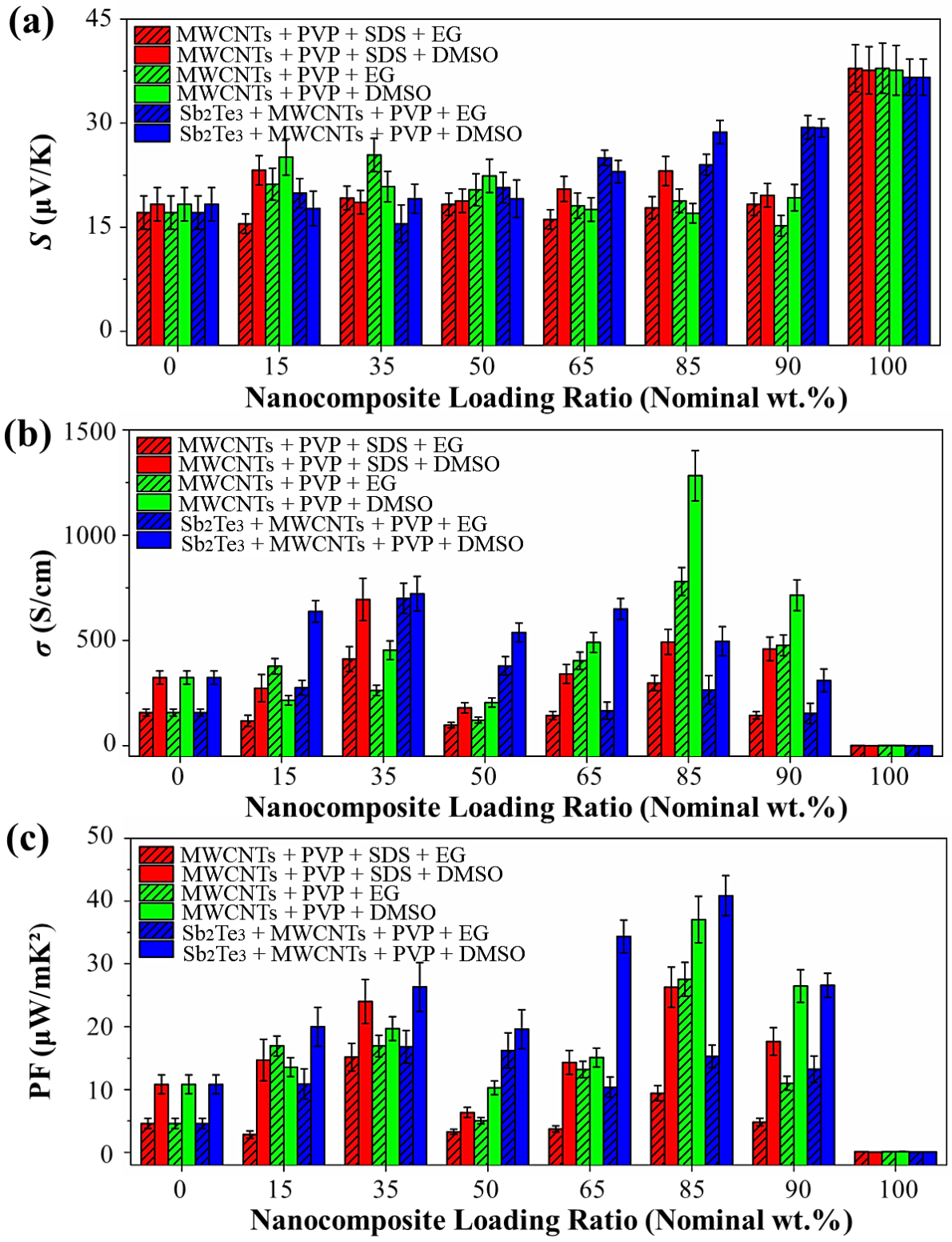

Figure 5.6 Thermoelectric measurements on (a) *S*, (b) σ and (c) PF of AJ-printed PEDOT:PSS-based nanocomposites loaded with various components and compositions, as well as surface-treated with different polar solvents. Error bars indicate the standard deviation of the measured values of two separate printed samples with the same loading components and printing conditions.(Figures taken from the author's work [96]. (CC BY 4.0))

5.6 Flexibility and Fatigue Tests

The mechanical properties of AJ-printed nanocomposites with the highest PF values were selectively compared here in response to flexing, as presented in Figures 5.7 (a) and (b). Simple manual bending tests and rigorous flexing tests were carried out to estimate their TE properties under various bending radii, by mounting them on various surfaces with different curvatures, as demonstrated in the inset of Figure 5.7 (b). It was observed that these AJ-printed nanocomposites exhibited an excellent conformability and retained their original smooth surface without forming any visible cracks or deformations after 5 flexing cycles. The electrical resistance of these nanocomposites only increased marginally, and then plateaued as the bending radius decreased. Meanwhile, the S values of these nanocomposites were found to diminish only slightly after being flexed at very low bending radius ~3.3 mm (see Figure 5.7 (b)). These results indicate that their excellent flexibility mainly stems from the innovative nanocomposite structure, comprising ductile and conducting MWCNTs networks within the flexible PEDOT:PSS polymer that served as a protective matrix to provide greater mechanical support.

A more extensive and continuous fatigue test was subsequently conducted on the AJ-printed 85 wt.% Sb_2Te_3-MWCNTs-PVP-PEDOT:PSS nanocomposite by subjecting it to up to 36,000 continuous bending cycles, i.e. 60 hours of continuous testing at a frequency of 0.15 Hz, as presented in Figure 5.7 (c). It can be seen that after an initial increment in the resistance value (R/R_o), the σ values retained stable for up to 60 hours of testing, indicating that these AJ-printed nanocomposites could be used as flexible TEGs to convert the ΔT into electricity over a prolonged period of time. Also, it should be noted that these AJ-printed nanocomposites were tested over a period of two months with negligible degradation in performance. These fatigue results are of vital importance, given that such extensive fatigue data are rarely presented in the literature for flexible TEGs.

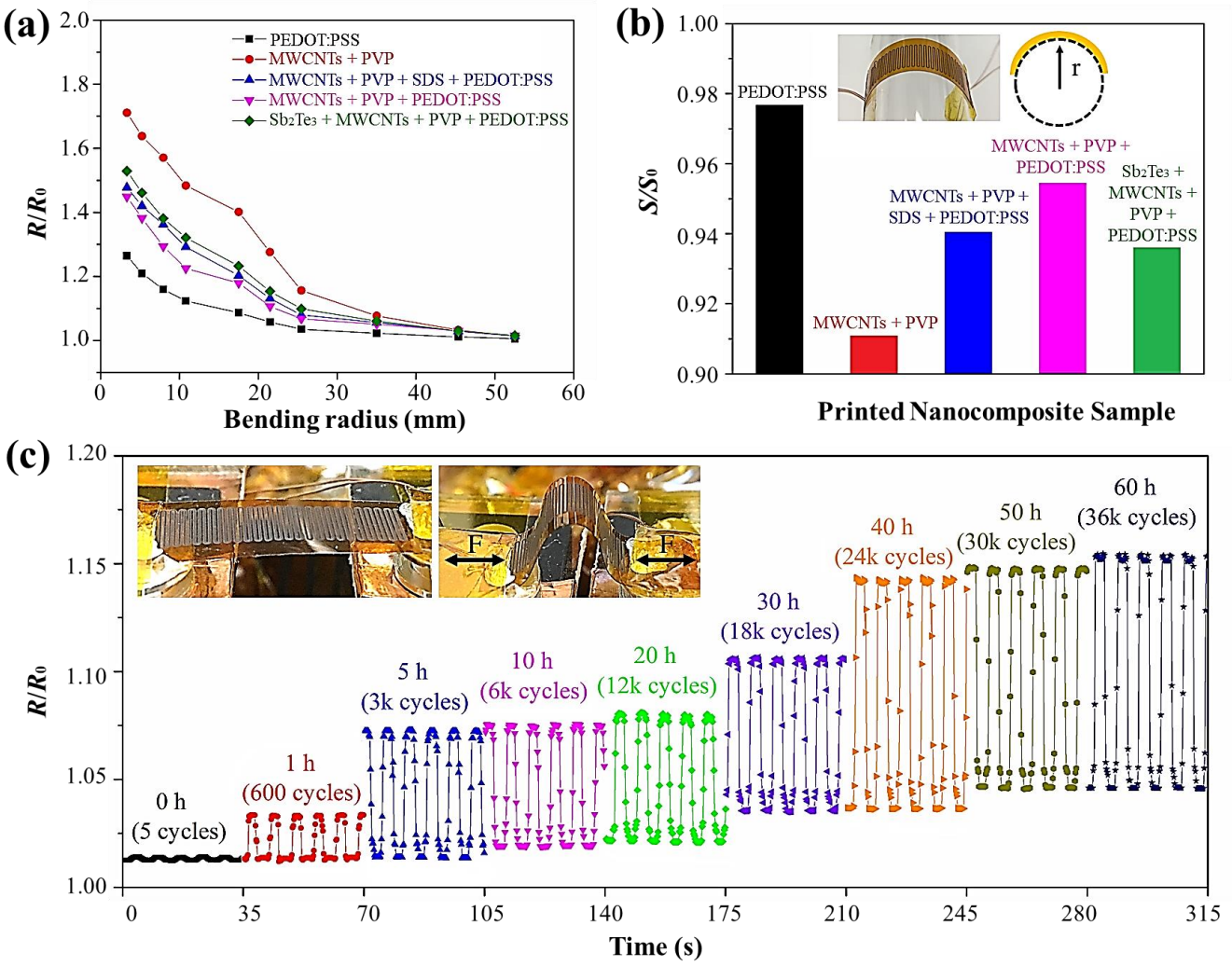

Figure 5.7 Flexing test on AJ-printed PEDOT:PSS-based nanocomposites with different loading ratios of MWCNTs and Sb_2Te_3 nanoflakes, where (a) the ratio of flat-to-flexed resistance was plotted as a function of the bending radius and (b) the ratio of flat-to-flexed Seebeck coefficient as a function of the loading composition, respectively. Inset: the sample was subjected to a bending radius of 5.3 mm. (c) Fatigue test of the AJ-printed 85 wt.% Sb_2Te_3-MWCNTs-PVP-PEDOT:PSS nanocomposite, continually flexing for 60 hours (i.e. 36,000 cycles) under the application of periodic compressive stress at a frequency of 0.15 Hz with an amplitude of ~10 mm. The data after different flexing cycles were recorded accordingly.

The resistance of these flexed nanocomposites did not revert to their original values after being released, and it might stem from the formation of fairly small cracks within the nanocomposite, as can be seen in the SEM micrographs taken before and after fatigue testing in Figure 5.8. In addition, it was seen that these interconnected MWCNTs bridged the cracks and/or voids formed within the nanocomposite, which could largely facilitate their mechanical robustness with little degradation in TE properties. It shows that after prolonged flexing and fatigue tests, the nanocomposite film was partially peeled off from the substrate, and there were only a few microcracks formed which tended to locate at and/or near the edges of the nanocomposite. Furthermore, the *S* values decreased by only ~15% after the 60-hour prolonged fatigue test, which indicates that the observed microcracks did not substantially affect *S*. These observations confirm the superior flexibility and mechanical stability of these AJ-printed flexible nanocomposites compared with their bulk counterparts. Since these TEGs possessed excellent flexibility, they could, for example, be mounted on a heat pipe with a very low bending radius down to 3.3 mm, or could be worn onto a human wrist due to their excellent robustness and mechanical stability. The fabricated TEG was very lightweight with a mass of ~0.05 g, which could ensure the comfortability for wearable applications.

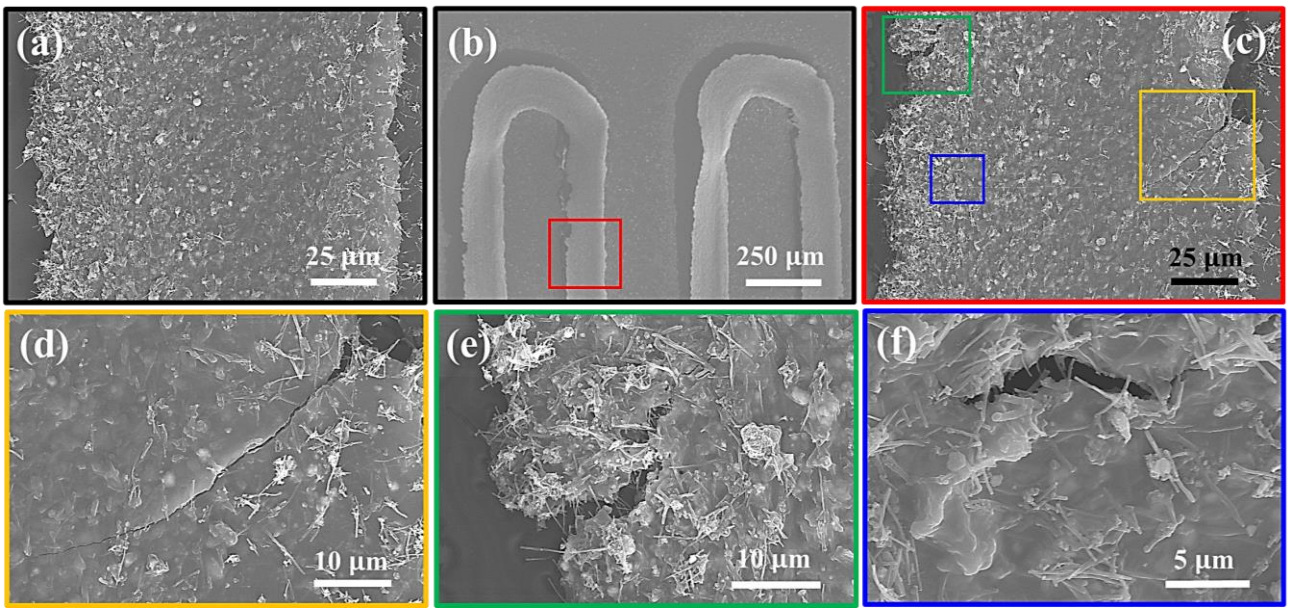

Figure 5.8 SEM images of the AJ-printed nanocomposite (a) before as well as (b) and (c) after the prolonged fatigue test, where the enlarged images (d), (e) and (f) reveal the microcracks formed within the nanocomposite after the fatigue test.

5.7 Summary

In summary, AJ-printed, flexible, all-organic and organic-inorganic hybrid TE nanocomposites have been prepared, incorporating the conducting PEDOT:PSS polymer, high electrical conductivity MWCNTs, and high Seebeck coefficient Sb_2Te_3 nanoflakes. The introduction of MWCNTs and Sb_2Te_3 nano-inclusions might also serve to lower the thermal conductivity by the phonon scattering at the organic/inorganic interfaces for the improved TE performance. To the best of the author's knowledge, these are some of the very first results where the AJP technique has been used to incorporate MWCNTs into flexible printed nanocomposite-based TE devices. A couple of important process modifications have been implemented in these nanocomposites wherein the *in situ* mixing of different component phases was employed to form nanocomposite structures. These methods can potentially provide many advantages in printing advanced composite devices. Different AJ-printed PEDOT:PSS-based nanocomposites have been treated with various polar solvents to improve their σ by de-doping the insulating PSS. The results from the TE measurements across different compositions and surface treatments were compared, with the DMSO-treated Sb_2Te_3-MWCNTs-PVP-PEDOT:PSS nanocomposite showing the best PF of ~41 μW/(m.K^2) (S of ~29 μV/K and σ of ~496 S/cm). Furthermore, rigorous flexing and fatigue tests have proved the superior mechanical flexibility and robustness of these AJ-printed TE nanocomposites, even after 60 hours of continuous flexing cycles (i.e. 36,000 cycles in total). These flexible TE nanocomposites with excellent durability, as demonstrated in this work, could find applications in thermal energy harvesters for wearable devices, or in applications requiring the ease of mounting and the surface conformability of the energy harvester.

Chapter 6

Compositionally Graded Thermoelectric Composites

Most research into functionally graded TE materials has been done by using inorganic TE materials. There is currently no report on adopting this concept for polymeric or composite TE materials, which could serve as a new way to boost the TE performance of hybrid TE materials and devices. This chapter therefore details the development of compositionally graded thermoelectric composites (CG-TECs) and their generators. Firstly, various loading ratios of inorganic nano-inclusions have been incorporated into PEDOT:PSS matrix by using the *in situ* mixing method to dynamically tune the composition of nanocomposites. Then, these fabricated nanocomposites have been measured to ascertain how the inserted nano-fillers contribute to their TE properties as a function of the temperature. Lastly, different CG-TECs have been developed to comprise multiple dissimilar segments having different TE properties into one whole TEG. Accordingly, the optimum TE performance of individual components could be fully utilised without compromising performance over a wide operating temperature range. It has proved that this CG-TEC design could be an alternative way to enhance TE performance and energy conversion efficiency of TEGs. Some parts discussed here have been published in "Compositionally Graded Organic-inorganic Nanocomposites for Enhanced Thermoelectric Performance". *Adv. Electron. Mater.*, 2019, 6 (1), 1900720,[252] and they have been adapted from that text with granted Copyright permission. It should be noted that the author performed all the experiment works and data analysis with the help of other co-authors of the paper.

6.1 Temperature-dependent Power Factor of Printed Nanocomposites

The graphs of PF vs. temperature of different AJ-printed PEDOT:PSS-based nanocomposites loaded with various wt.% of nano-inclusions were plotted in Figure 6.1 (a). It can be seen that each of the TE nanocomposites investigated here displayed different PF response profiles with temperature. For a better view and understanding of the trend of TE properties as a function of the temperature, the TE data for each composition has been separately plotted in the following sections.

In order to demonstrate the concept of using compositional grading to improve the overall TE performance, four specific compositions were selected for a closer view and plotted as shown in Figure 6.1 (b), to find out the appropriate combination of material compositions that would optimise TE performance over the temperature range of interest. The intention was to pair up compositions such that one had a higher PF at the lower temperature range, while the other had a higher PF at the higher temperature range when compared to each other, i.e. compositions with a 'crossover' of PF values across the entire temperature range. Therefore, by appropriately tuning the compositions across the whole range, an overall enhanced TE performance could be achieved, as compared to that of using individual compositions (i.e. single-phase counterparts) across the whole temperature range. If it were to have picked one of the other compositions with higher PF over the entire temperature range, it would not have been able to demonstrate the benefit of compositional grading. Further investigation of the device design and fabrication with the use of this compositional grading concept will be elaborated in Section 6.2.

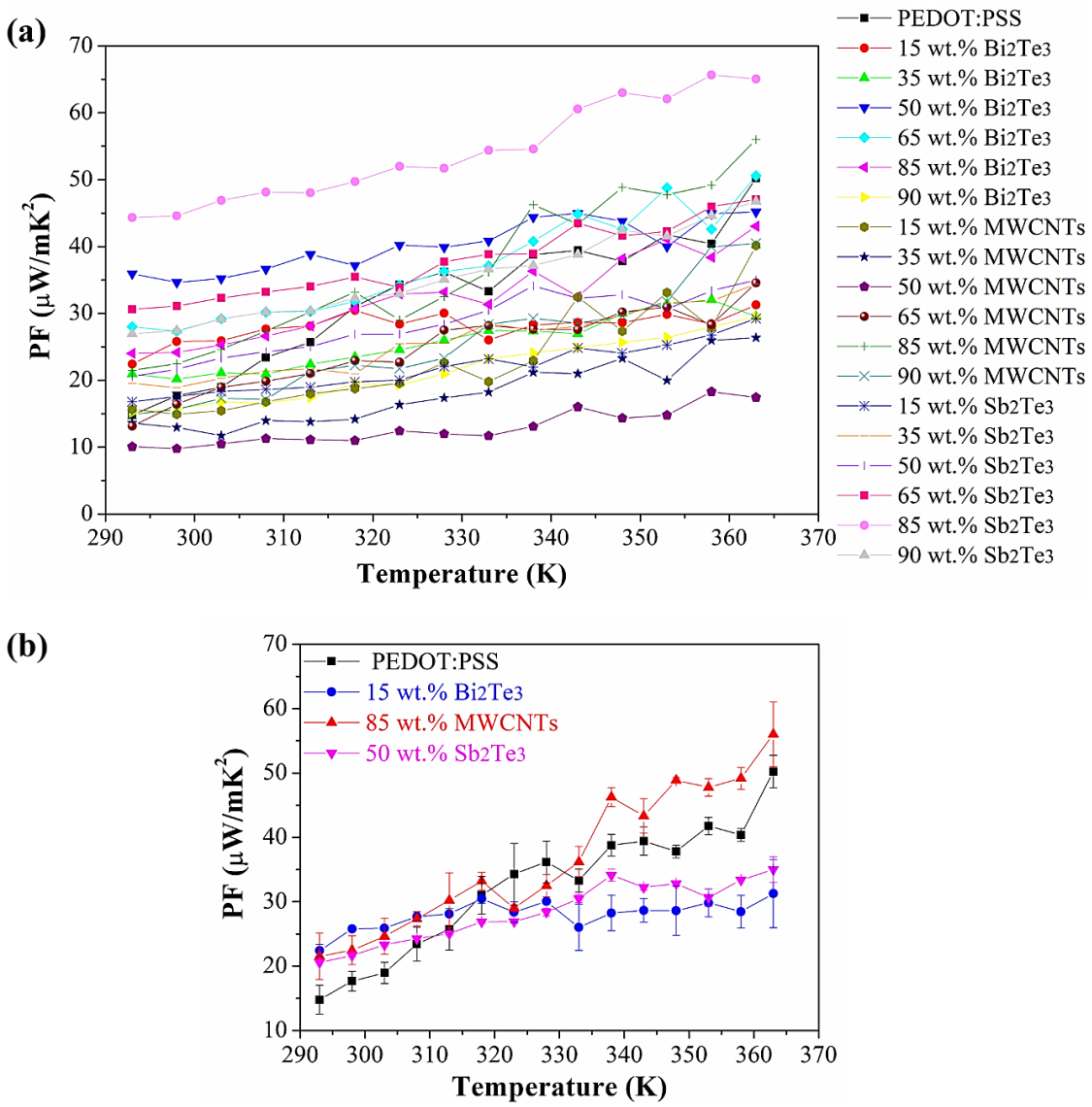

Figure 6.1 (a) Temperature-dependent PF measurements of AJ-printed PEDOT:PSS-based nanocomposites loaded with different wt.% of nano-inclusions (non-compositionally graded). (b) Closer view of 4 specific compositions for the subsequent design and fabrication of the compositionally graded structure. (Figures taken from the author's work [252]. (CC BY 4.0))

6.1.1 Pristine PEDOT:PSS Films

To start with, a pristine PEDOT:PSS film was prepared, and the temperature-dependent TE measurement was conducted over a temperature range of 293 K to 363 K, as shown in Figure 6.2. It can be seen that *S* increased in direct proportion to the sample temperature and yielded the highest value of ~26.8 μV/K at 363 K. For σ, it also increased with increasing temperature, peaking at the temperature of 343 K with a value of 704.5 S/cm. However, with further increase in temperature, σ began decreasing slightly. As a combination of both increased

S and σ, the maximum PF value of ~50.2 μW/(m.K^2) was recorded at 363 K. It was proposed that the trend of σ might be attributed to the inter-chain and intra-chain carrier hopping processes of the PEDOT:PSS polymer, which followed Mott's variable range hopping (VRH) model.[253] Since the average hopping distance between adjacent particles and the activation energy for the hopping of charge carriers were inversely related to the temperature due to the thermally activated transport, the carrier mobility of PETODT:PSS increased with increasing temperature, and thus an increment in the electrical conductivity.[232]

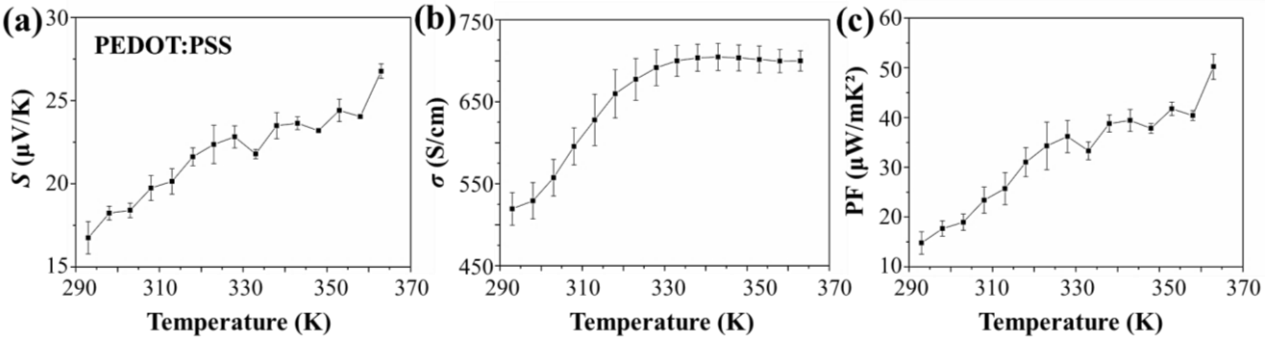

Figure 6.2 Temperature-dependent measurements of (a) *S*, (b) σ, and (c) PF of the AJ-printed pristine PEDOT:PSS film. (non-compositionally graded)

6.1.2 Bi_2Te_3-PEDOT:PSS Thermoelectric Nanocomposites

Then, Bi_2Te_3-PEDOT:PSS nanocomposites loaded with 15 wt.%, 35 wt.%, 50 wt.%, 65 wt.%, 85 wt.% and 90 wt.% Bi_2Te_3 nanoparticles were AJ-printed and measured, respectively, as shown in Figure 6.3. With the increased loading amount of inorganic components, the *S* values increased more dramatically, while the σ values dropped more steeply with increasing temperature. This resulted in a gradually increasing PF response profile as a function of the temperature, with PF values all reaching the highest at 363 K. A hypothesis was proposed here to explain the trend of σ of obtained hybrid nanocomposite structures. This trend might stem from the addition of Bi_2Te_3 nanoparticles within the PEDOT:PSS matrix, which rendered nanocomposites behaving from hopping transport to band-like transport.[232] As the number of free electrons in a unit volume of the conductor or semiconductor rose exponentially with increasing temperature, it led to the dramatic decline in the relaxation time as well as the mean free path, thereby a significant drop in electron carrier mobility and electrical conductivity.[254] With more loaded amount of Bi_2Te_3, this carrier scattering phenomenon became more distinct.

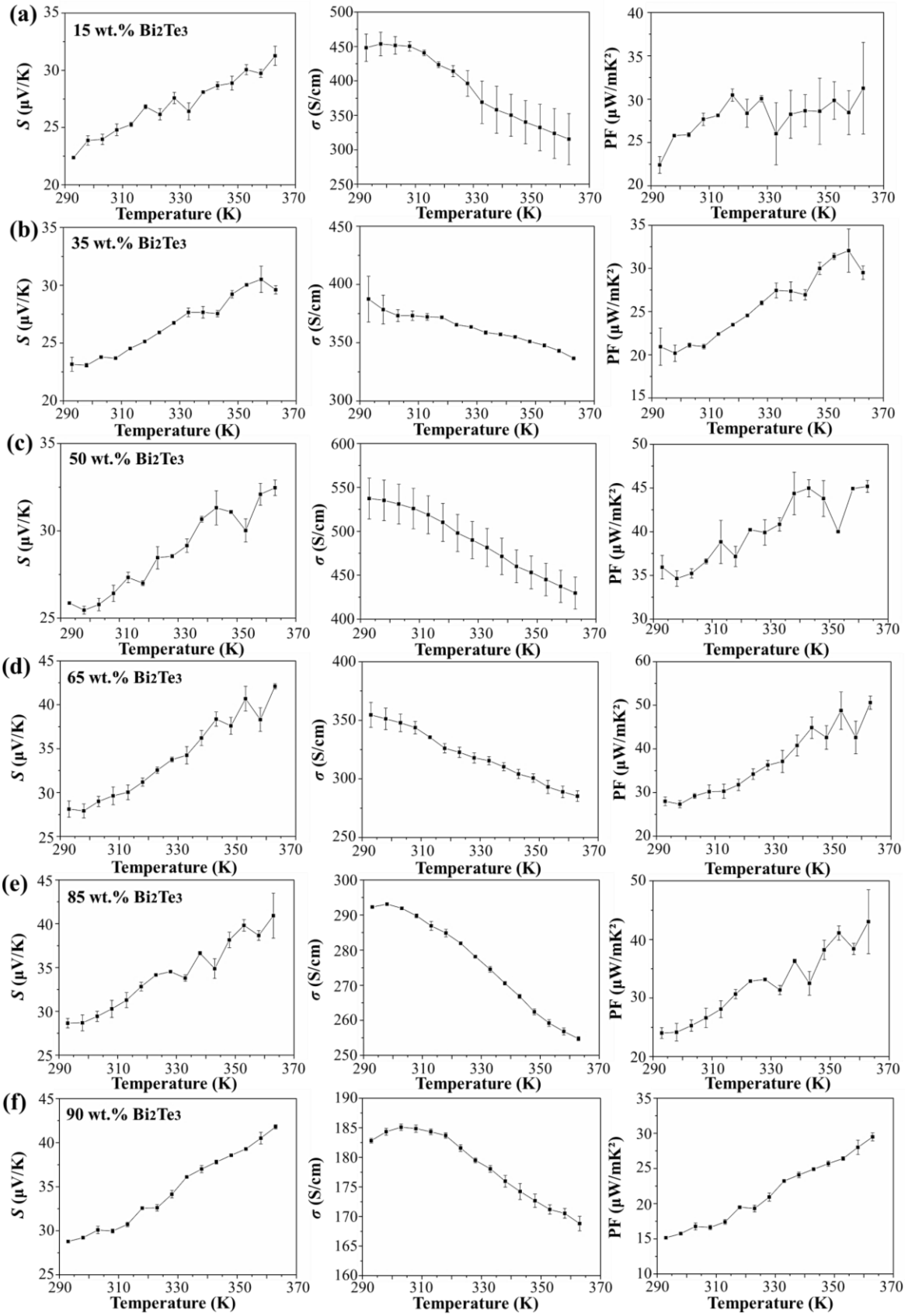

Figure 6.3 Temperature-dependent measurements of *S*, σ, and PF of AJ-printed Bi_2Te_3-PEDOT:PSS nanocomposites loaded with (a) 15 wt.%, (b) 35 wt.%, (c) 50 wt.%, (d) 65 wt.%, (e) 85 wt.%, and (f) 90 wt.% of Bi_2Te_3 nanoparticles, respectively. (non-compositionally graded)

6.1.3 MWCNTs-PEDOT:PSS Thermoelectric Nanocomposites

For the MWCNTs-PEDOT:PSS nanocomposites loaded with 15 wt.%, 35 wt.%, 50 wt.%, 65 wt.%, 85 wt.%, and 90 wt.% of MWCNTs, their σ values were observed to increase slightly, and then displayed a sharp downward trend with further increase in temperature, as displayed in Figure 6.4. Their *S* values increased gradually, with the resulting PF values all peaking at the temperature of 363 K. The possible reason behind this phenomenon might be that as the temperature increased at the beginning, the charge carrier density in the conduction band increased, resulting in a slightly augmented σ.[254] With more amount of added MWCNTs, the obtained nanocomposites were rendered to exhibit a metallic characteristic.[232] As free electrons gained energy and started oscillating, more significant electron vibrations and more collisions between electrons took place with increasing temperature, leading to the decrease of electron carrier mobility and thus an increment of electrical resistance. It should be noted that some large error bars shown in Figure 6.4 might stem from the measurement error from different batches of samples that were fabricated by different separate printings.

6.1.4 Sb_2Te_3-PEDOT:PSS Thermoelectric Nanocomposites

Lastly, the temperature-dependent TE properties of Sb_2Te_3-PEDOT:PSS nanocomposites loaded with 15 wt.%, 35 wt.%, 50 wt.%, 65 wt.%, 85 wt.%, and 90 wt.% of Sb_2Te_3 nanoflakes were plotted in Figure 6.5. In this group, it was found that the σ values deteriorated with the increase of temperature, which was similar to the case of Bi_2Te_3-PEDOT:PSS nanocomposites elaborated in Section 6.1.2. The significant enhancement in *S* led to all PF values of these AJ-printed nanocomposites peaking at 363 K, which might be attributed to higher *S* values of *p*-type Sb_2Te_3 nanoflakes. Note that AJ-printed structures comprising only inorganic nanomaterials without the conducting PEDOT:PSS polymer matrix were found to be electrically insulating, and their TE properties were unable to be measured, as previously discussed in Chapters 4 and 5. Therefore, they were not included here.

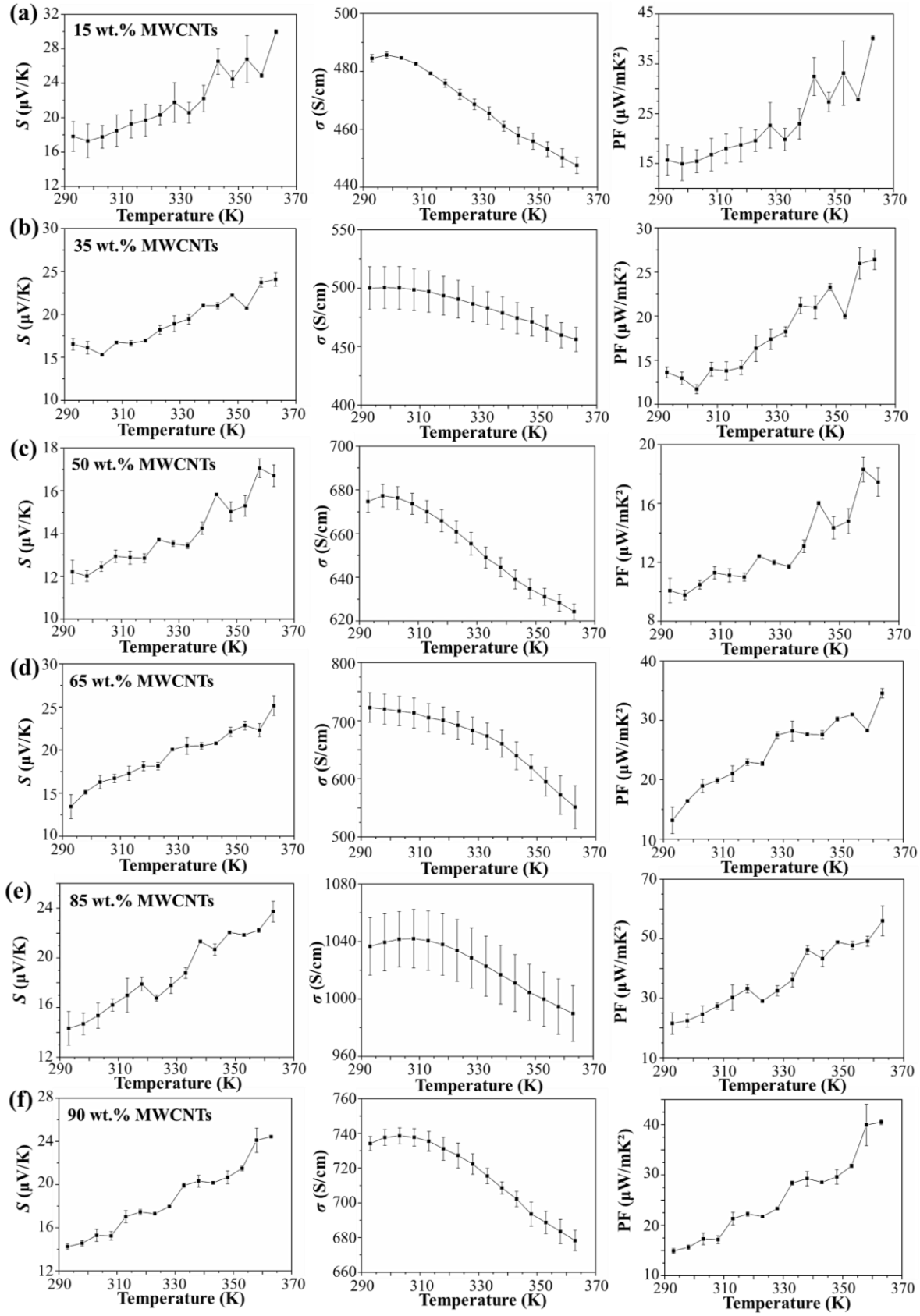

Figure 6.4 Temperature-dependent measurements of S, σ, and PF of AJ-printed MWCNTs-PEDOT:PSS nanocomposites loaded with (a) 15 wt.%, (b) 35 wt.%, (c) 50 wt.%, (d) 65 wt.%, (e) 85 wt.%, and (f) 90 wt.% of MWCNTs, respectively. (non-compositionally graded)

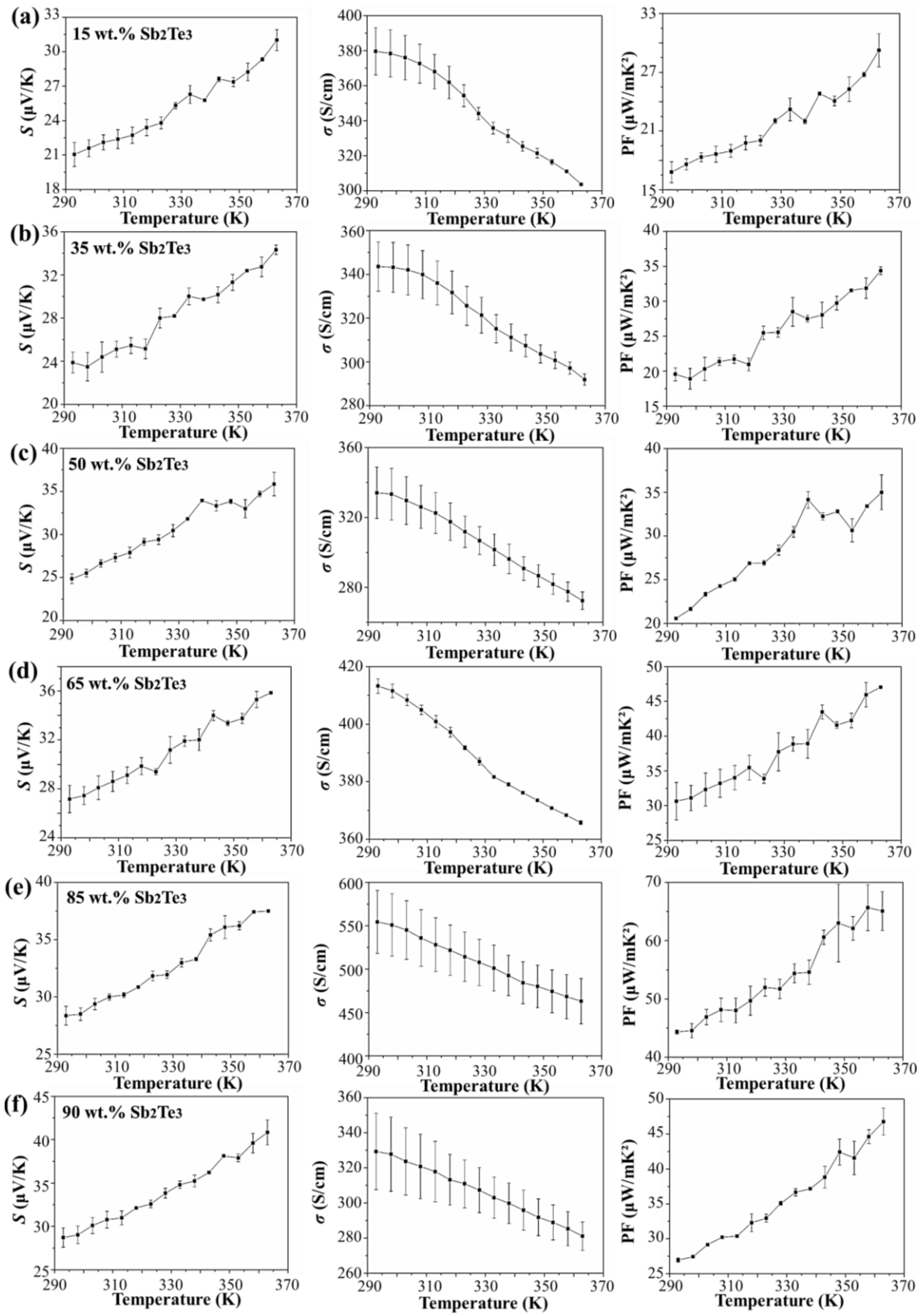

Figure 6.5 Temperature-dependent measurements of *S*, σ, and PF of AJ-printed Sb_2Te_3-PEDOT:PSS nanocomposites loaded with (a) 15 wt.%, (b) 35 wt.%, (c) 50 wt.%, (d) 65 wt.%, (e) 85 wt.%, and (f) 90 wt.% of Sb_2Te_3 nanoflakes, respectively. (non-compositionally graded)

6.2 Compositionally Graded Thermoelectric Composites

6.2.1 Design of Compositionally Graded Thermoelectric Composites

From the temperature-dependent PF values of different AJ-printed TE nanocomposites, the PF response profiles of different pairs of TE elements are presented in Figure 6.6, spanning the temperature range of interest. Figure 6.6 (a) shows the PF profiles of the 15 wt.% Bi_2Te_3-PEDOT:PSS nanocomposite and the pristine PEDOT:PSS film intersecting at a temperature T_x of 318 K. The 15 wt.% Bi_2Te_3-PEDOT:PSS nanocomposite exhibited higher PF values than that of the pristine PEDOT:PSS film below 318 K (blue curve in Figure 6.6 (a)), while above the T_x, the PEDOT:PSS film surpassed the nanocomposite in terms of its PF (black curve in Figure 6.6 (a)). Similarly, Figure 6.6 (b) displays the PF profiles of the 50 wt.% Sb_2Te_3-PEDOT:PSS nanocomposite and the pristine PEDOT:PSS film, where the T_x was 313 K. The solid green lines highlighted in Figure 6.6 indicate the highest PF values that could be obtained through a combination of the respective compositions above and below T_x, while the solid red lines in Figure 6.7 show the opposite case for comparison. Therefore, by using these graphs, compositionally graded thermoelectric composites (CG-TECs) could be designed and fabricated. Different material compositions were optimised to work across different temperature ranges, according to whichever correspondingly exhibited higher PF values.

As demonstrated in below schematic illustrations, a dual-segment TE leg could be composed of the 15 wt.% Bi_2Te_3-PEDOT:PSS nanocomposite or the 50 wt.% Sb_2Te_3-PEDOT:PSS nanocomposite at the cold side, with the pristine PEDOT:PSS film at the hot side. Then, the optimal length of each TE element could be determined according to the intersection temperature, which will be further discussed in the following sections. On top of that, the 85 wt.% MWCNTs-PEDOT:PSS nanocomposite was also examined, as presented in Figure 6.8. However, since the degree of the crossover was considerably low here, the resulting TE performance improvement derived from the CG-TEC design was marginal. As a result, this set of material combination was not further explored in this study.

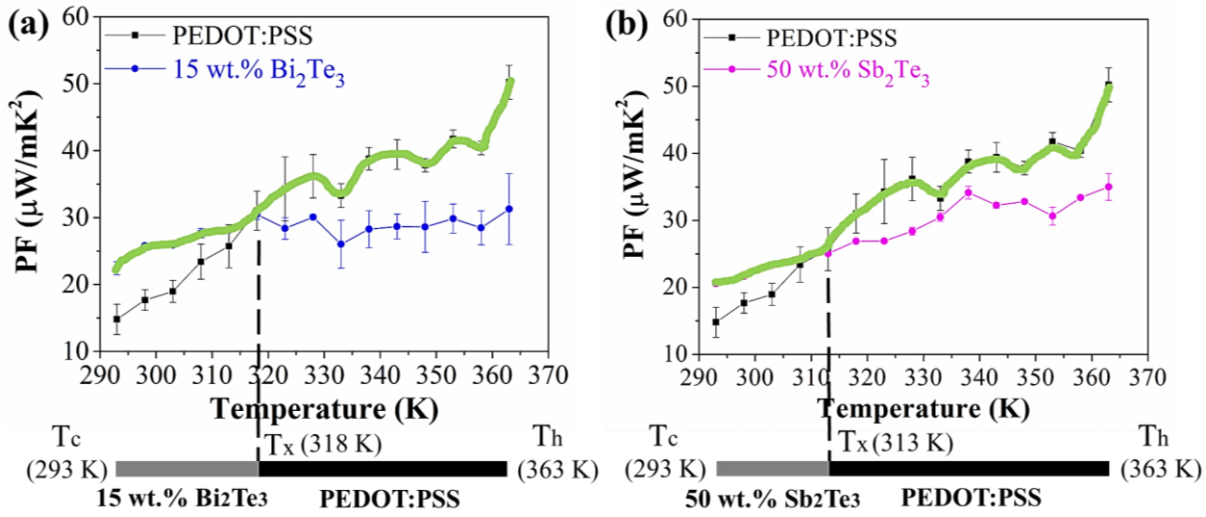

Figure 6.6 Temperature-dependent PF measurements of (a) 15 wt.% Bi_2Te_3-PEDOT:PSS nanocomposite and pristine PEDOT:PSS film, and (b) 50 wt.% Sb_2Te_3-PEDOT:PSS nanocomposite and pristine PEDOT:PSS film, respectively, indicating a crossover temperature where one composition outperforms the other. The insets illustrate the schematics of the design structure for the 'good design'. (Figures taken from the author's work [252]. (CC BY 4.0))

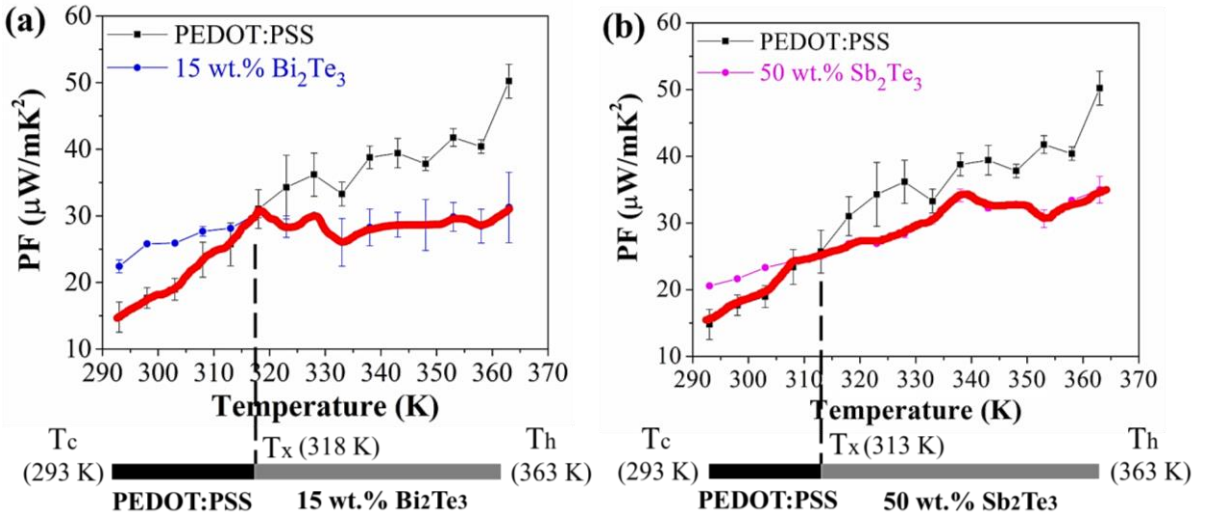

Figure 6.7 Temperature-dependent PF measurements of (a) 15 wt.% Bi_2Te_3-PEDOT:PSS nanocomposite and pristine PEDOT:PSS film, and (b) 50 wt.% Sb_2Te_3-PEDOT:PSS nanocomposite and pristine PEDOT:PSS film, respectively, indicating a crossover temperature where one composition underperforms the other. The insets illustrate the schematics of the design structure for the 'bad design'.

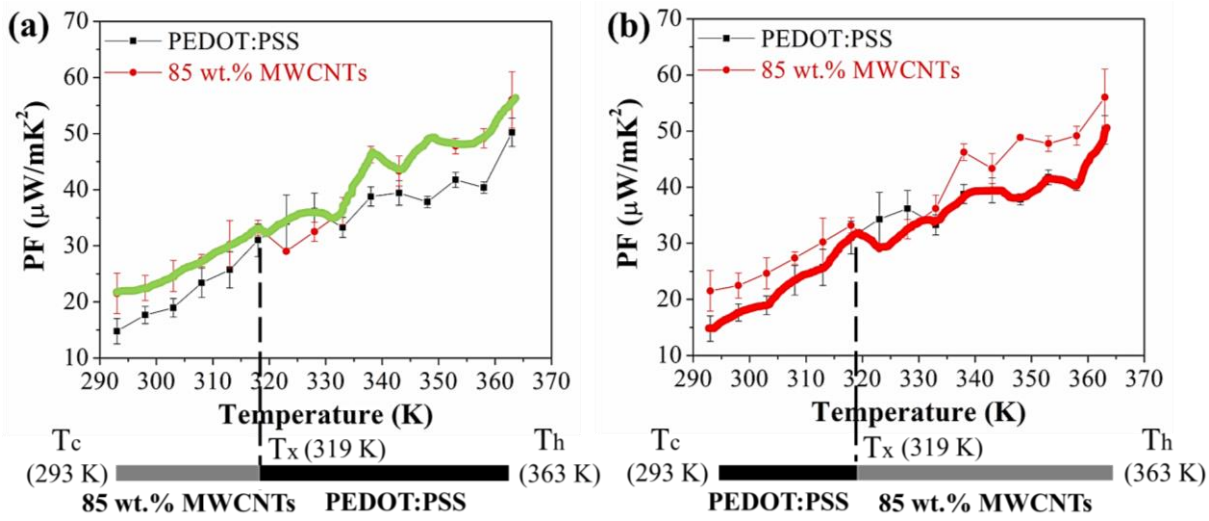

Figure 6.8 Temperature-dependent PF measurements of 85 wt.% MWCNTs-PEDOT:PSS nanocomposite and pristine PEDOT:PSS film for (a) the 'good design' and (b) the 'bad design', respectively, where the insets illustrate the schematics of the design structure.

6.2.2 Thermal Conductivity Calculation and Prediction of Nanocomposites

Since the thermal conductivity of the TE nanocomposite is an important parameter to be considered in the subsequent COMSOL simulation for the CG-TEC design and fabrication in the following sections. However, there are difficulties associated with measuring the thermal conductivity in the nanocomposite structures, which are essentially printed/patterned thin films on thick underlying substrates. As demonstrated by Zhang et al. in their review, the calculation and prediction of the thermal conductivity of polymer-based composites are highly complicated. Because their thermal conductivity is a function of the filler structure and its dispersion, the intrinsic thermal conductivity of both the filler and polymer, as well as the interfacial thermal resistance.[253] In order to address these issues, the effective thermal conductivity values of the nanocomposite structures were calculated and predicted here. Analytical calculations were carried out to ascertain by how much the thermal conductivity was affected in these nanocomposite structures by using a model based on Maxwell's equation,[255–257] where the phonon scattering effect was not considered here. Since the loaded inclusions in this work were mainly nanocrystals, the model for the spherical particulate was used here, where spherical particulates with the thermal conductivity of K^* were randomly dispersed in a medium with the

thermal conductivity of K. Equation 6-1 was firstly evaluated in the context of electrical conduction.[255] The model is valid for the volume fraction (φ) < 25% and does not include the effect of the interfacial phonon scattering effect. Thus, Equation 6-1 gives an upper limit to the effective thermal conductivity of the nanocomposite (K_{eff}).

$$\frac{K_{\text{eff}}}{K} = 1 + \frac{3\varphi}{\left(\frac{K^*+2K}{K-K^*}\right) - \varphi} \tag{6-1}$$

where K_{eff} is the effective thermal conductivity of the nanocomposite [W/(m·K)]; K is the thermal conductivity of the medium [W/(m·K)]; K^* is the thermal conductivity of the spherical particulate [W/(m·K)]; φ is the volume fraction occupied by the particulates.

Table 6-1 summarises the properties of different TE materials adopted for the thermal conductivity calculation and prediction of their resulting AJ-printed nanocomposite structures. It should be noted that for the ease of comparison, most data are sourced from the COMSOL built-in database except cited. The adopted data here matched well with the average range of different literature. For the 15wt.% Bi_2Te_3-PEDOT:PSS nanocomposite, its volume fraction was calculated to be ~3 vol.% according to its nominal wt.%. Its effective thermal conductivity was therefore calculated to be ~0.31 W/(m.K), with the density of ~1212 kg/m^3 and the heat capacity of ~975 J/(kg.K), which were calculated based on the volume fraction of the loaded Bi_2Te_3 particulates. For the 50 wt.% Sb_2Te_3-PEDOT:PSS nanocomposite, its volume fraction was calculated to be ~13 vol.% according to its nominal wt.%. Thus, its effective thermal conductivity was calculated to be ~0.38 W/(m.K), with the density of ~1725 kg/m^3 and the heat capacity of ~887 J/(kg.K), which were calculated based on the volume fraction of the loaded Sb_2Te_3 particulates. The increment in the thermal conductivity was found to be very low here, because the loading volume percentage values of these inorganic inclusions are much lower than their nominal weight percentage values (i.e. 3 vol.% for 15 wt.% Bi_2Te_3, and 13 vol.% for 50 wt.% Sb_2Te_3).

Figure 6.9 shows the K_{eff}/K vs. φ plot of different polymer-based TE nanocomposites loaded with Bi_2Te_3 or Sb_2Te_3 nano-inclusions within a PEDOT:PSS matrix as a function of the

filler volume fraction, which was calculated by Equation 6-1. The values of the φ relevant to this study are indicated on the graph. It can be seen that the K_{eff} value was increased by ~4% and ~25% for the Bi_2Te_3-based and Sb_2Te_3-based nanocomposites, respectively. This gave an upper bound for the thermal conductivity of nanocomposite structures, which was found to be only slightly higher than that of the pristine polymer matrix, owing to their low loading volume fractions. This result indicates the above estimates are in good agreement with the calculations here. Therefore, these small variations in the thermal conductivity have been accounted for. These calculated thermal conductivity values were adopted in the subsequent COMSOL simulations for the CG-TEC design. It should also be noted that these thermal conductivity values only represent the upper limit, as they will be further reduced when considering the phonon scattering effect at the organic-inorganic interfaces, as elucidated in Section 2.4.4.[3,4,19,253] This effect will serve to improve TE performance even further, and further optimisation of the thermal conductivity is hence not required, but is already inherently present.

Table 6-1 Summary of the properties of different TE materials adopted in the thermal conductivity calculation and prediction of their resulting AJ-printed nanocomposite structures.

Material	Density (kg/m^3)	Heat capacity (J/(kg.K))	Thermal conductivity [W/(m.K)]	Volume fraction (%)
Bi_2Te_3	7700	154	1.2	3
Sb_2Te_3	6500	129	1.65	13
PEDOT:PSS[93]	1011	1000	0.3	N.A.

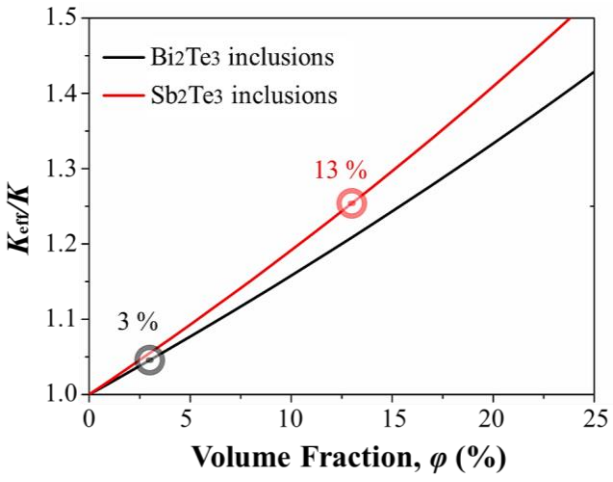

Figure 6.9 Calculation and prediction of the effective thermal conductivity of different polymer-based TE nanocomposite structures as a function of the filler volume fraction.

6.2.3 Simulation of Compositionally Graded Thermoelectric Composites

According to the above temperature-dependent TE measurement results, the intersection temperature (T_x) used for the CG-TEC design was located by varying the length of different components under the simulated temperature distribution. The simulated prediction was subsequently validated by fabricating geometrically optimised CG-TECs and characterising them using the laboratory-built TE measurement setups, where the appropriate boundary position between two different components was estimated based on the simulation results.

In the examples discussed below, the boundary between the first and second portions was selected to be at or near the location of the intersection temperature in the PF response profiles of two TE materials. The intersection location was calculated by modelling the theoretical temperature distribution along the length of a TE leg operating under a given ΔT. To design the printing pattern for the CG-TEC, a finite element computational model based on the COMSOL Multiphysics was used to simulate the heat flow and temperature distribution along the CG-TECs. The *Heat Transfer in Solids* physics interface was employed to define the temperature variation throughout the TE leg. The contribution of temperature-dependent TE properties and the influence of contact resistance were not considered in the simulation model here. The coloured lines represent the isotherm with a colour bar relating the colour to a temperature, where the black line indicates the location of T_x, which accordingly defines the boundary between the first and second components. The temperature at either end was set to 293 K and 363 K, respectively, to provide a ΔT of 70 K across the whole TE leg (see Figures 6.10 and 6.11). The optimal length of different segmented TE legs was determined according to their thermal conductivity values, as calculated in the above Section 6.2.2.

Regarding the effect of contact thermal resistance at the interfaces, it was neglected here. Because both components of the CG-TEC structure were AJ-printed with an imposed overlap zone without any hard physical interfaces, i.e. no step-change in the composition between the two components of the CG-TEC, which will be detailed in the following Section 6.25. In addition, the underlying polymeric matrix across the interface was the same in both cases

(i.e. PEDOT:PSS), and the loading volume fraction of inorganic nano-inclusions was relatively low. These could synergistically lead to a fairly small variation in the thermal conductivity and contact resistance across the compositional-graded interfaces.

Figure 6.10 (a) shows the temperature distribution profiles for determining the device structure of the 'good design' for the CG-TEC comprising 15 wt.% Bi_2Te_3-PEDOT:PSS nanocomposite + PEDOT:PSS, by varying the length of the 15 wt.% Bi_2Te_3-PEDOT:PSS nanocomposite part from 7 mm to 10 mm, where the 15 wt.% Bi_2Te_3-PEDOT:PSS nanocomposite was positioned on the cold side (see Figure 6.6 (a)). It was found that for the targeted intersection temperature of 318 K, 7.5 mm length of the nanocomposite was chosen for the 'good design'. For the 'bad design', the positions of both components were swapped, as highlighted in the solid red line in Figure 6.7 (a), i.e. the pristine PEDOT:PSS film on the cold side. Then, the length of the PEDOT:PSS part was varied from 5 to 8 mm. The targeted intersection temperature of 318 K was obtained at 6.5 mm from the end. This dimension was chosen for the device fabrication of the 'bad design'.

Similarly, for the 'good design' shown in Figure 6.6 (b), the length of the 50 wt.% Sb_2Te_3-PEDOT:PSS nanocomposite part was varied from 7 to 10 mm, as simulated in Figure 6.11 (a). The intersection temperature of 313 K occurred at 8 mm. This dimension was then used for the CG-TEC device fabrication. For the 'bad design' illustrated in Figure 6.7 (b), the length of the PEDOT:PSS was varied from 3 to 6 mm, and the intersection temperature of 313 K was found at 4 mm from the end (see Figure 6.11 (b)).

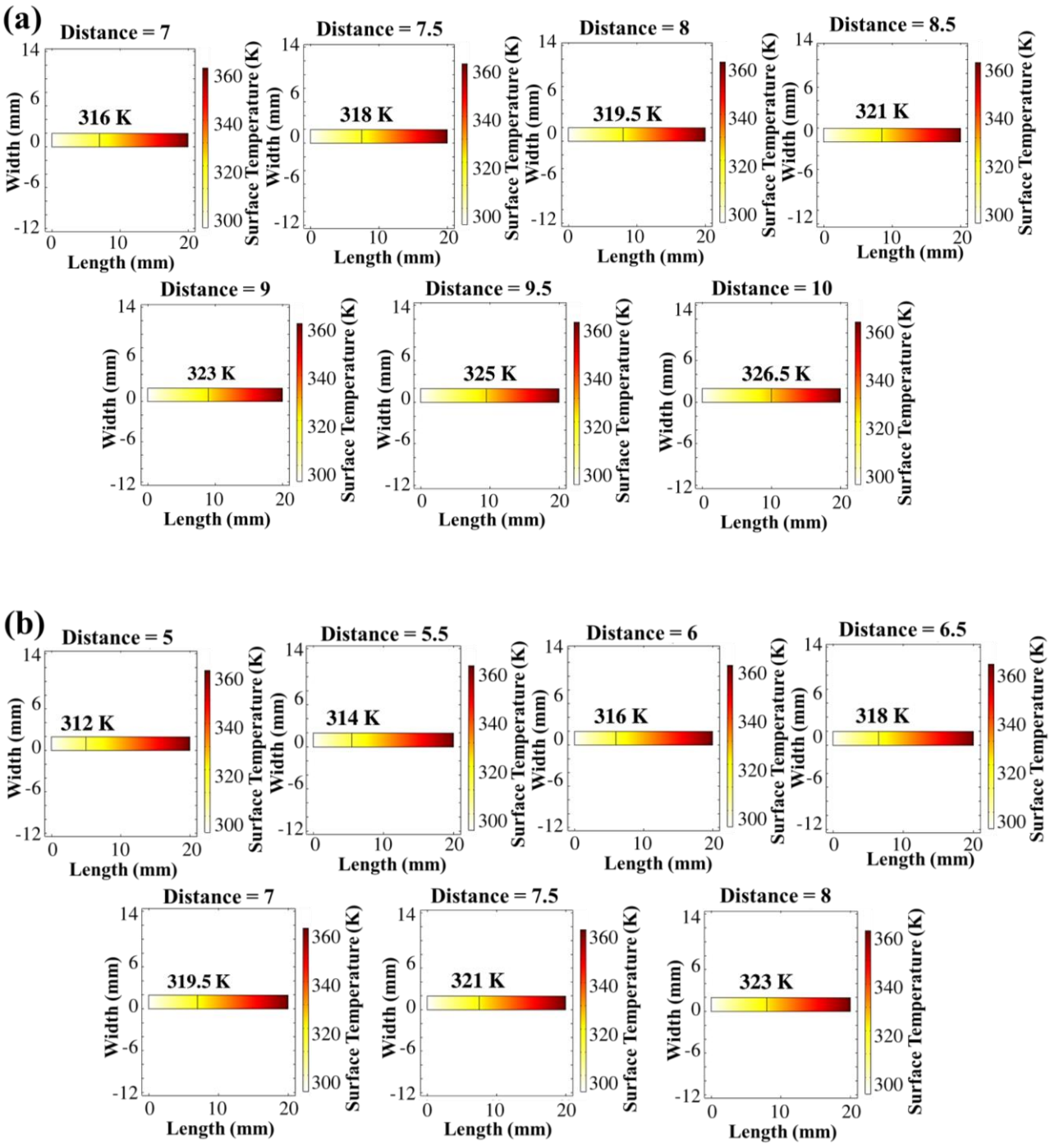

Figure 6.10 Temperature distribution profiles of (a) 'good design' and (b) 'bad design' for the CG-TECs comprising 15 wt.% Bi_2Te_3-PEDOT:PSS nanocomposite + PEDOT:PSS.

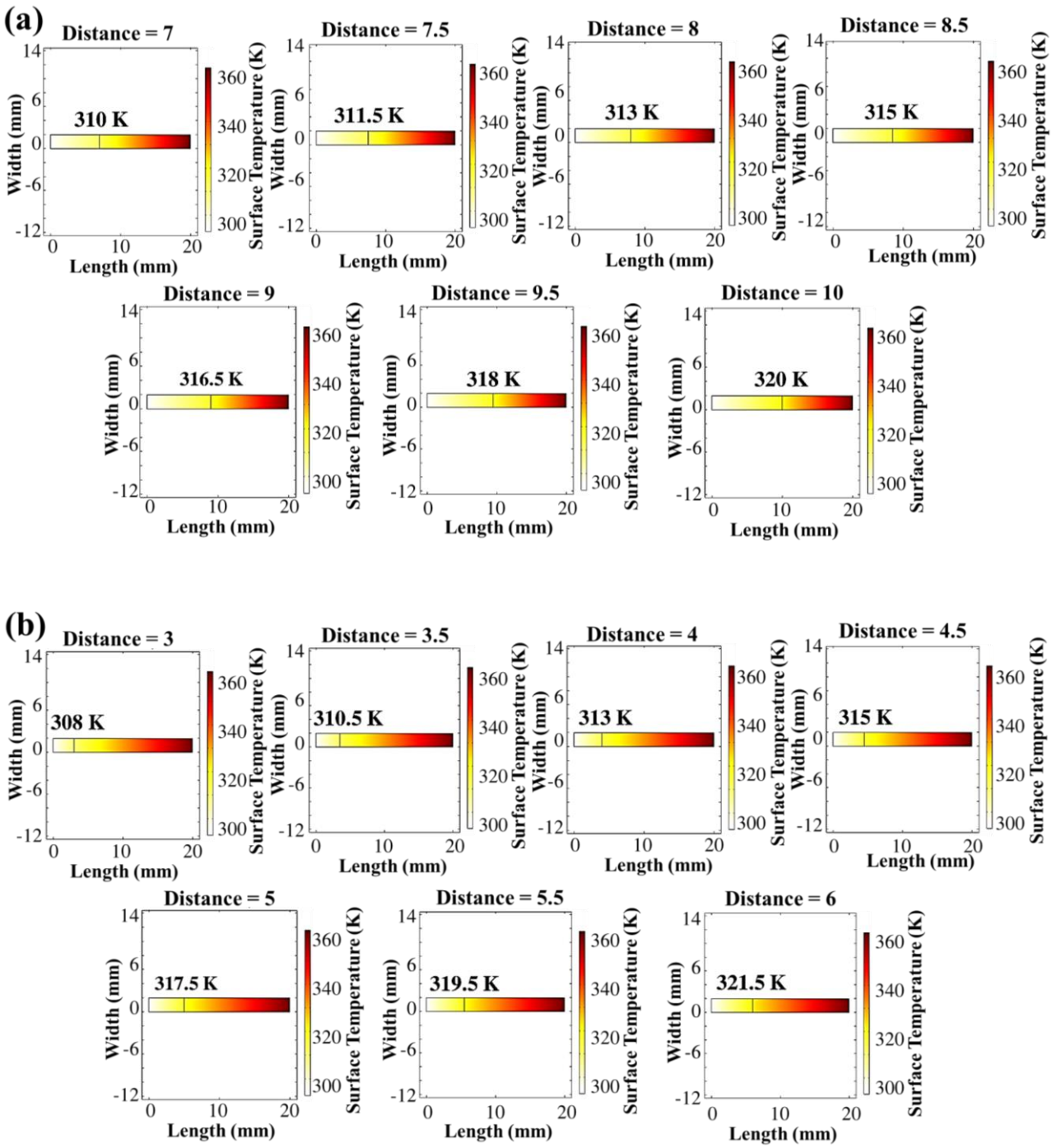

Figure 6.11 Temperature distribution profiles of (a) 'good design' and (b) 'bad design' for the CG-TECs comprising 50 wt.% Sb_2Te_3-PEDOT:PSS nanocomposite + PEDOT:PSS.

6.2.4 Fabrication of Compositionally Graded Thermoelectric Composites

For the CG-TEC comprising 15 wt.% Bi_2Te_3-PEDOT:PSS nanocomposite + PEDOT:PSS, the boundary location was determined to be approximately 7.5 mm from the cold end of a 20 mm long TE leg (i.e. 0 mm to 7.5 mm was composed of the 15 wt.% Bi_2Te_3-PEDOT:PSS nanocomposite, while 7.5 mm to 20 mm was the pristine PEDOT:PSS film, as shown in Figure 6.12 (a)). For the CG-TEC comprising 50 wt.% Sb_2Te_3-PEDOT:PSS + PEDOT:PSS, the boundary location was approximately 8 mm from the cold end (i.e. 0 mm to 8 mm was composed of the 50 wt.% Sb_2Te_3-PEDOT:PSS nanocomposite, whereas 8 mm to 20 mm was the pristine PEDOT:PSS film, as presented in Figure 6.12 (b)). As illustrated in Figures 6.12 (c) and (d), the AutoCAD-designed patterns were derived accordingly, and the CG-TECs were then printed via the AJP method.

Similarly, an extreme opposite case was designed by adopting a 'bad design' to verify the CG-TEC concept, as demonstrated in Figure 6.13. It should be noted that the individual components in these AJ-printed CG-TECs were connected without using additional electrical joints, thus avoiding the creation of interfaces and/or defects within the resulting TEG. The two parts were AJ-printed one after the other with a narrow overlap region (~250 μm in width), which will be further discussed in the next section. At the same time, TEGs that were based on the single-phase pristine PEDOT:PSS film, 15 wt.% Bi_2Te_3-loaded nanocomposite, and 50 wt.% Sb_2Te_3-loaded nanocomposite were prepared, respectively, as control samples to compare their TE performance with that of TEGs based on CG-TECs. The thickness values of all these AJ-printed TE nanocomposites used in this work ranged from 1 to 1.5 μm.

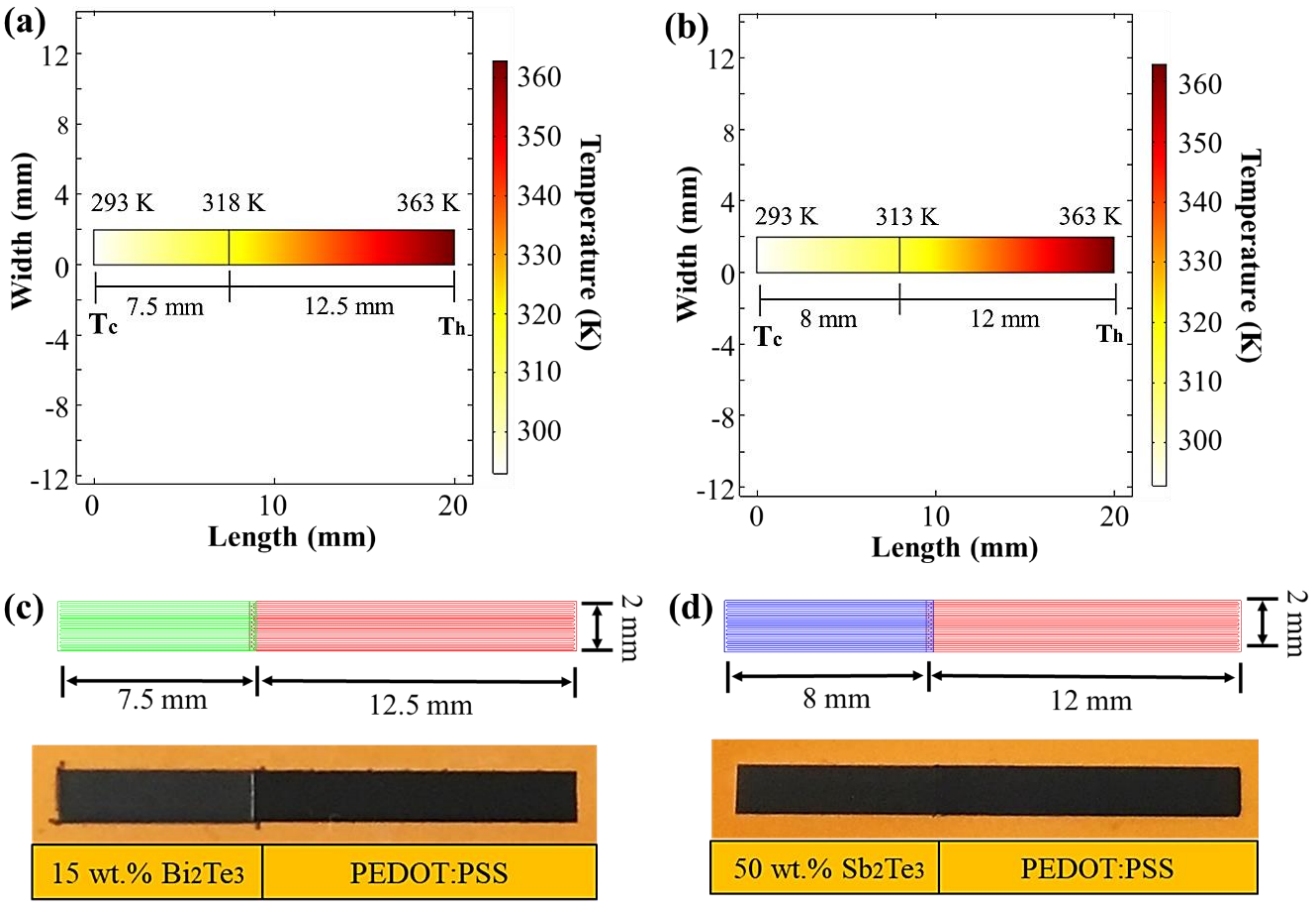

Figure 6.12 COMSOL simulation results showing the temperature distribution profile along (a) CG-TEC comprising 15 wt.% Bi_2Te_3-PEDOT:PSS nanocomposite + PEDOT:PSS for 'good design' and (b) CG-TEC comprising 50 wt.% Sb_2Te_3-PEDOT:PSS nanocomposite + PEDOT:PSS with 'good design', respectively. AutoCAD-designed pattern of the compositionally graded structure and photographic image of the AJ-printed of (c) CG-TEC comprising 15 wt.% Bi_2Te_3-PEDOT:PSS nanocomposite + PEDOT:PSS for 'good design', and (d) CG-TEC comprising 50 wt.% Sb_2Te_3-PEDOT:PSS nanocomposite + PEDOT:PSS for 'good design', respectively. (Figures taken from the author's work [252]. (CC BY 4.0))

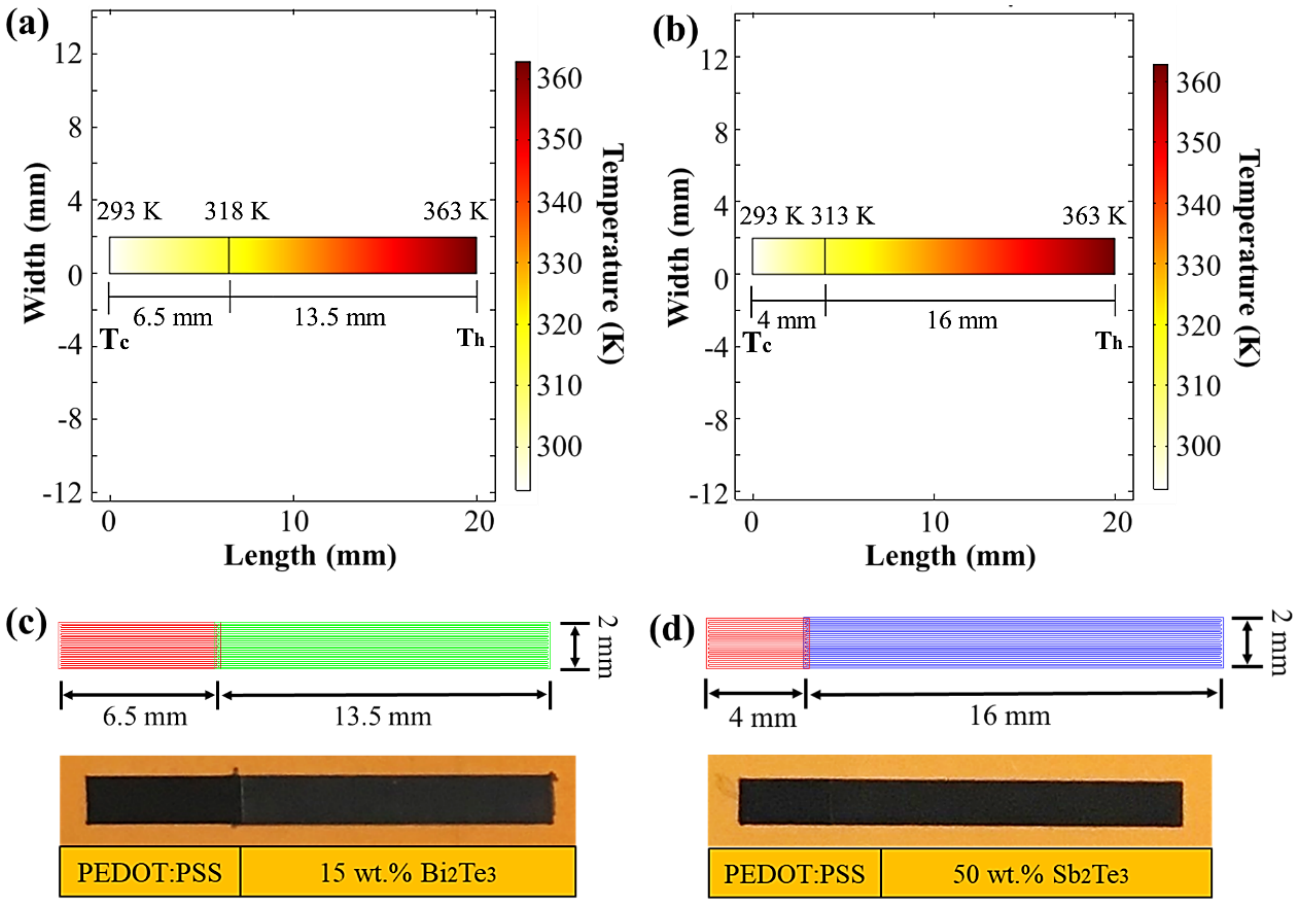

Figure 6.13 COMSOL simulation results showing the temperature distribution profile along (a) CG-TEC comprising PEDOT:PSS + 15 wt.% Bi_2Te_3-PEDOT:PSS nanocomposite for the 'bad design' and (b) CG-TEC comprising PEDOT:PSS + 50 wt.% Sb_2Te_3-PEDOT:PSS nanocomposite for the 'bad design', respectively. AutoCAD-designed patterns of the compositionally graded structure and photographic images of the AJ-printed (c) CG-TEC comprising PEDOT:PSS + 15 wt.% Bi_2Te_3-PEDOT:PSS nanocomposite for the 'bad design', and (d) CG-TEC comprising PEDOT:PSS + 50 wt.% Sb_2Te_3-PEDOT:PSS nanocomposite for the 'bad design', respectively. (Figures taken from the author's work [252]. (CC BY 4.0))

6.2.5 Interfaces of Compositionally Graded Thermoelectric Composites

As can be seen in Figure 6.14 (a), the AJ-printed CG-TEC structure had a transition region between each portion of the composite elements, wherein the transition region was continuously compositionally graded. The interface between two AJ-printed components was quite smooth and uniform. Based on the AutoCAD-designed pattern for printing in Figure 6.14 (b), there was a 250-μm overlap zone, where the material composition of that region should be a mixture of two components. However, since the printing order of the CG-TEC structure was such that the PEDOT:PSS part was printed first, followed by the 15 wt.% Bi_2Te_3-PEDOT:PSS nanocomposite on top, the optical microscope image in Figure 6.14 (c) and the SEM micrographs in Figures 6.14 (d) and (e) only show the surface morphology (i.e. mostly imaging the top layer of the 15 wt.% Bi_2Te_3-PEDOT:PSS nanocomposite part in the overlap zone). It should be noted that the lines seen in the images were artefacts of the printing, as it was done layer-by-layer. Moreover, by virtue of the fairly high printing resolution of the AJP technique as well as the precise control of the position and dimensions of deposited films, no connection issues were observed in the CG-TEC structures during fabrication. The overlap regions between different printed components were very well aligned in position, as revealed in Figures 6.14 (c) - (e). Also, the underlying PEDOT:PSS polymeric matrix could ensure the robust electrical contact across the interfaces.

Since the matrix of both components was PEDOT:PSS polymer across the whole length, the 15 wt.% Bi_2Te_3-PEDOT:PSS nanocomposite phase and the pure PEDOT:PSS phase were well mixed in the transition region, thereby providing a variation of composition over a narrow region across the interfaces. In other words, there was no step-change in composition between two components of the CG-TEC. This smoothly graded interface served to avoid otherwise common interface problems, e.g. cracks and other defects introduced and accumulated due to the thermal misfit and thermo-mechanical stress. In particular, the diffusion or contamination issues, arising at the joints of dissimilar components, could also significantly degrade the performance and lifetime of the TEG. More importantly, unlike other segmented FG-TEMs,

the joining and soldering processes to assemble different components could be avoided in the AJ-printed CG-TECs. In the case of a poor joining procedure, considerably high thermal and contact resistances are often introduced by the mismatch at the interfaces, which could largely reduce the power output of TEGs.[185] Besides, precisely positioning solders and/or electrodes at the interfaces is technically challenging.[172] To the best of the author's knowledge, this CG-TEC concept was proposed, for the first time, to solve interface-related issues effectively.

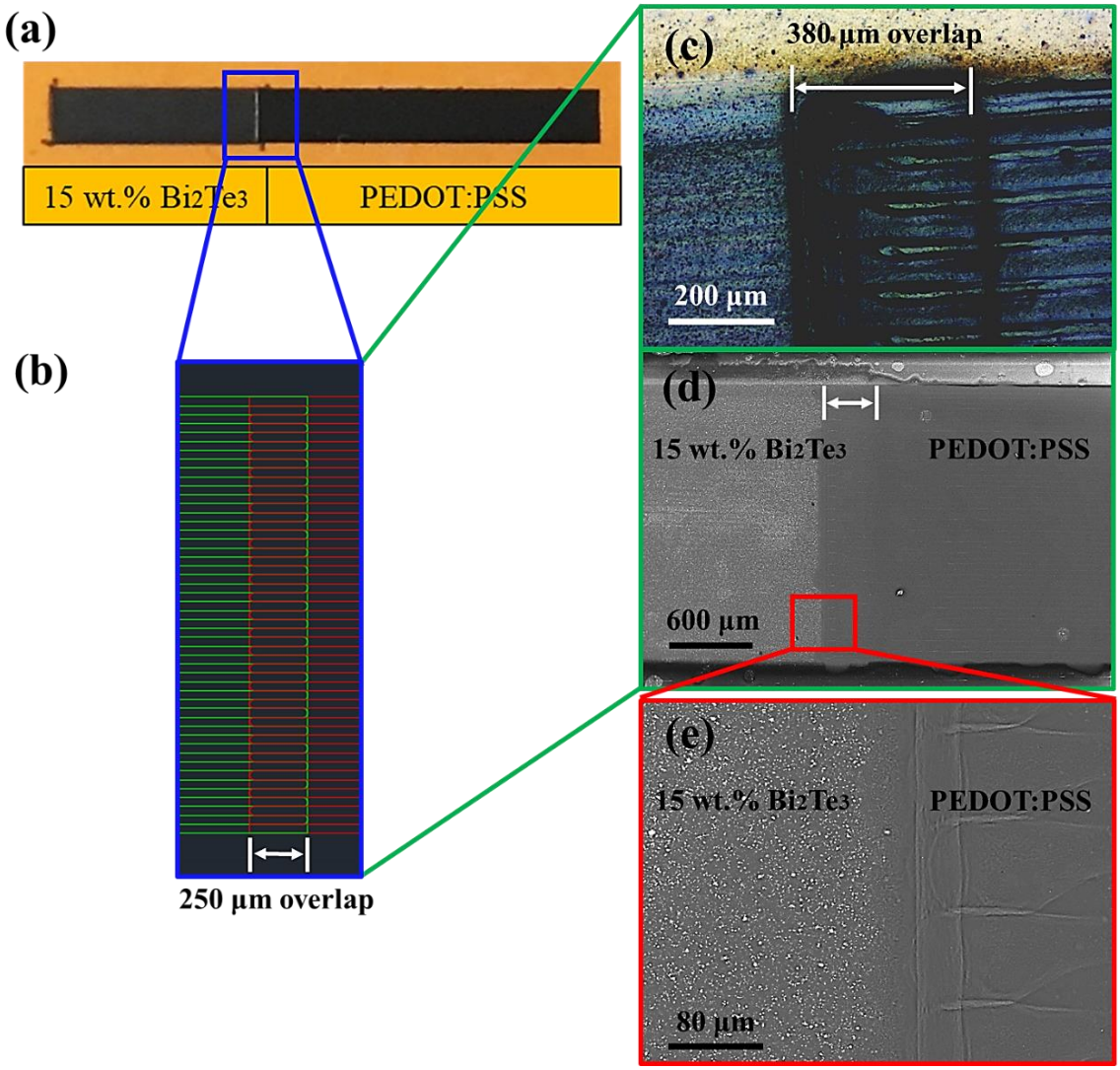

Figure 6.14 (a) Photographic image of the AJ-printed CG-TEC comprising 15 wt.% Bi_2Te_3-PEDOT:PSS nanocomposite + PEDOT:PSS. (b) Enlarged AutoCAD-designed pattern showing the overlap zone between two different components, where the green part represents the 15 wt.% Bi_2Te_3-PEDOT:PSS nanocomposite, while the red part is the pristine PEDOT:PSS film. (c) Optical microscope image and (d) SEM image of the transition region between two different components of the CG-TEC, where more details of the interface are revealed in (e) the enlarged SEM image. (Figures taken from the author's work [252]. (CC BY 4.0))

6.3 Compositionally Graded Thermoelectric Generators

6.3.1 Performance of Compositionally Graded Thermoelectric Generators

Here, different compositionally graded thermoelectric generators (CG-TEGs) and their non-compositionally graded homogeneous (i.e. single-phase) counterparts were fabricated, and their TE performance was subsequently evaluated, as detailed in Section 3.10.2. All these TEGs were tested under the same ΔT of 70 K, and a thermal camera was used here to monitor the localised temperature values of the cold and hot sides, as shown in Figure 6.15. Due to the resolution limit of the used thermal camera, the obtained temperature distribution profiles were not distinct. Future work by using a higher-resolution thermal camera is therefore required.

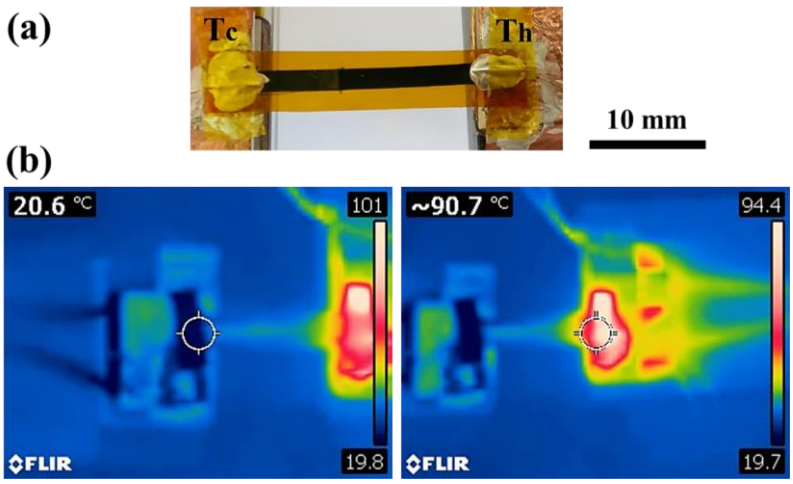

Figure 6.15 (a) Photographic and (b) thermal images of an AJ-printed CG-TEG under a constant applied ΔT of ~70 °C. The circle highlights the localised temperature reading.

Figure 6.16 presents measurements of voltage and power outputs plotted as a function of the external load resistance for different single-phase TEGs as well as CG-TEGs under the same ΔT. Impedance matching with all these TEGs revealed that they all delivered maximum power outputs across an external load resistance of 50 Ω. For a more straightforward comparison of the power output between different samples, all the power output values at the load resistance of 50 Ω were re-plotted in Figure 6.17, rather than comparing their *ZT* values. This would inherently include the effect of thermal conductivity, as it is the actual power outputs that are compared here, not the intrinsic *ZT* value. It is evident that each of the CG-

TEGs outperformed their single-phase counterparts in terms of both voltage and power outputs. Among them, the CG-TEG comprising 15 wt.% Bi_2Te_3-PEDOT:PSS nanocomposite + PEDOT:PSS exhibited the most enhanced power output up to ~13 nW and a power area density of ~0.03 μW/cm^2 (i.e. volumetric power density of ~100 μW/cm^3). The CG-TEG comprising 50 wt.% Sb_2Te_3-PEDOT:PSS nanocomposite + PEDOT:PSS came second with a power output of ~10 nW. The power outputs of these CG-TECs were higher than that of their single-phase counterparts by a factor of almost 2. Additionally, the CG-TEG comprising 15 wt.% Bi_2Te_3-PEDOT:PSS nanocomposite + 50 wt.% Sb_2Te_3-PEDOT:PSS nanocomposite still showed higher power outputs than their single-phase counterparts. But individually, these components had lower PF values than the PEDOT:PSS, which led to its relatively lower power output than the other two CG-TEGs. These results clearly show that the CG-TEG design is particularly effective in enhancing the TE performance and power outputs compared with non-compositionally graded TEGs, with more than double improvement in the power output. This provided the possibility of achieving higher average PF and/or *ZT* values over a wide temperature range by grading different compositions. Since only a single TE leg was utilised in each TEG for the ease of comparison between different samples, only a relatively small difference in the power output was seen. However, this difference could be significantly amplified by the use of a plurality of such TE legs in a practical TEG application.

In order to further verify this CG-TEC concept, the power outputs of CG-TEGs were tested in two configurations. Firstly, the ΔT was applied along the correct forward direction, i.e. the 15 wt.% Bi_2Te_3-loaded nanocomposite and the 50 wt.% Sb_2Te_3-loaded nanocomposite part on the cold side, respectively, while the PEDOT:PSS on the hot side, which was previously referred as the ‘good design’. Secondly, the ΔT direction was reversed, such that the respective PF values were not optimised in the right temperature range order, i.e. ‘bad design’. In the case of single-phase TEGs, there was no significant difference in their power outputs when switching the ΔT direction, as expected. However, more than 50% drop in P_{max} was seen in both CG-TEGs when the ΔT was applied in a reverse direction (see Figure 6.18), indicating that these CG-TEGs were not fully utilised in their optimum operating conditions. To further

prove the concept that this CG-TEC design is an effective way to optimise the TE performance, an extreme opposite case was designed by adopting a 'bad design' as referred above. It can be seen from Figure 6.19 that the power outputs of both CG-TEGs with 'bad design' were substantially deteriorated, leading to the values that were even lower than that of their single-phase counterparts. Hence, proper material matching and device design are of utmost importance to maximise the power output of the CG-TEGs.

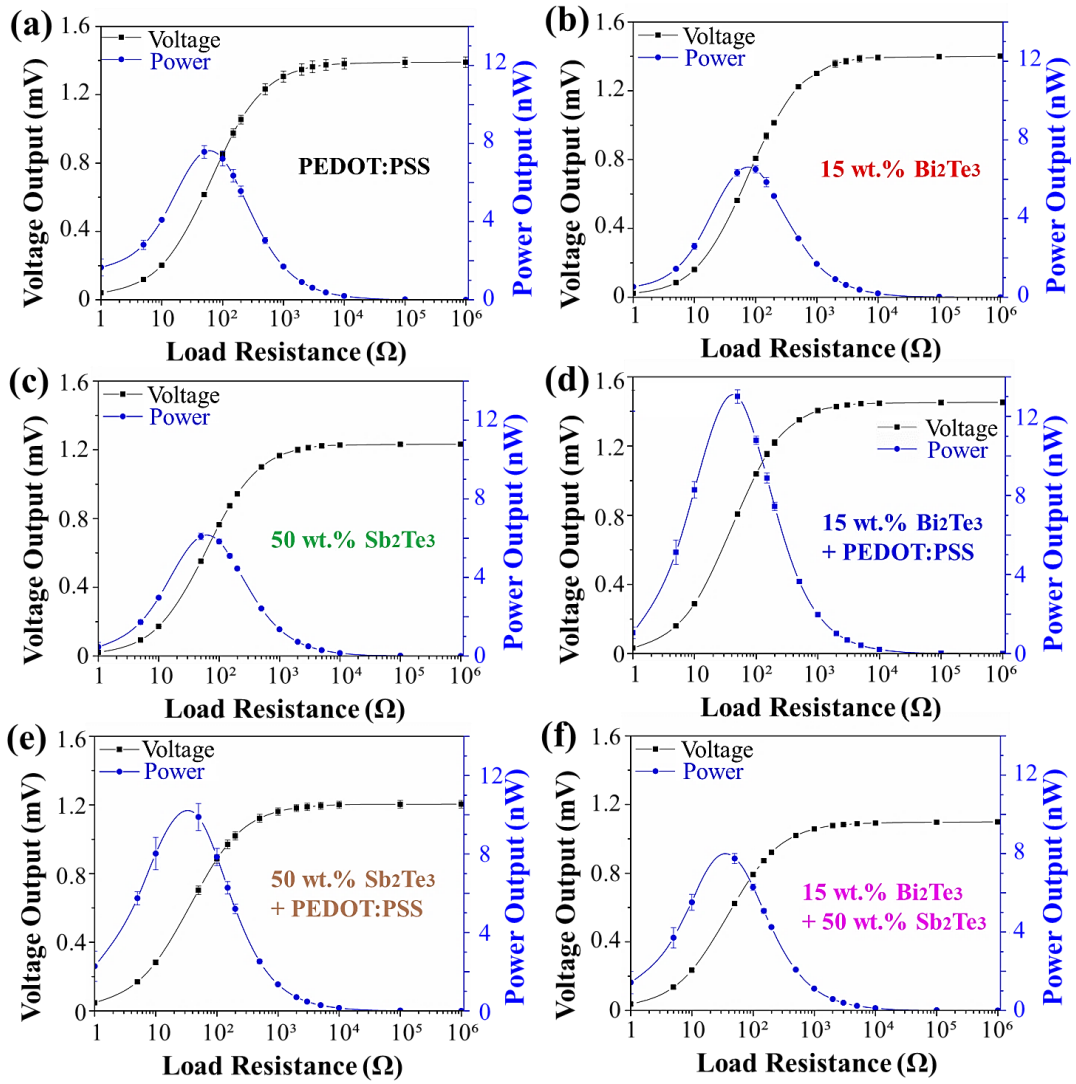

Figure 6.16 Measurements of voltage and power outputs against various external load resistances of (a) pristine PEDOT:PSS film (non-compositionally graded), (b) 15 wt.% Bi_2Te_3-PEDOT:PSS nanocomposite (non-compositionally graded), (c) 50 wt.% Sb_2Te_3-PEDOT:PSS nanocomposite (non-compositionally graded), (d) CG-TEG comprising 15 wt.% Bi_2Te_3-PEDOT:PSS nanocomposite + PEDOT:PSS, (e) CG-TEG comprising 50 wt.% Sb_2Te_3-PEDOT:PSS nanocomposite + PEDOT:PSS, and (f) CG-TEG comprising 15 wt.% Bi_2Te_3-PEDOT:PSS nanocomposite + 50 wt.% Sb_2Te_3-PEDOT:PSS nanocomposite, respectively, under the same ΔT of 70 K. (Figures taken from the author's work [252]. (CC BY 4.0))

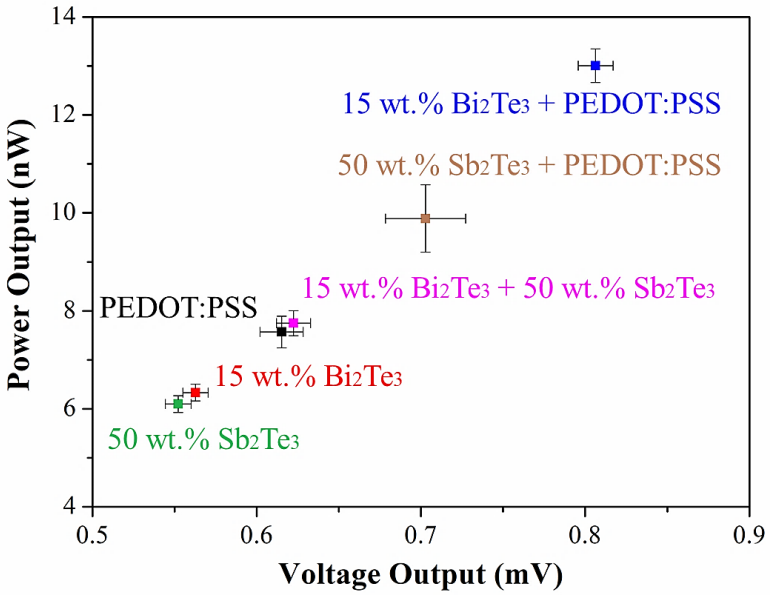

Figure 6.17 Comparison of voltage and power outputs of 6 different TEGs under the same applied ΔT of 70 K across an external load resistance of 50 Ω. (Figures taken from the author's work [252]. (CC BY 4.0))

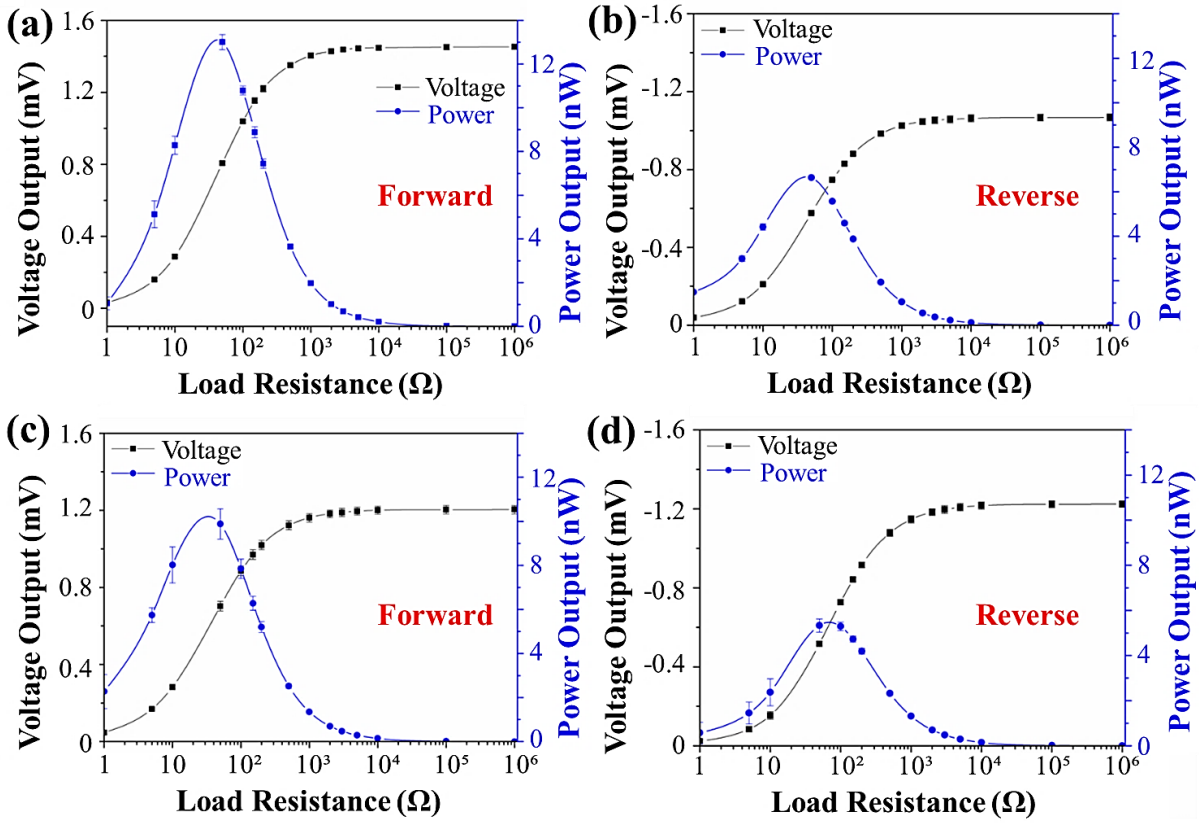

Figure 6.18 Measurements of voltage and power outputs of the CG-TEG comprising 15 wt.% Bi_2Te_3-PEDOT:PSS nanocomposite + PEDOT:PSS in (a) forward direction and (b) reverse direction, and the CG-TEG comprising 50 wt.% Sb_2Te_3-PEDOT:PSS nanocomposite + PEDOT:PSS in (c) forward direction and (d) reverse direction.

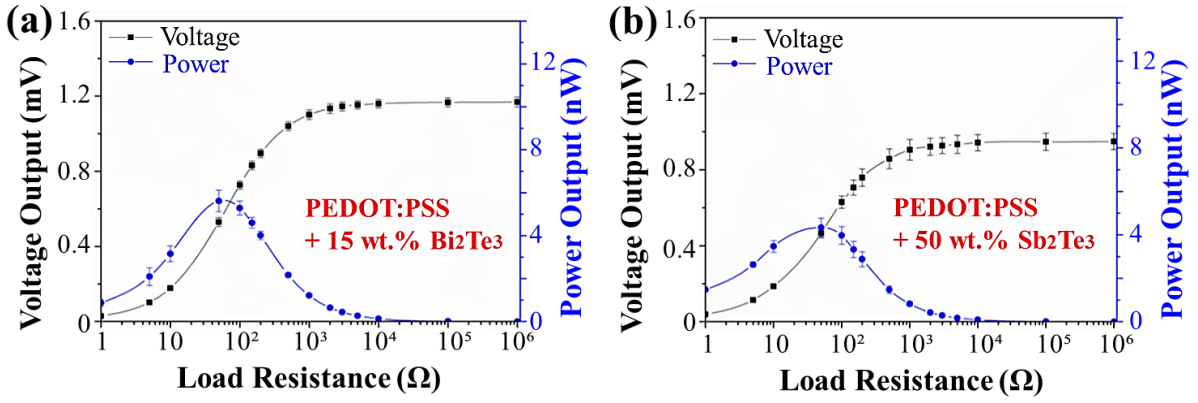

Figure 6.19 Measurements of voltage and power outputs of (a) the CG-TEG comprising 15 wt.% Bi_2Te_3-PEDOT:PSS nanocomposite + PEDOT:PSS for 'bad design', and (b) the CG-TEG comprising 50 wt.% Sb_2Te_3-PEDOT:PSS nanocomposite + PEDOT:PSS for 'bad design'.

6.3.2 Prototype of Compositionally Graded Thermoelectric Generator

To further demonstrate the practical application of these CG-TEGs, 20 repeating TE legs of CG-TECs comprising 15 wt.% Bi_2Te_3-PEDOT:PSS nanocomposite + PEDOT:PSS, were AJ-printed on a flexible PI sheet (see Figure 6.20 (a)). These TE legs were connected electrically in series and thermally in parallel by using AJ-printed Ag electrodes. This CG-TEG was then rolled into a coiled structure for practical applications, as demonstrated in Figures 6.20 (b) and 6.21 (a), showing its excellent mechanical flexibility. Thermal images of the CG-TEG in Figure 6.21 (b) were taken for measuring the ΔT between the top and bottom parts along these TE legs, where a hot plate was used as a heat source to create a ΔT. This coiled CG-TEG prototype with a total internal sample resistance (R_S) of ~954 Ω could deliver open-circuit voltage (V_{oc}) of ~12.5 mV, short-circuit current (I_{sc}) of ~11.3 μA, and maximum power output (P_{max}) of ~41nW, when exposed to an operating ΔT of ~40 °C. It shows that this CG-TEG could be used for the thermal energy harvesting in a wearable device, or for the waste heat recovery, such as from hot water pipes up to 100 °C. Moreover, its power output could be further enhanced by connecting with other *n*-type TE legs in series to form a number of *p*-*n* junctions, thereby possibly achieving the power density level that is necessary for an integrated self-powered system, e.g. wireless sensor networks and IoT applications.[50]

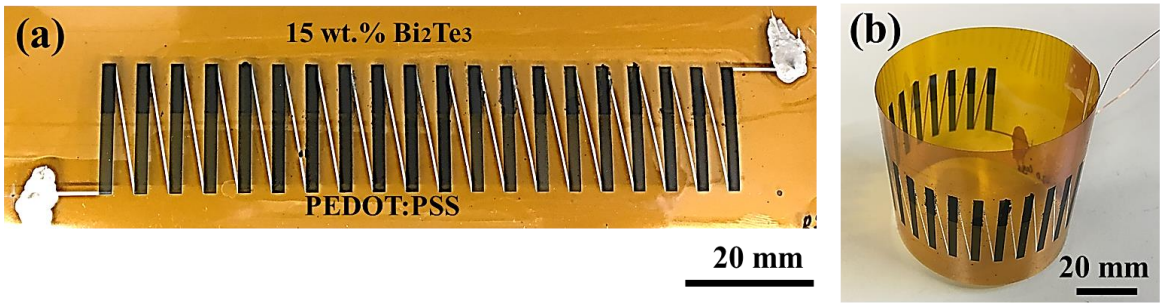

Figure 6.20 (a) Photographic image of a CG-TEG AJ-printed on a flexible PI sheet with 20 repeating TE legs of CG-TECs comprising 15 wt.% Bi_2Te_3-PEDOT:PSS nanocomposite + PEDOT:PSS. (b) It could be rolled into a coiled structure with excellent mechanical flexibility.

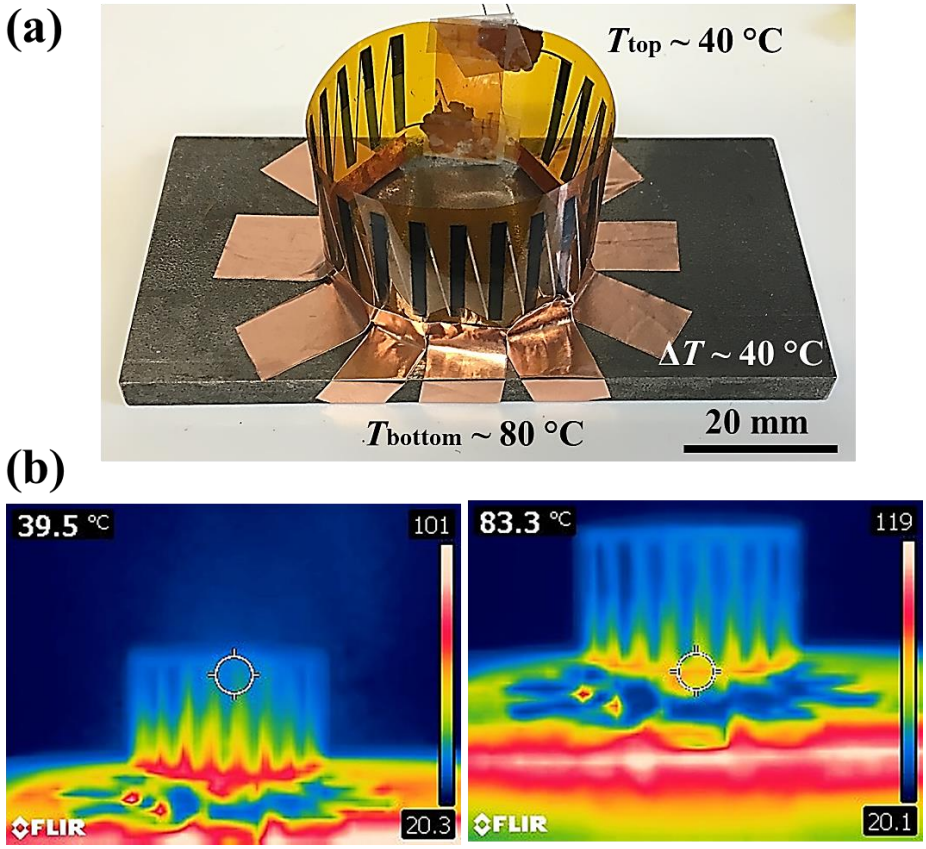

Figure 6.21 (a) Photographic image of the coiled CG-TEG prototype with electrical connections for the measurement of voltage and power outputs. (b) Thermal images showing the measurement of the temperature gradient between the top and bottom parts of the CG-TEG. The circle highlights the localised temperature reading.

6.4 Summary

In this work, the author has explored the temperature-dependent TE properties of different AJ-printed PEDOT:PSS-based nanocomposites loaded with various nano-inclusions, ranging from Bi_2Te_3 nanoparticles, Sb_2Te_3 nanoflakes, to MWCNTs. By selecting proper compositions based on the temperature-dependent PF profiles, different dual-segment CG-TECs have been designed to maximise their average PF values across the entire temperature gradient. Their power output values were then found to be superior to their non-compositionally graded counterparts. This proved that the CG-TEG design could provide a means of significantly improving the TE performance and energy conversion efficiency of the whole TEG device, highlighting its potential for being employed in practical energy harvesting applications. This finding hence opens the door to a wide range of material combinations comprising a variety of existing conducting polymers and/or inorganic TE nano-fillers, which could be tailored for the use across a specific temperature gradient. It is worthwhile mentioning that this work has led to the filing of a patent *"Thermoelectric materials, devices and methods of production thereof"*, earlier this year.

Chapter 7

Stretchable Thermoelectric Generators

Existing fabrication methods for stretchable TEGs in the literature are currently too sophisticated to be scaled up, and the associated cost may be too high.[204] Therefore, simple and scalable fabrication processes are paramount to be explored. In this chapter, the author has combined a highly stretchable serpentine structure with the facile and scalable aerosol-jet printing as well as film lift-off techniques for the fabrication of stretchable and potentially wearable TEGs. Single-layer free-standing stretchable TE structures having different device designs have been first developed. Subsequently, their TE performance and mechanical stretchability under different applied temperature gradients as well as imposed mechanical conditions have been evaluated by rigorous stretchability tests. A more extensive fatigue test has been carried out on these stretchable TE structures to test their reliability over prolonged stretching cycles. Furthermore, a multilayered structure has been fabricated as a stretchable TEG prototype. Also, the CG-TEC concept has been incorporated into the stretchable structure to attain further improvement of TE performance. Lastly, substrate-based stretchable TEGs have been explored by applying PDMS and PU elastomers as stretchable substrates.

7.1 Morphology Characterisation of Stretchable Structures

7.1.1 In-plane Structure

Figure 7.1 shows the morphology of the AJ-printed stretchable serpentine TE structure with in-plane design. A dense and compact film structure with smooth edges was obtained on each printed layer by virtue of the excellent printing quality of the AJP method. More cross-sectional features of the free-standing TE structure were revealed in Figure 7.2. No apparent cracks, fractures, or residual impurities were observed after the film lift-off process. This confirms that the film lift-off approach is a facile and efficient way to produce free-standing stretchable structures. As shown in Figure 7.3, single-layer structures of different components (i.e. PI and PEDOT:PSS) were individually AJ-printed and measured. The average thickness and width of the PI supporting layer were measured to be ~22 μm and ~240 μm, respectively, while the PEDOT:PSS film had the thickness of ~3 μm and width of ~165 μm. The total thickness of the free-standing TE structure was ~25 μm, and the width was ~240 μm.

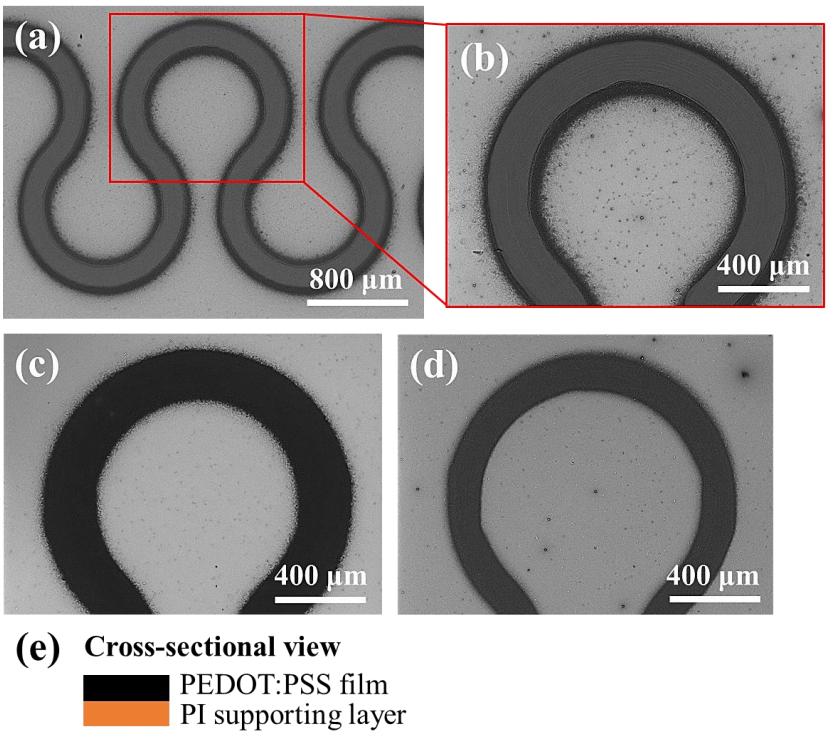

Figure 7.1 (a) Top-down SEM image of the serpentine TE structure with in-plane design, where (b) shows its enlarged view. (c) is the PI supporting layer. (d) is the PEDOT:PSS film. (e) The inset illustrates the cross-sectional design of different stacked layers.

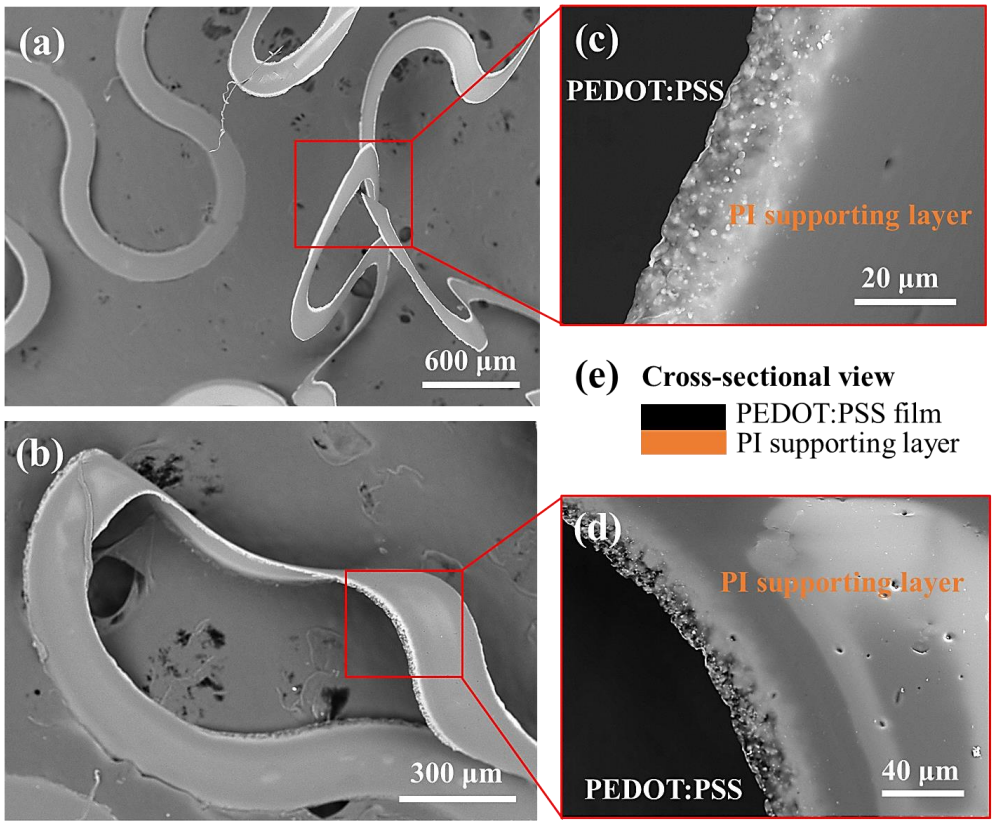

Figure 7.2 Cross-sectional SEM images (a) and (b) of the free-standing TE structure with in-plane design, where the enlarged images (c) and (d) reveal more details of their cross-section. (e) The inset illustrates the cross-sectional design of different stacked layers.

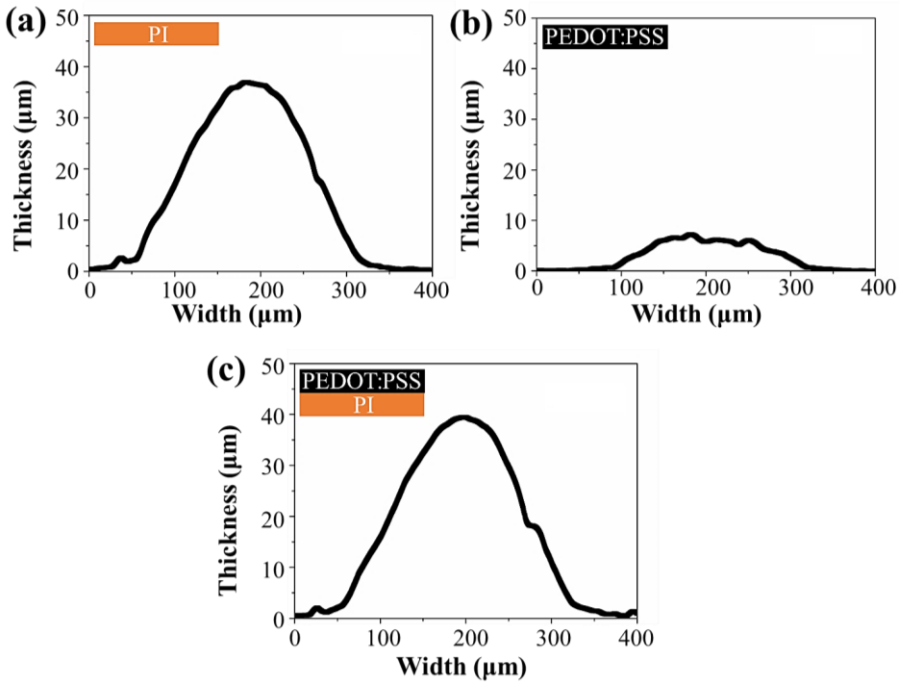

Figure 7.3 Profilometer thickness measurements of (a) the PI supporting layer, (b) the PEDOT:PSS film, and (c) the free-standing TE structure, respectively. Their insets illustrate the cross-sectional designs of different stacked layers.

7.1.2 Out-of-plane Structure

Figure 7.4 shows the morphology of the single-layer AJ-printed stretchable TE structure with out-of-plane design. The PI used as the supporting layer has the thickness of ~15 µm and the width of ~490 µm (see Figure 7.5 (a)). The PEDOT:PSS was employed as the active TE material with the thickness of ~4 µm and the width of ~320 µm (see Figure 7.5 (b)). The Ag was utilised as the conducting electrode with the thickness of ~5 µm and the width of ~160 µm (see Figure 7.5 (c)). Similar to the above-discussed in-plane structure, this out-of-plane structure possessed dense and compact film structures with smooth edges, which were seen in all the PI supporting layer, PEDOT:PSS film, and Ag electrode.

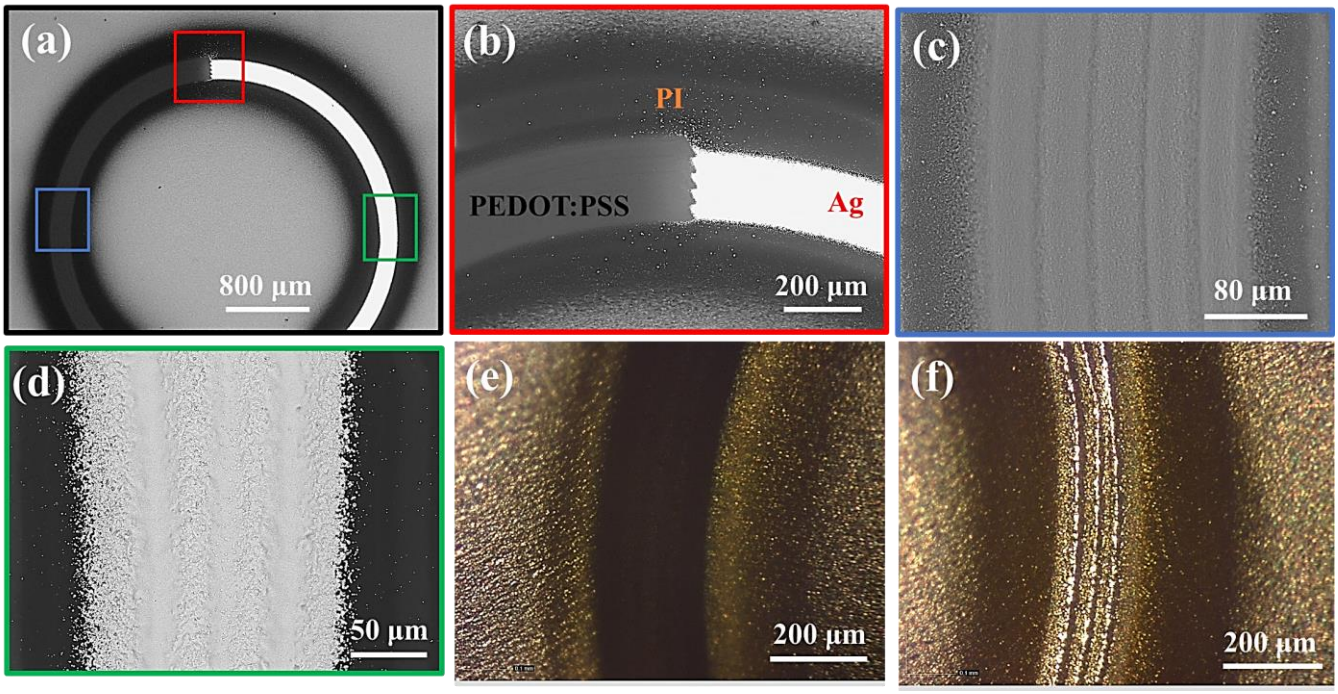

Figure 7.4 (a) Top-down SEM image of the single-layer AJ-printed stretchable TE structure with out-of-plane design. (b) reveals the interface between (c) the PEDOT:PSS film and (d) the Ag electrode. (e) and (f) show their optical microscope images, where the darker part represented the PEDOT:PSS film, while the brighter part was the Ag electrode.

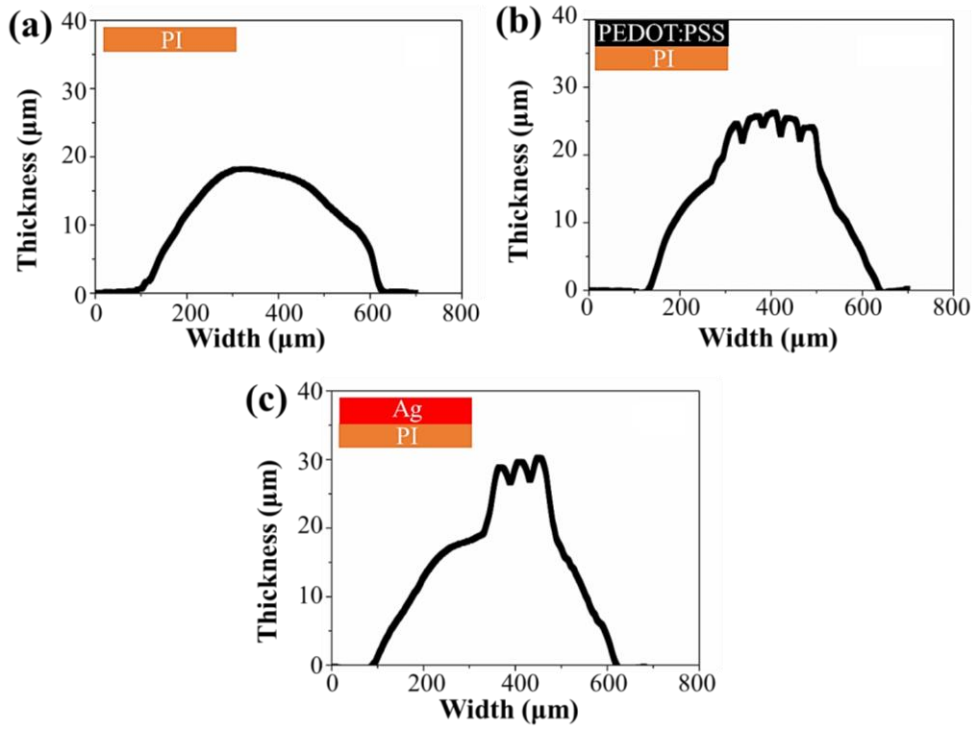

Figure 7.5 Profilometer thickness measurements of (a) the PI supporting layer, (b) the PEDOT:PSS film AJ-printed on top of the PI layer, and (c) the Ag electrode AJ-printed on top of the PI layer. Their insets illustrate the cross-sectional designs of different stacked layers.

7.1.3 Multilayered Structure

For practical stretchable TEG application, three layers of materials were stacked up into one whole free-standing stretchable TEG device via the multilayer printing method that was elaborated in Section 3.10.3. Figure 7.6 displays the morphology of the 3-layer AJ-printed stretchable TE structure. In between each layer, a PI film was employed as the supporting and encapsulating layer to prevent electrical shorting between other layer of materials. In order to protect the stretchable TE structure from detrimental environmental factors and/or mechanical failure during use, a PI encapsulation layer was AJ-printed on top to package the whole device, as presented in Figure 7.7. As plotted in Figure 7.8, the dimensions of different layered structures were investigated in detailed. The total thickness and width of this multilayered TE structure were found to be ~70 μm and ~400 μm, respectively.

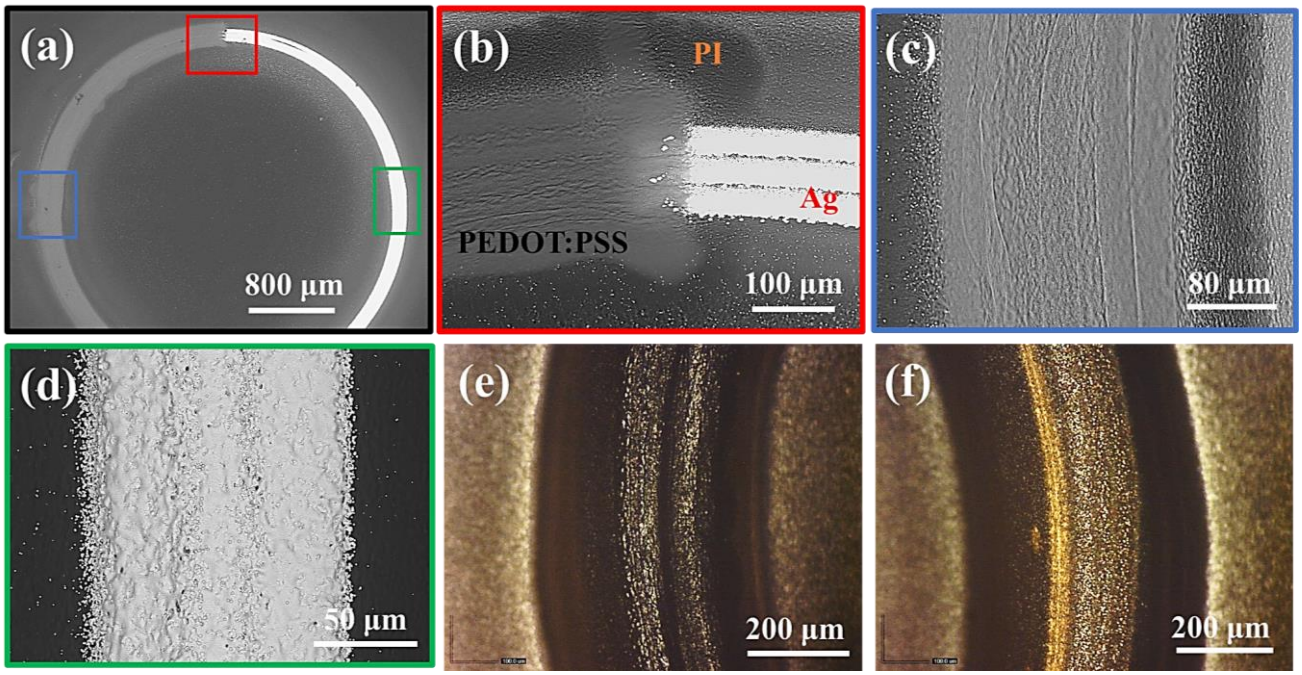

Figure 7.6 (a) Top-down SEM image of the 3-layer AJ-printed stretchable TE structure with out-of-plane design, which was stacked up with 3 layers of materials into one whole free-standing TE structure. (b) reveals the interface between (c) the PEDOT:PSS film and (d) the Ag electrode. (e) and (f) show their optical microscope images, where the darker part represented the PEDOT:PSS film, while the brighter part was the Ag electrode.

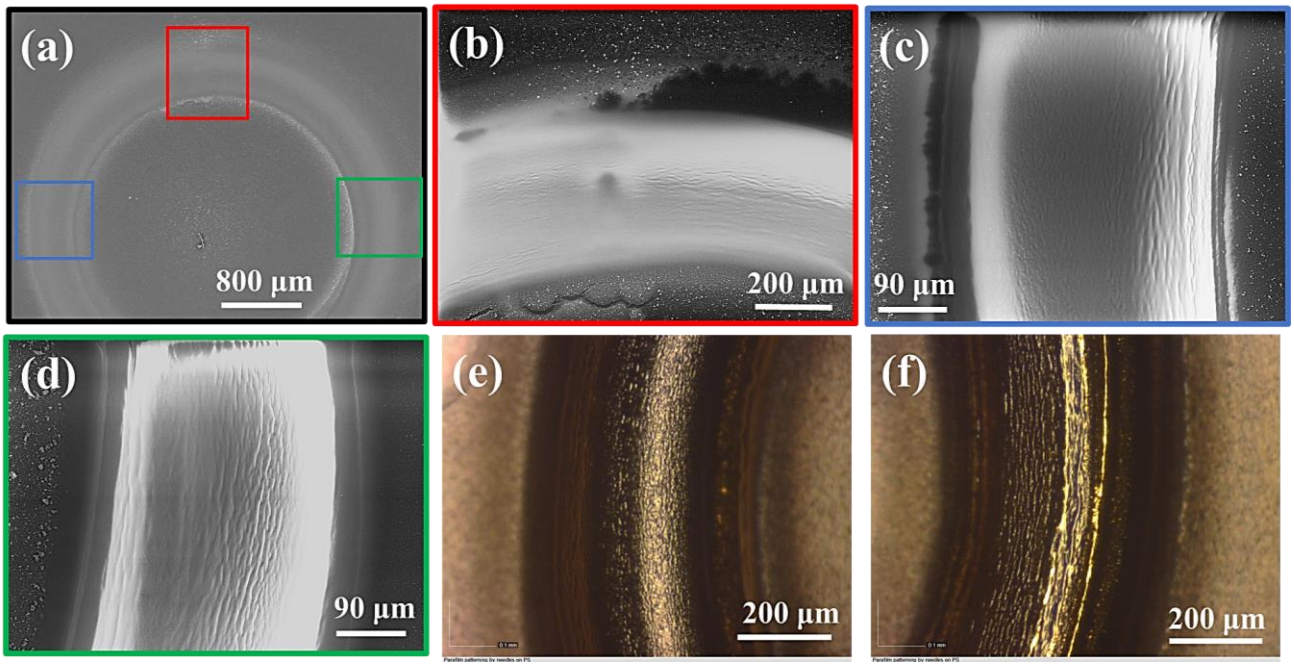

Figure 7.7 (a) Top-down SEM image of the 3-layer AJ-printed stretchable TE structure with out-of-plane design, which was encapsulated with a PI layer on top. (b) reveals the interface between (c) the PEDOT:PSS film and (d) the Ag electrode. (e) and (f) show their optical microscope images, where the PI film fully packaged the whole device.

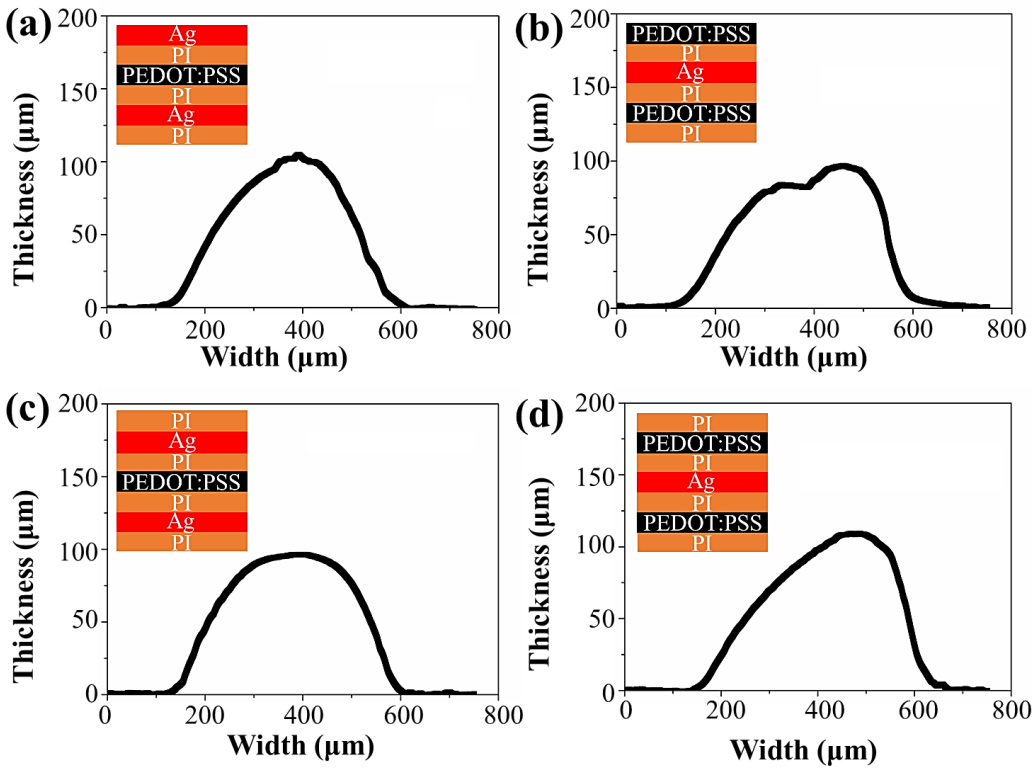

Figure 7.8 Profilometer thickness measurements of different parts of the 3-layer AJ-printed stretchable TE structure with out-of-plane design. Their insets illustrate the cross-sectional designs of different stacked layers.

7.2 Simulation of Stretchable Structures

7.2.1 In-plane Structure

Theoretical modelling based on the ABAQUS simulation has been conducted on different stretchable serpentine structures when being stretched to 50%. As can be seen in Figure 7.9, the local strain of the serpentine PI supporting structure was mainly concentrated at the edges, leaving the strain homogeneously distributed along the inner structure with comparatively low strain values. Due to the novel serpentine structure, the free-standing structure was mostly stretched via the deformation of its geometry rather than the materials theoretically. As a result, the mechanical stretchability of this structure was significantly improved owing to no damage on the materials when being stretched at lower strains.

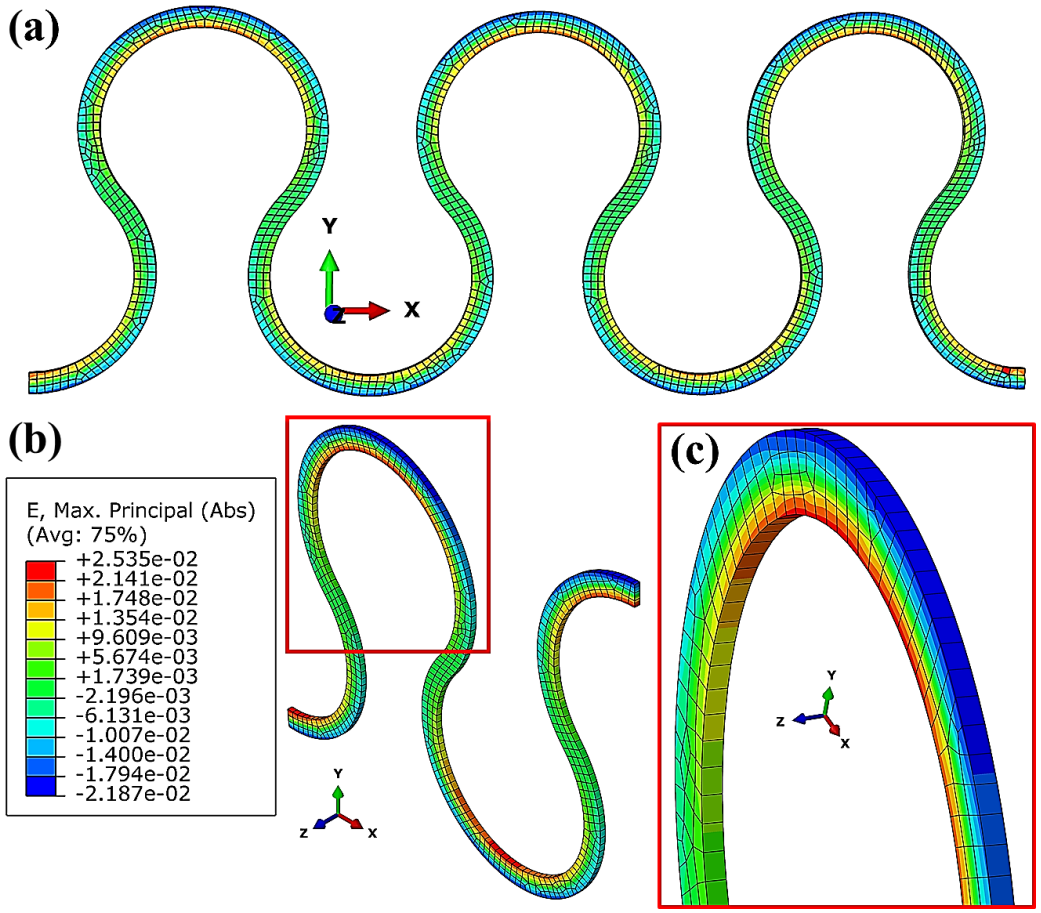

Figure 7.9 ABAQUS simulation on the strain distribution of the serpentine PI supporting structure when being stretched to 50%. (a) is the top-down view, (b) is the side view, and (c) is the enlarged view, revealing more details of the strain distribution.

Figure 7.10 demonstrates that the local strain distribution of the serpentine PEDOT:PPS-PI composite structure was akin to that of the above PI supporting structure. The twist of the serpentine geometry and the PI supporting layer synergistically helped accommodate most mechanical deformation and strain so as to protect the printed PEDOT:PSS film from high-stress level.[159] The tension on the surface of PEDOT:PPS film maintained almost unchanged as the original state, indicating that there was little influence on the inner active materials and their electrical characteristics when being stretched. Additionally, no evident strain concentration was seen at the interfaces between different material layers, which might be ascribed to the small difference in their Young's moduli as well as the good adhesion between different material layers where a firm bonding was formed by the co-curing process.

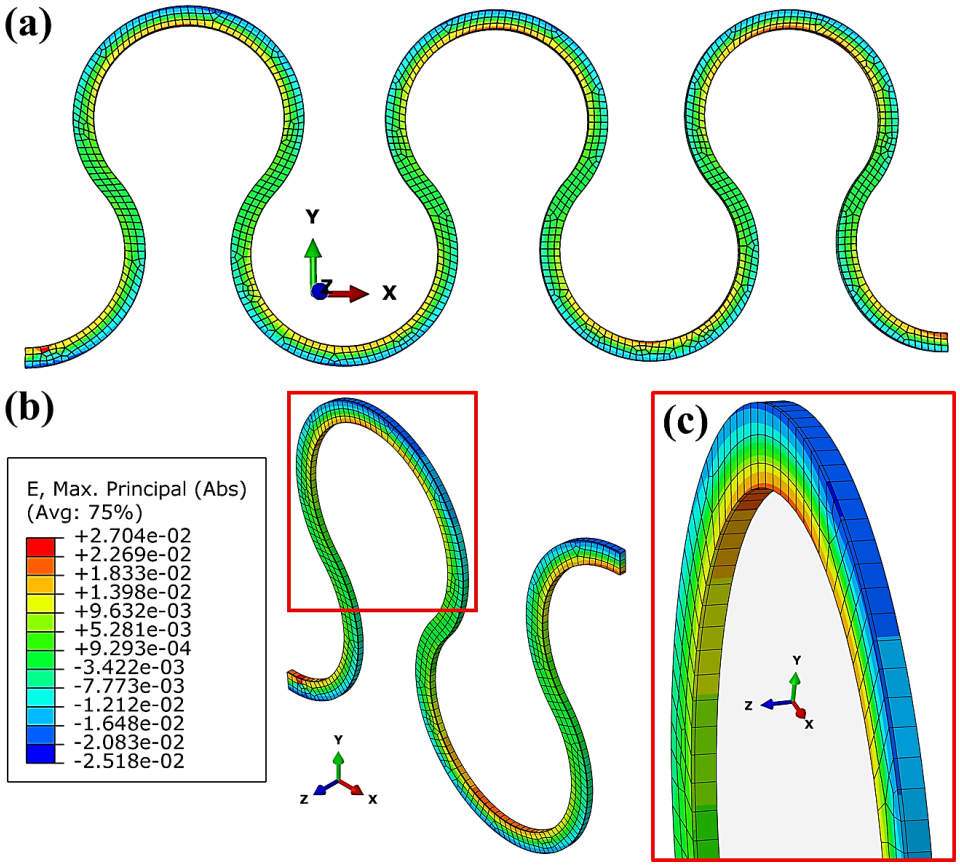

Figure 7.10 ABAQUS simulation on the strain distribution of the serpentine PEDOT:PSS-PI composite structure with in-plane design when being stretched to 50%. (a) is the top-down view, (b) is the side view, and (c) is the enlarged view, revealing more details of the strain distribution. The top thinner layer is the PEDOT:PSS, while the bottom thicker layer is the PI.

7.2.2 Out-of-plane Structure

The ABAQUS simulation result in Figure 7.11 reveals the strain distribution in the serpentine PEDOT:PPS-Ag-PI composite structure with out-of-plane design. It can be seen that both PEDOT:PSS films and Ag electrodes should be well protected by the PI supporting layer from mechanical strains. Akin to the above in-plane structure, the PI supporting layer was the major component that accommodated most local strains, which should be mainly concentrated at the edges of the out-of-plane composite structure. The PEDOT:PSS and Ag parts were the limiting factors that constrained the overall stretchability of the composite structure here. Thus, PEDOT:PSS films and Ag electrodes were designed to be AJ-printed in the centre so that they could be mostly unaffected when being stretched. More importantly, the serpentine shape could render both PEDOT:PPS films and Ag electrodes geometrically stretchable. Hence, the PI

supporting layer is indispensable here. Without the support and protection from the PI, AJ-printed PEDOT:PSS films and Ag electrodes could be prone to fracture, even when being stretched at lower strains. Due to the higher Young's modulus of the Ag electrodes, they were therefore designed to be comparatively thin and narrow here compared to the bulk PI supporting layer, and they were AJ-printed near the centre so that they could be well protected by the PI matrix from any external strains. Also, thinner and narrower Ag electrodes helped avoid the risk of thermal shorting of the TEG. Hence, no evident local strain concentration was seen within the Ag electrode, even though the Ag electrode has much higher Young's modulus than that of PI and PEDOT:PPS. It should also be pointed out that the excellent adhesion between different material layers formed here has played a vital role in bonding them into one unit, as the delamination issue at the interfaces could be avoided.

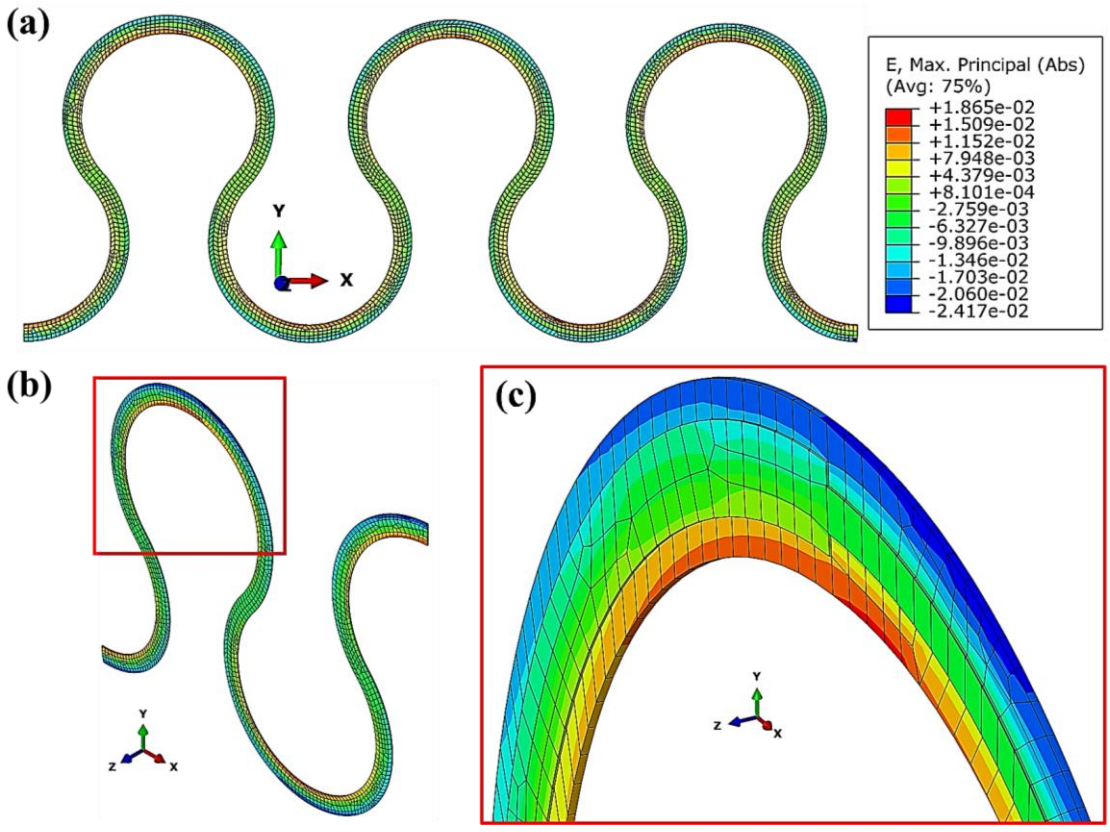

Figure 7.11 ABAQUS simulation on the strain distribution of the serpentine PEDOT:PSS-Ag-PI composite structure with out-of-plane design when being stretched to 50%. (a) is the top-down view, (b) is the side view, and (c) is the enlarged view, revealing more details of the strain distribution. The top-left thinner layer is the PEDOT:PSS, and the top-right thinnest layer is the Ag, while the bottom thickest layer is the PI.

7.3 Stretchability Tests

The stretchability limit of the serpentine structure was first evaluated here. Their electrical characteristics were measured when applying different levels of mechanical strain uniaxially along the in-plane direction. Figure 7.12 shows the resistance variation of the stretchable TE structure as a function of the wire extension, until being stretched to failure. The free-standing stretchable TE structure demonstrated superior mechanical stretchability and deformability, which could withstand a considerably high degree of uniaxial stretching, up to ~200% extension of its original length (i.e. fully stretched the serpentine geometry). This indicates that the self-supported nature of this free-standing structure has significantly improved the achievable stretchability of the serpentine geometry. The insets present the deformed structures in response to different extensions upon in-plane stretching. Only an ~18% increment in the resistance, from 1158 to 1369 Ω, was observed, without indicating any signs of electrical or mechanical failure. Below its plastic yielding threshold, the resistance increased almost linearly with increasing wire elongation. However, the serpentine shape did not revert to its original state after being released from around 150% extension, as it started to deform the PI and PEDOT:PSS materials, which caused unrecoverable plastic deformation. In this regard, this stretchable TE structure should be used at a lower strain level.

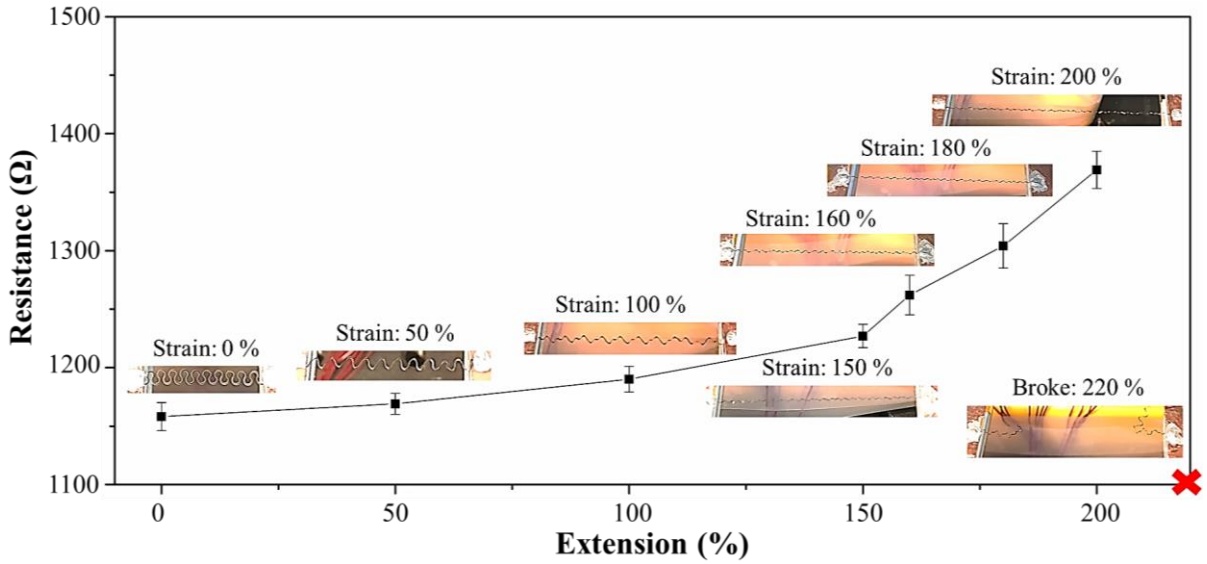

Figure 7.12 Resistance measurement of the free-standing stretchable TE structure when being stretched at different extensions, ranging from 0% up to 220%.

In order to experimentally verify that the AJ-printed stretchable TE structures could be applied as a stretchable power source, they were tested at a strain of 50% and 100%, which were well below their plastic yielding and fracture thresholds. It should be highlighted that these applied strains were much higher than the operating stretchability of current wearable electronic devices, in which the required strain was ~30%, given human motions.[220] In this work, the open-circuit voltage (V_{oc}) and maximum power (P_{max}) outputs of different AJ-printed stretchable TE structures were evaluated as a function of the applied ΔT, when being stretched at 0%, 50%, and up to 100%, respectively. As elaborated in Section 3.7.3, a constant steady-state ΔT was applied across the TE leg by making one side contacted with the hot surface of a Peltier module, while the other side was contacted with the cold surface of another Peltier module (for in-plane design), or with the ambient air (for out-of-plane design). The thermal distribution profiles of these stretchable TE structures under different imposed mechanical conditions were mapped by a thermal imaging camera. The value of ΔT between both ends was determined by focusing on and recording the real-time temperature values at different positions via the thermal imaging camera. The electrical characteristics of AJ-printed stretchable TE structures were measured by the measurement setup described in Section 3.7.3.

7.3.1 In-plane Structure

As plotted in Figure 7.13, only a marginal drop in the voltage and power output was seen in the single-layer AJ-printed stretchable TE structure with in-plane design with increasing stretching strain from 0% up to 100%. The insets present the deformed structures in response to different strains upon in-plane stretching. Their voltage and power outputs almost fully recovered to the original state after being released, suggesting that the influence of mechanical deformations on the TE performance was almost negligible here. The TE performance of this free-standing stretchable TE structure was mostly dependent on the applied ΔT and nearly immune to the imposed mechanical strains. However, the obtained P_{max} value was only ~0.06 nW (V_{oc} of ~0.43 mV and R_S of ~757 Ω with 1 TE leg unit) under a ΔT of ~25 °C and a stretching strain of 50%, which was rather low compared to that reported in the literature. These

low outputs might stem from the intrinsically low *ZT* value of PEDOT:PSS and the lack of forming multiple *n-p* connected TE legs to fully utilise the Δ*T*. Another reason might be due to the low fill factor of the current-developed device geometry. Thus, the out-of-plane and multilayered structures were integrated in the following section for comparison.

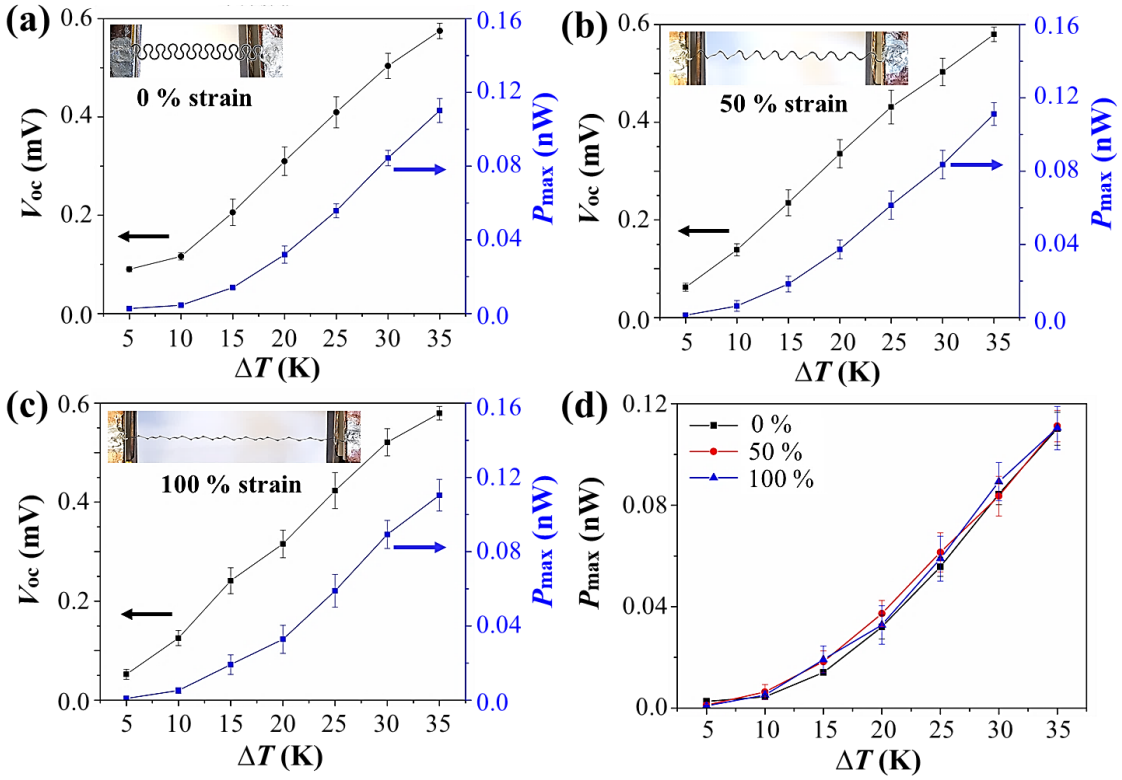

Figure 7.13 Voltage and power output measurements on the single-layer AJ-printed stretchable TE structure with in-plane design as a function of the applied Δ*T*, when being stretched at a strain of (a) 0%, (b) 50%, and (c) 100%, respectively. The insets show the deformed structures at different strains. (d) Overall comparison of P_{max} at various applied Δ*T* and strains.

The thermal images in Figure 7.14 display the temperature distribution across the serpentine-shaped TE structure, when being stretched at different strains: 0%, 50%, and 100%, respectively, under a constant applied Δ*T* of ~25 °C. From the left to right side, the colour gradient along the TE leg retained almost unchanged when being stretched, confirming that these mechanical deformations had little influence on the temperature distribution along the TE leg. This is mainly because the hollow and free-standing nature of this serpentine structure helped hinder the heat transfer, and the temperature gradient was maintained due to the relatively low *κ* of the air [~0.026 W/(m.K)] and the PI supporting layer [~0.45 W/(m.K)].[204]

However, due to the limitation of the current-use thermal camera, it was difficult to observe more details of the temperature distribution profile. Future work by using a thermal camera with higher resolution is therefore required.

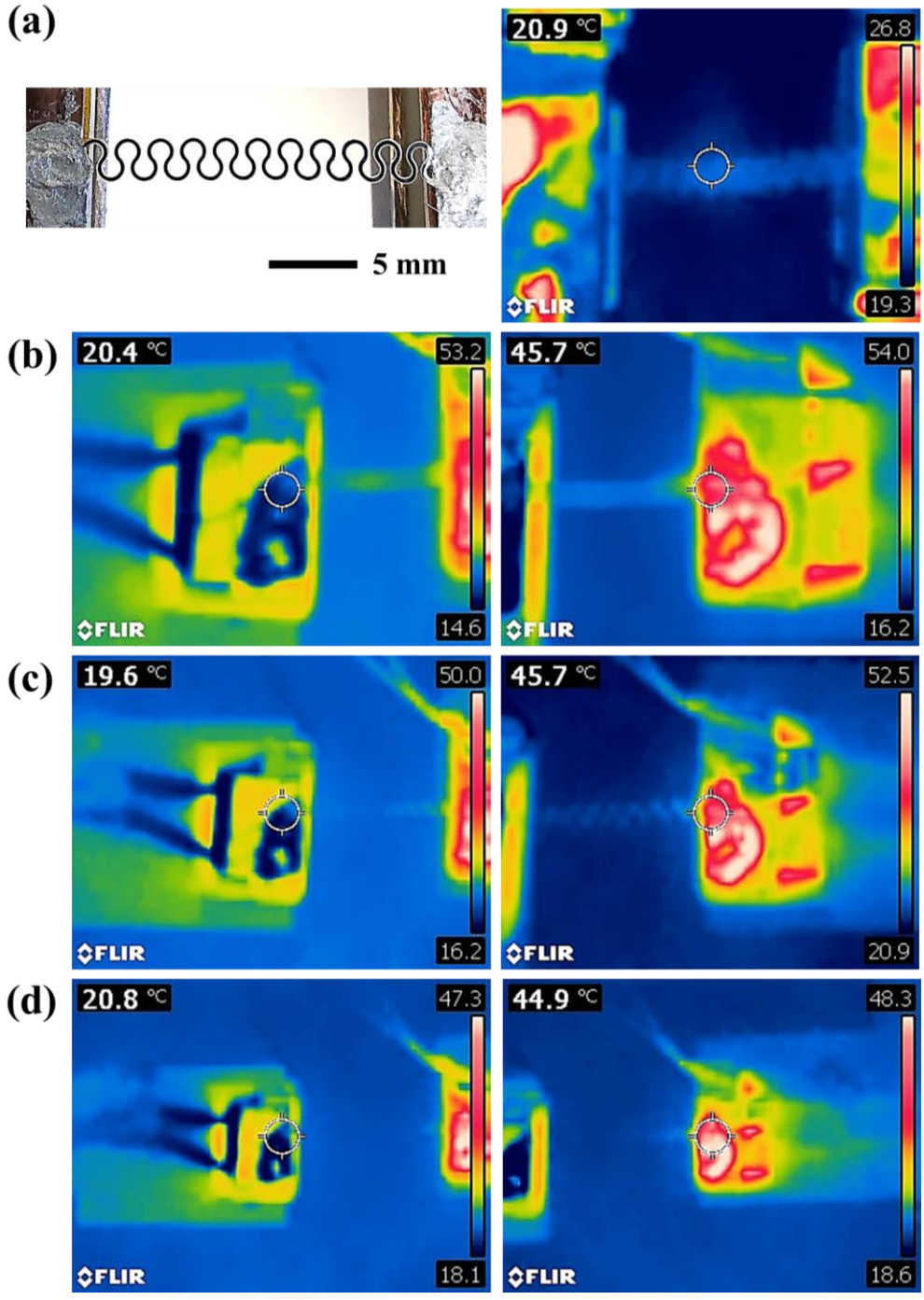

Figure 7.14 (a) Photographic and thermal images of the unstretched and unheated single-layer AJ-printed stretchable TE structure with in-plane design. Thermal images of the stretchable TE structure being stretched at a strain of (b) 0%, (c) 50%, and (d) 100%, respectively, under a constant applied ΔT of ~25 °C. The circle highlights the localised temperature reading.

7.3.2 Out-of-plane Structure

Compared with the in-plane structure discussed above, the out-of-plane structure exhibited a comparatively greater decrease in its V_{oc} and P_{max} values when being stretched at various deformation strains. As shown in Figure 7.15, the decrease in voltage and power outputs became more obvious, especially at higher applied ΔT. A maximum drop in P_{max} ~50% was seen at the ΔT of ~35 °C, which might be attributed to the reduced ΔT across the TE leg when the TE structure was stretched along the in-plane direction. As indicated in the thermal profiles in Figure 7.16, the TE legs were tilted by ~45° towards the horizontal hot surface of the Peltier module when being stretched from 0% to 100% strain. The hot ends of TE legs became less contact with and more away to the hot surface. Higher heat source temperature of the Peltier module was required to maintain the same ΔT. As a result, the applied ΔT along individual TE legs was not fully utilised here, and the device conversion efficiency was also deteriorated, which therefore led to the reduced V_{oc} and P_{max} values when operated at the same ΔT. Another reason that diminished the V_{oc} and P_{max} might be the increase of the sample resistance caused by the imposed mechanical deformations. In this regard, this stretchable TEG could perform better in the situation where it is stretched along the temperature gradient direction. Future work by using a better testing geometry is therefore required for further investigation.

Despite the greater drop in TE performance at higher applied ΔT, this stretchable TE structure exhibited stable TE performance even while undergoing different levels of mechanical deformations. This out-of-plane structure could achieve an increment of an order of magnitude in P_{max} ~0.78 nW (V_{oc} of ~0.92 mV and R_S of ~270 Ω with 5 TE leg units) compared to that of the in-plane structure with P_{max} ~0.06 nW (V_{oc} of ~0.43 mV and R_S of ~757 Ω with 1 TE leg unit) under the same ΔT of ~25 °C and same stretching strain of 50%. This proves that the out-of-plane structure is a more efficient device design for thermal energy harvesting It is noteworthy that no visible cracks or fractures were seen in this stretchable TE structure before and after the stretchability test. Also, it recovered to its original serpentine shape after being released.

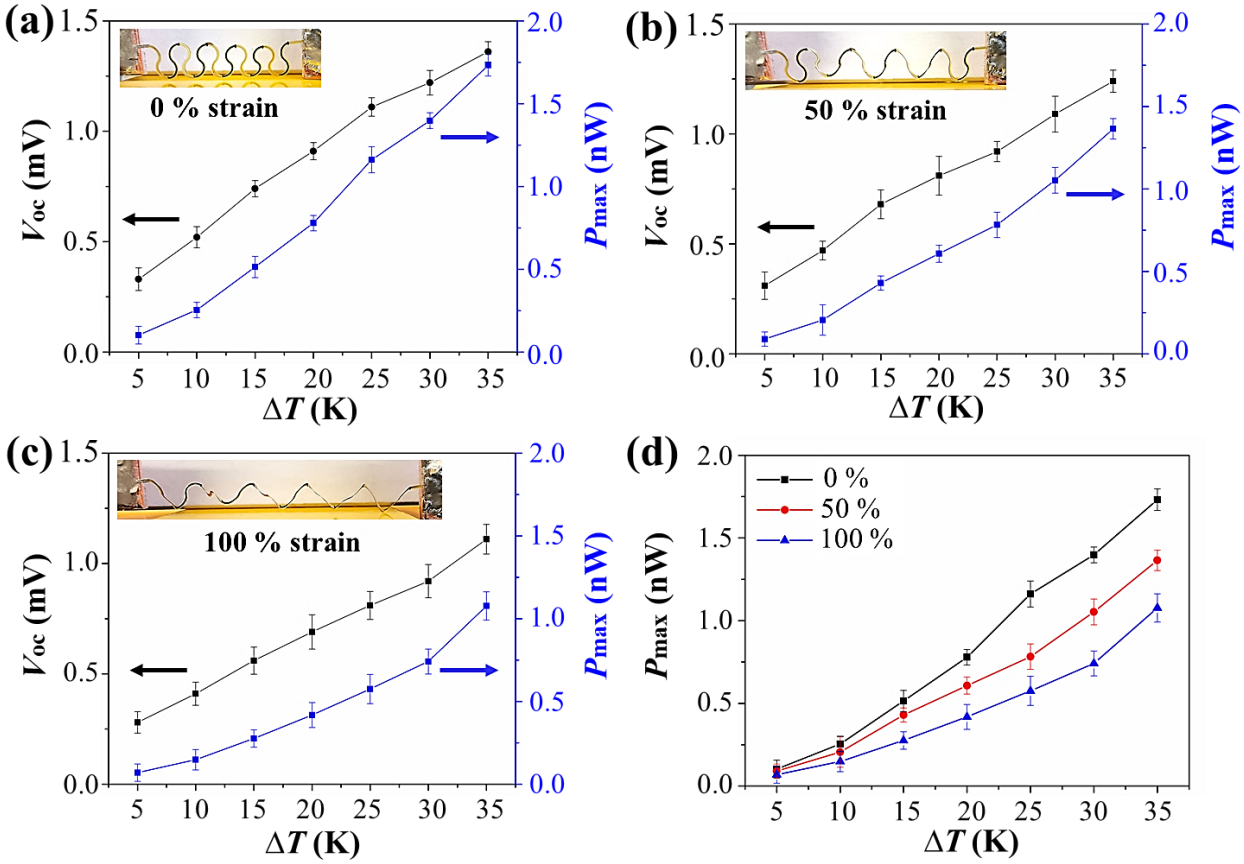

Figure 7.15 Voltage and power output measurements on the single-layer AJ-printed stretchable TE structure with out-of-plane design as a function of the applied ΔT, when being stretched at a strain of (a) 0%, (b) 50%, and (c) 100%, respectively. The insets show the deformed structures at different strains. (d) Overall comparison of P_{max} at various applied ΔT and strains.

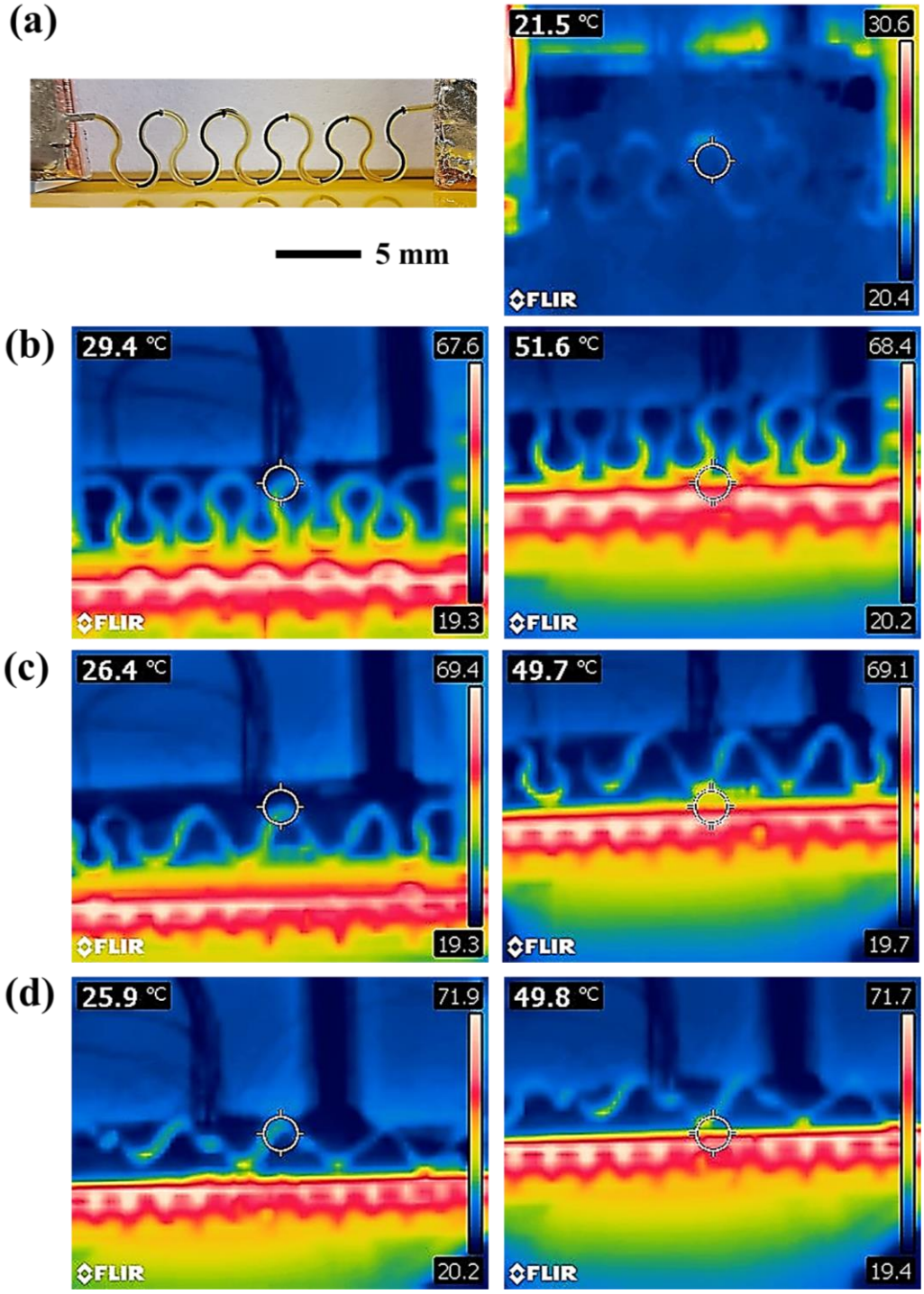

Figure 7.16 Photographic and thermal images of the unstretched and unheated single-layer AJ-printed stretchable TE structure with out-of-plane design. Thermal images of the stretchable TE structure being stretched at a strain of (b) 0%, (c) 50%, and (d) 100%, respectively, under a constant applied ΔT of ~25 °C. The circle highlights the localised temperature reading.

7.4 Fatigue Tests

The long-term cyclic strain stability of the stretchable TE structures was studied by a prolonged fatigue test. Both in-plane and out-of-plane free-standing structures were uniaxially stretched and released at an applied periodic strain of 50% up to 20,000 stretching cycles (i.e. 40 hours of continuous testing at a frequency of 0.15 Hz), as demonstrated in the lower right insets in Figures 7.17 and 7.18. The data after different stretching cycles were recorded accordingly via the bespoke measurement setup discussed in Section 3.8. The left insets reveal more details of the V/V_o and R/R_o profiles. It was found that the voltage output and resistance oscillated in response to the maximum and minimum mechanical strains across each stretching cycle. The shape change of the stretchable TE structure after each stretching cycle could cause a small drop in the voltage output and/or a small increment in the resistance. The changes of voltage output (V/V_o) and sample resistance (R/R_o) in both stretched and relaxed states were found to gradually decrease and increase, respectively, over the fatigue test.

The fatigue test results in Figures 7.17 and 7.18 show that a small drop in the voltage output was observed after the prolonged fatigue test without causing any significant mechanical or electrical damage (~15% decrease for the in-plane structure and ~20% decrease for the out-of-plane structure), which might be attributed to the decrease of their Seebeck coefficient values. While their sample resistance maintained nearly unchanged (~5% increment for the in-plane structure and ~12% increment for the out-of-plane structure). Since the voltage output fluctuated a bit more even when not being stretched, the resistance was preferably selected here to better evaluate the electrical characteristics as a function of the imposed mechanical strain. Beyond a certain point (~12,500 cycles for the in-plane structure and ~10,000 cycles for the out-of-plane structure), the sample resistance variation became less significant, and then plateaued as the stretching cycles increased. This result demonstrates that these stretchable TE structures reached a stable and reproducible conducting configuration.[159] These innovative free-standing serpentine structures thus facilitated the stretchable TE structures to be durable and mechanically robust, even when subjected to prolonged repetitive stretching cycles. These

structures outperformed other reported stretchable TEGs that were typically attached to elastomeric substrates.[204,207,221] Also, it should be noted that these stretchable TE structures were tested over a period of one month with negligible degradation in their TE performance. These fatigue test results are of vital importance, given that such extensive fatigue data are rarely reported in the literature for stretchable TEGs.

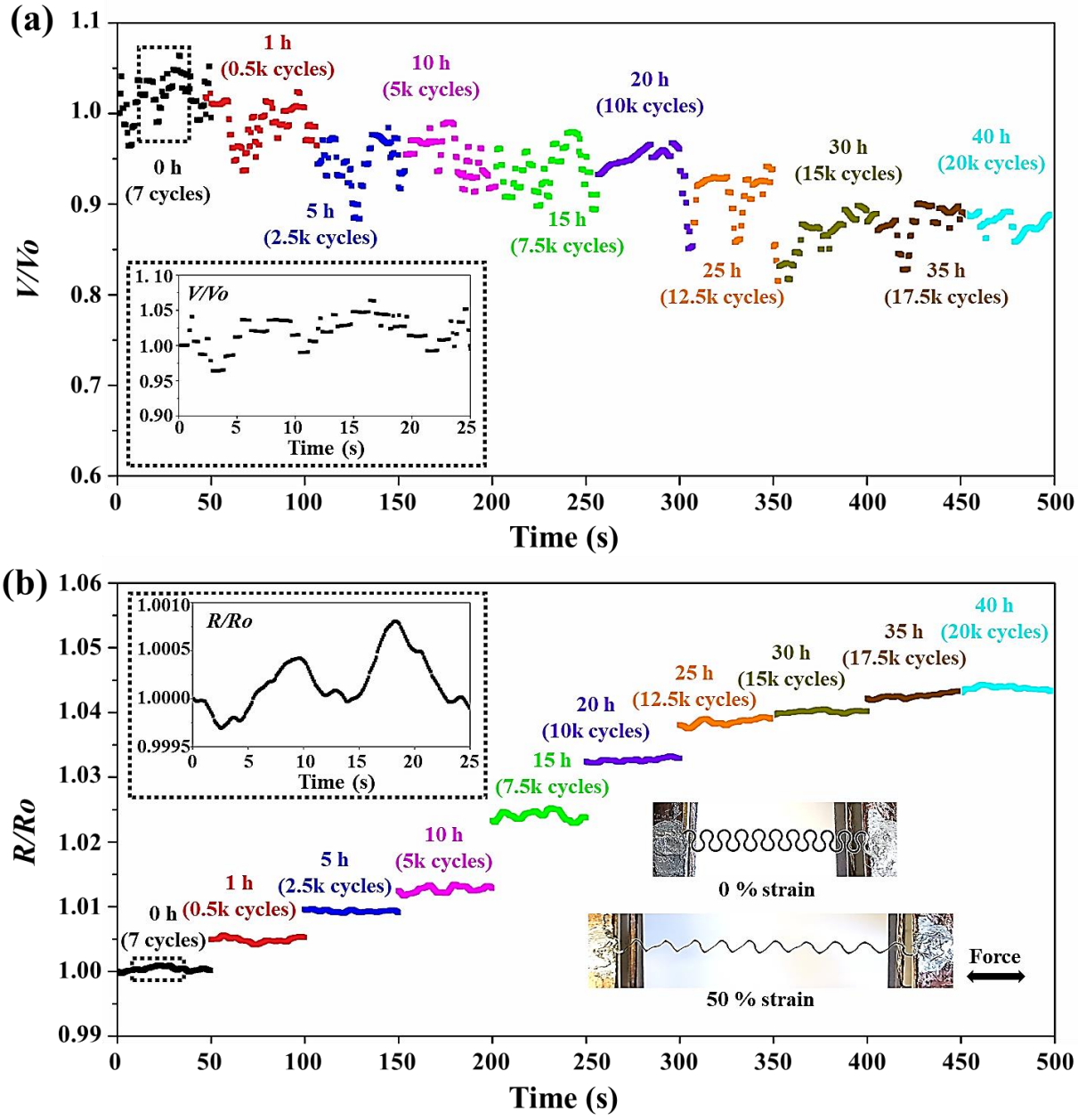

Figure 7.17 Fatigue test on the stretchable TE structure with in-plane design, which is continually tested under a periodic stretching strain of 50% at a frequency of 0.15 Hz for 40 hours (i.e. 20,000 cycles in total). (a) is the V/V_o profile under a constant ΔT of ~25 °C, and (b) is the R/R_o profile measured at the room temperature. The left enlarged insets reveal more details of their profiles, and the lower right inset demonstrates the stretching process.

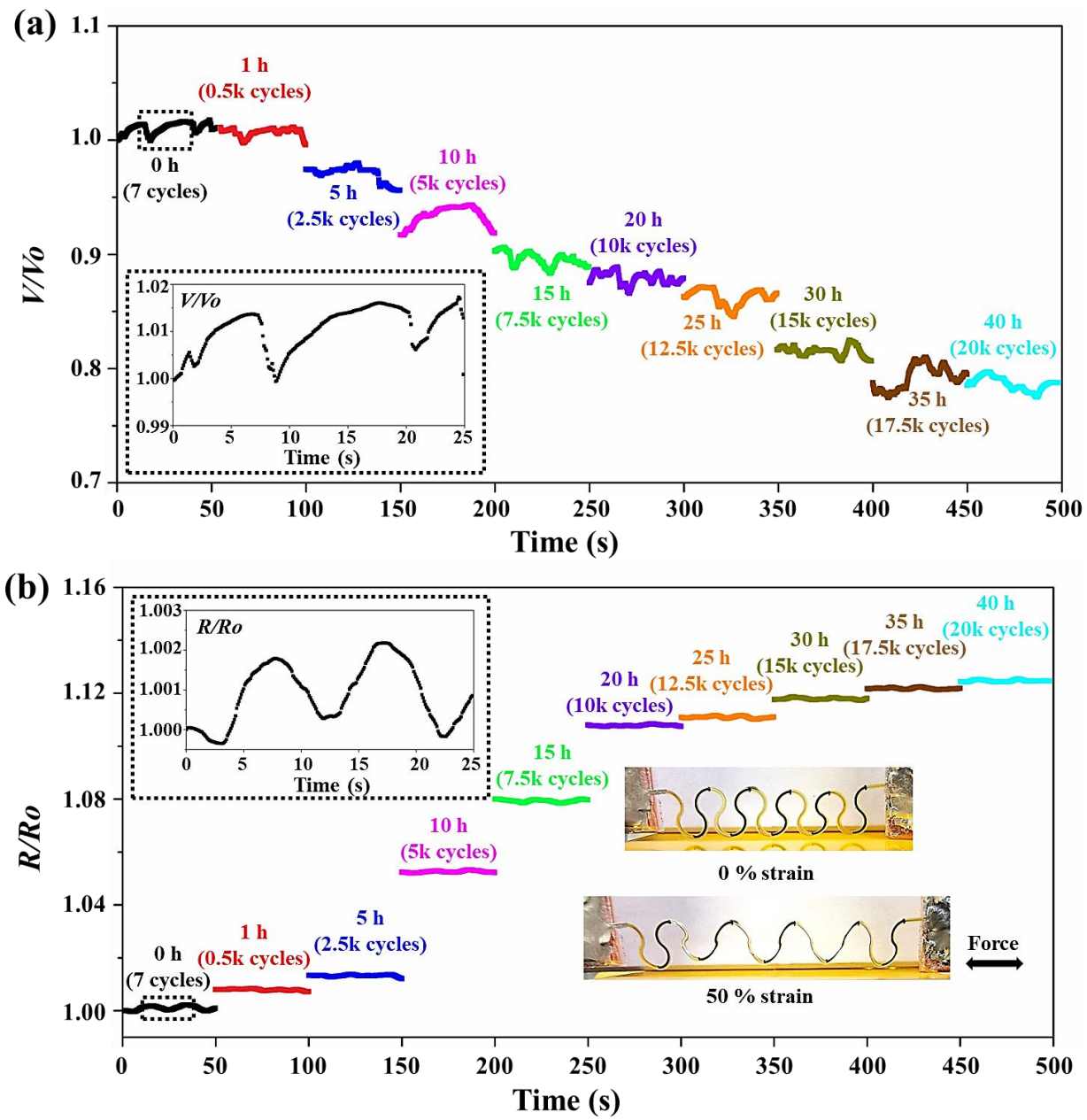

Figure 7.18 (a) Fatigue test on the stretchable TE structure with out-of-plane design, which is continually tested under a periodic stretching strain of 50% at a frequency of 0.15 Hz for 40 hours (i.e. 20,000 cycles in total). (a) is the V/V_o profile under a constant ΔT of ~25 °C, and (b) is the R/R_o profile measured at the room temperature. The left enlarged insets reveal more details of their profiles, and the lower right inset demonstrates the stretching process.

As observed in Figure 7.19, although these stretchable serpentine structures did not fully revert to their original shapes, they still exhibited good stretchability and retained their original smooth surface without forming any noticeable cracks or delamination after prolonged cyclic stretching. Their voltage output and resistance did not recover to their original values after being released, which might be ascribed to unrecoverable local damage occurring within the

TE structures that could limit their lifetime as reliable TEGs.[159] As can be seen in the SEM micrographs in Figures 7.20 and 7.21 taken after the prolonged fatigue test, some micron-sized cracks were prone to forming on the edges of the PI supporting layer, and some parts of the PI film had peeled off. Nevertheless, no visible cracks or fractures were observed in the main bulk of the PEDOT:PSS film that retained nearly intact. These microcracks initiated on the edges and then propagated towards the centre of the serpentine structure as the local strains accumulated over time. This could have led to fracture and/or failure as these microcracks joined across the serpentine TE structure. These experimental results indicate a good agreement with the ABAQUS simulation results in Section 7.2, and they explain the root cause of the observed mechanical stretchability and robustness in these stretchable TE structures. It was found that PEDOT:PSS films and Ag electrodes did not peel off or delaminate from the PI supporting layer, which could be attributed to the co-curing process that promoted the rigid PEDOT:PSS films and Ag electrodes to be firmly embedded within the ductile PI layer, forming a strong bonding in between. Since the PI layer was served as a supporting and protective matrix for PEDOT:PSS and Ag, a firm adhesion between them is crucial to guarantee a greater mechanical strength. Moreover, their overall mechanical robustness could be further improved by encapsulating another PI layer on top to protect PEDOT:PSS films, and to reinforce the overall mechanical strength by forming a sandwich structure, thereby elongating the TEG device lifetime. By virtue of these innovative serpentine designs, these stretchable free-standing TE structures exhibited excellent mechanical stretchability and robustness that were akin to a piece of rubber, and they could therefore sustain larger mechanical deformations without causing any physical damages. In comparison, most stretchable electronic devices can only be operated at deformation strains below ~50%.[221,258,259]

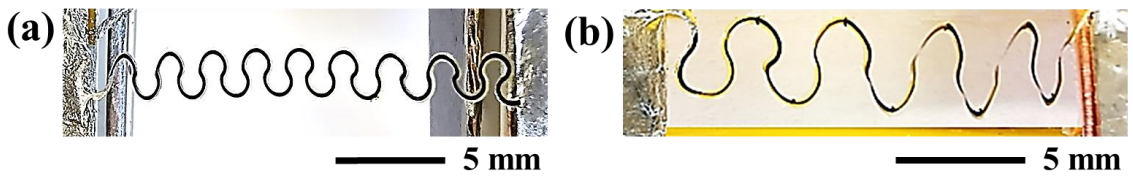

Figure 7.19 Photographic images of stretchable TE structures with (a) in-plane design and (b) out-of-plane design, respectively, after the prolonged fatigue test.

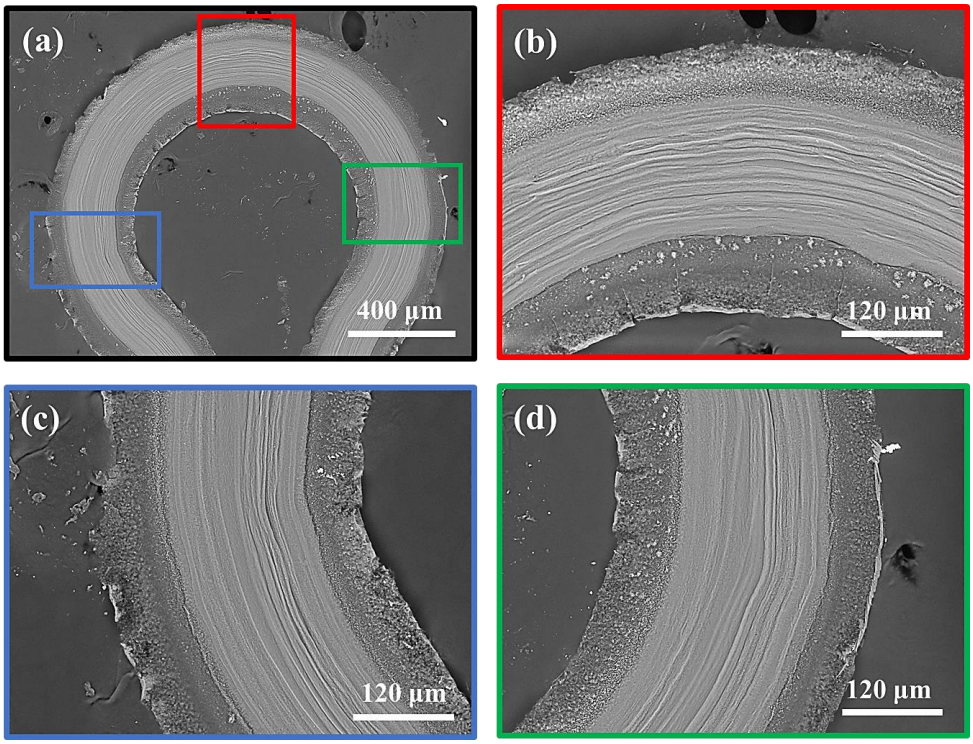

Figure 7.20 (a) SEM image of the stretchable TE structure with in-plane design after the prolonged fatigue test, where the enlarged images (b), (c) and (d) reveal the microcracks mainly formed on the edges of the PI supporting layer, and some parts of the PI film had peeled off.

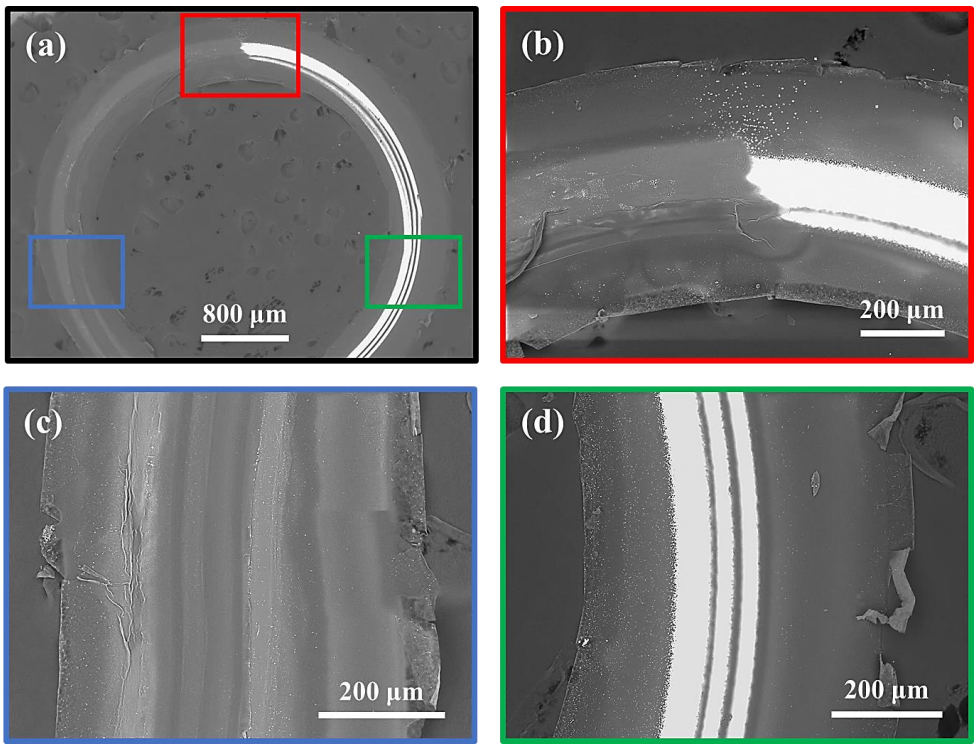

Figure 7.21 (a) SEM image of the stretchable TE structure with out-of-plane design after the prolonged fatigue test, where the enlarged images (b), (c) and (d) show the microcracks mainly appeared on the edges of the PI supporting layer, and some parts of the PI film had peeled off.

7.5 Multilayered Stretchable Thermoelectric Generators

According to the equation discussed in Section 3.10.2, $P_{max} = n(\Delta V)^2/4R_S$, a multilayered structure should be employed to increase the number of TE legs within the same TEG unit, thereby improving the power output level. Multiple layers containing a number of TE legs should be connected electrically in series and thermally in parallel. Here, as fabricated in Section 3.10.3, three layers of TE materials were stacked up into one whole TEG by using the AJP technique. It was found that this multilayered structure not only largely improved the power output, but it also significantly promoted the mechanical stretchability. As can be seen from Figure 7.22, the 3-layer AJ-printed stretchable TE structure with out-of-plane design has achieved a significant improvement in the TE performance even under higher mechanical strains. The P_{max} of ~3.89 nW (V_{oc} of ~2.23 mV and R_S of ~320 Ω with 15 TE leg units) was obtained under a ΔT of ~25 °C and a stretching strain of 50%. Its P_{max} value was found to be improved by a factor of 5 compared to that of its single-layer structure with P_{max} ~0.78 nW (V_{oc} of ~0.92 mV and R_S of ~270 Ω with 5 TE leg units). This result verifies that the power output can be easily enhanced by simply increasing the number of stacked layers without losing its excellent mechanical stretchability and without involving extra sophisticated and time-consuming processes. This therefore enables the stretchable TEG to achieve a sufficient power output level to satisfy the power requirement of current wearable electronic devices.

Figure 7.23 shows the temperature distribution profiles of the multilayered structure when being stretched. They were akin to that of the single-layer structure, where the TE legs were tilted by up to 45° under the in-plane stretching. However, a slightly smaller drop in the P_{max} with increasing strain was seen in Figure 7.22 (d). This indicates that with the multilayered PI encapsulation, the multilayered PEDOT:PSS films and Ag electrodes could be well supported and protected from detrimental environmental factors and/or mechanical failures, such as cracking or delamination when being stretched. This therefore remarkably enhanced the overall mechanical stretchability and robustness of the encapsulated multilayered stretchable TEG against handing and/or mechanical deformations following prolonged use. Moreover, since the

multilayered structure could hinder the phonon transport by introducing a multitude of scattering events across interfaces,[1,77] the overall thermal conductivity of this composite structure could be substantially reduced. This could thus significantly enhance the TE performance and energy conversion efficiency of the resulting stretchable TEG in practical use.

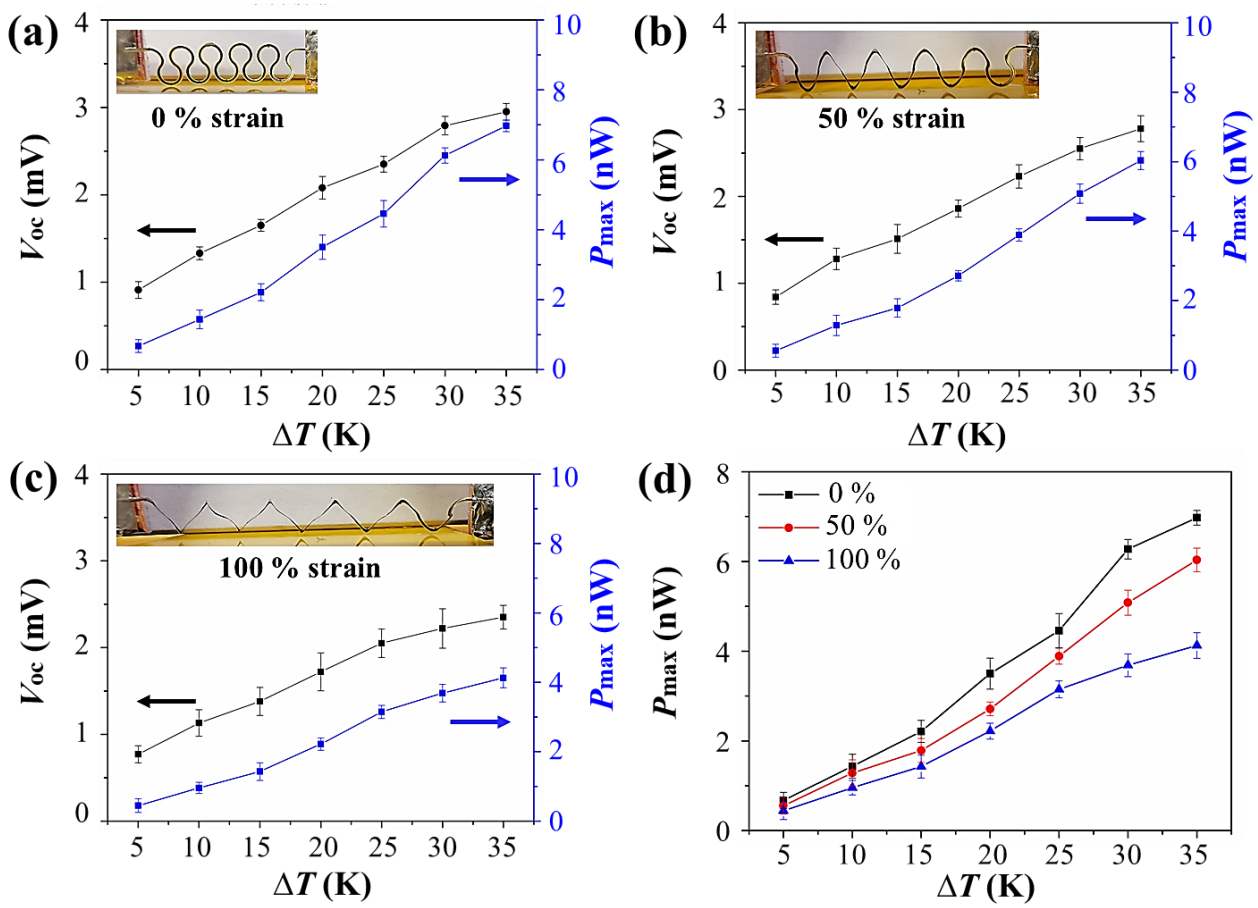

Figure 7.22 Voltage and power output measurements on the 3-layer AJ-printed stretchable TE structure with out-of-plane design as a function of the applied ΔT, when being stretched at a strain of (a) 0%, (b) 50%, and (c) 100%, respectively. The insets show the deformed structures at different strains. (d) Overall comparison of P_{max} at various applied ΔT and strains.

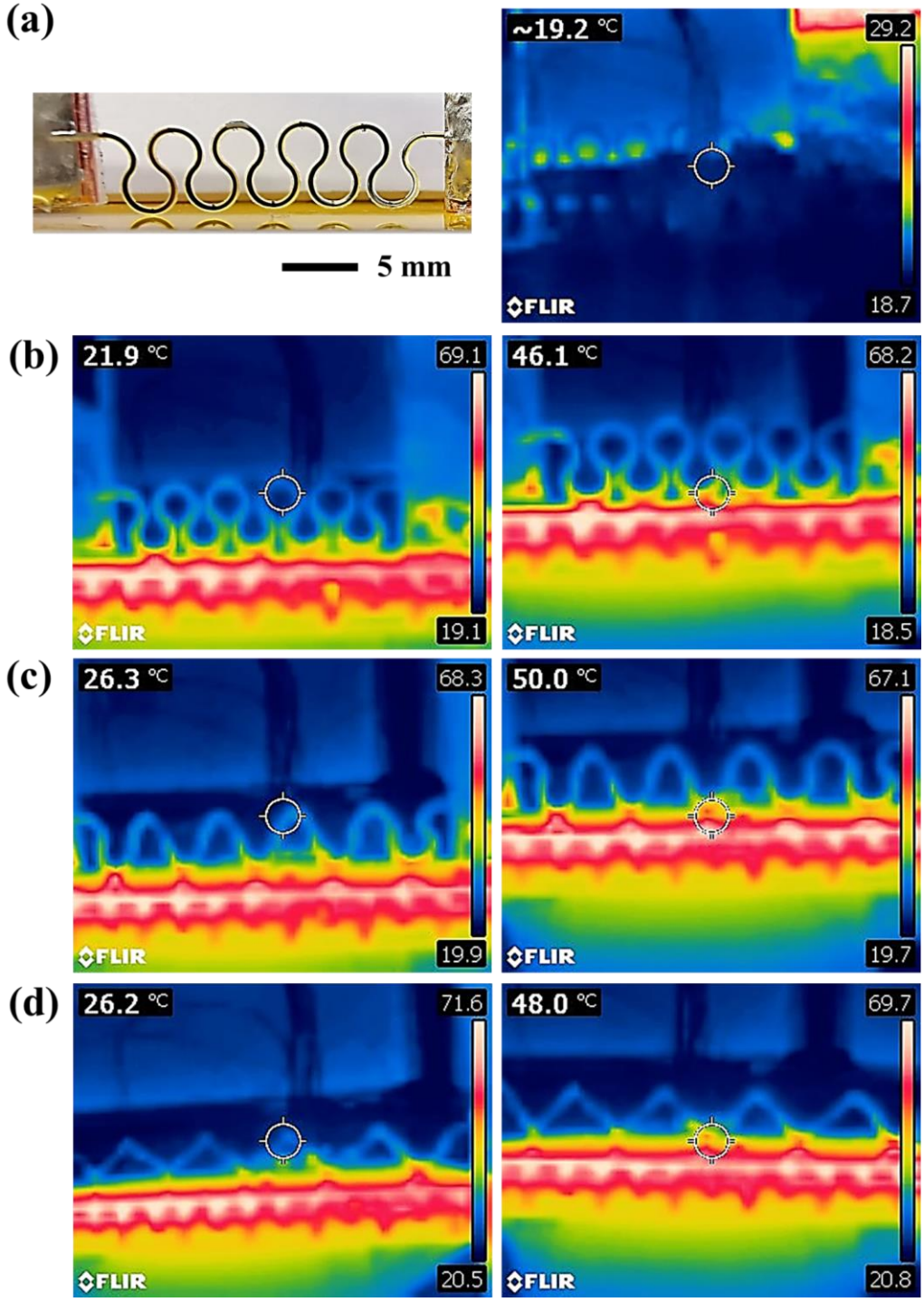

Figure 7.23 (a) Photographic and thermal images of the unstretched and unheated 3-layer AJ-printed stretchable TE structure with out-of-plane design. Thermal images of the stretchable TE structure being stretched at a strain of (b) 0%, (c) 50%, and (d) 100%, respectively, under a constant applied ΔT of ~25 °C. The circle highlights the localised temperature reading.

7.6 Prototype of Stretchable Thermoelectric Generator

Since these free-standing TEGs possessed superior flexibility and stretchability, they could be mounted onto various curved surfaces, even those with very high curvatures, such as heat pipes, or could be worn onto a human body by virtue of their excellent mechanical stability and shape conformance. These hollow and free-standing stretchable TEGs were very small and lightweight, with a mass of ~0.005 g and ~0.01 g for the single-layer in-plane and out-of-plane structure, respectively. Their power-to-weight ratios were calculated to be ~12 nW/g and ~78 nW/g, respectively, which reveals their promising potentials as comfortable and breathable TEGs for integration into wearable applications.

Here, in order to demonstrate the practical use of these stretchable TEGs in real-life applications, different prototypes of stretchable TEGs comprised of a different number of TE legs (5 and 10) were fabricated by the AJP technique. It should be mentioned that these AJ-printed stretchable TE structures were all single-layer structures with a PI encapsulation layer on top to give better TE performance as well as mechanical stretchability and robustness as discussed above. Subsequently, they were wrapped around the curved surface of glass tubes with curvatures of 63 m^{-1} and 126 m^{-1}, respectively, using double-sided tape, as displayed in Figures 7.24 (a) and 7.25 (a). The glass tubes were then filled with hot water to create a ΔT of ~35 °C between their surface and the ambient air, as measured from the thermal images in Figures 7.24 (b) and 7.25 (b). By virtue of the excellent stretchability of these stretchable TEGs, they were well aligned with the radial heat direction formed by the glass tube. A stable V_{oc} of ~1.1 mV and P_{max} of ~1.2 nW was generated from the stretchable TEG with 5 TE legs, while a V_{oc} of ~2.4 mV and P_{max} of ~2.7 nW was achieved from the stretchable TEG with 10 TE legs. It was found that the V_{oc} and P_{max} values obtained here were slightly lower than those achieved in Section 7.3.2. Because some TE legs were not set perfectly vertical to the surface of the glass tube and the whole TEG was stretched at the strain of roughly 30% to 50%, these led to inefficient use of the ΔT along individual TE legs. Nevertheless, this result demonstrates that these stretchable TEGs could be integrated with a variety of non-flat surface applications. It

also confirms the promising possibility of deploying these stretchable TEGs as an energy source for some 'small-power' applications, such as wearable devices and portable electronics.

Although the current power output of these stretchable TEGs is not sufficient enough to drive any mainstream portable and wireless electronics, like smartphone and wearable watch, it is believed these innovative stretchable TEGs could pave the way to the industrial commercialisation of next-generation self-powered electronic devices and wearable sensors. These microscale stretchable structures can be integrated with miniaturised electronic systems, e.g. transmitters or biosensors, which are operated at much lower power consumption level.[204] They are also compatible with the micro-electromechanical system (MEMS), which is one of the potential applications for TEGs. Since the versatile AJP technique is compatible with a variety of materials, including inorganics, organics, and their composite structures, as discussed in above Chapters 4 and 5, it may be feasible to achieve a higher power output up to the level of microwatts by combining with high-performance TE materials, such as Bi_2Te_3 and Sb_2Te_3 nanomaterials. Also, their power output can be enhanced by incorporating with other high-performance *n*-type TE materials to form *n-p* junctions. Furthermore, their power output can be further improved up to an order of magnitude by stacking up with multiple layers of TE materials via repeated printing, as demonstrated in Section 7.5.

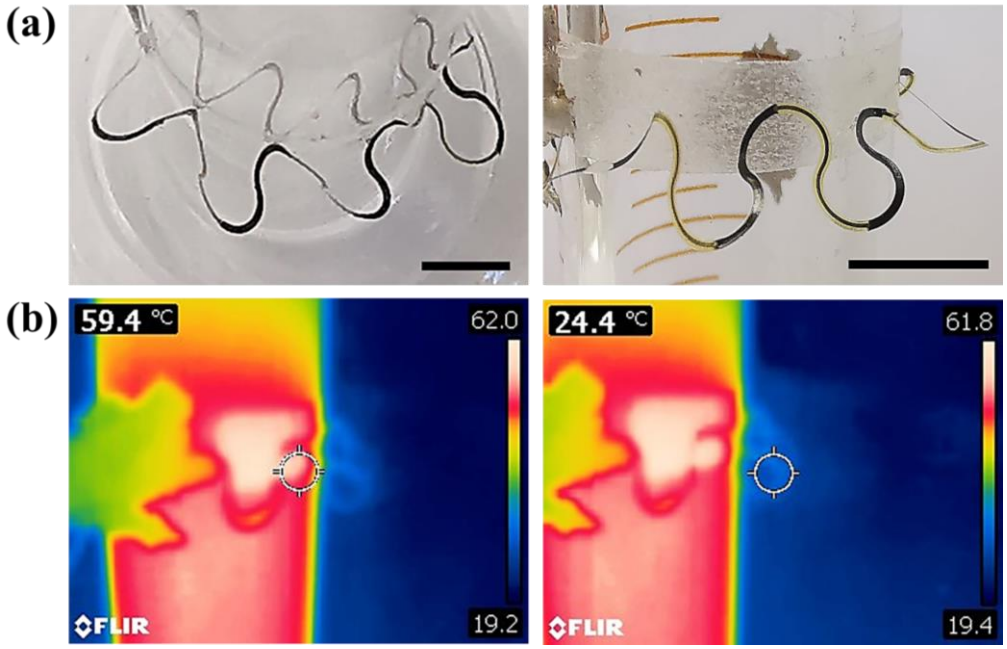

Figure 7.24 (a) Top-down and side-view images of the stretchable TEG with 5 TE legs, which was worn on a glass tube with a curvature of 63 m^{-1}. Scale bar: 5 mm. (b) Thermal images showing the measurement of the ΔT between the inner and outer temperatures of the TE leg. The circle highlights the localised temperature reading.

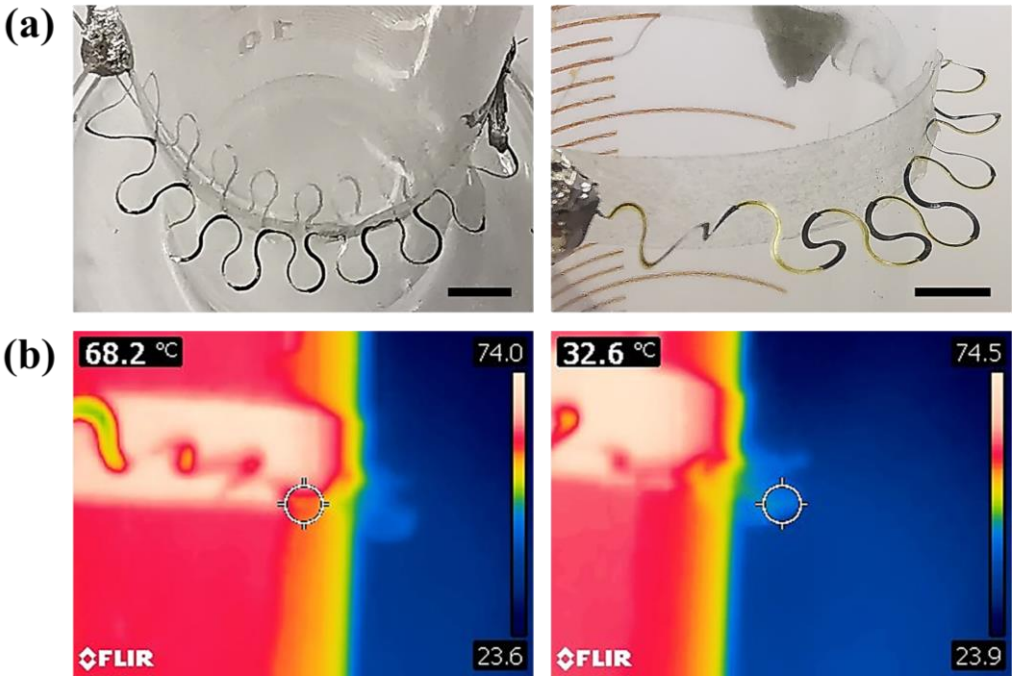

Figure 7.25 (a) Top-down and side-view images of the stretchable TEG with 10 TE legs, which was worn on a glass tube with a curvature of 126 m^{-1}. Scale bar: 5 mm. (b) Thermal images showing the measurement of the ΔT between the inner and outer temperatures of the TE leg. The circle highlights the localised temperature reading.

7.7 Stretchable Compositionally Graded Thermoelectric Generator

Here, the author also demonstrates another approach to enhancing the power output by incorporating the CG-TEC concept, as discussed in Chapter 6. Figure 7.26 shows the morphology of the stretchable CG-TEG with in-plane design, which was comprised of 15 wt.% Bi_2Te_3-PEDOT:PSS nanocomposite on the left side and PEDOT:PSS film on the right side. This stretchable CG-TEG exhibited P_{max} of ~0.91 nW (V_{oc} ~1.63 mV and R_S ~732 Ω with 1 TE leg unit), when it was exposed to an operating ΔT ~70 °C. The applied ΔT was monitored by a thermal imaging camera, as presented in Figure 7.27. In comparison, the stretchable single-phase TEG that was comprised of only the PEDOT:PSS film possessed P_{max} ~0.46 nW (V_{oc} ~1.34 mV and R_S ~959 Ω with 1 TE leg unit), under the same applied ΔT of ~70 °C. This result shows that the CG-TEC design has been successfully combined with the stretchable serpentine design to achieve both higher TE performance and larger mechanical stretchability.

As shown in Figures 7.28 and 7.29, this AJ-printed stretchable CG-TEG exhibited improved TE performance while retaining its intrinsically high stretchability. Compared to the stretchable single-phase TEG discussed in Section 7.3.1, a nearly 3-fold increase of the P_{max} was seen in this stretchable CG-TEG. A slightly greater drop in the P_{max} was observed upon stretching to 100% strain, which might be ascribed to the slightly lower stretchability of the 15 wt.% Bi_2Te_3-PEDOT:PSS nanocomposite. Nonetheless, this minor degradation in the TE performance can be compromised when compared with the significant power output improvement that was contributed by this CG-TEC design.

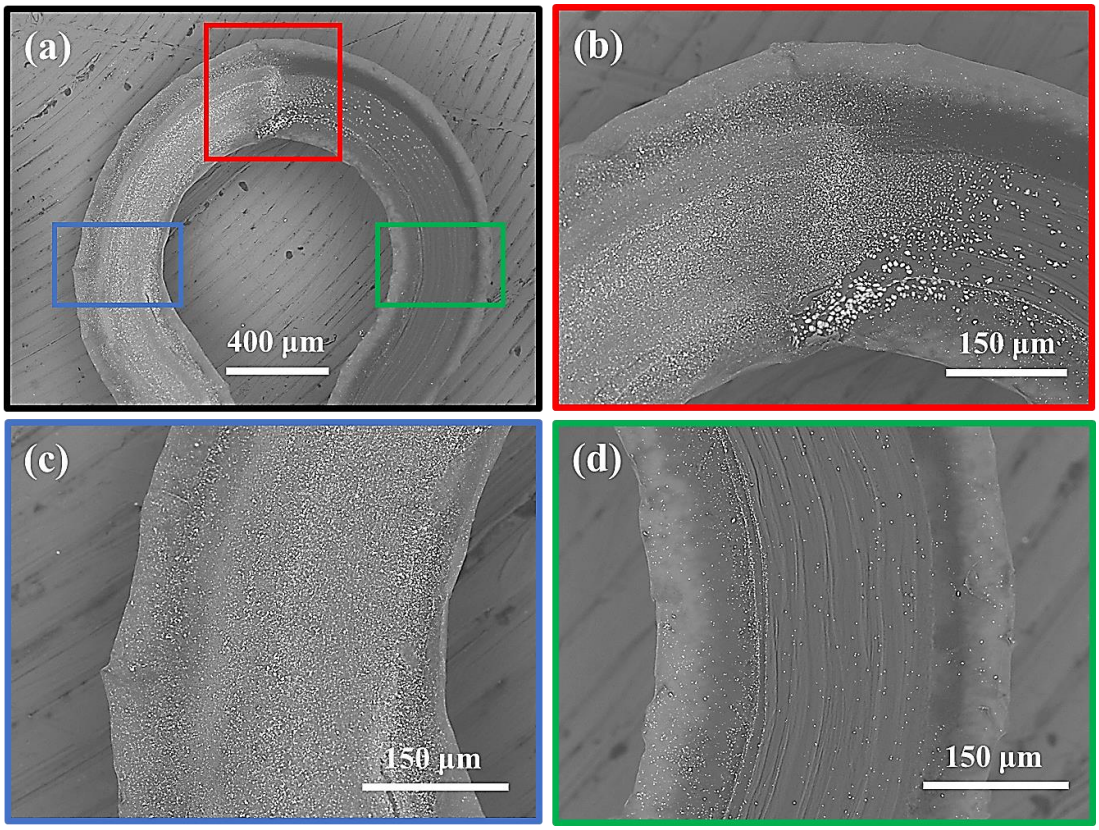

Figure 7.26 (a) Top-down SEM image of the stretchable CG-TEG with in-plane design, and (b) the enlarged view of its interface, which was comprised of (c) 15 wt.% Bi_2Te_3-PEDOT:PSS nanocomposite on the left side and (d) PEDOT:PSS film on the right side.

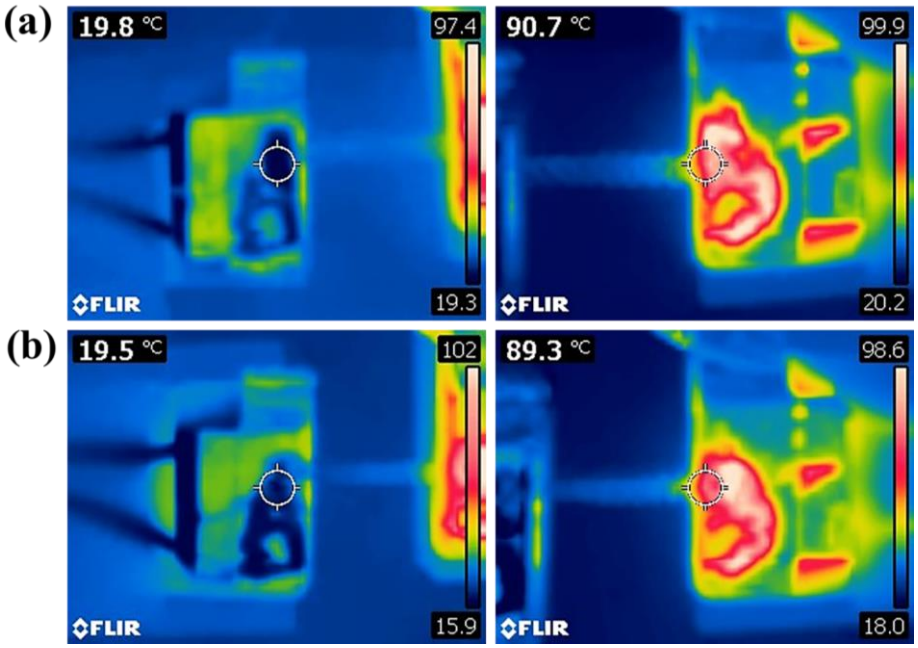

Figure 7.27 Thermal images of (a) the stretchable CG-TEG and (b) the stretchable single-phase TEG, respectively, under the same applied ΔT of ~70 °C. The circle highlights the localised temperature reading.

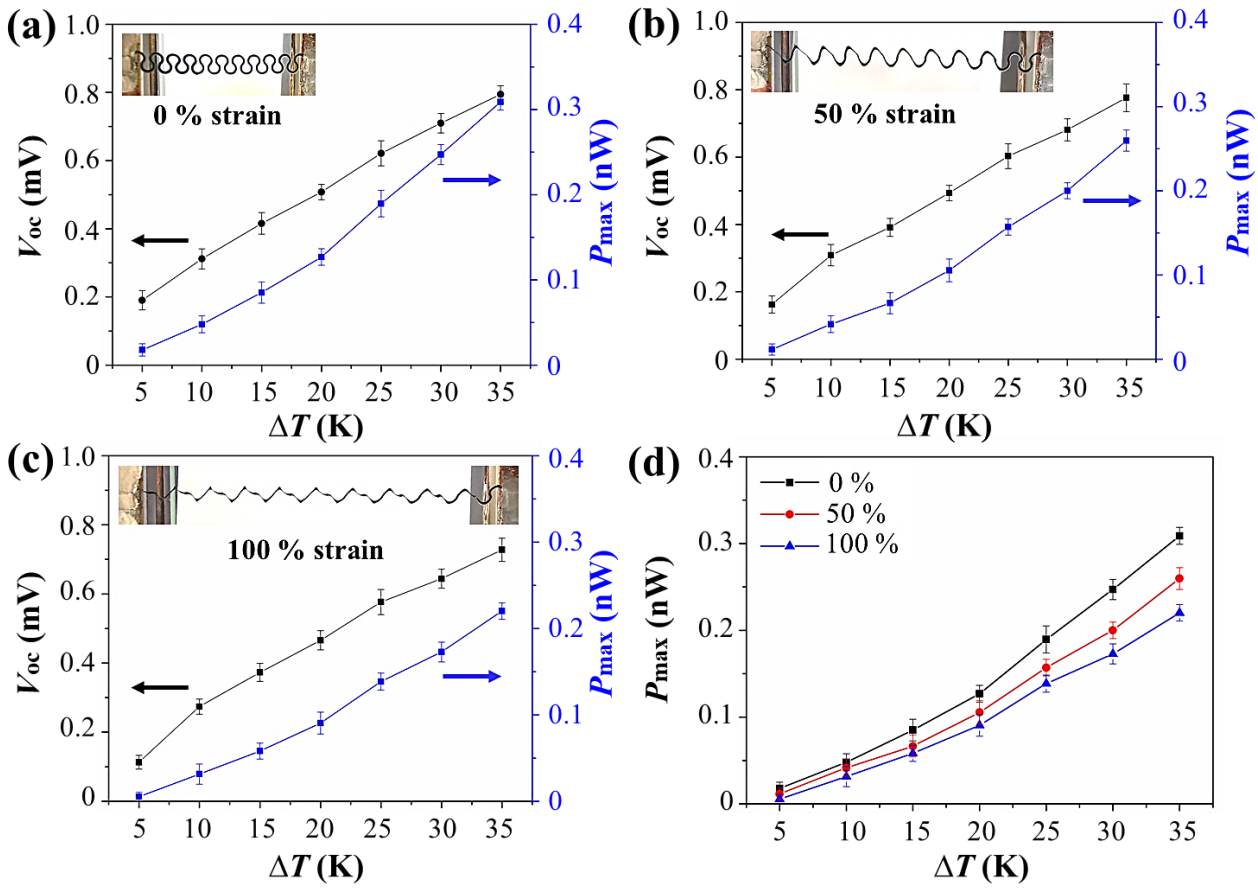

Figure 7.28 Voltage and power output measurements on the single-layer AJ-printed stretchable CG-TEG with in-plane design as a function of the applied ΔT, when being stretched at a strain of (a) 0%, (b) 50%, and (c) 100%, respectively. The insets show the deformed structures at different strains. (d) Overall comparison of P_{max} at various applied ΔT and strains.

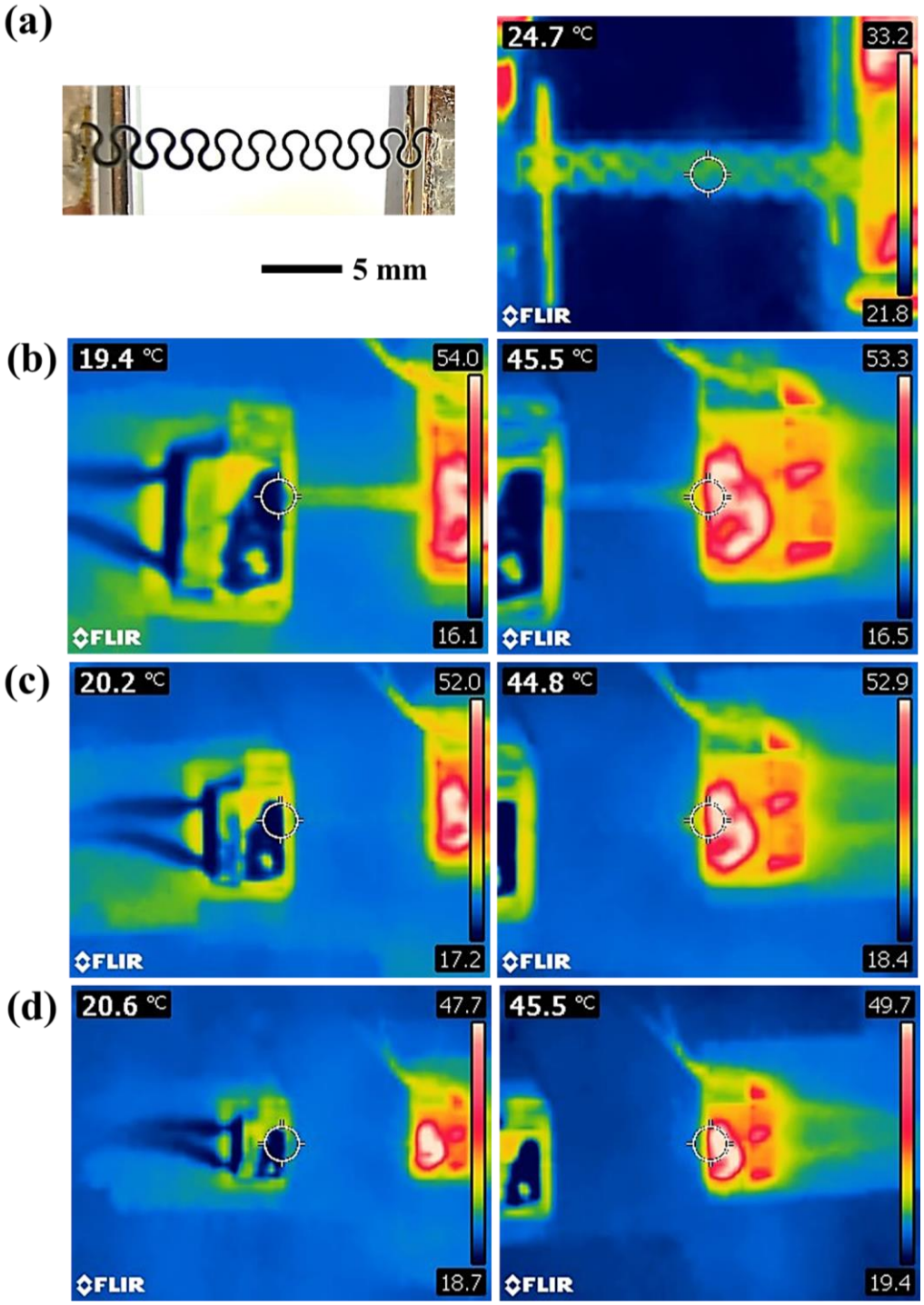

Figure 7.29 (a) Photographic and thermal images of the unstretched and unheated single-layer AJ-printed stretchable CG-TEG with in-plane design. Thermal images of the stretchable CG-TEG being stretched at a strain of (b) 0%, (c) 50%, and (d) 100%, respectively, under a constant applied ΔT of ~25 °C. The circle highlights the localised temperature reading.

7.8 Substrate-based Stretchable Thermoelectric Generators

As shown in Figures 7.30 (a) and (b), the serpentine-shaped PEDOT:PSS films and Ag electrodes were successfully embedded within a PDMS or PU matrix with a total thickness of ~1 mm and ~0.5 mm, respectively, via the AJP method. A strip-shaped structure was also fabricated in Appendix A.9 for comparison. Since both the PEDOT:PSS and Ag inks used for the AJP process were water-based, and the PDMS and PU substrates became hydrophilic after oxygen plasma treatment, the resulting printing quality was quite good here. It can be seen in Figures 7.30 (c) and (d) that AJ-printed PEDOT:PSS films and Ag electrodes firmly adhered to the PDMS or PU substrates, where a PDMS or PU encapsulation layer was coated on top to protect them. Nonetheless, when it came to the multilayered structure fabrication, the alignment of the subsequent layer deposition was extremely challenging. This might stem from the dimension change of the previously deposited layer, because the PDMS and PU substrates were prone to shrinkage after the high-temperature curing treatment and their thickness increased after the encapsulation layer deposition. Moreover, there existed some other issues in this approach. Firstly, AJ-printed PEDOT:PSS films and Ag electrodes were required to be co-cured with the pre-formed PDMS or PU substrates at 130 °C for 12 hours so as to ensure the electrical conduction of Ag electrodes and to give firm adhesion between AJ-printed films and elastomeric substrates. However, this prolonged high-temperature curing process substantially degraded the pre-formed PDMS and PU substrates, and they became quite rigid and lost their stretchability owing to their low thermal stability. Secondly, although no apparent cracks or delamination were found in PEDOT:PSS films or Ag electrodes from the optical microscope or SEM, they retained electrically disconnected. This might be because the thermal expansion of PDMS or PU substrates during the prolonged high-temperature curing treatment caused some internal disconnects within PEDOT:PSS films and/or Ag electrodes. Due to the higher thermal expansion coefficient of PDMS and PU, they expanded and shrunk to a larger extent than PEDOT:PSS and Ag when being heated and cooled during the curing process. After cooling down to the room temperature, the PDMS and PU substrates recovered to their original

shapes, and the cracks formed within PEDOT:PSS films and/or Ag electrodes were 'self-healed'. As a result, these cracks could not be seen in the optical microscope or SEM. However, they did exist, and they eventually caused electrical disconnects within these substrate-based stretchable TEGs.

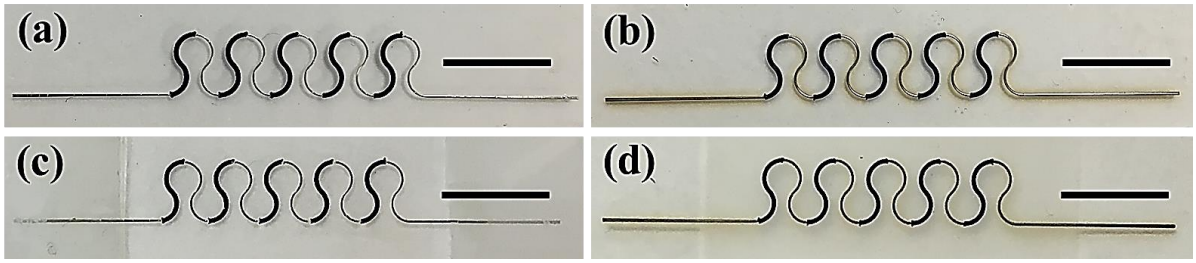

Figure 7.30 Photographic images of (a) PDMS or (b) PU substrate-based stretchable TEGs with (c) PDMS or (d) PU encapsulated on top. Scale bar: 10 mm.

Here, another approach is proposed to solve the above-mentioned problems by printing PEDOT:PSS films and Ag electrodes onto a PI supporting layer so that they could be well protected from electrical disconnects during the co-curing process. Additionally, the PI supporting layer is essential here to form the free-standing TE structure, as discussed in Section 7.1. Eventually, different free-standing TE structures were embedded within the PDMS or PU by the drop-casting method. As presented in Figures 7.31 (a) and (b), single-layer and 3-layer AJ-printed stretchable TE structures were successfully embedded within the PDMS by the one-step drop-casting method. Although these PDMS-based TEGs (cured at 80 ºC for 2 hours) became more stretchable than that of the above-developed PDMS-based one (cured at 130 ºC for 12 hours), they still suffered from the limited stretchability. Due to the limitation of the substrate that largely reduced their stretchability, they could endure only ~30% stretching strain prior to fracture and failure. The cracks were prone to initiating and propagating along both ends, where the PDMS-based TEGs were clamped and the highest local strains were induced. For the PU-based TEGs, since PU solution contained a high concentration of DMF solvent (95 wt.%), it was found that the subsequent PU layer deposition could partially dissolve the previously deposited and solidified PU film, thereby resulting in the deformed film with rough and non-uniform surfaces. This issue could be alleviated by heating the deposited PU film when

drop-casting the subsequent PU solution as well as by using less amount of PU solution in each deposition so that DMF solvent could be quickly evaporated prior to dissolving the previously cured and solidified PU film. Consequently, the thickness of PU film could be quickly built up by the multiple drop-casting method. However, some air bubbles were created during the drop-casting process, as presented in Figure 7.31 (c). Although these minor defects did not affect the mechanical strength of the TEG, they were prone to forming larger voids and cracks when being stretched cyclically, as demonstrated in Figure 7.31 (d). Unfortunately, fractures occurred in different positions of the embedded serpentine TE structure when being stretched at a small deformation strain of 30%. More apparent cracks and disconnects were seen, as the strain was increased to 50%. It was found that both the non-stretchable PEDOT:PSS films and Ag electrodes were stretched along with the PU substrate, rather than stretching the serpentine structure. This thus led to the loss of high stretchability in these serpentine-shaped TE structures.

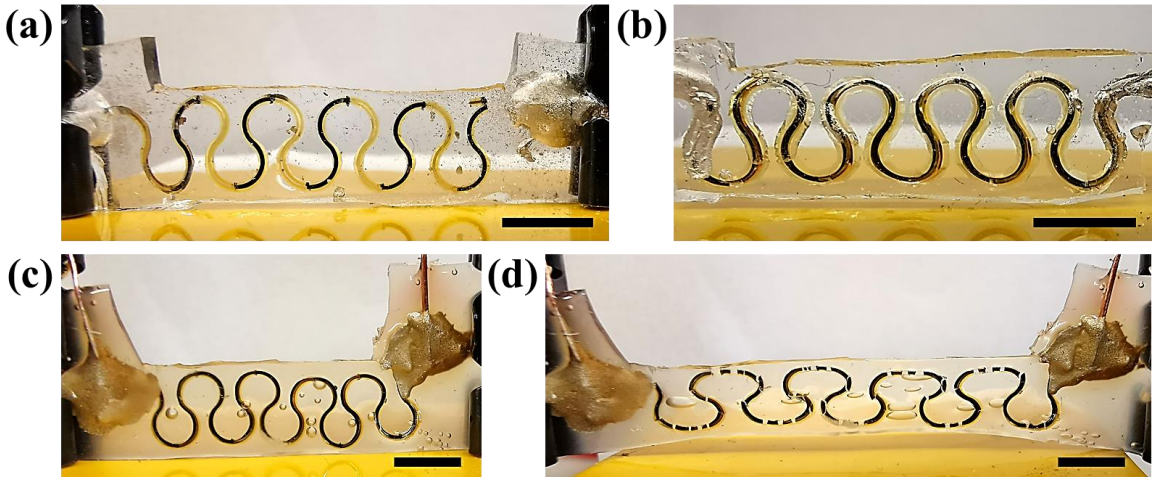

Figure 7.31 Photographic images of (a) single-layer and (b) 3-layer AJ-printed stretchable TE structures embedded within the PDMS, and (c) 3-layer AJ-printed stretchable TE structure embedded within the PU, (d) which was stretched at a strain of 50%. Scale bar : 5 mm.

Apart from the loss of high mechanical stretchability, another drawback of these substrate-based TEGs is their higher thermal conductivity. Since the air in the hollow structure described in Section 7.3 with lower κ [~0.026 W/(m.K)][204] was replaced by the PDMS or PU elastomers with higher κ [~0.17 W/(m.K) for PDMS[260] and ~0.2 W/(m.K) for PU[261]],

the heat conduction between the hot and cold sides could become much faster, and thus leading to a smaller temperature gradient created, as demonstrated in thermal images in Figure 7.32. Meanwhile, since no heat sink was employed here due to the difficulty of being mounted, these substrate-based TEGs had to be cooled naturally by the ambient air which is a bad heat sink. Consequently, this resulted in a substantial loss in their energy conversion efficiency during practical use. Considering these results, these substrate-based TEGs were not an ideal option for stretchable thermal energy harvesting applications.

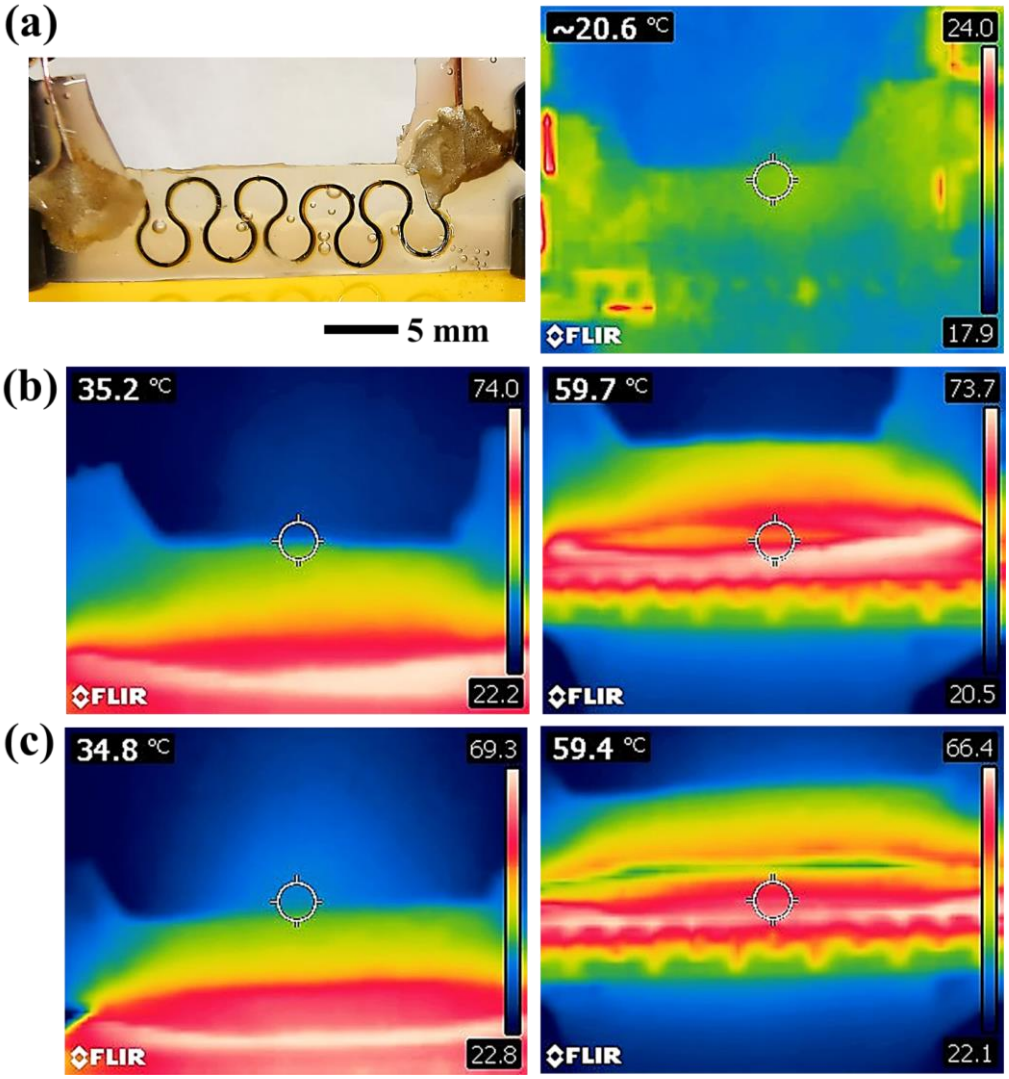

Figure 7.32 (a) Photographic and thermal images of the unstretched and unheated 3-layer AJ-printed stretchable TE structure embedded within the PU. Thermal images of the PU-based stretchable TEG being stretched at a strain of (b) 0% and (c) 50%, respectively, under a constant applied ΔT of ~25 °C. The circle highlights the localised temperature reading.

7.9 Summary

In conclusion, fully printed free-standing and stretchable TE structures have been developed, for the first time, by using the facile and versatile AJP method. The PEDOT:PSS and Ag inks have been AJ-printed and embedded within a PI supporting layer to form a stretchable serpentine structure. Some technological constraints of the PEDOT:PSS polymer, e.g. brittleness, poor processability, and high cost, could be overcome by this means. Different sacrificial substrate materials have also been explored to achieve free-standing structures via the in-house developed film lift-off method. These fabrication techniques could render the PEDOT:PSS polymer compatible with large-scale production of stretchable TEG applications. The in-plane and out-of-plane design structures have been adopted here for comparing their TE performance and mechanical properties. The thickness of these free-standing structures could be varied from ~15 μm to ~70 μm by varying the number of AJ-printed layers. The pristine PEDOT:PSS film is non-stretchable. Nevertheless, with these innovative serpentine structures, its strain-to-break value has been increased up to 200%, which has rendered the PEDOT:PSS particularly robust with superior mechanical stretchability. These PEDOT:PSS-based stretchable TE structures have shown excellent TE performance with P_{max} of ~0.78 nW and V_{oc} of ~0.92 mV at a ΔT of ~25 °C as well as no substantial loss in their electrical characteristics when subjected to being stretched at 50% mechanical strain over a prolonged period of time (continuous 20,000 stretching cycles for 40 hours). Also, the CG-TEC concept has been successfully incorporated into the stretchable structure so as to achieve further TE performance improvement. Lastly, substrate-based stretchable TEGs have been investigated by applying PDMS and PU elastomers as stretchable substrates. However, neither their obtained TE performance nor mechanical stretchability exhibited as good as that of free-standing structures.

Chapter 8

Conclusions and Future Work

8.1 Conclusions

This thesis has explored the feasibility of utilising organic-inorganic thermoelectric (TE) nanocomposites for application in harvesting thermal energy from low-grade heat sources. Flexible and stretchable thermoelectric generators (TEGs) have been developed to expand their applicability, particularly in wearable electronics. In order to address the rigidity of inorganic TE materials which hinders them from being applied in flexible and/or stretchable TEGs, a systematic investigation on the fabrication of a novel hybrid organic-inorganic nanocomposite structure has been presented, for the first time, by using a bespoke aerosol-jet printing (AJP) technique. Here, flexible and conducting poly(3,4-ethylenedioxythiophene) polystyrene sulfonate (PEDOT:PSS) has been used as a polymeric matrix to provide mechanical support and flexibility to high-performance inorganic TE nano-fillers, ranging from Bi_2Te_3 nanoparticles and Sb_2Te_3 nanoflakes to multiwall carbon nanotubes (MWCNTs). An innovative *in situ* mixing method has been developed to systematically vary the weight percentage of the loaded inorganic nano-inclusions within different PEDOT:PSS-based TE nanocomposites. Subsequently, these fully printed nanocomposite structures have been optimised by dynamically tuning their compositions during the AJP process alongside optimising printing quality. This approach has effectively solved previous issues related to poor distribution and dispersion of the loaded nano-fillers and resulted in well-dispersed hybrid nanocomposite

structures, thereby enhancing their final TE properties. Different design structures, according to specific applications, have also been fabricated. Moreover, compositionally graded composite structures have been demonstrated to further improve the energy conversion efficiency and power output of these AJ-printed TE nanocomposites across the entire operating temperature range. Finally, novel free-standing serpentine designs have been realised with the facile and scalable AJP technique to produce stretchable TEGs. The multilayered structure has also been developed to achieve higher power output. Although the currently generated electric output of these fabricated flexible and stretchable TEGs was not sufficient enough to directly power any sensor nodes, it is believed they have great potential for powering future low-power microelectronics by deploying higher-performance TE materials as well as forming higher-efficiency *n*-*p* junctions in the TEG. They also offer the pathway to large-scale manufacturing of flexible and stretchable TEGs as wearable energy harvesting or sensing components for the next-generation autonomous devices.

In Chapter 4, the fabrication of flexible *p*-type PEDOT:PSS-based nanocomposites have been demonstrated, for the first time, by using a versatile, cost-effective, and easily scalable AJP technique. Also, a facile, high-yield and scalable solvothermal synthesis approach has been developed for the synthesis of Bi_2Te_3 and Sb_2Te_3 nanomaterials. This low-temperature solution-based synthesis method allowed good control of size and shape at the nanoscale, thus enabling greater enhancement in the TE properties of the resulting nanocomposites. Here, various weight percentages of Bi_2Te_3/Sb_2Te_3 nanomaterials with higher S and higher σ have been integrated with the low-κ PEDOT:PSS polymer, for printing TE nanocomposites on a cheap and flexible PI sheet. By adopting the *in situ* mixing method, the aerosol flow rates from two separate atomisers in fluid connection with respective ink sources could be individually and independently adjusted during the printing process, thereby allowing fine-tuning the composition of the nanocomposite being AJ-printed. This therefore enabled various loading ratios of Bi_2Te_3/Sb_2Te_3 nano-fillers within the PEDOT:PSS matrix. By properly tuning the flux ratio and flow speed, as well as choosing the appropriate number of printed layers, improved TE properties with excellent mechanical flexibility and robustness have achieved in these

AJ-printed nanocomposites. Among them, the PEDOT:PSS-based nanocomposites loaded with 85 wt.% Sb_2Te_3 nanoflakes possessed the highest PF with a value of ~28.3 μW/(m.K^2). Importantly, they have exhibited stable and robust performance even upon repeated flexing. The demonstration of flexibility enables broader applications of these AJ-printed TE nanocomposites, particularly for wearable electronic devices. Moreover, the in-house developed *in situ* mixing approach can open up the possibility of using the same inks of individual constituent materials to print nanocomposite structures with various compositions.

Chapter 5 presented the results of AJ-printed hybrid TE nanocomposites on a flexible substrate, which were comprised of low-κ PEDOT:PSS, high-σ MWCNTs, and high-S Sb_2Te_3 nanoflakes. By virtue of the versatility of the AJP technique and the *in situ* mixing method, almost no surfactant has been added here to stabilise MWCNTs in solution form, which could significantly enhance their electrical conductivity. The well-dispersed MWCNTs and Sb_2Te_3 nano-inclusions also facilitated the reduction of the overall thermal conductivity by phonon scattering at the organic/inorganic interfaces, thereby improving their final TE performance. Different polar solvents have been used to surface-treat these nanocomposite structures to achieve higher σ by de-doping PSS moleculars. Among them, the DMSO-treated Sb_2Te_3-MWCNTs-PVP-PEDOT:PSS nanocomposite has presented the highest PF with a value of ~41 μW/(m.K^2). Furthermore, they have shown superior mechanical flexibility and robustness, even after 60 hours of continuous flexing cycles (i.e. 36,000 cycles in total), which demonstrated that the added ductile MWCNTs enabled greater mechanical flexibility. Consequently, these TE nanocomposites could be directly integrated into TEGs with minimal post-processing treatment. They were particularly robust and flexible with stable TE performance, which could be deployed as thermal energy harvesters for wearable devices, or in applications requiring ease of mounting or surface conformability of the energy harvester.

In Chapter 6, the temperature-dependent TE properties of these AJ-printed PEDOT:PSS-based nanocomposites developed in Chapters 4 and 5 have been explored. In order to overcome the problem of the temperature-variation of PF, compositionally graded

thermoelectric composites (CG-TECs) have been demonstrated to optimise their overall PF values across the temperature gradient they operate in between. The composition of nanocomposite structures could be systematically tuned along the length of the TEG via the bespoke AJP method with controlled *in situ* mixing capability, thus enabling the realisation of such CG-TECs, without problems arising due to interfaces, as the organic matrix remained the same throughout. By selecting proper compositions based on temperature-dependent PF profiles, different dual-segment CG-TECs have been designed, and their power outputs have been found to be superior as compared to their uniform-composition counterparts operating under the same ΔT. This proves that the CG-TECs design provides a means by which vast improvement in TE performance and energy conversion efficiency of the whole TEG device could be realised, thus highlighting its potential and capability of harvesting energy from low-grade waste heat (<100 °C). This work is particularly timely and relevant, as current TEGs notoriously suffer from inefficiency, which has been specifically addressed here. Importantly, the author has demonstrated a novel way by which the composition of nanocomposites could be varied to better suit the operating temperature range while maintaining excellent mechanical flexibility for conformable applications. This finding therefore opens the door to a wide range of combinations comprising a variety of polymeric matrices and inorganic TE nano-insertions that could be tailored for the use across a specific temperature gradient, thus driving research and innovation in this key energy sector.

In Chapter 7, to satisfy the growing need for alternative energy solutions to ‘small-power’ wearable electronic devices, the fabrication and integration strategies to free-standing and stretchable TEGs via the facile and versatile AJP technique have been proposed. Stretchable serpentine structures have been designed into either in-plane or out-of-plane design for harvesting heat from different directions. Single-layer and multi-layer free-standing structures have been achieved by AJ-printing and encasing the PEDOT:PSS and Ag within a PI supporting layer, with the aid of a sacrificial substrate. With the novel serpentine structure, the pristine PEDOT:PSS film that is intrinsically non-stretchable has shown an increased strain-to-break value up to 200%, as well as exceptional mechanical stretchability. These

PEDOT:PSS-based stretchable TEGs have exhibited outstanding TE performance with P_{max} of ~0.78 nW and V_{oc} of ~0.43 mV at ΔT of ~25 °C as well as no significant loss in their electric output when stretched at 50% strain over a prolonged period of time (continuous 20,000 stretching cycles in 40 hours). The CG-TEC concept discussed in Chapter 6 has also been successfully integrated with the stretchable design for further TE performance improvement of these stretchable TEGs. Lastly, substrate-based stretchable TEGs that were fabricated by using PDMS or PU elastomers as stretchable substrates have been demonstrated. Nevertheless, they did not perform as well as the free-standing structures. This has confirmed the hollow and free-standing structure is beneficial to the TE performance and mechanical stretchability, which are crucial to conformable applications, e.g. wrapping around heat pipes or skin-based electronics.

8.2 Future Work

Based on the above results and discussions, the flexible and stretchable TEGs developed in this thesis are still facing some challenges, in particular the low PF values obtained in AJ-printed TE nanocomposites and low power outputs in their resulting TEGs. From a material science perspective, there are several avenues, including material selection, characterisation and measurement techniques, as well as device fabrication, to address these issues, thereby improving their TE performance. Accordingly, some future works are provided as follows.

8.2.1 Materials Selection

(i) From the road map of current inorganic TE materials listed in Section 2.4, there exist some high-*ZT* TE inorganic materials that would be promising candidates for application in TEGs at or near room temperature. For example, *n*-type silver chalcogenides (Ag_2S) possessed *ZT* values of 0.44 at 300 K and 0.63 at 450 K.[262] They also exhibited extraordinary metal-like ductility with high plastic deformation strains at room temperature, which is beneficial to flexible or even stretchable TEG applications.[263] Regarding other low-cost and high-*ZT* TE inorganic materials, *p*-type SnSe is an applicable candidate. SnSe has a very high *ZT* of

2.62 at 923 K in its single-crystal form,[84] and it can be synthesised into various nanostructured forms via some surfactant-free solution-based synthesis methods,[123] with preliminary results shown in Appendix A.2. As a result, these high-performance TE materials can be explored in the printed TEG fabrication via the AJP method.

(ii) *n*-type TE materials are indispensable to form *n*-*p* junctions for the achievement of highly efficient TEGs. Nevertheless, as discussed in Section 2.4, the fabrication of *n*-type organic materials or composites via facile and scalable methods is rarely reported. Therefore, further efforts are urgently needed to develop high-performance and stable *n*-type TE polymers. Some conjugated polymers or coordination polymers, as mentioned in Section 2.4.2, can be potential candidates for the fabrication of high-performance *n*-type TE nanocomposite. Other cheaper insulating polymers, such as polyvinylpyrrolidone (PVP) or polyvinylidene fluoride (PVDF), can be fabricated into *n*-type TE nanocomposites by integrating with some *n*-type TE inorganic materials. At the same time, carbon-based nanomaterials, such as graphene, single-wall or double-wall CNTs, can be added to further increase the electrical conductivity of these nanocomposite structures.

(iii) For the improvement of stretchable TEGs developed in Chapter 7, high-performance PEDOT:PSS-based nanocomposites developed in Chapters 4 and 5 can be deployed to replace the pristine PEDOT:PSS. Furthermore, since the inorganic TE materials can be fully encased within the PI polymer to form a stretchable structure via the AJP technique, these encapsulated inorganic TE materials can be sintered at a high temperature without being oxidised (up to the melting point of PI ~450 °C) to obtain a dense microstructure. By this means, higher TE performance can be achieved without using the conducting polymer as a matrix. At the same time, these stretchable serpentine structures can also add extra stretchability to the rigid inorganic TE materials, which can further expand their applications.

8.2.2 Characterisation and Measurement Techniques

(i) The out-of-plane Seebeck coefficient and electrical conductivity measurements (see Appendix A.4) on AJ-printed thin-film structures are desired to compare with their in-plane results. This measurement setup can also be modified for the TE property measurement of those out-of-plane stretchable TEGs developed in Chapter 7. In addition, further investigation of the thermal conductivity measurement of these AJ-printed thin-film structures is required, as discussed in Appendix 1. Efforts are currently underway in this project.

(ii) To evaluate the TE properties of these AJ-printed nanocomposite structures at a more fundamental level, the Hall-effect measurement method (see Appendix A.5) should be used to understand their charge transport properties. Scanning thermal microscopy should also be utilised for mapping their thermal conductivity and Seebeck coefficient values at the nanoscale. Moreover, a thermal infrared camera with higher imaging resolution and faster data recording speed should be employed to map the temperature distribution of the tested sample more accurately, thereby measuring more accurate TE properties.

(iii) As demonstrated in Chapter 7, only an in-plane horizontal elongation test on these free-standing stretchable TEGs has been conducted. However, for wearable applications in real life, mechanical forces can be imposed in various directions, not just limiting to the 2D direction. In this context, an out-of-plane vertical compression test is desired to further evaluate their mechanical stretchability. This compression test can be implemented by sandwiching the stretchable TEG between two rigid plates and displacing the top or bottom plate with the control of a piezoelectric stage or other motion controllers. The out-of-plane measurement setup described in Appendix A.4 can be modified to achieve this goal.

8.2.3 Device Fabrication

(i) Our AJP technique and in-house developed *in situ* mixing method can be applied to other functional organic and inorganic material systems, in particular on the development of *n*-type materials, where the formed *n-p* junction can substantially improve the power output. Furthermore, the multilayered structure can be exploited, as it can increase the power output and enhance the mechanical stretchability of the TEG by increasing the number of layers.

(ii) Our high-resolution AJP technique can promote broader applications of these flexible and stretchable nanocomposite structures at the microscale. For instance, these microscale nanocomposite structures can be designed into a self-powered strain sensor and temperature sensor for integration into wearable electronics. It would also be interesting to demonstrate a 3D structure by using the AJP technique. For example, PEDOT:PSS hydrogel with higher viscosity can be potentially AJ-printed into a 3D structure to form 3D TE legs, which can be encased within an elastomer for stretchable TEG or sensor applications. By virtue of their good biocompatibility, they can also be incorporated into future bioelectronic devices.

(iii) Because of the versatility of the AJP technique, a wide range of ink materials can be compatible with printing microscale device structures. In this context, energy storage devices, such as supercapacitors and batteries, can be fabricated and integrated with these flexible and stretchable energy harvesters into the all-in-one energy device. Moreover, the *in situ* mixing method can ensure excellent dispersion and uniform distribution of nano-fillers that can facilitate the performance of formed nanocomposite structures in the energy storage devices.

Appendix

A.1 Thermal Conductivity Measurement

Here, some preliminary results on the thermal conductivity measurement of the AJ-printed thin-film structures by using the transmission line model are presented. This work was conducted in collaboration with Dr Sanjiv Sambandan, where Dr Sambandan built the theoretical model, and the author performed the experimental work.

A.1.1 Introduction

The thermal conductivity, κ, takes into consideration the combined contribution of both electrons and phonons, as discussed in Section 2.3.2. In bulk metals, both κ and σ are determined by the scattering of electrons in the lattice, and are hence related by the Wiedemann-Franz law as $\kappa = \sigma L_0 T$, with L_0 being the Lorenz number. Since $ZT \sim \alpha^2 L_0 T^2$, with α representing the Seebeck coefficient here, bulk metals rely mostly on the improvement in α to improve ZT. However, if the phonon contribution of the thermal conduction becomes significant, the scaling relation between κ and σ can deviate from $L_0 T$. This would also be the case, if charge transport is confined to one-dimension. Both these possibilities are achieved in organic polymers. In the case of organic TE materials, it becomes necessary to determine all three parameters, α, σ, and κ in order to make an informed decision on the suitability of the material for TEGs. However, the determination of these parameters in organic polymers can be quite challenging, especially the measurement of κ. With regards to the measurement of in-plane thermal conductivity in thin films, the techniques used can be broadly classified into two methods. (1) Steady-state methods, which are based on forcing a constant heat flow through the film and measuring the steady-state temperature difference, dT, between two points

separated a distance, *dl*, along the length of the film. Usually, heat is generated by driving a constant current *I* through a heating coil of resistance, *R*, so that the rate of heat generation is I^2R. Then, $\kappa \sim I^2 R\ (dl / a)\ dT$, with *a* being the area of cross-section of the film. However, parasitic heat losses and the large time constants involved in achieving steady state do not yield accurate results. (2) Transient methods, which use a time-varying current, $I(t)$, to heat the coil for extracting κ. One technique involves the application of a periodic current waveform comprising of rectangular pulses. The time-varying temperature difference, $dT(t)$, between two points separated a distance, *dl*, now responds to the time-varying heat pulses. The time constant of the time variation in $dT(t)$ contains the information on κ. Another popular transient method to measure the in-plane κ is the 3-ω method. In this technique, the current through the coil is varied sinusoidally, $I(t) \propto cos(\omega t)$. This results in the heat generation rate varying as $cos(2\omega t)$ along with a DC component. This, in turn, results in temperature also varying as $cos(2\omega t)$ along with a DC component. The magnitude of temperature variation depends upon the thermal conductivity of the film that draws the heat away from the coil. The change in temperature causes the resistance of the coil to fluctuate in a similar manner as the temperature. Therefore, the voltage measured across the coil has the components of ω and 3ω. Thus, for a driving current at ω, the voltage at 3ω is directly dependent on the temperature variations observed at 2ω. Therefore, the measurement of the 3ω component of the voltage is an indirect measurement on κ. Any of these above-discussed approaches could be used to determine α, σ and κ in printed films used for TEG applications. However, printed polymer-based TEGs are intended to be used in a very dynamic environment subject to mechanical forces due to bending and/or stretching, electrostatic discharge events owing to the contact with the body, extreme chemical environments due to washing or drying of wearables, and so forth. Considering these factors, it is very likely that the *ZT* of polymer is a dynamic parameter itself, making the performance of the TEG a time-dependent parameter, thereby impacting any circuits or systems driven by the TEG. Hence, it becomes essential to enable the online monitoring of the TEG, where α, σ and κ of the polymer film is periodically extracted by online measurements on the system.

A.1.2 Transmission Line Model

In this work, one possible setup of this kind of a system that enables the real-time extraction of *ZT* is discussed. The real-time measurement of σ in various materials is a well-studied problem, and therefore the real-time measurements of α and κ alone are focused here. Both these parameters are measured with transient techniques wherein the temperature of one end of the TE element is pulsed. A major advantage of using thermoelectrics is that all measurements are possible in the electrical domain without the need for other sensors. Since a temperature difference results in a potential difference in a TE material, the extraction of κ is possible by the analysis of the time constants of the dynamic of the Seebeck voltage, whereas the measurement of α is possible by the measurement of the magnitude of the Seebeck voltage. The author makes use of this advantage and designs a system and methodology around this concept. The accuracy of parameter extraction is improved by designing the signal processing and electronics based on the model of the polymer film viewed as a transmission line. Ignoring parasitics, the in-plane heat transferred by conduction in the polymer film can be defined by the Fourier equation:

$$\frac{\partial T}{\partial t} = \frac{\kappa}{\rho s}\frac{\partial^2 T}{\partial x^2} \tag{A-1}$$

where ρ is the mass density, and s is the specific heat capacity of the polymer film.

Drawing analogies to an electrical circuit, the thermal circuit of the polymer film can be represented by an equivalent electrical circuit of a distributed *resistor-capacitor transmission line*, as shown in Figure A.1.

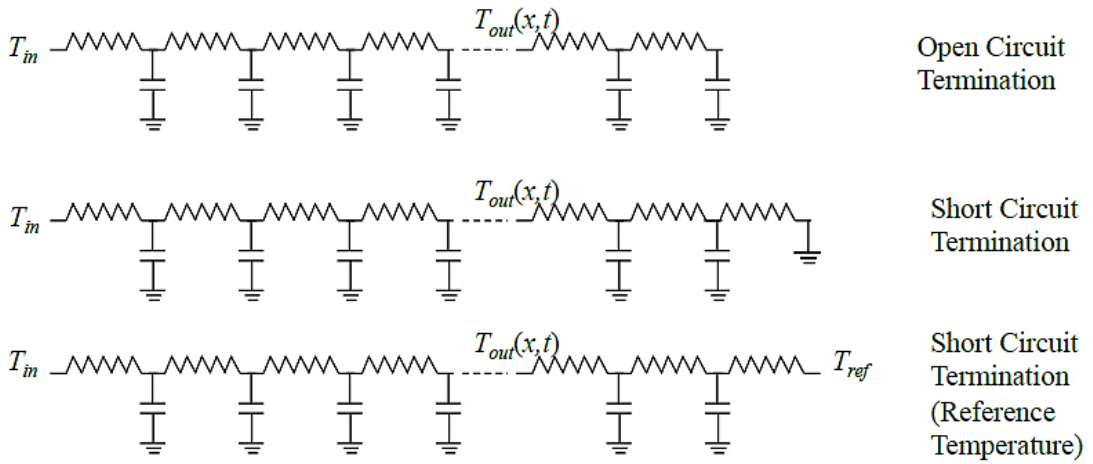

Figure A.1 Schematic drawing of the distributed resistor-capacitor transmission line.

The temperature is analogous to the voltage, while the heat flux is analogous to the charge resulting in a rate of change of heat flux being the current. For a polymer film of uniform cross-section area, a, the thermal resistance and thermal capacitance of the segment of length, dx, can be defined by the thermal resistance per unit length, r, and thermal capacitance per unit length, c, to be given by

$$r = (\kappa a)^{-1}$$
$$c = \rho s a \tag{A-2}$$

Thus, Equation A-1 becomes $dT/dt = (1 / r\,c)\, d^2T/dx^2$. It must be noted that the substrate affects r and c. Moreover, if the ends of the polymer film are at widely different temperatures, there is a gradual variation in r and c from one end to the other.

The temperature at the hot end of the film, $T_{in}(t)$, is controlled by the control of input current to the coil, the local thermal mass of the source and the heat dissipated in the polymer film and other pathways. Therefore, the region from the heater coil to the polymer film can itself be modelled as a *transmission line*. If the effective thermal impedance of this transmission line is much smaller than the thermal impedance of the polymer substrate ($\kappa_{line} << \kappa_{substrate}$), the temperature $T_{in}(t)$ can be said to increase or decrease instantly and can be modelled as a step input with $T_{in}(t) = T_{in0}\,u(t)$ with $u(t)$ being the unit step function and T_{in0}. Given this input in temperature, $T_{in}(t)$, the thin polymer film now begins to conduct heat to a thermal mass that is

allowed to float. At any time, t, the temperature, $T_{out}(x, t)$, at a point located along the length of the film and at a distance, x, from the heat source can be shown to be described by the complementary error function. However, if the effective thermal impedance of path between the heating coil and the polymer film is not insignificant, the temperature transients at the source of the polymer film can be expected to have the nature of the complementary error function itself. However, if the thermal impedance of the pathway from the coil to the polymer film is minimised and made much smaller compared to the thermal impedance of the polymer film, $T_{in}(t)$ can be modelled as a ramp that quickly achieves its steady-state value, T_{in0} at time $t = t_0$ with the ramp rate being T_{in0}/t_0. This temperature profile can be defined as the superposition of two semi-infinite ramp inputs $T_{in}(t) = (T_{in0}/t_0)tu(t) - (T_{in0}/t_0)(t - t_0)u(t - t_0)$ and $T_{out}(x, t)$ responding to these ramp inputs. Assuming that the values of r and c do not change along the length of the film despite the difference in temperature, it can be shown that

$$T_{out}(x,t) = \begin{cases} T_{in0}\text{erfc}(p(x,t)) & \text{if } T_{in}\text{:Step} \\ T_{in0}(g(x,t) - g(x,t-t_0)) & \text{if } T_{in}\text{:Ramp} \end{cases} \quad \text{(A-3)}$$

with $p(x,t) = (rc/t)^{1/2}x/2$ and $g(x,t) = (t/t_0)((1+2p(x,t)^2)\text{erfc}(p(x,t)) - (2/\pi)^{1/2}p(x,t)e^{-p(x,t)^2/2})u(t)$.

In both cases, the information about κ is contained in the term $p(x, t)$ and more specifically in r. Since the polymer film is also a TE material, the temperature difference between two points also translates to a voltage difference between two points. If the hot end of the polymer film having temperature $T_{in}(t)$ is considered to be electrical ground for voltage measurements, the voltage, $V_{out}(x, t) = \alpha(T_{out}(x, t) - T_{in}(t))$ and

$$V_{out}(x,t) = \begin{cases} -\alpha T_{in0}\text{erf}(p(x,t)) & \text{if } T_{in}\text{:Step} \\ -\alpha T_{in0}(h(x,t) - h(x,t-t_0)) & \text{if } T_{in}\text{:Ramp} \end{cases} \quad \text{(A-4)}$$

with $h(x, t) = (t/t_0)(-2p(x, t)^2 + (1 + 2p(x, t)^2)\text{erf}(p) + (2/\pi)^{1/2}p(x, t)e^{-p(x,t)^2/2})u(t)$.

This voltage signal can now be processed to compute p. It is possible to do this for both

cases by storing and sending data to an external computer, it is desirable to construct a simple analog computer on the substrate to enable real-time measurement of κ and α to enable real-time performance prediction of TEGs used on wearable devices.

To demonstrate the case, the author engineers the system so that compared to the time constants associated with the thermal circuit of the polymer film, $T_{in}(t)$ appears as a step input for all practical purposes. Even if $T_{in}(t)$ follows a ramp response, the ramp response can be viewed as a step input in the limit $t_0 \rightarrow 0$, or in a more practical sense if t_0 is much smaller than the time taken to reach steady state. Furthermore, for practical purposes, it is convenient to approximate the error function in more simple terms that maintain reasonable accuracy in the domain of interest. The first three terms of the Taylor approximation of the error function is $\text{erf}(y) = 2y/\pi^{1/2} - 2y^3/3\pi^{1/2} + y^5/5\pi^{1/2} - \ldots$ On the other hand, a reasonably close approximation to erf(y) is seen in $(2/\pi^{1/2})\tanh(y) = 2y/\pi^{1/2} - 2y^3/3\pi^{1/2} + 4y^5/15\pi^{1/2} - \ldots$ Therefore, with the aim of developing an analog electronic computing system, $\text{erf}(p(x, t)) \approx 2/\pi^{1/2}\tanh(p(x, t))$ is approximated. Therefore, for the case of T_{in} being a step input

$$V_{out}(x,t) \approx -\frac{2}{\pi^{1/2}}\alpha T_{in0}\frac{1-\exp(-2p(x,t))}{1+\exp(-2p(x,t))} \tag{A-5}$$

A.1.3 Extractions of α and κ

If the voltage is measured at the instant close to $t = 0$, (or immediately after $t = t_0$ in the case of a ramp-like input), $V_{out}(x, t) \approx -(2/\pi^{1/2})\alpha T_{in0}$. This therefore becomes a direct measure of α. Since the measurement is being made at very small t, it may be difficult to make the assumption of a step input (since t can be $< t_0$). However, even if the input is ramp-like, $V_{out}(x, t) \approx -(2/\pi^{1/2})\alpha T_{in0}t/t_0$, and the time derivative obtained at close to $t = 0$ is a direct measure of α.

From the above measurements, the quantity $-(2/\pi^{1/2})\alpha T_{in0}$ can be expected to be known for all practical purposes. In order to obtain information on κ, the parameter $p(x, t)$ must be measured. It is noted that

$$p(x,t) = \frac{1}{2}\ln\left(\frac{(2/\pi^{1/2})\alpha T_{in0} + V_{out}(x,t)}{(2/\pi^{1/2})\alpha T_{in0} - V_{out}(x,t)}\right) \tag{A-6}$$

Once the location of measurement x and time of measurement t for $V_{out}(x, t)$ is known, the product $rc = \kappa/\rho s$ becomes defined as

$$\frac{\kappa}{\rho s} = \left[\ln\left(\frac{(2/\pi^{1/2})\alpha T_{in0} + V_{out}(x,t)}{(2/\pi^{1/2})\alpha T_{in0} - V_{out}(x,t)}\right)\right]^{-2}\frac{x^2}{t} \tag{A-7}$$

In order to extract κ specifically, the thermal capacitance defined by ρs needs to be identified. However, a measure of the relative variation in κ is provided by the extraction of the term $\kappa/\rho s$.

A.1.4 Device Fabrication and Measurement

As can be seen in Figure A.2 (a), two PEDOT:PSS films with a length of 5 mm and 10 mm, respectively, were printed on a PI sheet via the AJP method for the measurement of their α and κ. Prior to the printing of PEDOT:PSS film, two Ag thermometers were firstly AJ-printed with a design pattern illustrated in Figure A.2 (b), due to their higher curing temperature (minimum 150-200 ^{o}C to obtain acceptable electrical conduction). Furthermore, as plotted in Figures A.2 (c) and (d), these AJ-printed Ag thermometers were calibrated by a commercial Pt-100 thermometer before being used for the subsequent α and κ measurements. Since these Ag thermometers were printed adjacent to the PEDOT:PSS film, they could give a faster response and more accurate measurement of the localised temperature compared to that measured by a Pt-100 thermometer which was physically taped onto the substrate. Since all these components were fully printed, the PEDOT:PSS could be easily replaced by other TE materials here, which could largely expand the application of this ‘on-chip’ measurement technique.

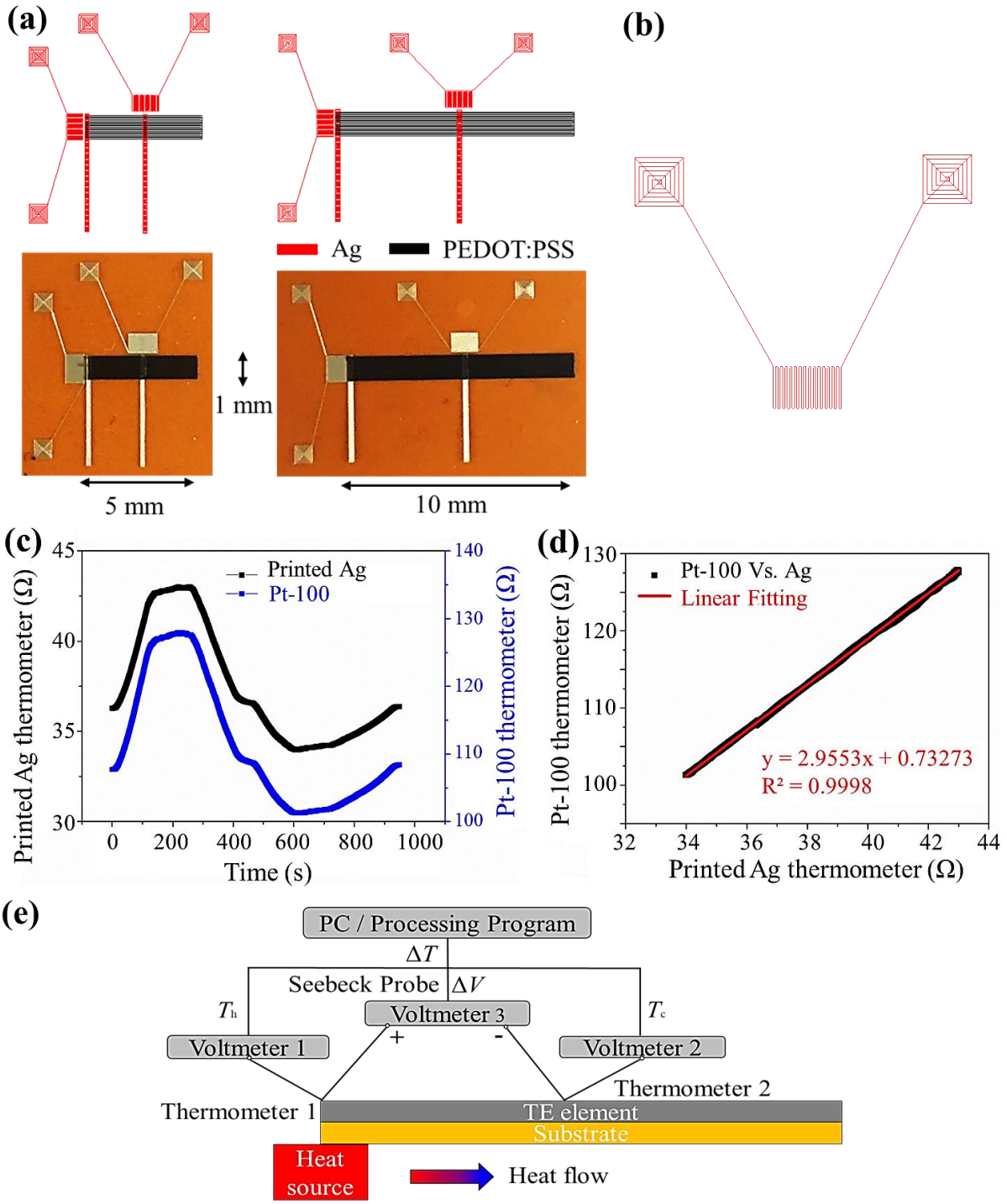

Figure A.2 (a) AutoCAD-design patterns and photographs of Ag thermometers, Ag electrodes, and PEDOT:PSS films (left: 5 mm in length, right: 10 mm in length), which were fully printed on a PI sheet via the AJP method. (b) Enlarged AutoCAD-design pattern of the Ag thermometer. (c) Measurement and (d) calibration of the AJ-printed Ag thermometer by using a commercial Pt-100 thermometer. (e) Schematic illustration of the Seebeck coefficient and thermal conductivity measurement setup.

As illustrated in Figure A.2 (e), AJ-printed samples with various dimensions were placed on a heat source. Subsequently, the localised temperature of different positions and the voltage output were recorded simultaneously for the extraction of α and κ. The input temperature (T_{in}), output temperature (T_{out}), and voltage output (V_{out}) values at the function of time were plotted in Figures A.3 (a) - (c), respectively. With this transmission line model method, both α and κ values could be measured simultaneously, by employing the same transient recording. The α value of this AJ-printed PEDOT:PSS film was calculated to be ~19.99 μV/K, as extracted in Figure A.3 (d). The κ value was estimated to be 0.2 to 0.4 W/(m.K), by using the lumped model which was elaborated in Section A.1.5. This estimated κ value was acceptable compared to that reported in the literature, ~0.3 W/(m.K).[93] However, more experimental works are required to verify the accuracy of this transmission line model. Another limitation of this model is that the mass density and specific heat capacity of the sample are needed to be known before estimation, which adds another new measurement difficulty for the thin-film sample.

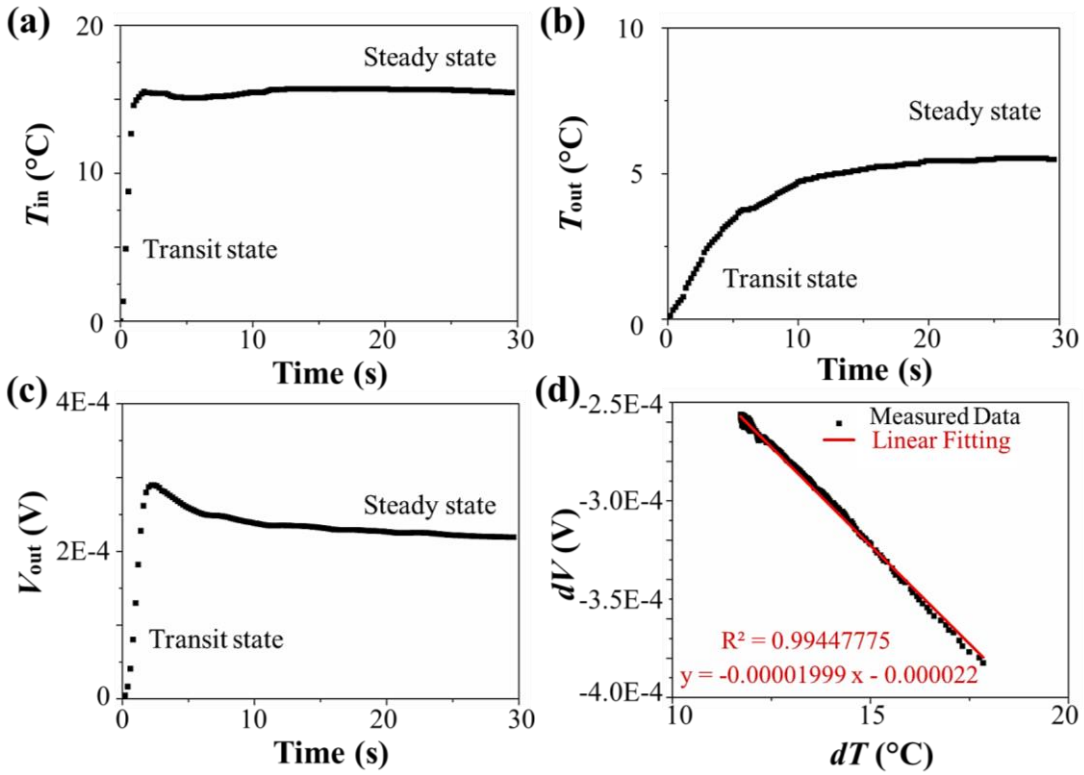

Figure A.3 Plotting of (a) input temperature, T_{in}, (b) output temperature, T_{out}, (c) voltage output, V_{out}, and (d) extracted Seebeck coefficient, α, in response to the step heating on the 5 mm-length PEDOT:PSS film.

A.1.5 Matlab Code for Extractions of α and κ

This section presents the Matlab code (MathWorks) used for the extraction of α and κ by using the transmission line model. The code was mostly written by Dr Sanjiv Sambandan, with some input from the author.

```
clear all;
%-------------------------------------------------------------------------
-------------
%%1. LUMPED MODEL - BY EXTRACTION (WORKS WELL, USE THIS, WILL GIVE YOU
RELIABLE MEANS TO COMPARE MATERIALS)

a=xlsread('ThermData2.xls');
%Use SI units everywhere and Use Celsius everywhere
L=5e-3; %length of your sample in m
x=L/2;  %the location where you are tapping the voltage, i.e. distance of
this location from the heat source

datalength=100; %Only using the first 100 data points to extract data

%READ ALL DATA
datalength=size(a(:,1));
for i=1:1:datalength
    t(i)=a(i,5);    %t is the offset time in column 5
    Tin(i)=a(i,8);  %Tin is the offset Tleft in column 8
    Tout(i)=a(i,6); %Tout is the offset Tmid in column 6
    Vout(i)=a(i,7); %Vout is the offset  V in column 7
end

%1. At Steady State (where t=infinite, with ambient loss)
Tin0=28;               %Input steady-state temperature in Celsius
Tout0=8;             %Steady State output temperature in Celsius
beta=Tout0/(Tin0-Tout0); %Defined from the steady-state

%2. At Transient State (where t before reaching stabilised temperature)
for i=1:1:datalength
    s(i)=log(1-(Tout(i)*(beta+1)/(beta*Tin0))); %Plot s versus time t for
finding slope
end
%plot(t,s,'bo'); %Use this to find the slope
slope=0.2;      %Linear fitting from the above plot
```

```
for i=1:1:datalength
    Toutmodel_lump(i)=(beta/(beta+1))*Tin0*(1-exp(-t(i)*slope));
end
plot(t,Tout,'bo',t,Toutmodel_lump,'r'); %Use this to check model
RCmodellump=(beta+1)/(beta*slope);      %This is the RC of the material,
this is resistance and capacitance, not per unit length
rclump=RCmodellump/(x^2);               %This it the (R per unit length)*(C
per unit length) <<<<THIS IS THE ANSWER YOU NEED

%3. Thermal Conductivity Calculation
rho=1011;       %rho is the mass density in Kg.m^-3
Cp=1300;        %Cp is the specific heat capacity in J.K^-1.Kg^-1)
k =rho*Cp/rclump; %k is the thermal conductivity in W.m^-1.K^-, the value
should range from 0.2 to 0.4 for PEDOT:PSS

%4. Seebeck Coefficient Calculation
%Vmax=2.42E-04;   %Maximum voltage in the plot
%alpha=Vmax/Tin0; %Seebeck coefficient calculation
```

A.2 Solvothermal-synthesised SnSe Nanosheets

Tin selenide (SnSe) nanosheets with the layered structure were synthesised by a facile and surfactant-free solvothermal synthesis method, which was similar to the method discussed in Section 3.1.2, except using $SnCl_2$ and Se as material sources here for 'Sn' and 'Se', respectively. The SEM and XRD results in Figures A.4 and A.5 show that these synthesised SnSe nanosheets exhibited fairly good crystallinity quality. Deficiency in 'Sn' or exceeding in 'Se' was seen, because few of 'Se' element remained in the form of Se nanoparticle, which needed more reaction time to form a stoichiometric chemical composition at a ratio of 1:1.

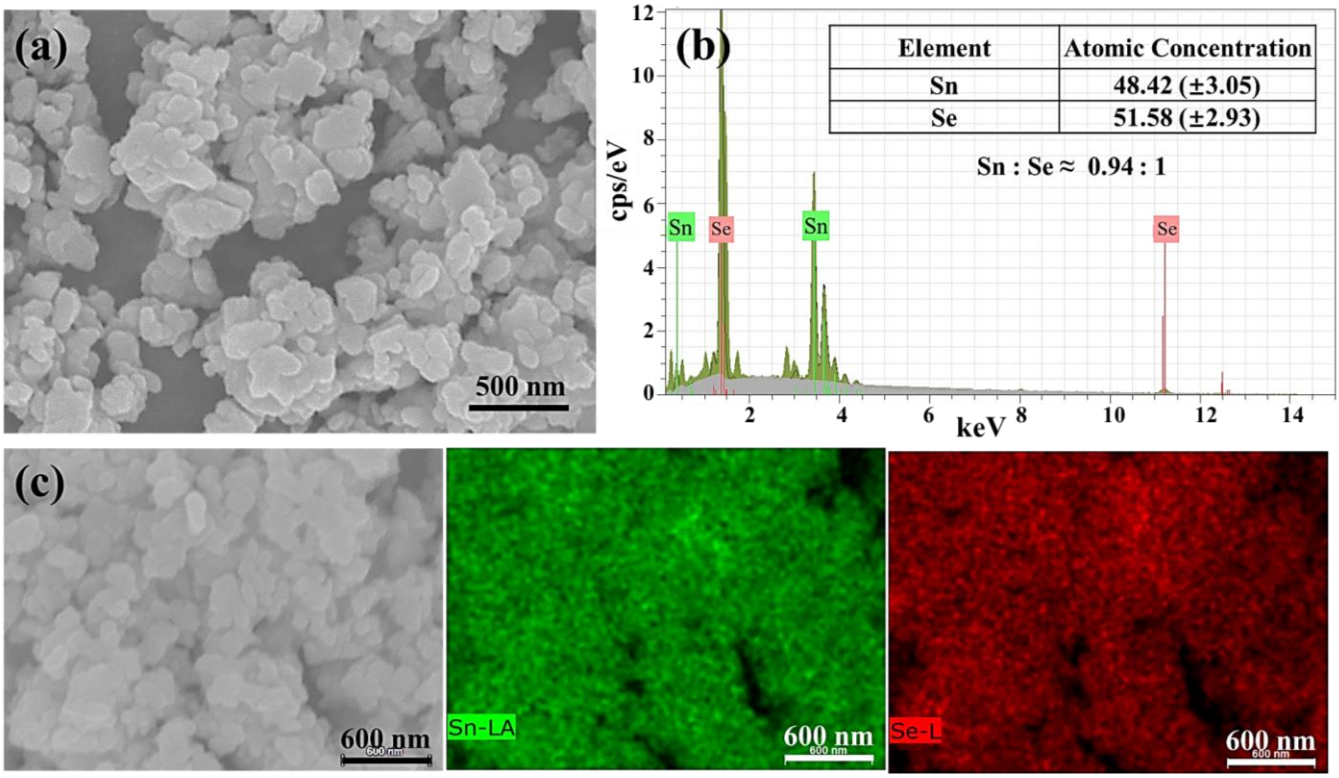

Figure A.4 (a) SEM images, (b) EDX analysis, and (c) EDX mapping of solvothermal-synthesised SnSe nanosheets.

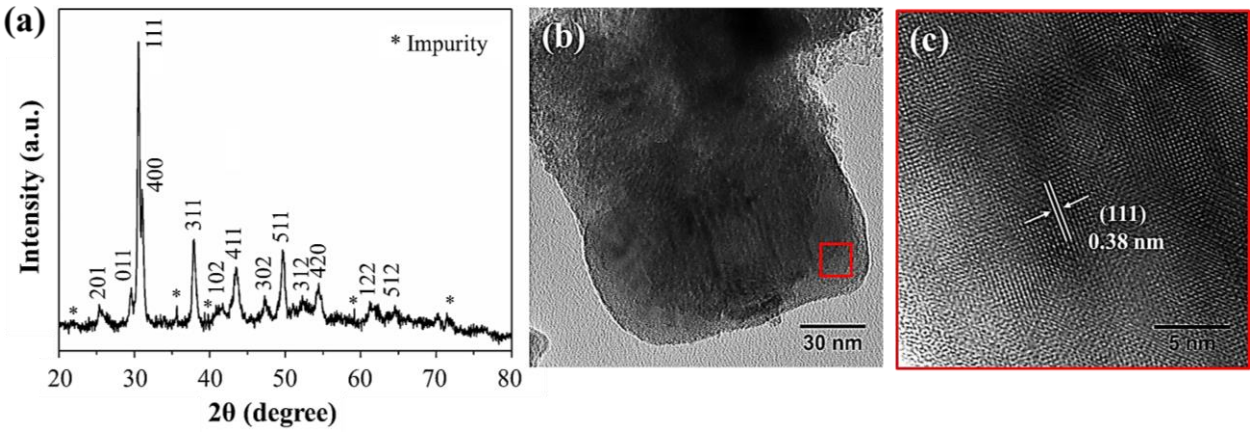

Figure A.5 (a) XRD results and (b) TEM analysis of solvothermal-synthesised SnSe nanosheets, where (c) the enlarge HRTEM image reveals their lattice fringe patterns.

A.3 Differential Scanning Calorimetry (DSC) Thermal Analysis

A differential scanning calorimeter (DSC, Q2000, TA Instruments) was used to measure the oxidation temperature and melting temperature of these fabricated inorganic TE particles. The powder samples were loaded into an aluminium pan (T-Zero pan, TA Instruments), and their mass was weighed by using a precision balance (Ultramicro, Sartorius). The DSC measurements were undertaken from 20 to 600 °C under a linear temperature ramp of 10 °C/min. The DSC analysis in Figure A.6 indicates the oxidation temperature and the melting temperature of Bi_2Te_3 and Sb_2Te_3 powders fabricated via different approaches. A first down-point exothermic peak was observed, possibly suggesting the partial oxidation of Bi_2Te_3 or Sb_2Te_3 alloys because of some residual air trapped inside the aluminium pan.[264] Since the solvothermal-synthesised particles were in the nanostructured form, leading to more surface area exposed to the oxygen, which led to a more prominent oxidation process. As a result, their oxidation peaks were more distinct compared to that of their hand-ground counterparts. Then, a sharper and more intense up-point endothermic peak existed upon heating beyond its oxidation temperature, which was attributed to the melting and/or decomposition of Bi_2Te_3 or Sb_2Te_3. It was found that both the hand-ground and solvothermal-synthesised Bi_2Te_3 and Sb_2Te_3 particles shared almost the same melting temperature ~580 °C and ~420 °C, respectively. Their oxidation and melting temperatures are summarised in Table A-1 in comparison with other organic polymers that are applicable for the nanocomposite fabrication in this project.

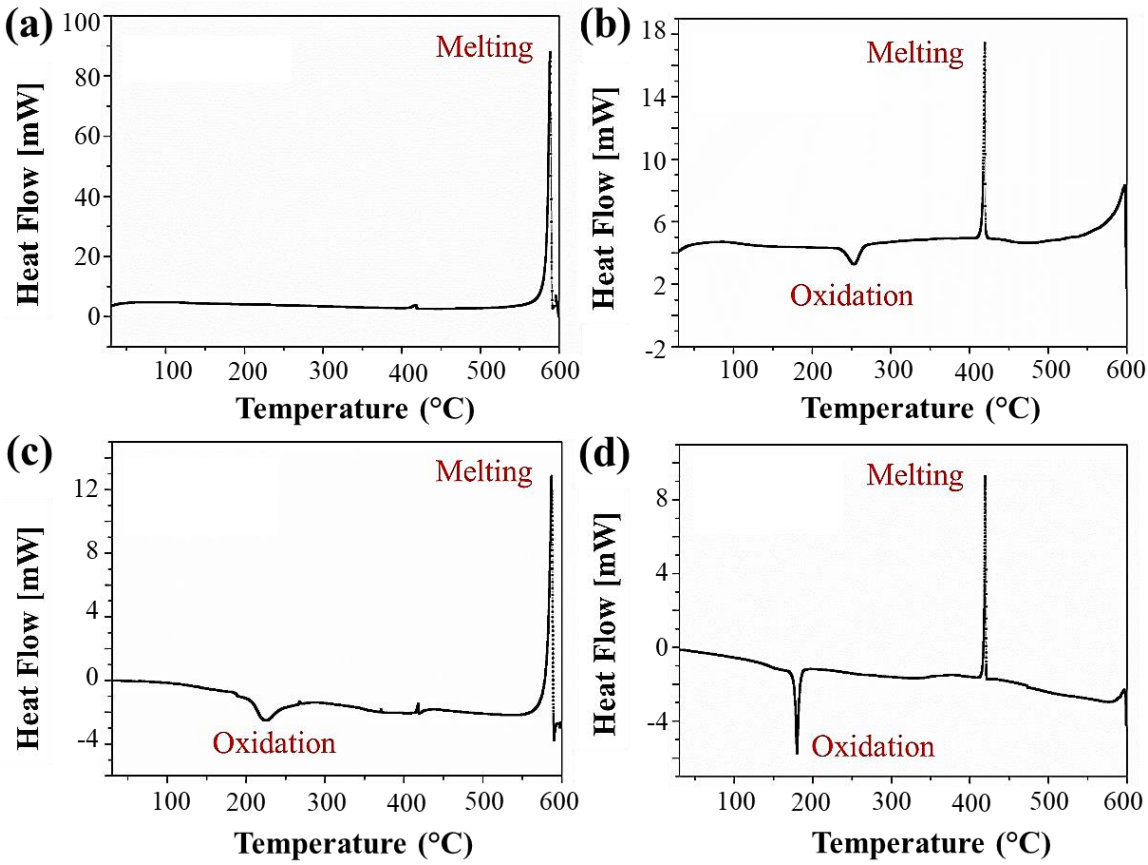

Figure A.6 DSC analysis of (a) hand-ground Bi_2Te_3 powder, (b) hand-ground Sb_2Te_3 powder, (c) solvothermal-synthesised Bi_2Te_3 nanoparticles, and (d) solvothermal-synthesised Sb_2Te_3 nanoflakes, indicating their oxidation temperature and melting temperature, respectively.

Table A-1 Comparison of the oxidation and melting temperature of different materials.[135,265]

Temperature /Material	Commercial Bi_2Te_3	Commercial Sb_2Te_3	Synthesised Bi_2Te_3	Synthesised Sb_2Te_3	PEDOT:PSS	PVDF
Oxidation Temp. (°C)	N/A	~250	~220	~180	N/A	N/A
Melting Temp. (°C)	~580	~420	~580	~420	~145	~177

A.4 Out-of-plane Measurement Setup

Figure A.7 illustrates the test bench for measuring the out-of-plane Seebeck coefficient and electrical conductivity, where the INSTEC mK1000 series precise temperature controllers coupled with two copper plates were used as a heater and/or cooler that could provide a temperature control accuracy down to 1 mK. A graphite sheet was used as the thermal contact material. Thermal interface materials, such as thermal paste, were also employed to spread heat identically. Since the measurements should be done at different ambient temperatures to investigate the operating temperature range of TEGs, the whole test bench was inserted into a vacuum chamber, and the ambient temperature could be controlled from 77 to 290 K via a liquid nitrogen cooling system (INSTEC) or a water-cooling refrigerator (Thermo Haake Chiller). An electrical measurement system consisted of a programmable DC electronic load (BK PRECISION 8500) and a digital multimeter (BK PRECISION 2831E), was served for measuring the voltage difference generated from the TE sample. A data translation instrument (MEASURpoint DT 9874) was employed as a mixed temperature and voltage measurement instrument that could collect and transfer data to the LabVIEW program for the data acquisition through a computer. This setup could be used for the TE measurement on the 3D-structured stretchable TEGs, where the heat flow direction is out-of-plane, as discussed in Chapter 7.

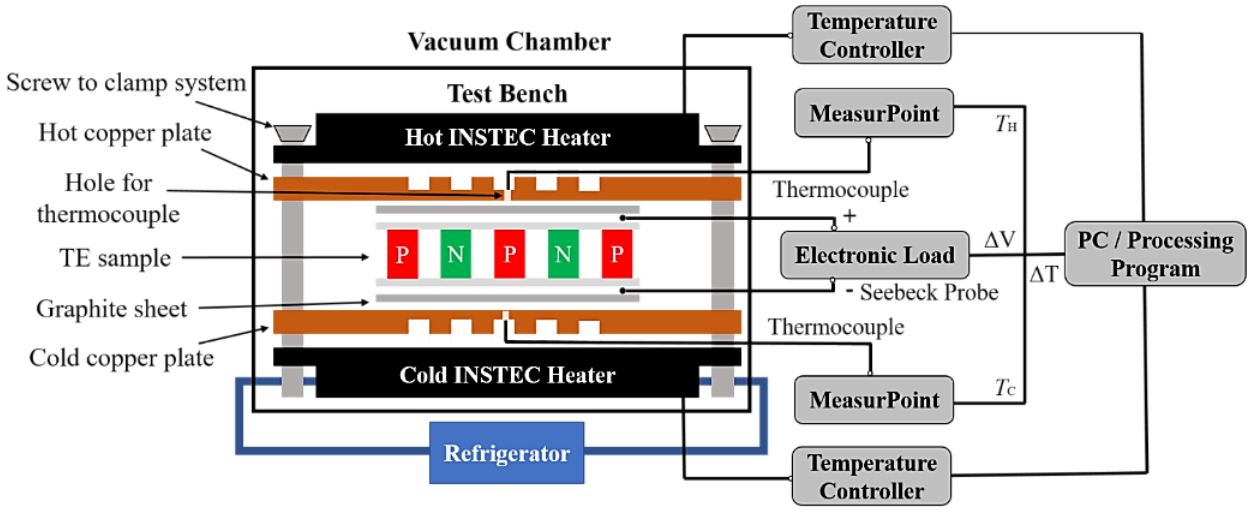

Figure A.7 Schematic drawing of the test bench for out-of-plane Seebeck coefficient and electrical conductivity measurements.

A.5 Hall-effect Measurement

The electrical conductivity of these printed films can be measured by the Hall-effect measurement method, as it can determine the resistivity, charge carrier type, carrier concentration, and carrier mobility of semiconductors.[92] This method can be used to compare and calibrated the results measured from the in-house designed TE measurement setup. As illustrated in Figure A.8 (a), a 5 mm x 5 mm square dense TE thin film was AJ-printed on a PI substrate, and Ag electrodes were also AJ-printed at four corners that could be used as electrical contacts for the subsequent wire bonding. It should be noted that the printed thin film is required to be flat and homogeneous with uniform thickness as well as without any voids or holes, to ensure the accuracy of measurement results. Figure A.8 (b) demonstrates the measurement configuration for the Van der Pauw's method by using the in-house built Cryogen Free Magnet 1-Tesla Measurement System. A magnetic field was applied perpendicular to the surface of the sample and a current flow was applied along two corners of the thin film while measuring the voltage created across the other two corners. Then, the electrical conductivity can be calculated from Maxwell's equation $J = \sigma \, . \, E$, where J is current density [A/m^2], σ is electrical conductivity [S/m], and E is electric field [V/m].[266]

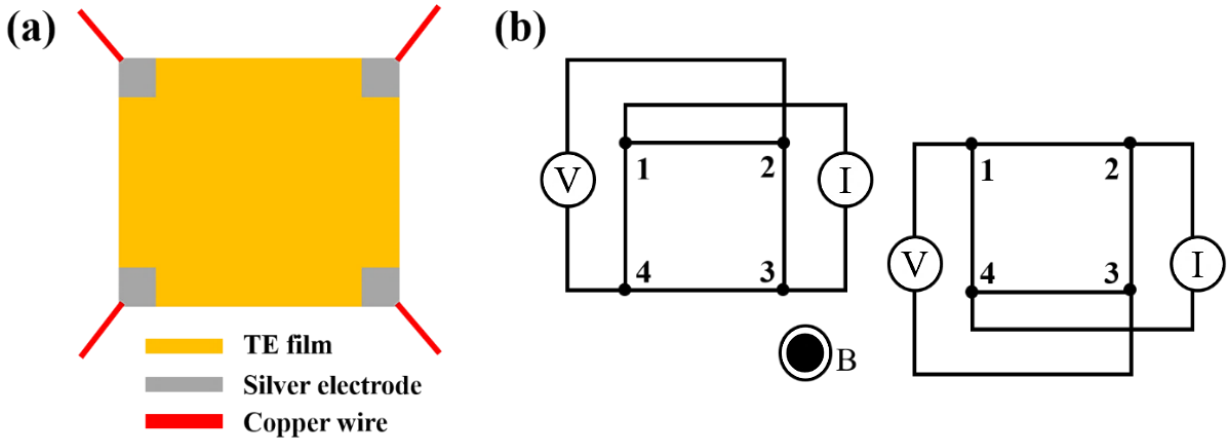

Figure A.8 Schematic illustrations of (a) the sample preparation and (b) the measurement configuration for the Hall-effect measurement by the van der Pauw's method.

A.6 Hand-ground Sb_2Te_3 + PEDOT:PSS Nanocomposites

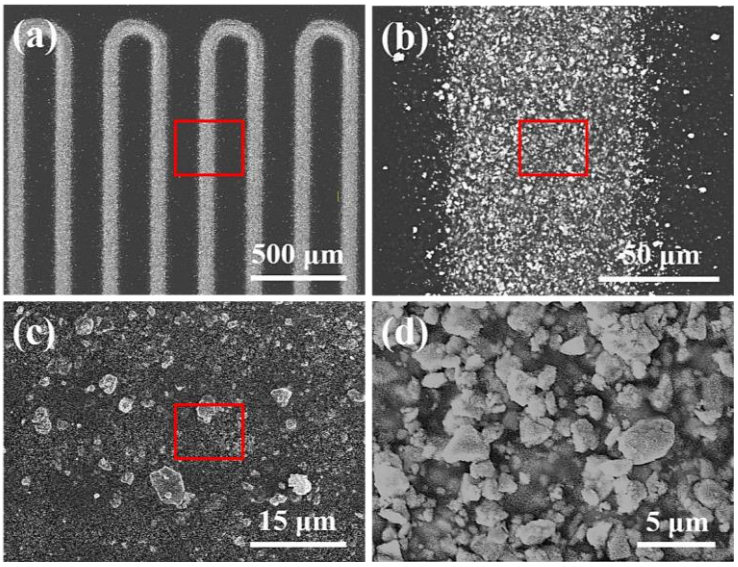

Figure A.9 SEM images showing the morphology of the 10-layer AJ-printed PEDOT:PSS-based nanocomposite loaded with 10 wt.% (nominal) hand-ground Sb_2Te_3 powder.

A.7 solvothermal-synthesised Sb_2Te_3 + PVDF Nanocomposites

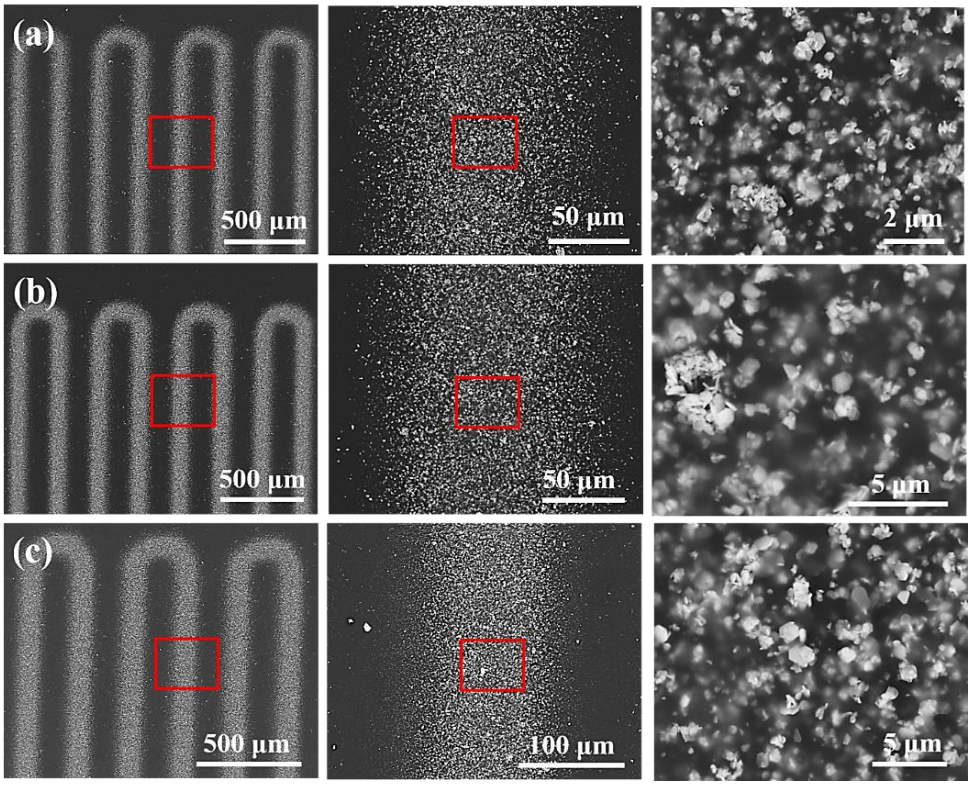

Figure A.10 SEM images of (a) 1-layer, (b) 5-layer, and (c) 10-layer AJ-printed PVDF-based nanocomposites loaded with 10 wt.% (nominal) solvothermal-synthesised Sb_2Te_3 nanoflakes.

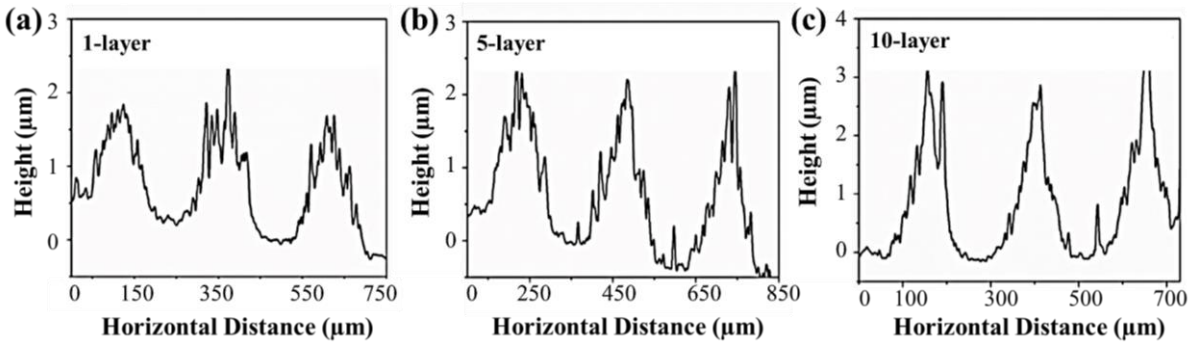

Figure A.11 Profilometer thickness measurements of (a) 1-layer, (b) 5-layer, and (c) 10-layer AJ-printed PVDF-based nanocomposites loaded with 10 wt.% (nominal) Sb_2Te_3 nanoflakes.

A.8 Influence of TE Leg Dimension on Voltage and Power Outputs

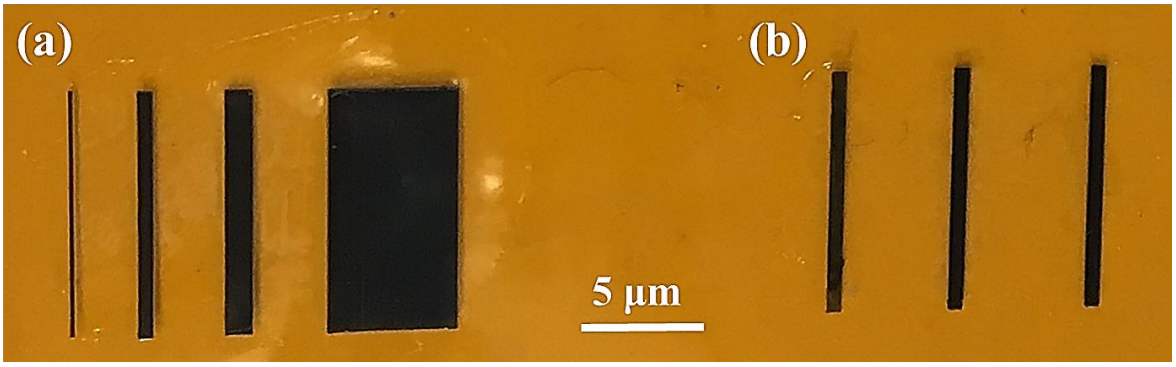

Figure A.12 Photographic images of different AJ-printed PEDOT:PSS films as a function of (a) width and (b) thickness.

Table A-2 Comparison of voltage and power outputs as a function of the TE leg dimension.

PEDOT:PSS film		V_{oc} **(mV)**	I_{sc} **(µA)**	R_S **(Ω)**	P_{max} **(nW)**
Width-dependent Thickness (5 layers) Length (10 mm)	Width (0.1 mm)	0.21	0.4	435	0.025
	Width (0.5 mm)	0.28	0.6	198	0.099
	Width (1 mm)	0.29	1.0	115	0.183
	Width (5 mm)	0.26	2.2	15	1.13
Thickness-dependent Width (0.5 mm) Length (10 mm)	Thickness (1 layer)	0.23	0.1	1340	0.01
	Thickness (5 layer)	0.29	0.8	180	0.12
	Thickness (10 layer)	0.31	1.8	75	0.32

A.9 Substrate-based Stretchable Structure

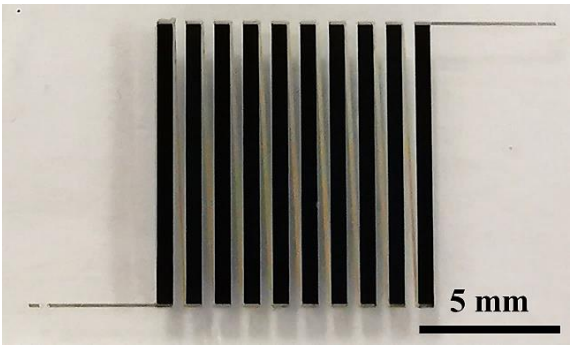

Figure A.13 Photographic image of the PDMS substrate-based stretchable TEG with the strip-shaped structure.

Reference List

[1] M. Zebarjadi, K. Esfarjani, M.S. Dresselhaus, Z.F. Ren, G. Chen, Perspectives on thermoelectrics: from fundamentals to device applications, Energy Environ. Sci. 5 (2012) 5147–5162. doi:10.1039/C1EE02497C.

[2] A. Shakouri, Recent Developments in Semiconductor Thermoelectric Physics and Materials, Annu. Rev. Mater. Res. 41 (2011) 399–431. doi:10.1146/annurev-matsci-062910-100445.

[3] B. Poudel, Q. Hao, Y. Ma, Y. Lan, A. Minnich, B. Yu, X. Yan, D. Wang, A. Muto, D. Vashaee, X. Chen, J. Liu, M.S. Dresselhaus, G. Chen, Z. Ren, High-Thermoelectric Performance of Nanostructured Bismuth Antimony Telluride Bulk Alloys, Science. 320 (2008) 634–638. doi:10.1126/science.1156446.

[4] M.S. Dresselhaus, G. Chen, M.Y. Tang, R.G. Yang, H. Lee, D.Z. Wang, Z.F. Ren, J.-P. Fleurial, P. Gogna, New Directions for Low-Dimensional Thermoelectric Materials, Adv. Mater. 19 (2007) 1043–1053. doi:10.1002/adma.200600527.

[5] A.J. Minnich, M.S. Dresselhaus, Z.F. Ren, G. Chen, Bulk nanostructured thermoelectric materials: current research and future prospects, Energy Environ. Sci. 2 (2009) 466–479. doi:10.1039/b822664b.

[6] G.J. Snyder, E.S. Toberer, Complex thermoelectric materials, Nat. Mater. 7 (2008) 105–114. doi:10.1038/nmat2090.

[7] L.D. Hicks, M.S. Dresselhaus, Effect of quantum-well structures on the thermoelectric figure of merit, Phys. Rev. B. 47 (1993) 12727–12731. doi:10.1103/PhysRevB.47.12727.

[8] M. Orrill, S. LeBlanc, Printed thermoelectric materials and devices: Fabrication techniques, advantages, and challenges, J. Appl. Polym. Sci. 134 (2017) 44256–44270. doi:10.1002/app.44256.

[9] F. Suarez, A. Nozariasbmarz, D. Vashaee, M.C. Öztürk, Designing thermoelectric generators for self-powered wearable electronics, Energy Environ. Sci. 9 (2016) 2099–2113. doi:10.1039/C6EE00456C.

[10] B. Russ, A. Glaudell, J.J. Urban, M.L. Chabinyc, R.A. Segalman, Organic

thermoelectric materials for energy harvesting and temperature control, Nat. Rev. Mater. 1 (2016) 16050–16062. doi:10.1038/natrevmats.2016.50.

[11] Y. Chen, Y. Zhao, Z. Liang, Solution processed organic thermoelectrics: towards flexible thermoelectric modules, Energy Environ. Sci. 8 (2015) 401–422. doi:10.1039/C4EE03297G.

[12] Q. Zhang, Y. Sun, W. Xu, D. Zhu, Organic Thermoelectric Materials: Emerging Green Energy Materials Converting Heat to Electricity Directly and Efficiently, Adv. Mater. 26 (2014) 6829–6851. doi:10.1002/adma.201305371.

[13] C. Wan, X. Gu, F. Dang, T. Itoh, Y. Wang, H. Sasaki, M. Kondo, K. Koga, K. Yabuki, G.J. Snyder, R. Yang, K. Koumoto, Flexible n-type thermoelectric materials by organic intercalation of layered transition metal dichalcogenide TiS 2, Nat. Mater. 14 (2015) 622–627. doi:10.1038/nmat4251.

[14] C. Wan, R. Tian, M. Kondou, R. Yang, P. Zong, K. Koumoto, Ultrahigh thermoelectric power factor in flexible hybrid inorganic-organic superlattice, Nat. Commun. 8 (2017) 1024–1032. doi:10.1038/s41467-017-01149-4.

[15] M. He, F. Qiu, Z. Lin, Towards high-performance polymer-based thermoelectric materials, Energy Environ. Sci. 6 (2013) 1352–1361. doi:10.1039/c3ee24193a.

[16] C. Yu, Y.S. Kim, D. Kim, J.C. Grunlan, Thermoelectric Behavior of Segregated-Network Polymer Nanocomposites, Nano Lett. 8 (2008) 4428–4432. doi:10.1021/nl802345s.

[17] G.J. Snyder, A.H. Snyder, Figure of merit ZT of a thermoelectric device defined from materials properties, Energy Environ. Sci. 10 (2017) 2280–2283. doi:10.1039/C7EE02007D.

[18] E.J. Bae, Y.H. Kang, K.-S. Jang, S.Y. Cho, Enhancement of Thermoelectric Properties of PEDOT:PSS and Tellurium-PEDOT:PSS Hybrid Composites by Simple Chemical Treatment, Sci. Rep. 6 (2016) 18805. doi:10.1038/srep18805.

[19] B. Zhang, J. Sun, H.E. Katz, F. Fang, R.L. Opila, Promising Thermoelectric Properties of Commercial PEDOT:PSS Materials and Their Bi 2 Te 3 Powder Composites, ACS Appl. Mater. Interfaces. 2 (2010) 3170–3178. doi:10.1021/am100654p.

[20] R.R. Søndergaard, M. Hösel, N. Espinosa, M. Jørgensen, F.C. Krebs, Practical evaluation of organic polymer thermoelectrics by large-area R2R processing on flexible substrates, Energy Sci. Eng. 1 (2013) 81–88. doi:10.1002/ese3.8.

[21] J. Li, Y. Du, R. Jia, J. Xu, S. Shen, Thermoelectric Properties of Flexible PEDOT:PSS/Polypyrrole/Paper Nanocomposite Films, Materials. 10 (2017) 780–787. doi:10.3390/ma10070780.

[22] S.K. Yee, S. LeBlanc, K.E. Goodson, C. Dames, $ per W metrics for thermoelectric power generation: beyond ZT, Energy Environ. Sci. 6 (2013) 2561–2571. doi:10.1039/C3EE41504J.

[23] C. Ou, P.E. Sanchez-Jimenez, A. Datta, F.L. Boughey, R.A. Whiter, S.-L. Sahonta, S. Kar-Narayan, Template-Assisted Hydrothermal Growth of Aligned Zinc Oxide Nanowires for Piezoelectric Energy Harvesting Applications, ACS Appl. Mater. Interfaces. 8 (2016) 13678–13683. doi:10.1021/acsami.6b04041.

[24] A. Datta, A. Sangle, N. Hardingham, C. Cooper, M. Kraan, D. Ritchie, V. Narayan, S. Kar-Narayan, Structure and Thermoelectric Properties of Bi2−xSbxTe3 Nanowires Grown in Flexible Nanoporous Polycarbonate Templates, Materials. 10 (2017) 553–564. doi:10.3390/ma10050553.

[25] C. Ou, A.L. Sangle, A. Datta, Q. Jing, T. Busolo, T. Chalklen, V. Narayan, S. Kar-Narayan, Fully Printed Organic–Inorganic Nanocomposites for Flexible Thermoelectric Applications, ACS Appl. Mater. Interfaces. 10 (2018) 19580–19587. doi:10.1021/acsami.8b01456.

[26] M. Culebras, C. Gómez, A. Cantarero, Review on Polymers for Thermoelectric Applications, Materials. 7 (2014) 6701–6732. doi:10.3390/ma7096701.

[27] J. Yang, H.-L. Yip, A.K.-Y. Jen, Rational Design of Advanced Thermoelectric Materials, Adv. Energy Mater. 3 (2013) 549–565. doi:10.1002/aenm.201200514.

[28] C.L. Cramer, H. Wang, K. Ma, Performance of Functionally Graded Thermoelectric Materials and Devices: A Review, J. Electron. Mater. 47 (2018) 5122–5132. doi:10.1007/s11664-018-6402-7.

[29] X. Wang, X. Lu, B. Liu, D. Chen, Y. Tong, G. Shen, Flexible Energy-Storage Devices: Design Consideration and Recent Progress, Adv. Mater. 26 (2014) 4763–4782. doi:10.1002/adma.201400910.

[30] G. Zhou, F. Li, H.-M. Cheng, Progress in flexible lithium batteries and future prospects, Energy Environ. Sci. 7 (2014) 1307–1338. doi:10.1039/C3EE43182G.

[31] M. Martín-González, O. Caballero-Calero, P. Díaz-Chao, Nanoengineering thermoelectrics for 21st century: Energy harvesting and other trends in the field, Renew. Sustain. Energy Rev. 24 (2013) 288–305. doi:10.1016/j.rser.2013.03.008.

[32] J.-H. Bahk, H. Fang, K. Yazawa, A. Shakouri, Flexible thermoelectric materials and device optimization for wearable energy harvesting, J. Mater. Chem. C. 3 (2015) 10362–10374. doi:10.1039/C5TC01644D.

[33] A. Datta, Y.S. Choi, E. Chalmers, C. Ou, S. Kar-Narayan, Piezoelectric Nylon-11

Nanowire Arrays Grown by Template Wetting for Vibrational Energy Harvesting Applications, Adv. Funct. Mater. 27 (2017) 1604262–1604271. doi:10.1002/adfm.201604262.

[34] S. Patel, H. Park, P. Bonato, L. Chan, M. Rodgers, A review of wearable sensors and systems with application in rehabilitation, J. Neuroeng. Rehabil. 9 (2012) 21. doi:10.1186/1743-0003-9-21.

[35] S.J. Kim, J.H. We, B.J. Cho, A wearable thermoelectric generator fabricated on a glass fabric, Energy Environ. Sci. 7 (2014) 1959–1965. doi:10.1039/c4ee00242c.

[36] M.K. Kim, M.S. Kim, S. Lee, C. Kim, Y.J. Kim, Wearable thermoelectric generator for harvesting human body heat energy, Smart Mater. Struct. 23 (2014). doi:10.1088/0964-1726/23/10/105002.

[37] Y. Du, K. Cai, S. Chen, H. Wang, S.Z. Shen, R. Donelson, T. Lin, Thermoelectric Fabrics: Toward Power Generating Clothing, Sci. Rep. 5 (2015) 6411–6416. doi:10.1038/srep06411.

[38] F.L. Boughey, T. Davies, A. Datta, R.A. Whiter, S.-L. Sahonta, S. Kar-Narayan, Vertically aligned zinc oxide nanowires electrodeposited within porous polycarbonate templates for vibrational energy harvesting, Nanotechnology. 27 (2016) 28LT02. doi:10.1088/0957-4484/27/28/28LT02.

[39] R.A. Whiter, V. Narayan, S. Kar-Narayan, A Scalable Nanogenerator Based on Self-Poled Piezoelectric Polymer Nanowires with High Energy Conversion Efficiency, Adv. Energy Mater. 4 (2014) n/a-n/a. doi:10.1002/aenm.201400519.

[40] Z.L. Wang, Triboelectric nanogenerators as new energy technology for self-powered systems and as active mechanical and chemical sensors, ACS Nano. 7 (2013) 9533–9557. doi:10.1021/nn404614z.

[41] Y.S. Choi, Q. Jing, A. Datta, C. Boughey, S. Kar-Narayan, A triboelectric generator based on self-poled Nylon-11 nanowires fabricated by gas-flow assisted template wetting, Energy Environ. Sci. 10 (2017) 2180–2189. doi:10.1039/C7EE01292F.

[42] Y. Zi, J. Wang, S. Wang, S. Li, Z. Wen, H. Guo, Z.L. Wang, Effective energy storage from a triboelectric nanogenerator, Nat. Commun. 7 (2016) 1–8. doi:10.1038/ncomms10987.

[43] V. Misra, A. Bozkurt, B. Calhoun, T. Jackson, J. Jur, J. Lach, B. Lee, J. Muth, O. Oralkan, M. Ozturk, S. Trolier-McKinstry, D. Vashaee, D. Wentzloff, Y. Zhu, Flexible Technologies for Self-Powered Wearable Health and Environmental Sensing, Proc. IEEE. 103 (2015) 665–681. doi:10.1109/JPROC.2015.2412493.

[44] C.B. Vining, An inconvenient truth about thermoelectrics, Nat. Mater. 8 (2009) 83–85. doi:10.1038/nmat2361.

[45] A.S. Rattner, S. Garimella, Energy harvesting, reuse and upgrade to reduce primary energy usage in the USA, Energy. 36 (2011) 6172–6183. doi:10.1016/j.energy.2011.07.047.

[46] C. Cho, K.L. Wallace, P. Tzeng, J.-H. Hsu, C. Yu, J.C. Grunlan, Outstanding Low Temperature Thermoelectric Power Factor from Completely Organic Thin Films Enabled by Multidimensional Conjugated Nanomaterials, Adv. Energy Mater. 6 (2016) 1502168–1502175. doi:10.1002/aenm.201502168.

[47] H. Ohta, Thermoelectrics based on strontium titanate, Mater. Today. 10 (2007) 44–49. doi:10.1016/S1369-7021(07)70244-4.

[48] A. Chen, P. Wright, Medical Applications of Thermoelectrics, in: D.M. Rowe (Ed.), Modul. Syst. Appl. Thermoelectr., CRC Press, 2012: pp. 1–22. doi:10.1201/b11892-30.

[49] P.J. Taroni, I. Hoces, N. Stingelin, M. Heeney, E. Bilotti, Thermoelectric Materials: A Brief Historical Survey from Metal Junctions and Inorganic Semiconductors to Organic Polymers, Isr. J. Chem. 54 (2014) 534–552. doi:10.1002/ijch.201400037.

[50] A. Nikolaenko, G. Anderson, T. Fletcher, S. King, Progress on Flexible Low-Cost Organic Thermoelectric Material and Device Development at CDT, in: Print. Electron. Eur., Berlin, Germany, 2016.

[51] D. Bhatia, S. Bairagi, S. Goel, M. Jangra, Pacemakers charging using body energy, J. Pharm. Bioallied Sci. 2 (2010) 51–54. doi:10.4103/0975-7406.62713.

[52] J.Y. Oh, J.H. Lee, S.W. Han, S.S. Chae, E.J. Bae, Y.H. Kang, W.J. Choi, S.Y. Cho, J.-O. Lee, H.K. Baik, T. Il Lee, Chemically exfoliated transition metal dichalcogenide nanosheet-based wearable thermoelectric generators, Energy Environ. Sci. 9 (2016) 1696–1705. doi:10.1039/C5EE03813H.

[53] C.R. Bowen, J. Taylor, E. LeBoulbar, D. Zabek, A. Chauhan, R. Vaish, Pyroelectric materials and devices for energy harvesting applications, Energy Environ. Sci. 7 (2014) 3836–3856. doi:10.1039/C4EE01759E.

[54] A. McEvoy, T. Markvart, L. Castaner, Practical Handbook of Photovoltaics: Fundamentals and Applications., Elsevier New York. (2003) 72–74.

[55] Z.L. Wang, On Maxwell's displacement current for energy and sensors: the origin of nanogenerators, Mater. Today. 20 (2017) 74–82. doi:10.1016/j.mattod.2016.12.001.

[56] V.F. Janas, A. Safari, Overview of Fine-Scale Piezoelectric Ceramic/Polymer Composite

Processing, J. Am. Ceram. Soc. 78 (1995) 2945–2955. doi:10.1111/j.1151-2916.1995.tb09068.x.

[57] K.A. Cook-Chennault, N. Thambi, A.M. Sastry, Powering MEMS portable devices—a review of non-regenerative and regenerative power supply systems with special emphasis on piezoelectric energy harvesting systems, Smart Mater. Struct. 17 (2008) 043001. doi:10.1088/0964-1726/17/4/043001.

[58] S. Boisseau, G. Despesse, B. Ahmed, Electrostatic Conversion for Vibration Energy Harvesting, in: Small-Scale Energy Harvest., InTech, 2012: p. 64. doi:10.5772/51360.

[59] Z.L. Wang, T. Jiang, L. Xu, Toward the blue energy dream by triboelectric nanogenerator networks, Nano Energy. 39 (2017) 9–23. doi:10.1016/j.nanoen.2017.06.035.

[60] K. Koumoto, T. Mori, Thermoelectric Nanomaterials, Springer, 2013. doi:10.1007/978-3-642-37537-8.

[61] I.B. Cadoff, E. Miller, Thermoelectric materials and devices, New York : Reinhold Pub. Corp., 1960.

[62] H.J. Kim, J.R. Skuza, Y. Park, G.C. King, S.H. Choi, A. Nagavalli, System to Measure Thermal Conductivity and Seebeck Coefficient for Thermoelectrics, 2012.

[63] C.. Heusch, H.-G. Moser, A. Kholodenko, Direct measurements of the thermal conductivity of various pyrolytic graphite samples (PG,TPG) used as thermal dissipation agents in detector applications, Nucl. Instruments Methods Phys. Res. Sect. A Accel. Spectrometers, Detect. Assoc. Equip. 480 (2002) 463–469. doi:10.1016/S0168-9002(01)01208-6.

[64] D.M. Rowe, Thermoelectrics handbook: macro to nano, Taylor & Francis Group, 1995.

[65] T.M. Tritt, M. a Subramanian, Thermoelectric Materials, Phenomena, and Applications: A Bird's Eye View, MRS Bull. 31 (2006) 188–198. doi:10.1557/mrs2006.44.

[66] A. Datta, G.S. Nolas, Thermoelectric Nanomaterials, Springer, Berlin, Heidelberg, 2013.

[67] A. Nozariasbmarz, Z. Zamanipour, P. Norouzzadeh, J.S. Krasinski, D. Vashaee, Enhanced thermoelectric performance in a metal/semiconductor nanocomposite of iron silicide/silicon germanium, RSC Adv. 6 (2016) 49643–49650. doi:10.1039/C6RA01947A.

[68] K. Koumoto, R. Funahashi, E. Guilmeau, Y. Miyazaki, A. Weidenkaff, Y. Wang, C. Wan, Thermoelectric Ceramics for Energy Harvesting, J. Am. Ceram. Soc. 96 (2013) 1–23. doi:10.1111/jace.12076.

[69] Y. Lin, C. Norman, D. Srivastava, F. Azough, L. Wang, M. Robbins, K. Simpson, R.

Freer, I.A. Kinloch, Thermoelectric Power Generation from Lanthanum Strontium Titanium Oxide at Room Temperature through the Addition of Graphene, ACS Appl. Mater. Interfaces. 7 (2015) 15898–15908. doi:10.1021/acsami.5b03522.

[70] C.B. Satterthwaite, R.W. Ure, Electrical and Thermal Properties of Bi2Te3, Phys. Rev. 108 (1957) 1164–1170. doi:10.1103/PhysRev.108.1164.

[71] Y. Chen, C. Chen, P. Lee, M. Ou, Nanowires - Fundamental Research, InTech, 2011. doi:10.5772/681.

[72] A. Datta, J. Paul, A. Kar, A. Patra, Z. Sun, L. Chen, J. Martin, G.S. Nolas, Facile Chemical Synthesis of Nanocrystalline Thermoelectric Alloys Based on Bi−Sb−Te−Se, Cryst. Growth Des. 10 (2010) 3983–3989. doi:10.1021/cg100560s.

[73] J.P. Heremans, The ugly duckling, Nature. 508 (2014) 327–328. doi:10.1038/508327a.

[74] Y. Chen, M. He, B. Liu, G.C. Bazan, J. Zhou, Z. Liang, Bendable n-Type Metallic Nanocomposites with Large Thermoelectric Power Factor, Adv. Mater. 29 (2017) 1604752. doi:10.1002/adma.201604752.

[75] O. Bubnova, Z.U. Khan, H. Wang, S. Braun, D.R. Evans, M. Fabretto, P. Hojati-Talemi, D. Dagnelund, J. Arlin, Y.H. Geerts, S. Desbief, D.W. Breiby, J.W. Andreasen, R. Lazzaroni, W.M. Chen, I. Zozoulenko, M. Fahlman, P.J. Murphy, M. Berggren, X. Crispin, Semi-metallic polymers, Nat. Mater. 13 (2014) 190–194. doi:10.1038/nmat3824.

[76] Y. Zhang, Y.-J. Heo, M. Park, S.-J. Park, Recent Advances in Organic Thermoelectric Materials: Principle Mechanisms and Emerging Carbon-Based Green Energy Materials, Polymers. 11 (2019) 167. doi:10.3390/polym11010167.

[77] N. Dubey, M. Leclerc, Conducting polymers: Efficient thermoelectric materials, J. Polym. Sci. Part B Polym. Phys. 49 (2011) 467–475. doi:10.1002/polb.22206.

[78] A. Datta, A. Popescu, L. Woods, G.S. Nolas, The Bottom-Up Approach to Bulk Thermoelectric Materials with Nanoscale Domains, in: D.M. Rowe (Ed.), Mater. Prep. Charact. Thermoelectr., CRC Press, 2012: pp. 1–25. https://www.taylorfrancis.com/books/9781315216904/chapters/10.1201/b11891-14.

[79] J.J. Urban, Prospects for thermoelectricity in quantum dot hybrid arrays, Nat. Nanotechnol. 10 (2015) 997–1001. doi:10.1038/nnano.2015.289.

[80] A.M. Rao, X. Ji, T.M. Tritt, Properties of Nanostructured One-Dimensional and Composite Thermoelectric Materials, MRS Bull. 31 (2006) 218–223. http://journals.cambridge.org/abstract_S088376940000991X.

[81] T. Tynell, A. Giri, J. Gaskins, P.E. Hopkins, P. Mele, K. Miyazaki, M. Karppinen, Efficiently suppressed thermal conductivity in ZnO thin films via periodic introduction of organic layers, J. Mater. Chem. A. 2 (2014) 12150. doi:10.1039/C4TA02381A.

[82] H.J. Goldsmid, Introduction to Thermoelectricity, Springer Berlin Heidelberg, Berlin, Heidelberg, 2010. doi:10.1007/978-3-642-00716-3.

[83] Y. Du, J. Xu, B. Paul, P. Eklund, Flexible thermoelectric materials and devices, Appl. Mater. Today. 12 (2018) 366–388. doi:10.1016/j.apmt.2018.07.004.

[84] L.-D. Zhao, S.-H. Lo, Y. Zhang, H. Sun, G. Tan, C. Uher, C. Wolverton, V.P. Dravid, M.G. Kanatzidis, Ultralow thermal conductivity and high thermoelectric figure of merit in SnSe crystals, Nature. 508 (2014) 373–377. doi:10.1038/nature13184.

[85] G. Han, S.R. Popuri, H.F. Greer, J.W.G. Bos, W. Zhou, A.R. Knox, A. Montecucco, J. Siviter, E.A. Man, M. MacAuley, D.J. Paul, W.G. Li, M.C. Paul, M. Gao, T. Sweet, R. Freer, F. Azough, H. Baig, N. Sellami, T.K. Mallick, D.H. Gregory, Facile surfactant-free synthesis of p-type snse nanoplates with exceptional thermoelectric power factors, Angew. Chemie - Int. Ed. 55 (2016) 6433–6437. doi:10.1002/anie.201601420.

[86] S. Hébert, D. Berthebaud, R. Daou, Y. Bréard, D. Pelloquin, E. Guilmeau, F. Gascoin, O. Lebedev, A. Maignan, Searching for new thermoelectric materials: some examples among oxides, sulfides and selenides, J. Phys. Condens. Matter. 28 (2016) 013001. doi:10.1088/0953-8984/28/1/013001.

[87] G. Tan, L.-D. Zhao, M.G. Kanatzidis, Rationally Designing High-Performance Bulk Thermoelectric Materials, Chem. Rev. 116 (2016) 12123–12149. doi:10.1021/acs.chemrev.6b00255.

[88] C. Yu, K. Choi, L. Yin, J.C. Grunlan, Light-weight flexible carbon nanotube based organic composites with large thermoelectric power factors, ACS Nano. 5 (2011) 7885–7892. doi:10.1021/nn202868a.

[89] Q. Wei, M. Mukaida, K. Kirihara, Y. Naitoh, T. Ishida, Recent Progress on PEDOT-Based Thermoelectric Materials, Materials. 8 (2015) 732–750. doi:10.3390/ma8020732.

[90] R. Kroon, D.A. Mengistie, D. Kiefer, J. Hynynen, J.D. Ryan, L. Yu, C. Müller, Thermoelectric plastics: from design to synthesis, processing and structure–property relationships, Chem. Soc. Rev. 45 (2016) 6147–6164. doi:10.1039/C6CS00149A.

[91] L. Stepien, A. Roch, R. Tkachov, T. Gedrange, Progress in Polymer Thermoelectrics, in: Thermoelectr. Power Gener. - A Look Trends Technol., InTech, 2016: pp. 75–100. doi:10.5772/66196.

[92] B.T. McGrail, A. Sehirlioglu, E. Pentzer, Polymer Composites for Thermoelectric

Applications, Angew. Chemie Int. Ed. 54 (2015) 1710–1723. doi:10.1002/anie.201408431.

[93] G.-H. Kim, L. Shao, K. Zhang, K.P. Pipe, Engineered doping of organic semiconductors for enhanced thermoelectric efficiency, Nat. Mater. 12 (2013) 719–723. doi:10.1038/nmat3635.

[94] S. Jo, S. Choo, F. Kim, S.H. Heo, J.S. Son, Ink Processing for Thermoelectric Materials and Power-Generating Devices, Adv. Mater. 1804930 (2018) 1804930. doi:10.1002/adma.201804930.

[95] O. Bubnova, Z.U. Khan, A. Malti, S. Braun, M. Fahlman, M. Berggren, X. Crispin, Optimization of the thermoelectric figure of merit in the conducting polymer poly(3,4-ethylenedioxythiophene), Nat. Mater. 10 (2011) 429–433. doi:10.1038/nmat3012.

[96] C. Ou, A.L. Sangle, T. Chalklen, Q. Jing, V. Narayan, S. Kar-Narayan, Enhanced thermoelectric properties of flexible aerosol-jet printed carbon nanotube-based nanocomposites, APL Mater. 6 (2018) 096101. doi:10.1063/1.5043547.

[97] L. Groenendaal, F. Jonas, D. Freitag, H. Pielartzik, J.R. Reynolds, Poly(3,4-ethylenedioxythiophene) and Its Derivatives: Past, Present, and Future, Adv. Mater. 12 (2000) 481–494. doi:10.1002/(SICI)1521-4095(200004)12:7<481::AID-ADMA481>3.0.CO;2-C.

[98] I. Petsagkourakis, K. Tybrandt, X. Crispin, I. Ohkubo, N. Satoh, T. Mori, Thermoelectric materials and applications for energy harvesting power generation, Sci. Technol. Adv. Mater. 19 (2018) 836–862. doi:10.1080/14686996.2018.1530938.

[99] Z. Fan, D. Du, H. Yao, J. Ouyang, Higher PEDOT Molecular Weight Giving Rise to Higher Thermoelectric Property of PEDOT:PSS: A Comparative Study of Clevios P and Clevios PH1000, ACS Appl. Mater. Interfaces. 9 (2017) 11732–11738. doi:10.1021/acsami.6b15158.

[100] W. Meng, R. Ge, Z. Li, J. Tong, T. Liu, Q. Zhao, S. Xiong, F. Jiang, L. Mao, Y. Zhou, Conductivity Enhancement of PEDOT:PSS Films via Phosphoric Acid Treatment for Flexible All-Plastic Solar Cells, ACS Appl. Mater. Interfaces. 7 (2015) 14089–14094. doi:10.1021/acsami.5b03309.

[101] Y. Sun, L. Qiu, L. Tang, H. Geng, H. Wang, F. Zhang, D. Huang, W. Xu, P. Yue, Y. Guan, F. Jiao, Y. Sun, D. Tang, C. Di, Y. Yi, D. Zhu, Flexible n-Type High-Performance Thermoelectric Thin Films of Poly(nickel-ethylenetetrathiolate) Prepared by an Electrochemical Method, Adv. Mater. 28 (2016) 3351–3358. doi:10.1002/adma.201505922.

[102] H. Peng, X. Sun, W. Weng, X. Fang, Polymer materials for energy and electronic

applications, Elsevier, 2017.

[103] F.-P. Du, N.-N. Cao, Y.-F. Zhang, P. Fu, Y.-G. Wu, Z.-D. Lin, R. Shi, A. Amini, C. Cheng, PEDOT:PSS/graphene quantum dots films with enhanced thermoelectric properties via strong interfacial interaction and phase separation, Sci. Rep. 8 (2018) 6441. doi:10.1038/s41598-018-24632-4.

[104] H. Wang, S. Yi, X. Pu, C. Yu, Simultaneously Improving Electrical Conductivity and Thermopower of Polyaniline Composites by Utilizing Carbon Nanotubes as High Mobility Conduits, ACS Appl. Mater. Interfaces. 7 (2015) 9589–9597. doi:10.1021/acsami.5b01149.

[105] L. Wang, Q. Yao, H. Bi, F. Huang, Q. Wang, L. Chen, PANI/graphene nanocomposite films with high thermoelectric properties by enhanced molecular ordering, J. Mater. Chem. A. 3 (2015) 7086–7092. doi:10.1039/C4TA06422D.

[106] C. Bounioux, P. Díaz-Chao, M. Campoy-Quiles, M.S. Martín-González, A.R. Goñi, R. Yerushalmi-Rozen, C. Müller, Thermoelectric composites of poly(3-hexylthiophene) and carbon nanotubes with a large power factor, Energy Environ. Sci. 6 (2013) 918. doi:10.1039/c2ee23406h.

[107] D. Kim, Y. Kim, K. Choi, J.C. Grunlan, C. Yu, Improved thermoelectric behavior of nanotube-filled polymer composites with poly(3,4-ethylenedioxythiophene) poly(styrenesulfonate), ACS Nano. 4 (2010) 513–523. doi:10.1021/nn9013577.

[108] W. Lee, Y.H. Kang, J.Y. Lee, K.-S. Jang, S.Y. Cho, Improving the thermoelectric power factor of CNT/PEDOT:PSS nanocomposite films by ethylene glycol treatment, RSC Adv. 6 (2016) 53339–53344. doi:10.1039/C6RA08599G.

[109] G.P. Moriarty, J.N. Wheeler, C. Yu, J.C. Grunlan, Increasing the thermoelectric power factor of polymer composites using a semiconducting stabilizer for carbon nanotubes, Carbon N. Y. 50 (2012) 885–895. doi:10.1016/j.carbon.2011.09.050.

[110] D. Yoo, J. Kim, S.H. Lee, W. Cho, H.H. Choi, F.S. Kim, J.H. Kim, Effects of one- and two-dimensional carbon hybridization of PEDOT:PSS on the power factor of polymer thermoelectric energy conversion devices, J. Mater. Chem. A. 3 (2015) 6526–6533. doi:10.1039/C4TA06710J.

[111] S.L. Kim, K. Choi, A. Tazebay, C. Yu, Flexible Power Fabrics Made of Carbon Nanotubes for Harvesting Thermoelectricity, ACS Nano. 8 (2014) 2377–2386. doi:10.1021/nn405893t.

[112] D. Madan, Z. Wang, P.K. Wright, J.W. Evans, Printed flexible thermoelectric generators for use on low levels of waste heat, Appl. Energy. 156 (2015) 587–592. doi:10.1016/j.apenergy.2015.07.066.

[113] V. Vijayakumar, Y. Zhong, V. Untilova, M. Bahri, L. Herrmann, L. Biniek, N. Leclerc, M. Brinkmann, Bringing Conducting Polymers to High Order: Toward Conductivities beyond 10 5 S cm −1 and Thermoelectric Power Factors of 2 mW m −1 K −2, Adv. Energy Mater. 9 (2019) 1900266. doi:10.1002/aenm.201900266.

[114] Q. Yao, Q. Wang, L. Wang, Y. Wang, J. Sun, H. Zeng, Z. Jin, X. Huang, L. Chen, The synergic regulation of conductivity and Seebeck coefficient in pure polyaniline by chemically changing the ordered degree of molecular chains, J. Mater. Chem. A. 2 (2014) 2634. doi:10.1039/c3ta14008c.

[115] A. Hamidi-Sakr, L. Biniek, J.-L. Bantignies, D. Maurin, L. Herrmann, N. Leclerc, P. Lévêque, V. Vijayakumar, N. Zimmermann, M. Brinkmann, A Versatile Method to Fabricate Highly In-Plane Aligned Conducting Polymer Films with Anisotropic Charge Transport and Thermoelectric Properties: The Key Role of Alkyl Side Chain Layers on the Doping Mechanism, Adv. Funct. Mater. 27 (2017) 1700173. doi:10.1002/adfm.201700173.

[116] N.T. Kemp, A.B. Kaiser, C.-J. Liu, B. Chapman, O. Mercier, A.M. Carr, H.J. Trodahl, R.G. Buckley, A.C. Partridge, J.Y. Lee, C.Y. Kim, A. Bartl, L. Dunsch, W.T. Smith, J.S. Shapiro, Thermoelectric power and conductivity of different types of polypyrrole, J. Polym. Sci. Part B Polym. Phys. 37 (1999) 953–960. doi:10.1002/(SICI)1099-0488(19990501)37:9<953::AID-POLB7>3.0.CO;2-L.

[117] Y. Hiroshige, M. Ookawa, N. Toshima, Thermoelectric figure-of-merit of iodine-doped copolymer of phenylenevinylene with dialkoxyphenylenevinylene, Synth. Met. 157 (2007) 467–474. doi:10.1016/j.synthmet.2007.05.003.

[118] B. Russ, M.J. Robb, F.G. Brunetti, P.L. Miller, E.E. Perry, S.N. Patel, V. Ho, W.B. Chang, J.J. Urban, M.L. Chabinyc, C.J. Hawker, R.A. Segalman, Power Factor Enhancement in Solution-Processed Organic n-Type Thermoelectrics Through Molecular Design, Adv. Mater. 26 (2014) 3473–3477. doi:10.1002/adma.201306116.

[119] R.A. Schlitz, F.G. Brunetti, A.M. Glaudell, P.L. Miller, M.A. Brady, C.J. Takacs, C.J. Hawker, M.L. Chabinyc, Solubility-Limited Extrinsic n-Type Doping of a High Electron Mobility Polymer for Thermoelectric Applications, Adv. Mater. 26 (2014) 2825–2830. doi:10.1002/adma.201304866.

[120] D. Moses, J. Chen, A. Denenstein, M. Kaveh, T.-C. Chung, A.J. Heeger, A.G. MacDiarmid, Y.-W. Park, Inter-soliton electron hopping transport in trans-(CH)x, Solid State Commun. 40 (1981) 1007–1010. doi:10.1016/0038-1098(81)90055-7.

[121] T. Menke, D. Ray, J. Meiss, K. Leo, M. Riede, In-situ conductivity and Seebeck measurements of highly efficient n-dopants in fullerene C 60, Appl. Phys. Lett. 100 (2012) 093304. doi:10.1063/1.3689778.

[122] Z.H. Wang, K. Ichimura, M.S. Dresselhaus, G. Dresselhaus, W.-T. Lee, K.A. Wang, P.C. Eklund, Electronic transport properties of KxC70 thin films, Phys. Rev. B. 48 (1993) 10657–10660. doi:10.1103/PhysRevB.48.10657.

[123] H. Ju, J. Kim, Chemically Exfoliated SnSe Nanosheets and Their SnSe/Poly(3,4-ethylenedioxythiophene):Poly(styrenesulfonate) Composite Films for Polymer Based Thermoelectric Applications, ACS Nano. 10 (2016) 5730–5739. doi:10.1021/acsnano.5b07355.

[124] N. Toshima, M. Imai, S. Ichikawa, Organic–Inorganic Nanohybrids as Novel Thermoelectric Materials: Hybrids of Polyaniline and Bismuth(III) Telluride Nanoparticles, J. Electron. Mater. 40 (2011) 898–902. doi:10.1007/s11664-010-1403-1.

[125] M. He, J. Ge, Z. Lin, X. Feng, X. Wang, H. Lu, Y. Yang, F. Qiu, Thermopower enhancement in conducting polymer nanocomposites via carrier energy scattering at the organic–inorganic semiconductor interface, Energy Environ. Sci. 5 (2012) 8351. doi:10.1039/c2ee21803h.

[126] S. Ferhat, C. Domain, J. Vidal, D. Noël, B. Ratier, B. Lucas, Organic thermoelectric devices based on a stable n-type nanocomposite printed on paper, Sustain. Energy Fuels. 2 (2018) 199–208. doi:10.1039/C7SE00313G.

[127] F. Jiao, C.-A. Di, Y. Sun, P. Sheng, W. Xu, D. Zhu, Inkjet-printed flexible organic thin-film thermoelectric devices based on p- and n-type poly(metal 1,1,2,2-ethenetetrathiolate)s/polymer composites through ball-milling, Philos. Trans. R. Soc. A Math. Phys. Eng. Sci. 372 (2014) 20130008–20130008. doi:10.1098/rsta.2013.0008.

[128] J.H. We, S.J. Kim, B.J. Cho, Hybrid composite of screen-printed inorganic thermoelectric film and organic conducting polymer for flexible thermoelectric power generator, Energy. 73 (2014) 506–512. doi:10.1016/j.energy.2014.06.047.

[129] E.J. Bae, Y.H. Kang, K.-S. Jang, C. Lee, S.Y. Cho, Solution synthesis of telluride-based nano-barbell structures coated with PEDOT:PSS for spray-printed thermoelectric generators, Nanoscale. 8 (2016) 10885–10890. doi:10.1039/C5NR07032E.

[130] Y. Wang, G. Liu, M. Sheng, C. Yu, Y. Deng, Flexible thermopower generation over broad temperature range by PANI/nanorod hybrid-based p–n couples, J. Mater. Chem. A. (2019). doi:10.1039/C8TA11008E.

[131] L.E. Bell, Cooling, Heating, Generating Power, and Recovering Waste Heat with Thermoelectric Systems, Science. 321 (2008) 1457–1461. doi:10.1126/science.1158899.

[132] S. Chu, Y. Cui, N. Liu, The path towards sustainable energy, Nat. Mater. 16 (2016) 16–22. doi:10.1038/nmat4834.

[133] J. Gao, L. Miao, C. Liu, X. Wang, Y. Peng, X. Wei, J. Zhou, Y. Chen, R. Hashimoto, T. Asaka, K. Koumoto, A novel glass-fiber-aided cold-press method for fabrication of n-type Ag 2 Te nanowires thermoelectric film on flexible copy-paper substrate, J. Mater. Chem. A. 5 (2017) 24740–24748. doi:10.1039/C7TA07601K.

[134] W. Glatz, E. Schwyter, L. Durrer, C. Hierold, Bi2Te3-Based Flexible Micro Thermoelectric Generator With Optimized Design, J. Microelectromechanical Syst. 18 (2009) 763–772. doi:10.1109/JMEMS.2009.2021104.

[135] T. Whelan, Polymer Technology Dictionary, Springer Netherlands, Dordrecht, 1994. doi:10.1007/978-94-011-1292-5.

[136] K. D'Arezzo, Aerosol Jet AJ 200 System User Manual, Optomec Inc, 2016.

[137] I. Toray Research Center, Printing Technology for Flexible Substrates, InterLingua Publishing, 2006.

[138] M. Smith, Y.S. Choi, C. Boughey, S. Kar-narayan, Controlling and assessing the quality of aerosol jet printed features for large area and flexible electronics, Flex. Print. Electron. 2 (2017) 015004–015014. doi:10.1088/2058-8585/aa5af9.

[139] Z. Lu, M. Layani, X. Zhao, L.P. Tan, T. Sun, S. Fan, Q. Yan, S. Magdassi, H.H. Hng, Fabrication of Flexible Thermoelectric Thin Film Devices by Inkjet Printing, Small. 10 (2014) 3551–3554. doi:10.1002/smll.201303126.

[140] B. Chen, M. Kruse, B. Xu, R. Tutika, W. Zheng, M.D. Bartlett, Y. Wu, J.C. Claussen, Flexible thermoelectric generators with inkjet-printed bismuth telluride nanowires and liquid metal contacts, Nanoscale. 11 (2019) 5222–5230. doi:10.1039/C8NR09101C.

[141] B. Chen, S.R. Das, W. Zheng, B. Zhu, B. Xu, S. Hong, C. Sun, X. Wang, Y. Wu, J.C. Claussen, Inkjet Printing of Single-Crystalline Bi 2 Te 3 Thermoelectric Nanowire Networks, Adv. Electron. Mater. 3 (2017) 1600524. doi:10.1002/aelm.201600524.

[142] T. Juntunen, H. Jussila, M. Ruoho, S. Liu, G. Hu, T. Albrow-Owen, L.W.T. Ng, R.C.T. Howe, T. Hasan, Z. Sun, I. Tittonen, Inkjet Printed Large-Area Flexible Few-Layer Graphene Thermoelectrics, Adv. Funct. Mater. 28 (2018) 1800480. doi:10.1002/adfm.201800480.

[143] A. Hobby, Screen Printing For the Industrial User, 1997.

[144] Q. Wei, M. Mukaida, K. Kirihara, Y. Naitoh, T. Ishida, Polymer thermoelectric modules screen-printed on paper, RSC Adv. 4 (2014) 28802–28806. doi:10.1039/C4RA04946B.

[145] S. Shin, R. Kumar, J.W. Roh, D.-S. Ko, H.-S. Kim, S. Il Kim, L. Yin, S.M. Schlossberg, S. Cui, J.-M. You, S. Kwon, J. Zheng, J. Wang, R. Chen, High-Performance Screen-

Printed Thermoelectric Films on Fabrics, Sci. Rep. 7 (2017) 7317–7332. doi:10.1038/s41598-017-07654-2.

[146] Z. Cao, E. Koukharenko, M.J. Tudor, R.N. Torah, S.P. Beeby, Screen printed flexible Bi 2 Te 3 -Sb 2 Te 3 based thermoelectric generator, J. Phys. Conf. Ser. 476 (2013) 012031–012036. doi:10.1088/1742-6596/476/1/012031.

[147] T. Varghese, C. Hollar, J. Richardson, N. Kempf, C. Han, P. Gamarachchi, D. Estrada, R.J. Mehta, Y. Zhang, High-performance and flexible thermoelectric films by screen printing solution-processed nanoplate crystals, Sci. Rep. 6 (2016) 33135. doi:10.1038/srep33135.

[148] Z. Cao, E. Koukharenko, R.N. Torah, J. Tudor, S.P. Beeby, Flexible screen printed thick film thermoelectric generator with reduced material resistivity, J. Phys. Conf. Ser. 557 (2014) 012016. doi:10.1088/1742-6596/557/1/012016.

[149] Y.J. Kim, S.J. Kim, H. Choi, C.S. Kim, G. Lee, S.H. Park, B.J. Cho, Realization of High-Performance Screen-Printed Flexible Thermoelectric Generator by Improving Contact Characteristics, Adv. Mater. Interfaces. 4 (2017) 1700870. doi:10.1002/admi.201700870.

[150] Z. Yuan, X. Tang, Z. Xu, J. Li, W. Chen, K. Liu, Y. Liu, Z. Zhang, Screen-printed radial structure micro radioisotope thermoelectric generator, Appl. Energy. 225 (2018) 746–754. doi:10.1016/j.apenergy.2018.05.073.

[151] C. Han, G. Tan, T. Varghese, M.G. Kanatzidis, Y. Zhang, High-Performance PbTe Thermoelectric Films by Scalable and Low-Cost Printing, ACS Energy Lett. 3 (2018) 818–822. doi:10.1021/acsenergylett.8b00041.

[152] S.J. Kim, H.E. Lee, H. Choi, Y. Kim, J.H. We, J.S. Shin, K.J. Lee, B.J. Cho, High-Performance Flexible Thermoelectric Power Generator Using Laser Multiscanning Lift-Off Process, ACS Nano. 10 (2016) 10851–10857. doi:10.1021/acsnano.6b05004.

[153] H. Choi, S.J. Kim, Y. Kim, J.H. We, M.-W. Oh, B.J. Cho, Enhanced thermoelectric properties of screen-printed Bi 0.5 Sb 1.5 Te 3 and Bi 2 Te 2.7 Se 0.3 thick films using a post annealing process with mechanical pressure, J. Mater. Chem. C. 5 (2017) 8559–8565. doi:10.1039/C7TC01797A.

[154] Z. Cao, E. Koukharenko, M.J. Tudor, R.N. Torah, S.P. Beeby, Flexible screen printed thermoelectric generator with enhanced processes and materials, Sensors Actuators A Phys. 238 (2016) 196–206. doi:10.1016/j.sna.2015.12.016.

[155] Z. Cao, J.J. Shi, R.N. Torah, M.J. Tudor, S.P. Beeby, All dispenser printed flexible 3D structured thermoelectric generators, J. Phys. Conf. Ser. 660 (2015) 012096–012100. doi:10.1088/1742-6596/660/1/012096.

[156] D. Madan, Z. Wang, A. Chen, R. Juang, J. Keist, P.K. Wright, J.W. Evans, Enhanced Performance of Dispenser Printed MA n-type Bi 2 Te 3 Composite Thermoelectric Generators, ACS Appl. Mater. Interfaces. 4 (2012) 6117–6124. doi:10.1021/am301759a.

[157] A. Chen, D. Madan, P.K. Wright, J.W. Evans, Dispenser-printed planar thick-film thermoelectric energy generators, J. Micromechanics Microengineering. 21 (2011) 104006–104013. doi:10.1088/0960-1317/21/10/104006.

[158] E.B. Secor, Principles of aerosol jet printing, Flex. Print. Electron. 3 (2018) 035002. doi:10.1088/2058-8585/aace28.

[159] Q. Jing, Y.S. Choi, M. Smith, C. Ou, T. Busolo, S. Kar-Narayan, Freestanding Functional Structures by Aerosol-Jet Printing for Stretchable Electronics and Sensing Applications, Adv. Mater. Technol. 4 (2019) 1900048. doi:10.1002/admt.201900048.

[160] K. Hong, S.H. Kim, A. Mahajan, C.D. Frisbie, Aerosol jet printed p- and n-type electrolyte-gated transistors with a variety of electrode materials: Exploring practical routes to printed electronics, ACS Appl. Mater. Interfaces. 6 (2014) 18704–18711. doi:10.1021/am504171u.

[161] C.S. Jones, X. Lu, M. Renn, M. Stroder, W.S. Shih, Aerosol-jet-printed, high-speed, flexible thin-film transistor made using single-walled carbon nanotube solution, Microelectron. Eng. 87 (2010) 434–437. doi:10.1016/j.mee.2009.05.034.

[162] M.S. Saleh, J. Li, J. Park, R. Panat, 3D printed hierarchically-porous microlattice electrode materials for exceptionally high specific capacity and areal capacity lithium ion batteries, Addit. Manuf. 23 (2018) 70–78. doi:10.1016/j.addma.2018.07.006.

[163] N.G. Di Novo, E. Cantù, S. Tonello, E. Sardini, M. Serpelloni, Support-Material-Free Microfluidics on an Electrochemical Sensors Platform by Aerosol Jet Printing, Sensors. 19 (2019) 1842. doi:10.3390/s19081842.

[164] J. Ouyang, D. Cormier, S.A. Williams, D.A. Borkholder, Photonic Sintering of Aerosol Jet Printed Lead Zirconate Titanate (PZT) Thick Films, J. Am. Ceram. Soc. 99 (2016) 2569–2577. doi:10.1111/jace.14272.

[165] Q. Jing, Y.S. Choi, M. Smith, N. Ćatić, C. Ou, S. Kar-Narayan, Aerosol-Jet Printed Fine-Featured Triboelectric Sensors for Motion Sensing, Adv. Mater. Technol. 1800328 (2018) 1–7. doi:10.1002/admt.201800328.

[166] M. Saeidi-Javash, W. Kuang, C. Dun, Y. Zhang, 3D Conformal Printing and Photonic Sintering of High-Performance Flexible Thermoelectric Films Using 2D Nanoplates, Adv. Funct. Mater. 1901930 (2019) 1901930. doi:10.1002/adfm.201901930.

[167] R.S. Salary, J.P. Lombardi, M.S. Tootooni, R. Donovan, P.K. Rao, M.D. Poliks, In Situ

Sensor-Based Monitoring and Computational Fluid Dynamics (CFD) Modeling of Aerosol Jet Printing (AJP) Process, in: Vol. 2 Mater. Biomanufacturing; Prop. Appl. Syst. Sustain. Manuf., ASME, 2016: p. V002T04A049. doi:10.1115/MSEC2016-8535.

[168] P.R. Ghediya, T.K. Chaudhuri, Dark and photo-conductivity of doctor-bladed CZTS films above room temperature, J. Phys. D. Appl. Phys. 48 (2015) 455109. doi:10.1088/0022-3727/48/45/455109.

[169] M. Hokazono, H. Anno, N. Toshima, Thermoelectric Properties and Thermal Stability of PEDOT:PSS Films on a Polyimide Substrate and Application in Flexible Energy Conversion Devices, J. Electron. Mater. 43 (2014) 2196–2201. doi:10.1007/s11664-014-3003-y.

[170] S.H. Park, S. Jo, B. Kwon, F. Kim, H.W. Ban, J.E. Lee, D.H. Gu, S.H. Lee, Y. Hwang, J.-S. Kim, D.-B. Hyun, S. Lee, K.J. Choi, W. Jo, J.S. Son, High-performance shape-engineerable thermoelectric painting, Nat. Commun. 7 (2016) 13403–13412. doi:10.1038/ncomms13403.

[171] L. Francioso, C. De Pascali, I. Farella, C. Martucci, P. Cretì, P. Siciliano, A. Perrone, Flexible thermoelectric generator for ambient assisted living wearable biometric sensors, J. Power Sources. 196 (2011) 3239–3243. doi:10.1016/j.jpowsour.2010.11.081.

[172] Y. Wang, Y. Shi, D. Mei, Z. Chen, Wearable thermoelectric generator to harvest body heat for powering a miniaturized accelerometer, Appl. Energy. 215 (2018) 690–698. doi:10.1016/j.apenergy.2018.02.062.

[173] E.J. Bae, Y.H. Kang, C. Lee, S.Y. Cho, Engineered nanocarbon mixing for enhancing the thermoelectric properties of a telluride-PEDOT:PSS nanocomposite, J. Mater. Chem. A. 5 (2017) 17867–17873. doi:10.1039/C7TA04280A.

[174] C.T. Hong, Y.H. Kang, J. Ryu, S.Y. Cho, K.-S. Jang, Spray-printed CNT/P3HT organic thermoelectric films and power generators, J. Mater. Chem. A. 3 (2015) 21428–21433. doi:10.1039/C5TA06096F.

[175] K.C. See, J.P. Feser, C.E. Chen, A. Majumdar, J.J. Urban, R.A. Segalman, Water-Processable Polymer−Nanocrystal Hybrids for Thermoelectrics, Nano Lett. 10 (2010) 4664–4667. doi:10.1021/nl102880k.

[176] Y. Wang, S.M. Zhang, Y. Deng, Flexible low-grade energy utilization devices based on high-performance thermoelectric polyaniline/tellurium nanorod hybrid films, J. Mater. Chem. A. 4 (2016) 3554–3559. doi:10.1039/C6TA01140C.

[177] R.M. Mahamood, E.T. Akinlabi, Types of Functionally Graded Materials and Their Areas of Application, in: Funct. Graded Mater., Springer, 2017: pp. 9–21. doi:10.1007/978-3-319-53756-6_2.

[178] C.C. Ge, X.F. Wu, G.Y. Xu, Functionally Graded Thermoelectric Materials, Key Eng. Mater. 336–338 (2007) 2600–2604. doi:10.4028/www.scientific.net/KEM.336-338.2600.

[179] J. Teraki, T. Hirano, A design procedure of functionally graded thermoelectric materials, in: I. Shiota, Y. Miyamoto (Eds.), 4th Int. Symp. Funct. Graded Mater., Elsevier Science B.V., 1997: p. 483.

[180] A.F. Ioffe, Byulleten' Izobretenii, 126158, 1960.

[181] E. Müller, Č. Drašar, J. Schilz, W.A. Kaysser, Functionally graded materials for sensor and energy applications, Mater. Sci. Eng. A. 362 (2003) 17–39. doi:10.1016/S0921-5093(03)00581-1.

[182] I. Shiota, A. Nishida, Development of FGM thermoelectric materials in Japan -The state of the art, in: 16th Int. Conf. Thermoelectr., 1997: pp. 364–370.

[183] Q. Ma, H. Fang, M. Zhang, Theoretical analysis and design optimization of thermoelectric generator, Appl. Therm. Eng. 127 (2017) 758–764. doi:10.1016/j.applthermaleng.2017.08.056.

[184] D.M. Rowe, Thermoelectrics handbook: macro to nano, Taylor & Francis Group, 2006.

[185] E. Hazan, O. Ben-Yehuda, N. Madar, Y. Gelbstein, Functional Graded Germanium-Lead Chalcogenide-Based Thermoelectric Module for Renewable Energy Applications, Adv. Energy Mater. 5 (2015) 1500272. doi:10.1002/aenm.201500272.

[186] C.L. Cramer, W. Li, Z.-H. Jin, J. Wang, K. Ma, T.B. Holland, Techniques for Mitigating Thermal Fatigue Degradation, Controlling Efficiency, and Extending Lifetime in a ZnO Thermoelectric Using Grain Size Gradient FGMs, J. Electron. Mater. 47 (2018) 866–872. doi:10.1007/s11664-017-5879-9.

[187] I. Bharti, N. Gupta, K.M. Gupta, Novel applications of functionally graded nano, optoelectronic and thermoelectric materials., Int. J. Mater. Mech. Manuf. 1 (2013) 221–224. doi:10.7763/IJMMM.2013.V1.47.

[188] J.L. Cui, X.B. Zhao, The design and properties of pseudobinary alloys (PbTe)1-x-(SnTe)x with gradient composition, Mater. Lett. 57 (2003) 2466–2471. doi:10.1016/S0167-577X(02)01268-5.

[189] Y. Gelbstein, Z. Dashevsky, M.P. Dariel, Powder metallurgical processing of functionally graded p-Pb1-xSnxTe materials for thermoelectric applications, Phys. B Condens. Matter. 391 (2007) 256–265. doi:10.1016/j.physb.2006.10.001.

[190] J. Schilz, L. Helmers, Y.S. Kang, Y. Noda, M. Niino, Bismuth-telluride/iron-disilicide

segmented thermoelectric elements: patterning, preparation and properties, in: 16th Int. Conf. Thermoelectr., 1997: pp. 375–378.

[191] T. Muto, K. Tokuda, T. Itoh, K. Kitagwa, Fabrication of segmented p-type AgSbTe2/Sb2Te3Bi0.4/Sb1.6Te3 thermoelectric module and its performance, in: 2005 Int. Conf. Thermoelectr., IEEE, 2005: pp. 524–527. doi:10.1109/ICT.2005.1520001.

[192] T. Itoh, T. Muto, K. Kitagawa, Performance of segmented thermoelectric elements fabricated by simultaneous sintering method, in: 2006 Int. Conf. Thermoelectr., IEEE, 2006: pp. 623–626. doi:10.1109/ICT.2006.331391.

[193] O. Meroz, Y. Gelbstein, Thermoelectric Bi 2 Te 3−x Se x alloys for efficient thermal to electrical energy conversion, Phys. Chem. Chem. Phys. 20 (2018) 4092–4099. doi:10.1039/C7CP06176E.

[194] G. Komisarchik, D. Fuks, Y. Gelbstein, High thermoelectric potential of n -type Pb 1− x Ti x Te alloys, J. Appl. Phys. 120 (2016) 055104. doi:10.1063/1.4960573.

[195] E.M.J. Hedegaard, S. Johnsen, L. Bjerg, K.A. Borup, B.B. Iversen, Functionally Graded Ge 1– x Si x Thermoelectrics by Simultaneous Band Gap and Carrier Density Engineering, Chem. Mater. 26 (2014) 4992–4997. doi:10.1021/cm502042e.

[196] Y. Gelbstein, Z. Dashevsky, M.P. Dariel, High performance n-type PbTe-based materials for thermoelectric applications, Phys. B Condens. Matter. 363 (2005) 196–205. doi:10.1016/j.physb.2005.03.022.

[197] Z. Dashevsky, S. Shusterman, M.P. Dariel, I. Drabkin, Thermoelectric efficiency in graded indium-doped PbTe crystals, J. Appl. Phys. 92 (2002) 1425–1430. doi:10.1063/1.1490152.

[198] C.L. Cramer, J. Gonzalez-Julian, P.S. Colasuonno, T.B. Holland, Continuous functionally graded material to improve the thermoelectric properties of ZnO, J. Eur. Ceram. Soc. 37 (2017) 4693–4700. doi:10.1016/j.jeurceramsoc.2017.07.019.

[199] E.M.J. Hedegaard, A.A.H. Mamakhel, H. Reardon, B.B. Iversen, Functionally Graded (PbTe) 1– x (SnTe) x Thermoelectrics, Chem. Mater. 30 (2018) 280–287. doi:10.1021/acs.chemmater.7b04473.

[200] Y. Wang, C. Zhu, R. Pfattner, H. Yan, L. Jin, S. Chen, F. Molina-Lopez, F. Lissel, J. Liu, N.I.N.I. Rabiah, Z. Chen, J.W.J.W. Chung, C. Linder, M.F.M.F. Toney, B. Murmann, Z. Bao, A highly stretchable, transparent, and conductive polymer, Sci. Adv. 3 (2017) 1–11. doi:10.1126/sciadv.1602076.

[201] N. Matsuhisa, M. Kaltenbrunner, T. Yokota, H. Jinno, K. Kuribara, T. Sekitani, T. Someya, Printable elastic conductors with a high conductivity for electronic textile

applications, Nat. Commun. 6 (2015) 7461. doi:10.1038/ncomms8461.

[202] D.-H. Kim, N. Lu, R. Ma, Y.-S. Kim, R.-H. Kim, S. Wang, J. Wu, S.M. Won, H. Tao, A. Islam, K.J. Yu, T. -i. Kim, R. Chowdhury, M. Ying, L. Xu, M. Li, H.-J. Chung, H. Keum, M. McCormick, P. Liu, Y.-W. Zhang, F.G. Omenetto, Y. Huang, T. Coleman, J.A. Rogers, Epidermal Electronics, Science. 333 (2011) 838–843. doi:10.1126/science.1206157.

[203] W. Dang, V. Vinciguerra, L. Lorenzelli, R. Dahiya, Printable stretchable interconnects, Flex. Print. Electron. 2 (2017). doi:10.1088/2058-8585/aa5ab2.

[204] K. Nan, S.D. Kang, K. Li, K.J. Yu, F. Zhu, J. Wang, A.C. Dunn, C. Zhou, Z. Xie, M.T. Agne, H. Wang, H. Luan, Y. Zhang, Y. Huang, G.J. Snyder, J.A. Rogers, Compliant and stretchable thermoelectric coils for energy harvesting in miniature flexible devices, Sci. Adv. 4 (2018) eaau5849. doi:10.1126/sciadv.aau5849.

[205] J.A. Rogers, T. Someya, Y. Huang, Materials and Mechanics for Stretchable Electronics, Science. 327 (2010) 1603–1607. doi:10.1126/science.1182383.

[206] Y. Gao, L. Yu, J.C. Yeo, C.T. Lim, Flexible Hybrid Sensors for Health Monitoring: Materials and Mechanisms to Render Wearability, Adv. Mater. 1902133 (2019) 1902133. doi:10.1002/adma.201902133.

[207] X. Fan, W. Nie, H. Tsai, N. Wang, H. Huang, Y. Cheng, R. Wen, L. Ma, F. Yan, Y. Xia, PEDOT:PSS for Flexible and Stretchable Electronics: Modifications, Strategies, and Applications, Adv. Sci. 6 (2019) 1900813. doi:10.1002/advs.201900813.

[208] Y. Liu, K. He, G. Chen, W.R. Leow, X. Chen, Nature-Inspired Structural Materials for Flexible Electronic Devices, Chem. Rev. 117 (2017) 12893–12941. doi:10.1021/acs.chemrev.7b00291.

[209] T. Sekitani, Y. Noguchi, K. Hata, T. Fukushima, T. Aida, T. Someya, A Rubberlike Stretchable Active Matrix Using Elastic Conductors, Science. 321 (2008) 1468–1472. doi:10.1126/science.1160309.

[210] K.-Y. Chun, Y. Oh, J. Rho, J.-H. Ahn, Y.-J. Kim, H.R. Choi, S. Baik, Highly conductive, printable and stretchable composite films of carbon nanotubes and silver, Nat. Nanotechnol. 5 (2010) 853–857. doi:10.1038/nnano.2010.232.

[211] C. Teng, X. Lu, Y. Zhu, M. Wan, L. Jiang, Polymer in situ embedding for highly flexible, stretchable and water stable PEDOT:PSS composite conductors, RSC Adv. 3 (2013) 7219. doi:10.1039/c3ra41124a.

[212] P.J. Taroni, G. Santagiuliana, K. Wan, P. Calado, M. Qiu, H. Zhang, N.M. Pugno, M. Palma, N. Stingelin-Stutzman, M. Heeney, O. Fenwick, M. Baxendale, E. Bilotti, Toward Stretchable Self-Powered Sensors Based on the Thermoelectric Response of

PEDOT:PSS/Polyurethane Blends, Adv. Funct. Mater. 28 (2018) 1704285. doi:10.1002/adfm.201704285.

[213] K. Wan, P.J. Taroni, Z. Liu, Y. Liu, Y. Tu, G. Santagiuliana, I. Hsia, H. Zhang, O. Fenwick, S. Krause, M. Baxendale, B.C. Schroeder, E. Bilotti, Flexible and Stretchable Self-Powered Multi-Sensors Based on the N-Type Thermoelectric Response of Polyurethane/Na x (Ni-ett) n Composites, Adv. Electron. Mater. (2019) 1900582. doi:10.1002/aelm.201900582.

[214] D. Zhang, K. Zhang, Y. Wang, Y. Wang, Y. Yang, Thermoelectric effect induced electricity in stretchable graphene-polymer nanocomposites for ultrasensitive self-powered strain sensor system, Nano Energy. 56 (2019) 25–32. doi:10.1016/j.nanoen.2018.11.026.

[215] Q. Hua, J. Sun, H. Liu, R. Bao, R. Yu, J. Zhai, C. Pan, Z.L. Wang, Skin-inspired highly stretchable and conformable matrix networks for multifunctional sensing, Nat. Commun. 9 (2018) 1–11. doi:10.1038/s41467-017-02685-9.

[216] J.P. Rojas, D. Singh, D. Conchouso, A. Arevalo, I.G. Foulds, M.M. Hussain, Stretchable helical architecture inorganic-organic hetero thermoelectric generator, Nano Energy. 30 (2016) 691–699. doi:10.1016/j.nanoen.2016.10.054.

[217] K. Fukuie, Y. Iwata, E. Iwase, Design of Substrate Stretchability Using Origami-Like Folding Deformation for Flexible Thermoelectric Generator, Micromachines. 9 (2018) 315. doi:10.3390/mi9070315.

[218] S.H. Jeong, F.J. Cruz, S. Chen, L. Gravier, J. Liu, Z. Wu, K. Hjort, S.-L. Zhang, Z.-B. Zhang, Stretchable Thermoelectric Generators Metallized with Liquid Alloy, ACS Appl. Mater. Interfaces. 9 (2017) 15791–15797. doi:10.1021/acsami.7b04752.

[219] M.D. Dickey, Stretchable and Soft Electronics using Liquid Metals, Adv. Mater. 29 (2017). doi:10.1002/adma.201606425.

[220] J.Y. Kim, J.Y. Oh, T. Il Lee, Multi-dimensional nanocomposites for stretchable thermoelectric applications, Appl. Phys. Lett. 114 (2019) 043902. doi:10.1063/1.5080622.

[221] X. Xu, Y. Zuo, S. Cai, X. Tao, Z. Zhang, X. Zhou, S. He, X. Fang, H. Peng, Three-dimensional helical inorganic thermoelectric generators and photodetectors for stretchable and wearable electronic devices, J. Mater. Chem. C. 6 (2018) 4866–4872. doi:10.1039/C8TC01183D.

[222] J. Jo, I. Oh, M.-J. Jin, J. Park, J.S. Son, K.-S. An, J.-W. Yoo, Highly stretchable organic thermoelectrics with an enhanced power factor due to extended localization length, Org. Electron. 50 (2017) 367–375. doi:10.1016/j.orgel.2017.08.013.

[223] B. Lu, H. Yuk, S. Lin, N. Jian, K. Qu, J. Xu, X. Zhao, Pure PEDOT:PSS hydrogels, Nat. Commun. 10 (2019) 1043. doi:10.1038/s41467-019-09003-5.

[224] P. Li, K. Sun, J. Ouyang, Stretchable and Conductive Polymer Films Prepared by Solution Blending, ACS Appl. Mater. Interfaces. 7 (2015) 18415–18423. doi:10.1021/acsami.5b04492.

[225] M. Jung, S. Jeon, J. Bae, Scalable and facile synthesis of stretchable thermoelectric fabric for wearable self-powered temperature sensors, RSC Adv. 8 (2018) 39992–39999. doi:10.1039/C8RA06664G.

[226] A. Datta, G.S. Nolas, Composition controlled synthesis of Bi rich Bi1−xSbx alloy nanocrystals by a low temperature polyol process, CrystEngComm. 13 (2011) 2753–2757. doi:10.1039/c0ce00706d.

[227] P. Scherrer, Nachrichten von der Gesellschaft der Wissenschaften zu Göttingen, Göttinger Nachrichten Gesell. 2 (1918) 98–99.

[228] H.-Y. Chen, H.-L. Huang, Numerical and experimental study of virtual impactor design and aerosol separation, J. Aerosol Sci. 94 (2016) 43–55. doi:10.1016/j.jaerosci.2015.12.001.

[229] A.K. Cheek, Aerosol Jet Deposition System Operator's Guide, 2013.

[230] S. Binder, M. Glatthaar, E. Rädlein, Analytical Investigation of Aerosol Jet Printing, Aerosol Sci. Technol. 48 (2014) 924–929. doi:10.1080/02786826.2014.940439.

[231] A. Mahajan, C.D. Frisbie, L.F. Francis, Optimization of Aerosol Jet Printing for High-Resolution, High-Aspect Ratio Silver Lines, ACS Appl. Mater. Interfaces. 5 (2013) 4856–4864. doi:10.1021/am400606y.

[232] S.K. Yee, N.E. Coates, A. Majumdar, J.J. Urban, R.A. Segalman, Thermoelectric power factor optimization in PEDOT:PSS tellurium nanowire hybrid composites, Phys. Chem. Chem. Phys. 15 (2013) 4024–4032. doi:10.1039/c3cp44558e.

[233] N. Massonnet, A. Carella, O. Jaudouin, P. Rannou, G. Laval, C. Celle, J.-P. Simonato, Improvement of the Seebeck coefficient of PEDOT:PSS by chemical reduction combined with a novel method for its transfer using free-standing thin films, J. Mater. Chem. C. 2 (2014) 1278–1283. doi:10.1039/C3TC31674B.

[234] R. Venkatasubramanian, E. Siivola, T. Colpitts, B. O'Quinn, Thin-film thermoelectric devices with high room-temperature figures of merit, Nature. 413 (2001) 597–602. doi:10.1038/35098012.

[235] U. Lang, N. Naujoks, J. Dual, Mechanical characterization of PEDOT:PSS thin films,

Synth. Met. 159 (2009) 473–479. doi:10.1016/j.synthmet.2008.11.005.

[236] H. Pu, D. Wang, Studies on proton conductivity of polyimide/H3PO4/imidazole blends, Electrochim. Acta. 51 (2006) 5612–5617. doi:10.1016/j.electacta.2006.02.035.

[237] E. Schab-Balcerzak, M. Wegrzyn, H. Janeczek, B. Jarzabek, P. Rannou, A. Iwan, The synthesis and thermal, optical and electrical properties of novel aromatic–aliphatic five- and six-membered thermotropic polyimides, Liq. Cryst. 37 (2010) 1347–1359. doi:10.1080/02678292.2010.506578.

[238] H.Y. Lee, J.K. Lee, Dissolution of Thermoelectric Materials Containing Te with Acidic Solutions, Sep. Sci. Technol. 50 (2015) 1665–1670. doi:10.1080/01496395.2014.980004.

[239] H. Li, J.-T. Sun, C. Wang, S. Liu, D. Yuan, X. Zhou, J. Tan, L. Stubbs, C. He, High Modulus, Strength, and Toughness Polyurethane Elastomer Based on Unmodified Lignin, ACS Sustain. Chem. Eng. 5 (2017) 7942–7949. doi:10.1021/acssuschemeng.7b01481.

[240] H. Shi, C. Liu, Q. Jiang, J. Xu, Effective Approaches to Improve the Electrical Conductivity of PEDOT:PSS: A Review, Adv. Electron. Mater. 1 (2015) 1–16. doi:10.1002/aelm.201500017.

[241] S. Shin, J.W. Roh, H.-S. Kim, R. Chen, Role of surfactant on thermoelectric behaviors of organic-inorganic composites, J. Appl. Phys. 123 (2018) 205106. doi:10.1063/1.5033920.

[242] Y. Du, K.F. Cai, S. Chen, P. Cizek, T. Lin, Facile Preparation and Thermoelectric Properties of Bi 2 Te 3 Based Alloy Nanosheet/PEDOT:PSS Composite Films, ACS Appl. Mater. Interfaces. 6 (2014) 5735–5743. doi:10.1021/am5002772.

[243] C. Biswas, K.K. Kim, H. Geng, H.K. Park, S.C. Lim, S.J. Chae, S.M. Kim, Y.H. Lee, M. Nayhouse, M. Yun, Strategy for High Concentration Nanodispersion of Single-Walled Carbon Nanotubes with Diameter Selectivity, J. Phys. Chem. C. 113 (2009) 10044–10051. doi:10.1021/jp9017629.

[244] W.H. Duan, Q. Wang, F. Collins, Dispersion of carbon nanotubes with SDS surfactants: a study from a binding energy perspective, Chem. Sci. 2 (2011) 1407–1413. doi:10.1039/c0sc00616e.

[245] H. Menon, R. Aiswarya, K.P. Surendran, Screen printable MWCNT inks for printed electronics, RSC Adv. 7 (2017) 44076–44081. doi:10.1039/C7RA06260E.

[246] S. Liu, H. Deng, Y. Zhao, S. Ren, Q. Fu, The optimization of thermoelectric properties in a PEDOT:PSS thin film through post-treatment, RSC Adv. 5 (2015) 1910–1917.

doi:10.1039/C4RA09147G.

[247] J. Luo, D. Billep, T. Waechtler, T. Otto, M. Toader, O. Gordan, E. Sheremet, J. Martin, M. Hietschold, D.R.T. Zahn, T. Gessner, Enhancement of the thermoelectric properties of PEDOT:PSS thin films by post-treatment, J. Mater. Chem. A. 1 (2013) 7576–7583. doi:10.1039/c3ta11209h.

[248] B. Fan, X. Mei, J. Ouyang, Significant Conductivity Enhancement of Conductive Poly(3,4-ethylenedioxythiophene):Poly(styrenesulfonate) Films by Adding Anionic Surfactants into Polymer Solution, Macromolecules. 41 (2008) 5971–5973. doi:10.1021/ma8012459.

[249] A.M. Nardes, R.A.J. Janssen, M. Kemerink, A Morphological Model for the Solvent-Enhanced Conductivity of PEDOT:PSS Thin Films, Adv. Funct. Mater. 18 (2008) 865–871. doi:10.1002/adfm.200700796.

[250] S. Zhang, P. Kumar, A.S. Nouas, L. Fontaine, H. Tang, F. Cicoira, Solvent-induced changes in PEDOT:PSS films for organic electrochemical transistors, APL Mater. 3 (2015) 014911. doi:10.1063/1.4905154.

[251] E.E. Tkalya, M. Ghislandi, G. de With, C.E. Koning, The use of surfactants for dispersing carbon nanotubes and graphene to make conductive nanocomposites, Curr. Opin. Colloid Interface Sci. 17 (2012) 225–232. doi:10.1016/j.cocis.2012.03.001.

[252] C. Ou, L. Zhang, Q. Jing, V. Narayan, S. Kar-Narayan, Compositionally Graded Organic–Inorganic Nanocomposites for Enhanced Thermoelectric Performance, Adv. Electron. Mater. (2019) 1900720. doi:10.1002/aelm.201900720.

[253] C.J. Yao, H.L. Zhang, Q. Zhang, Recent progress in thermoelectric materials based on conjugated polymers, Polymers. 11 (2019) 1–19. doi:10.3390/polym11010107.

[254] N.W. Ashcroft, N.D. Mermin, Solid State Physics, Harcourt, 1976.

[255] J.C. Maxwell, A Treatise on Electricity and Magnetism, 3rd ed., Oxford University Press, 1904.

[256] R.B. Bird, W.E. Stewart, E.N. Lightfoot, Transport Phenomena, 2nd ed., John Wiley & Sons, 2007.

[257] K. Pietrak, T.S. Wisniewski, A review of models for effective thermal conductivity of composite materials, J. Power Technol. 95 (2015) 14–24.

[258] A. Miyamoto, S. Lee, N.F. Cooray, S. Lee, M. Mori, N. Matsuhisa, H. Jin, L. Yoda, T. Yokota, A. Itoh, M. Sekino, H. Kawasaki, T. Ebihara, M. Amagai, T. Someya, Inflammation-free, gas-permeable, lightweight, stretchable on-skin electronics with

nanomeshes, Nat. Nanotechnol. 12 (2017) 907–913. doi:10.1038/nnano.2017.125.

[259] P. Gutruf, E. Zeller, S. Walia, H. Nili, S. Sriram, M. Bhaskaran, Stretchable and Tunable Microtectonic ZnO-Based Sensors and Photonics, Small. 11 (2015) 4532–4539. doi:10.1002/smll.201500729.

[260] Q. Wei, C. Uehara, M. Mukaida, K. Kirihara, T. Ishida, Measurement of in-plane thermal conductivity in polymer films, AIP Adv. 6 (2016) 045315. doi:10.1063/1.4948447.

[261] H.-J. Hong, S.M. Kwan, D.S. Lee, S.M. Kim, Y.H. Kim, J.S. Lim, J.Y. Hwang, H.S. Jeong, Highly flexible and stretchable thermally conductive composite film by polyurethane supported 3D networks of boron nitride, Compos. Sci. Technol. 152 (2017) 94–100. doi:10.1016/j.compscitech.2017.09.020.

[262] J. Liang, T. Wang, P. Qiu, S. Yang, C. Ming, H. Chen, Q. Song, K. Zhao, T. Wei, D. Ren, Y.-Y. Sun, X. Shi, J. He, L. Chen, Flexible thermoelectrics: from silver chalcogenides to full-inorganic devices, Energy Environ. Sci. 12 (2019) 2983–2990. doi:10.1039/C9EE01777A.

[263] X. Shi, H. Chen, F. Hao, R. Liu, T. Wang, P. Qiu, U. Burkhardt, Y. Grin, L. Chen, Room-temperature ductile inorganic semiconductor, Nat. Mater. 17 (2018) 421–426. doi:10.1038/s41563-018-0047-z.

[264] R. Setnescu, I. Bancuta, T. Setnescu, V. Cimpoca, S. Jipa, I. V Popescu, Thermal characterization of semiconductor Bi2Te3 materials using DSC, J. Sci. Arts. 1 (2010) 95–102.

[265] M.D. Irwin, D.A. Roberson, R.I. Olivas, R.B. Wicker, E. MacDonald, Conductive polymer-coated threads as electrical interconnects in e-textiles, Fibers Polym. 12 (2011) 904–910. doi:10.1007/s12221-011-0904-8.

[266] L.J. van der Pauw, A method of measuring the resistivity and hall coefficient of discs of arbitrary shape., Philips Res. Reports. 13 (1958) 1–9.